Scanning Tunneling Spectroscopy on Graphene Nanostructures

I n a u g u r a l - D i s s e r t a t i o n

zur

Erlangung des Doktorgrades

der Mathematisch-Naturwissenschaftlichen Fakultät

der Universität zu Köln

vorgelegt von

Diplom-Physiker Fabian Craes

aus Werl

Köln 2014

Erster Berichterstatter:	Priv.-Doz. Dr. Carsten Busse
Zweiter Berichterstatter:	Prof. Dr. Achim Rosch
Vorsitz Prüfungskommission:	Prof. Dr. Ladislav Bohatý
Tag der mündlichen Prüfung:	08.04.2014

Abstract

This thesis describes investigations on graphene nanostructures by the means of scanning tunneling microscopy (STM) and spectroscopy (STS) in ultra high vacuum at low temperature (5.5 K), focused on their electronic structure on the local scale. The experiments are based on structurally highly perfect epitaxial graphene on Ir(111) [gr/Ir(111)], but extend the range towards new graphene based nanomaterials.

The first topic comprises the development of new nanomaterials which keep the structural coherency of epitaxial graphene on Ir(111) at a reduced electronic substrate interaction, in particular concerning graphene's quasi-relativistic Dirac particles. Therefor, we present the first study on graphene quantum dots (GQDs) on silver (gr/Ag). In STS, we observe the Ag(111) surface state on 15 ML of Ag on Ir(111), study its behavior in the presence of graphene, and discuss its role in the observation of Dirac electron confinement on GQDs. We find the surface state suppressed in 1 ML of Ag on Ir(111).

In a next step we present an experimental advancement towards a system, where the metallic surface states are completely absent, namely oxygen covered Ir(111) [O/Ir(111)]. In an STS study, we discover new oxygen superstructures on iridium under graphene and two types of charge effects in the GQDs' local density of states (LDOS). We present the first unambiguous experimental observation of Dirac electron confinement on GQDs [1]. We calculate the Dirac dispersion relation on the basis of our experimental data and confirm the efficient decoupling by DFT calculations and the direct observation of a Dirac feature in point spectroscopy and characteristic electron scattering processes. In addition to the benefit for the observation of Dirac confinement, our findings gain universal insight into the decoupling of graphene's electronic system from the metallic substrate by oxygen intercalation.

The studies are extended towards the unoccupied surface state spectrum at high energies in form of image potential states (IPSs). For the first time we experimentally prove the size dependence of IPSs due to confinement on GQDs acting as a quantum well [2]. We explain the occurrence of a strongly pronounced state, which is not the ground state, by an interplay of the LDOS and momentum conservation during tunneling. The positions of the IPSs can be tuned by chemical gating, which means the experimental realization of a quantum well tunable in both width and depth. We discuss the benefit of a direct

measurement of the local workfunction for the determination of the local doping level in graphene intercalation compounds.
In a next step we propose a route how to experimentally access the binding situation at the boundaries of GQDs on Ir(111), using the advanced technique of Inelastic Electron Tunneling Spectroscopy (IETS).
Finally, we observe metallic features in the LDOS which are related to one dimensional defects in an extended monolayer of epitaxial graphene on Ir(111).

Frequently used Symbols and Abbreviations

ARPES	-	Angle Resolved Photo-Emission Spectroscopy
BZ	-	Brillouin zone
CVD	-	Chemical Vapor Deposition
DFT	-	Density Functional Theory
(L)DOS	-	(Local) Density of States
fcc	-	face centered cubic
FWHM	-	Full Width at Half Maximum
FT	-	Fourier Transformation
GQD	-	Graphene Quantum Dot
gr	-	Graphene
IETS	-	Inelastic Electron Tunneling Spectroscopy
L	-	Langmuir, $1\,\mathrm{L} = 1 \times 10^{-6}\,\mathrm{Torr} \cdot \mathrm{s} \approx 1.33 \times 10^{-6}\,\mathrm{mbar} \cdot \mathrm{s}$
LEED	-	Low-Energy Electron Diffraction [3]
LT-STM	-	Low Temperature Scanning Tunneling Microscope
ML	-	Monolayer
QMS	-	Quadrupole Mass Spectrometer
STS/STS	-	Scanning Tunneling Microscopy/Spectroscopy
TPG	-	Temperature Programmed Growth
UHV	-	Ultra High Vacuum
XPS	-	X-Ray Photoemission Spectroscopy
XSW	-	X-Ray Standing Wave

Contents

PART I

Introduction

Layered and two dimensional materials provide access to exciting new physics as reduced dimensionality both offers a playground for testing important models in solid state physics and is of high relevance for technological applications. Two-dimensional materials differ significantly in their electronic, optical, mechanical and chemical properties from three dimensional bulk systems [4]. Very influential discoveries connected to reduced dimensionality include the quantum Hall effect [5], high temperature superconductivity [6, 7], topologically protected surface states [8], the Dirac electron systems of graphene [9, 10].

In recent years the two dimensional material graphene has become one of the most studied topics in solid state physics. Being the thinnest material in the world, graphene features a variety of stunning properties, ranging from outstanding structural to electronic properties, providing better electrical conductivity than silicon [11], better heat conductivity than copper [12], optical transparency [13, 14] and extreme mechanical robustness while being flexible at the same time [15].

The most striking properties of graphene are covered by its unique bandstructure, providing a usable energy range, where electrons move with a propagation speed independent of their energy, which is a behavior expected for massless particles [9, 16, 17]. Due to their mathematical description in a certain linear approximation, these charge carriers are called Dirac electrons [9]. For the first time revealing these striking features, in 2010 Andre Geim and Konstantin Novoselov were awarded the Nobel Prize in Physics "for groundbreaking experiments regarding the two-dimensional material graphene" [18]. Graphene evokes totally new physics, ranging from a high charge carrier mobility [19], easy doping [20], long spin coherence time [21] and the emergence of chiral edge states [22] to a half-integer quantum hall effect [16] and Klein-tunneling [23].

Two-dimensional materials are produced either directly by in-situ growth processes like the catalytic decomposition of a precursor on a substrate surface or molecular beam epitaxy, or by mechanical or chemical exfoliation from layered bulk crystals [24]. For the preparation of graphene all of these techniques have successfully been used. While actually the first detailed investigations have been performed on mechanically exfoliated layers of graphite [10, 24], an up-scalable process is predestined by liquid exfoliation [25, 26]. The preparation of graphene by in-situ growth processes on a substrate is obtained by either thermally induced surface segregation from a carbon containing bulk substrate like ruthenium or carbides (e.g. SiC) [27, 28] or by catalytic decomposition of organic molecules on a metal surface [29]. These methods are successfully used for obtaining samples with a high structural coherency [30, 31]. A further method of growing graphene on metal surfaces is provided by ethylene cracking with an ion source and subsequent

thermally activated decomposition [32], directing the beam of ethylene fractions even to catalytically inactive noble metal surfaces [e.g. Cu(111), Au(111)]. With some of these methods graphene production can already reach the industrial scale with an implication for industrial applications [33, 34]. Potential applications for example include electromechanical devices [35], gas sensors [36, 37], photovoltaics [38], supercapacitors [39], and high frequency transistors [40].

Despite this promising perspective, there are of course obstacles in turning the new physics into applications. These are mainly based on the fact that on the one hand the in-situ growth of graphene on a substrate provides superior structural quality but on the other hand alters its electronic properties which are closely connected to a perfect energetic equivalence of all carbon atoms [41, 42]. Another fact is that in order to use graphene in semiconductor applications [43–45], it has to rest on an insulating substrate [30, 46]. However, playing the game of controlled graphene disturbance can also be a key to exciting new physics as well as applications on its own, since the presence of a tailored substrate enables the tuning of graphene with respect to its electronic and morphological structure, as well as its chemical properties [47–50]. Thus a tailored substrate aims either at quasi-freestanding graphene or tuned properties.

A very flexible way of obtaining such substrates is the intercalation of foreign species between epitaxial graphene and the supporting substrate. Here progress has been made concerning numerous different intercalants yielding a variety of new properties, including the species of oxygen [47, 51], silver [52], caesium [53], europium [49, 50], hydrogen [54], potassium [55], and bromine [56].

This work addresses the ambivalence of the substrate influence on graphene directly, playing with both structural and chemical degrees of freedom in highly tunable graphene systems. The regime of the 2 D material restricted even down to 1 D or 0 D extents reveals new physics, using the combination of scanning tunneling spectroscopy and electron confinement for addressing the electronic properties of the material in a nutshell:

We explore new graphene based nanomaterials with simultaneous structural coherency of the carbon layer and maximum decoupling from the substrate, reporting on both silver (Chap. 4) and oxygen intercalated graphene quantum dots (Chap. 5 and Chap. 6). Our criterion for decoupling is the absence of covalent bonds to the substrate, still allowing interaction in form of such an amount of charge transfer (doping) that the Fermi level still resides in the energy range where the charge carriers are Dirac-like. We answer associated questions referring to the critical parameters for observing Dirac electron features in these systems and describe a route to suppress disturbing contributions of metallic surface

states to the local density of states. Several new aspects of the local electronic structure of graphene quantum dots are discovered, namely inducing a shift of the silver surface state (Chap. 4), new oxygen superstructures on Ir(111) (Chap. 5), charge effects (Chap. 5) and the confinement of both Dirac (Chap. 6,[1]) and high energy free-electron surface states (Chap. 7,[2]). Finally, we propose a way how to address the binding character at the boundaries of graphene quantum dots (Chap. 8) and prove the existence of metallic wires in one dimensional defects in extended graphene on Ir(111) (Chap. 9). Details on the electronic structure of graphene, the most relevant aspects on surface electrons and the envolved experimental techniques are provided in Chap. 1. The sample preparation routines are discussed in very detail in Chap. 3 and a brief introduction to our experimental setup appears in Chap. 2.

CHAPTER 1

Fundamentals

In this chapter a dense introduction to the most relevant aspects affecting this work is given. Starting with the experimental techniques which have been employed for this work we continue with an introduction into the field of graphene. We provide an overview on the aspects of electronic behavior in systems with reduced dimensionality, especially covering the topics of electron scattering on surfaces and 2D confinement with a graphene bias. Finally, the latter aspects are discussed from an STM point of view.

1.1 Scanning Tunneling Microscopy and Spectroscopy

The topic of this section will be a brief introduction into the techniques of STM and STS as excellent tools for addressing alterations of the LDOS. Detailed descriptions of the STM principles are presented in Ref. [57].

Scanning Tunneling Microscopy

The scanning tunneling microscope (STM) has been developed in 1982 by G. Binnig and H. Rohrer [58]. In 1986 they were awarded the Nobel Prize in Physics for this work. Based on the quantum mechanical tunneling effect, the microscope uses a very sharp - in the ideal case atomically sharp - conductive tip above a conductive sample surface in a distance of 5..10 Å , forming two electrodes. In such a small distance the electronic wavefunctions of the closest atom of the tip and the sample overlap. Once applying a bias voltage V_0 between them, a tunneling current I sets in. The value of I depends on the LDOS of the tip and the sample, their distance z and the tunneling matrix element (i.e. the coupling of the initial and the final states). The exponential dependence of I on the distance z yields the extremely high vertical resolution of STM: A change in z of 1 Å results in a change in I of approximately one order of magnitude [59]. For imaging, the tip is moved along the surface, using piezo actuators. During this scanning process the distance z is controlled by a feedback loop circuit to a setpoint value of I (in constant current mode). Therefore, STM imaging is mainly determined by five parameters: The bias voltage V_0, the tunneling current I and the spatial parameters z, x, y. According to Bardeen [60], I is given by

$$I \propto \int_{-\infty}^{+\infty} |M(E)|^2 \rho_{\mathrm{S}}(E - eV_0)\rho_{\mathrm{P}}(E)[f(E - eV_0) - f(E)]\mathrm{d}E \tag{1.1}$$

with $|M(E)|$ the tunneling matrix element, $\rho_{\mathrm{S}}(E - eV_0)$ and $\rho_{\mathrm{P}}(E)$ the density of states of the tip and the sample at an applied bias voltage V_0 and $f(E)$ the Fermi function.
A simple theory of STM is derived from (1.1) by Tersoff and Hamann [61], assuming a metallic s-orbital as the tip electrode and a bias voltage V_0 which is small compared to the workfunction of the sample Φ_{sample} ($eV_0 << \Phi_{\mathrm{sample}}$):

$$I \propto V_0 \cdot \rho_{\mathrm{S}}(E_{\mathrm{F}})\rho_{\mathrm{P}}(\mathbf{R}_{\mathrm{tip}}, E_{\mathrm{F}}), \tag{1.2}$$

with $\rho_{\mathrm{P}}(\mathbf{R}_{\mathrm{tip}}, E_{\mathrm{F}})$ the density of states of the sample surface at the center of the s-orbital of the STM-tip $\mathbf{R}_{\mathrm{tip}}$. Since the DOS in first approximation decays exponentially into the vacuum, one obtains an I depending inversely exponential on the distance z:

$$I(z) \propto e^{-2\kappa z}. \tag{1.3}$$

For the example of semiconductors $eV_0 \ll \Phi_{\text{sample}}$ does not hold anymore, therefore the description of I has to be modified. Especially deviating from the simple picture used above (Tersoff-Hamann), a finite energy range defined by V has to be taken into account by integration. A transmission probability (compare to Wentzel-Kramers Brillouin (WKB) approximation) $T(V,W)$ is introduced, depending on V_0 and on the workfunction Φ_{sample} of the sample surface. With this one obtains

$$I \propto \int_{E_\text{F}}^{E_\text{F}+eV_0} |T(V_0,\Phi_{\text{sample}})| \rho_\text{S}(E) \rho_\text{P}(\mathbf{R}_\text{tip},E) \text{d}E. \tag{1.4}$$

The STM can be operated in different modes, depending on how the parameters V, I, and x,y,z are varied. For topographic imaging, all measurement in this work were performed using the constant current mode. This means keeping I and V_0 constant while varying the tip sample distance with a z feedback-loop in order to compensate for a varying sample LDOS while scanning the surface in the x and y directions. In this case the voltage which is used to elongate and shrink the z-piezo actuator for the distance variation on each surface coordinate (x,y) is recorded as the measurement quantity. Data recording is performed in an assignment of the modus operandi dependent measurement quantity to a matrix of N rows and M columns of discrete (x,y) surface coordinate tuples (STM image pixels).

Scanning Tunneling Spectroscopy

Scanning Tunneling Spectroscopy comprises all modes providing access to the LDOS of the surface. The most widely used modes are $\text{d}I/\text{d}V(E - E_\text{F})$ point spectroscopy and spatial constant energy mapping. Performing $\text{d}I/\text{d}V(E - E_\text{F})$ point spectroscopy requires fixing the tip-sample distance z at a certain coordinate (x,y) on the surface by choosing an appropriate setpoint of a bias voltage V_0 and a tunneling current I with closed feedback-loop and performing a subsequent onsite voltage sweep with open feedback-loop. The latter means that the variation in the tunneling current as the measurement quantity during the voltage sweep is not influenced by a varying orbital overlap of the tip and the sample states by varying the tip-sample distance. Thus, the measurement signal is $I(V)$ depending on the sample LDOS at energies defined by $\mathbf{eV} = \mathbf{E} - \mathbf{E}_\text{F}$. Decisive aspects are the stability of the tip-surface distance (and also lateral position) regarding thermal drift, the suppression of diffusion processes at the tip and the sample, and an improved energy resolution (see below). Therefore, STS measurements are generally performed at low

temperature (5.5K). According to Tersoff and Hamann the DOS at a surface coordinate is proportional to the differential conductivity $\mathrm{d}I/\mathrm{d}V$ at fixed V_0 [61, 62]:

$$\frac{\mathrm{d}I}{\mathrm{d}V} \propto |T|^2 \rho_{\mathrm{S}}(E_{\mathrm{F}}) \rho_{\mathrm{P}}(E_{\mathrm{F}}). \tag{1.5}$$

Since the transmission probability is difficult to access, $|T|$ is often approximated by the total conductivity of the tunneling junction $\overline{I/V}$ [62]. The approximation works well for higher energies (several hundreds of meV to eV) and is problematical close to zero voltage since $I(V = 0)$ vanishes and thus $\overline{I/V}$ diverges.
Experimentally these values can be accessed by a direct measurement of $\frac{\mathrm{d}I}{\mathrm{d}V}$ using the lock-in technique [61]. Therefor a weak AC voltage $V_{\mathrm{mod}}\cos(\omega \mathrm{t})$ is added to V_0:

$$V = V_0 + V_{\mathrm{mod}}\cos(\omega \mathrm{t}).$$

The resulting tunneling current I is used as an input signal to a lock-in amplifier. This filters the ω AC fraction of the tunneling current via an integration of the product of I with a reference signal with the same frequency ω. As obtained by a Taylor expansion at V_0 in first order, the amplitude of the AC current fraction is proportional to $\mathrm{d}I/\mathrm{d}V$, and in second order proportional to the second derivative [63]:

$$\begin{aligned}
I(V_0 + V_{\mathrm{mod}}\cos(\omega \mathrm{t}) &= I(V_0 + \Delta V) \\
&\simeq I(V_0) + \frac{dI(V)}{dV}(\Delta V) + \frac{d^2 I(V)}{dV^2}\frac{1}{2}(\Delta V)^2 + ... \\
&\simeq I(V_0) + \frac{dI(V)}{dV}(V_{\mathrm{mod}}\cos(\omega \mathrm{t})) + \frac{\mathrm{d}^2\mathrm{I(V)}}{\mathrm{dV}^2}\frac{1}{2}(\mathrm{V}_{\mathrm{mod}}\cos(\omega \mathrm{t}))^2 + ... \\
&\simeq I(V_0) + \frac{dI(V)}{dV}(V_{\mathrm{mod}}\cos(\omega \mathrm{t})) + \frac{\mathrm{d}^2\mathrm{I(V)}}{\mathrm{dV}^2}\frac{1}{4}\mathrm{V}_{\mathrm{mod}}^2(1 + \cos(2\omega \mathrm{t})) + ...
\end{aligned}$$

The output signal of the lock-in amplifier can therefore be used for direct spectroscopic representation [64], either in $\mathrm{d}I/\mathrm{d}V$ point spectra or in $\mathrm{d}I/\mathrm{d}V$ spatial mapping at constant energy. In case of the latter one, a constant current topograph (integrated density of states) and a spatial map of the lock-in signal $\mathrm{d}I/\mathrm{d}V$ at a fixed bias voltage V_0 are recorded simultaneously. One obtains a spatial distribution of the LDOS at an energy $E = E_{\mathrm{F}} + eV$.
STS provides the most local technique for spectroscopic investigations on a surface.
Difficulties include the facts that in reality the tip is not featureless in the sense of a free electron gas as assumed in many calculations that due to vanishing tunneling transmission probability it is impossible to measure sample states that do not overlap with states of the tip and that it lacks chemical sensitivity. Controlling the microscopical shape of the tip and thus the orbital which is involved in the tunneling process remains though, although

there are numerous efforts reported in literature for certain tip-sample combinations, e.g. by adding molecules to the tip [65] or in spin-polarized STM [66].
The energy resolution depends on the temperature and the bias modulation used for the lock-in technique. According to [67] it amounts to:

$$\Delta E = \pm\frac{1}{2}\sqrt{(3.3k_{\mathrm{B}}T)^2 + (1.8eV_{\mathrm{mod}})^2}.$$

Details of the lock-in preferences and parameters used for this work are described in Chap. B.

Inelastic Electron Tunneling Spectroscopy

As mentioned above, the second derivative is proportional to the second harmonic lock-in signal. Now I would like to draw a connection to the associated phenomenon of inelastic electron tunneling.
Inelastic Electron Tunneling Spectroscopy (IETS) in a simple picture is based on the fact that the charge transfer occurring with tunneling is able to cause a temporary charge redistribution in the object under investigation on the sample surface (e.g. a molecule) which is related to a change in molecular bond length. Since this redistribution might relax by exchanging charge with the substrate, a vibrational mode (phonon) is created and therefore directly connected to the tunneling current [68]. The tunneling process thus becomes inelastic via the relaxation process. Inelastic processes might also include the emission of light. The tunneling process mentioned is only possible if the connected phonon energy is allowed in the system. Thus, in the $\mathrm{d}I/\mathrm{d}V$ spectrum this process will appear as a second tunneling channel in addition to the standard tunneling process generally assumed to be elastic. It shows a sudden step-like increase in the signal at a certain threshold energy (the phonon excitation energy $\hbar\nu$) for both positive and negative bias voltages. The steps in $\mathrm{d}I/\mathrm{d}V$ of course correspond to peaks in $\mathrm{d}^2I/\mathrm{d}V^2$, which is therefore a suitable quantity in IETS (see Fig. 1.1). Due to this mechanism, the most important criterion for identifying peaks in the second derivative of the $I(V)$ characteristics as signatures of inelastic tunneling is their $\pm\hbar\nu$ mirror antisymmetry in energy with respect to 0 V (E_{F}): Of course the direction of current does not induce any change to the excitation process. The principles of charge redistribution and relaxation remain the same.
IETS is widely used to study molecular excitations on the local scale, requiring not more than just one single molecule, making it the most sensitive technique for vibrational excitation studies (e.g. [63, 69–71]). Another advantage is that, compared to infrared (IR) and Raman spectroscopy [72], also optically forbidden excitations can be observed.

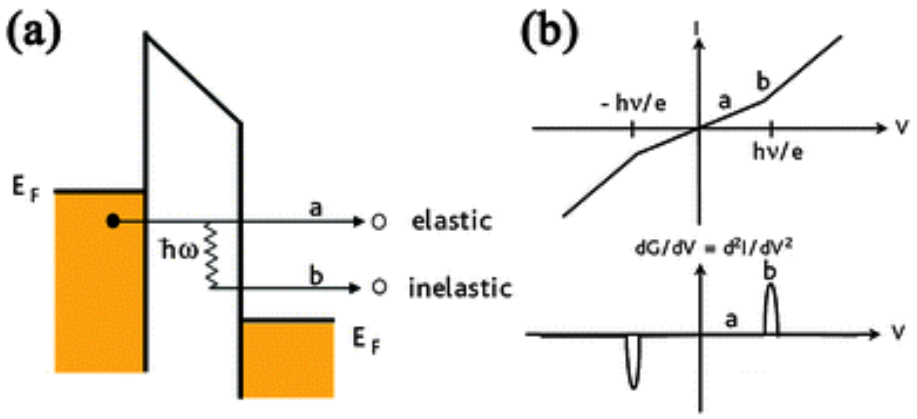

Figure 1.1: (a) Schematic representation of elastic **a** and inelastic **b** tunneling processes between two electrodes (e.g. STM-tip and sample) at an applied bias voltage. (b) Conductivity $I(V)$ (top) and its second derivative (bottom), indicating the features of the curves associated with elastic **a** and inelastic **b** tunneling processes. Reproduced from [69] with permission of The Royal Society of Chemistry.

Having its roots in metal/oxide/metal tunneling junctions (e.g. [73, 74]), it can be also realized in fixed-point STS as well as in STS spatial mapping [68, 75–78]. In the framework of this work it is therefore referred to as STM-IETS. This measurement technique has been extensively developed and used by the group of Wilson Ho [75, 79]. Via molecular excitations, STM-IETS provides chemical sensitivity in an indirect way which is lacking in elastic STM and STS.

In general STM-IETS requires the use of two lock-in amplifiers with a synchronized reference signal, since this combination enables the simultaneous measurement of $\mathrm{d}I/\mathrm{d}V$ and $\mathrm{d}^2I/\mathrm{d}V^2$. In the framework of this thesis STM-IETS is applied for investigations on the boundaries of GQDs presented in Chap. 8.

1.2 Angle-Resolved Photoelectron Spectroscopy

Angle-Resolved Photoelectron Spectroscopy (ARPES) is an experimental technique primarily aiming at the investigation of the occupied electronic structure in the reciprocal space of a solid's surface and near-surface region. It also yields information on the lifetimes of excited states. ARPES is based on the photoelectric effect, measuring the kinetic energy of electrons emitted from the surface of an initial state with binding energy E_B in the solid after absorption of a photon with energy $\hbar\nu$ [59]. In the framework of this work photons were created with a helium discharge lamp (ultraviolet photoelectron spectroscopy). The kinetic energy of the photoelectrons leaving the surface is measured with an electron energy analyzer.

Often, the process is treated as a **three-step process**: The *'optical excitation between the initial and final bulk Bloch eigenstates, travel of the excited electron to the surface, and escape of the photoelectron into vacuum after transmission through the surface potential barrier'* [80].

For the energy the process yields

$$E_\mathrm{kin} = \hbar\nu - \Phi - E_\mathrm{B} \tag{1.6}$$

with Φ the workfunction and E_B the binding energy. If the translational symmetry of the sample surface is conserved, the in-plane component of the initial state momentum is also conserved:

$$\hbar k_{i\parallel} = \hbar k_{f\parallel} = \hbar^{-1}\sqrt{2mE_\mathrm{kin}}\sin\theta \tag{1.7}$$

with θ the polar angle. Since the translational symmetry is not conserved in normal direction to the surface, $k_\perp$ is also not conserved. Details on ARPES are described in Refs. [80, 81].

The unoccupied spectrum can be probed using a more complex process called two-photon photoemission. Here, using a pulsed laser, a photon is used to excite an electron into an intermediate state in the unoccupied spectrum, a second one is used to probe the excited state in a photoemission process [82, 83].

In this thesis ARPES measurements are involved in the investigations on quantum confinement of Dirac electrons (see Chap. 6).

1.3 Freestanding Graphene

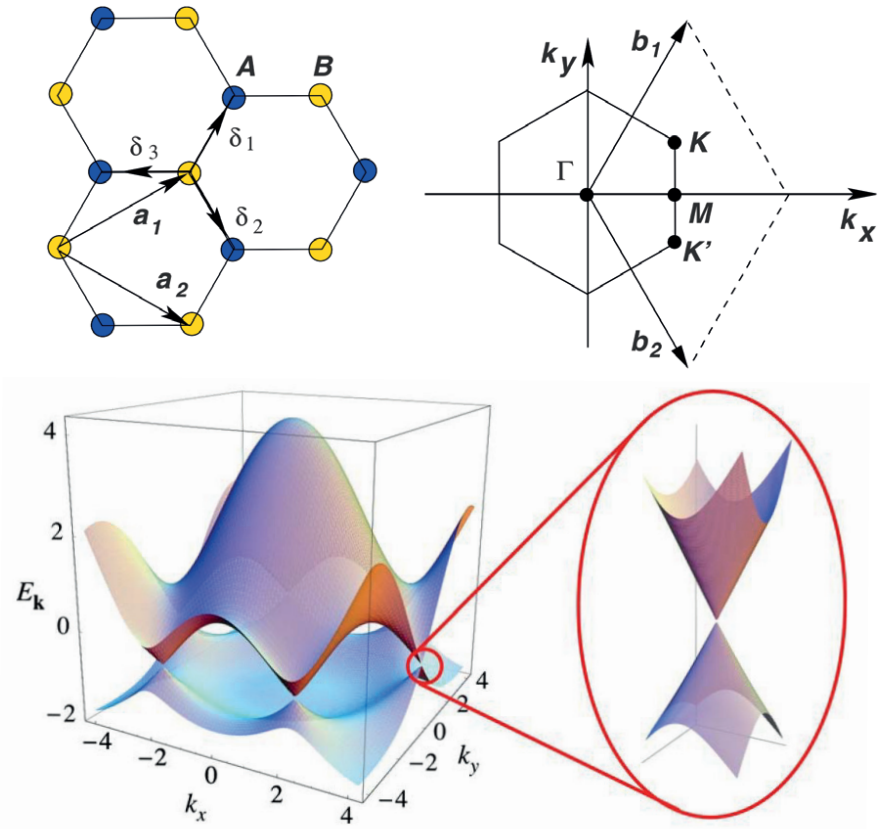

Figure 1.2: Honeycomb lattice and its Brillouin zone. Top left: honeycomb lattice structure of graphene, made out of two interpenetrating triangular lattices (a_1 and a_2 are the lattice unit vectors, and δ_i, $i = 1,2,3$ are the nearest-neighbor vectors). Top right: corresponding first Brillouin zone in reciprocal space with unit vectors b_1 and b_2, K and K' points. The Dirac cones are located at the K and K' points. Bottom: energy spectrum in the units of the hopping parameter t as obtained from a tight binding calculation [9, 84]. Reprinted figures with permission from [9]. Copyright 2009 by the American Physical Society.

Freestanding graphene provides the basis for understanding the electronic structure in absence of the complications induced by interactions with a substrate. The following section gives a brief overview on the most important electronic properties of freestanding graphene. For a more detailed introduction the reader is referred to literature, e.g. the reviews of A. H. Castro Neto [9] and A. K. Geim [10].

Graphene is formed by one monolayer of sp^2 hybridized carbon atoms in a honeycomb lattice, thus providing in total three sp^2 and one p_z orbital at each of the two identical atoms in a unit cell. The structure can also be viewed as a superposition of two displaced triangular sublattices [9]. In the honeycomb lattice structure each atom is bound to three neighbors with a nearest-neighbor-distance of a_{nn} =1.42 Å[1], resulting in three orbitals forming interconnecting σ bonds in-plane and leaving one p_z-orbital out-of-plane. The neighboring, half-filled p_z orbitals also overlap and form graphene's π-system, giving rise to a delocalized electron system.

The unique electronic properties of graphene are intimately connected to the bandstructure at the K and K' points in the Brillouin Zone (BZ) (Dirac points, see Fig. 1.2) where the bonding and anti-bonding π bands touch at an energy $E_{\mathrm{D}} = E_{\mathrm{F}}$ with E_{D} the Dirac energy and E_{F} the Fermi energy (see Fig. 1.2). The band structure can be calculated with a tight-binding calculation [9, 26, 84], leading to

$$E(\mathbf{q}) = \pm t\sqrt{3 + 2\cos\left(\sqrt{3}k_y a_{\mathrm{nn}}\right) + 4\cos\left(\frac{\sqrt{3}}{2}k_y a_{\mathrm{nn}}\right)\cos\left(\frac{3}{2}k_x a_{\mathrm{nn}}\right)}$$

with t the nearest neighbor hopping energy, the - sign for the occupied π-band, + for the unoccupied π^*, a_{nn} the nearest neighbor distance, and $\mathbf{q} = \mathbf{k} - \mathbf{K}$ the wavevector measured with respect to the K point.

At the Dirac points the bandstructure can be described in a linear approximation, using two-component wave functions and the 2 D relativistic Dirac-Weyl equation for massless quasiparticles [9, 10] with the Hamiltonian

$$H = v_f \sigma \mathbf{q}.$$

The two-component wave functions resemble properties of a spinor wavefunction and give rise to a pseudospin variable [9].

In this model, graphene's electrons at the K points feature an energy-independent propagation speed with a (Fermi) velocity of $v_{\mathrm{F}} = 1 \times 10^6$ m/s [85]. The character of graphene as a zero bandgap semiconductor is closely related to the perfect sublattice symmetry in freestanding graphene, with two identical C atoms in the unit cell. Unique properties like e.g. the anomalous integer quantum Hall effect [86], Klein tunneling [23] and 1D edge states [9] and Zitterbewegung [87] are related to the exceptional electronic features. Note that due to the low density of states in the vicinity of E_D doping of graphene is highly effective and is achieved even by backgating [20].

[1] the lattice constant results to a =1.42 Å$\times\sqrt{3}$=2.46 Å [84]

A new class of Dirac electron systems is given by Topological Insulators (TIs). These 3(2)-dimensional bulk materials show 2(1)-dimensional surface states at their surface, which also behave like massless Dirac particles driven by a combination of strong spin-orbit coupling (SOC) and certain symmetries, e.g. connected to time reversal invariance (TRI) [8] or mirror symmetry [88, 89] of their bandstructure. Both classes of Dirac electron systems (graphene and TI) are distinguished by different topological invariants [$\nu = 0$ (graphene), $\nu = 1$ (TI)] which experimentally e.g. lead to different quantization in the fractional quantum hall effect [90].

Since it is the main issue of this section I would like to emphasize the importance of the sublattice symmetry of freestanding graphene. Since the two carbon atoms in the unit cell A and B are identical, *'there are thus two zero-energy states: one in which the electron resides on atom A, the other in which the electron resides on atom B. Both the electron and hole states exist at exactly zero energy, hence zero band gap and zero mass'* [41]. This in turn means that massless dirac particles gain mass once the perfect sublattice symmetry is broken, the two C atoms in each unit cell are not at the same energy anymore [41]. Mass gain in graphene was recently shown for van der Waals heterostructures [42]. Sublattice asymmetry is basically also present for the systems discussed in the following sections together with hints how to restore it.

1.4 Interacting Graphene

Up to now large graphene areas can only be prepared by epitaxial growth on a substrate. The best structural quality of graphene films is obtained by the decomposition of carbon containing precursors on catalytically active metal surfaces, e.g. Pt(111) or Ir(111). The presence of a substrate always influences the electronic properties of the graphene layer, the deviation thus depends on the specific binding character to the substrate which in general may vary spatially between a dominating physisorbed and chemisorbed character [17, 26]. Due to a lattice mismatch with the respective substrate, epitaxial graphene shows characteristic moiré superstructures as for example reported for the metal substrates Ir(111) [91, 92], Cu(111) [93], Rh(111) [94], Pt(111) [95] and Ru(0001) [27]. The presence of a substrate and the associated disturbance of graphene's electronic system may be viewed as a tradeoff for structural quality on a large scale. But it also opens new possibilities of specifically tuning the electronic properties. Interesting comments on the pros and cons of disturbing graphene are provided by Hasegawa et al. in Ref. [48] (references adapted to the list of this work): *'Electronic properties of this pristine nanostructure*

are easily modified by mechanical strains, deformations, metal contacts, adsorption of foreign atoms or molecules, external fields, and other physical contacts with environment. These influences are unavoidable in most experiments as well as possible applications and easily impair intrinsic, novel properties of graphene. However, we can also make use of these effects to modulate electronic properties, thereby extending a range of technological applications. One of these examples is a bandgap opening, which is essential for graphene to be used for semiconductor devices. A substantial bandgap can be induced in several ways. Early examples are bandgap openings in epitaxial graphene on SiC (Refs.[96] and [97]) and graphene on hexagonal boron nitride (h-BN) [98]. A bandgap is also induced by electron confinement (nanoribbon) [99, 100], biasing [101, 102] or doping [103] bilayer graphene, patterning graphene with periodic holes (nanomesh or antidote lattice) [104, 105], or moiré-patterned hydrogen adsorption [106], and so on. These bandgap openings can be interpreted in terms of either the hybridization of electronic states at K and K' points in the Brillouin zone or the symmetry breaking of A and B sublattices by external or internal perturbations [96].'

This work uses gr/Ir(111) as a basis system for all experiments. Therefore, the next section provides an overview on the altering of graphene's properties by the presence of the Ir(111) surface underneath.

Graphene on Ir(111)

The mismatch between the lattice constants of freestanding graphene $a_{\mathrm{gr}} = 2.46\,\text{Å}$ and Ir(111) $a_{\mathrm{Ir(111)}} = 2.72\,\text{Å}$ leads to a moiré superstructure with a lattice constant of $a_{\mathrm{m}} = 25.24$ Å [17, 26]. The experimentally easily accessible moiré lattice constant together with the precisely known lattice constant of Ir(111) yields a lattice constant of gr/Ir(111) of $a_{\mathrm{gr/Ir(111)}} = 2.452(5)$ Å [17, 26]. Though providing superior structural quality and yielding a weak substrate interaction from the structural point of view [17], gr/Ir(111) shows significant signs of a substrate influence when it comes to the phononic and electronic properties. First, the typical Raman features of freestanding graphene are absent in gr/Ir(111) [107]. Second, altering of the electronic properties includes a band gap opening at the K point by about 70 meV [26], a doping of $E_D \approx 100\,\text{meV}$, the emergence of replica cones and minigaps caused by the moiré potential [108], the absence of defect states [109], the absence of characteristic $(\sqrt{3} \times \sqrt{3})\mathrm{R}\,30^\circ$ intervalley scattering patterns on extended areas and the unclear observations of Dirac electron confinement on GQDs on Ir(111) [110–113]. Further on, one of the two IPS series expected for freestanding graphene is absent [114] (unlike e.g. in gr on SiC [115, 116]), indicating that the graphene surface

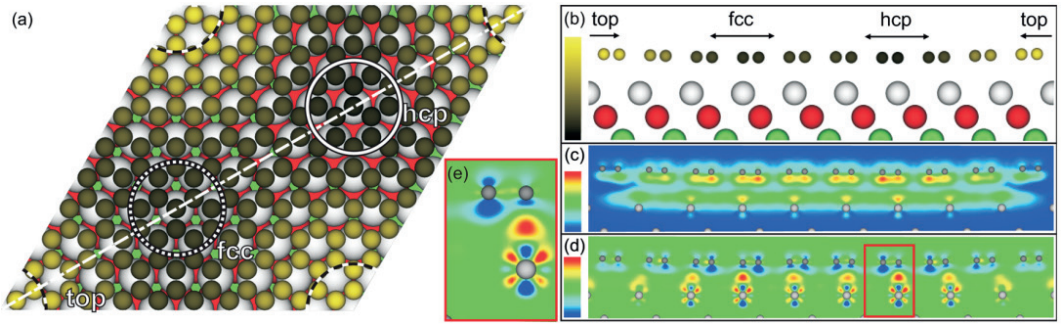

Figure 1.3: DFT calculation of the moiré unit cell of gr/Ir(111). Top view (a) of the moiré unit cell with high symmetry regions (hcp, fcc, top) indicated by circles. Side view (b) along the dashed line in (a) showing the first three layers of iridium atoms (white, red, and green spheres) and the carbon atoms (yellow) in same colour code as (a). Visualisation of the nonlocal-correlation binding-energy density (c) due to adsorption. Charge transfer (d) induced by adsorption, with magnification of the red box in (e). The range of the colour scale is -0.0138 Å^{-3} (blue) for a reduced electron density to +0.013 Å^{-3} (red) for an enhanced one, while green indicates the average electron density. Reprinted figure with permission from [17]. Copyright 2011 by the American Physical Society.

facing the substrate is definitely different from that one facing the vacuum side. Mostly this disturbance of graphene's electronic structure can be viewed as a local instability of the predominating van der Waals bonding towards a more chemical character as mentioned above [17, 26], see Fig. 1.3.

In more detail, all the local electronic effects mentioned before face the fact that Ir(111) presumably provides two different types of surface states: First there is a typical Shockley-type surface state dispersing in the way of free electrons (parabolic dispersion) which was observed in several ARPES studies [92, 108, 114]. Second, there is a very local type of surface state, presumably originating from the localized, out-of-plane Ir(111) d_z-orbitals, providing a flat dispersing surface state with high effective mass which hybridizes with graphene's π-system [107]. The Shockley type surface state S_0 is known to be Rashba-split [1, 117]. It changes its properties when graphene is located on the surface [117]: The unperturbed Rashba-split band, evolving from $E_0 = -0.34$eV with negative effective mass, shifts upwards to $E_0 = -0.19$eV when graphene is on the surface.

Whereas the argument of missing intervalley scattering might be challenged by the fact that the observation requires a certain value of defect concentration on the substrate providing a sufficient amount of scatterers which is not present in gr/Ir(111) due to its high structural

quality, especially graphene's behavior at defects [109] and edges of nanostructures like quantum dots [110] shows an even enhanced favored chemical binding of graphene to the substrate [118].

1.5 Weakly Interacting Graphene

Graphene Intercalation Compounds

One possible way of tuning the graphene-substrate interaction is the intercalation of species between the carbon layer and the substrate. Intercalation opens the window to a broad range of interesting topics as the presence of intercalants tunes the chemical character of the graphene sheet e.g. in the sense of adsorption sites for clusters [51] or ionic adsorbates [50] as well as the bonding character towards the substrate, depending on the specific intercalant with dramatic effects on the charge transfer occurring between graphene and the substrate. This immediately leads to the possibility of tuning the occupied density of states at E_{F} by doping epitaxial graphene via intercalation [47]. Also structural changes in the graphene layer are closely connected to the changes in the binding character, e.g. reduced moiré corrugation due to a reduced substrate interaction. One can even envision that intercalation processes can be used to tailor electronically structured graphene with neighboring regions of different doping levels [50] by using self-organized structures as observed in europium intercalation [49]. Aiming at freestanding graphene, by choosing an appropriate intercalant decoupling of the carbon layer in both a structural and an electronic sense is achievable. Intercalation can even be used for the exfoliation of an epitaxial graphene layer [56].

Oxygen Intercalated Graphene

Oxygen intercalation of gr/Ir(111) is achieved by exposing gr/Ir(111) to a dosage of molecular oxygen at an intercalation temperature where etching processes are absent [51]. The molecular oxygen dissociates on the uncovered Ir(111) surface. This necessary step in the intercalation process limits the procedure to non closed graphene layers. Recent publications comprising XPS and STM experiments report on the need for constant oxygen pressure to make it favorable for the graphene edges to unbind from the substrate [51]. This mechanism implies that the probability of a graphene area to be successfully intercalated depends on the edge length. This leads to the fact that small islands with short boundaries tend to resist intercalation. Vice versa the required temperature for

successful intercalation also depends on the average size of the graphene structures. Results for small nanostructures, namely GQDs, are presented in Chap. 5. We show the first real space observations of the intercalation temperature influence on the oxygen superstructure realized underneath the GQDs. High temperatures (448 K) result in a dominating (2×1) intercalation superstructure with respect to Ir(111). Those iridium areas which are not covered by graphene show the (2×1) superstructure well known from the oxygen covered pristine iridium surface [51, 119]. Comparing pristine Ir covered by the (2×1) oxygen superstructure with the situation of gr/O/Ir(111), XPS experiments report no difference in the Ir surface atoms binding energies [51]. In addition, no splitting of the C1s binding energies due to a hypothetical existence of C-O bonds is observed. In total, this indicates a situation where the oxygen is bound to the iridium. Especially the observed superstructures are expected to be with respect to Ir(111), yielding a weak interaction with the carbon layer. These findings are well supported by the results of XSW measurements on graphene intercalation compounds performed by Sven Runte [120], stating for oxygen intercalated graphene a closer distance of the oxygen atoms to the iridium substrate compared with the distance to the carbon layer. DFT calculations by Nicolae Atodiresei and Vasile Caciuc support the experimental findings by yielding the emergence of an oxygen-iridium hybrid state at the surface but absent binding between the oxygen and the carbon layers in contrast to the situation without an intercalant [1, 26]. Therefore oxygen is a decent intercalant to achieve decoupling of the carbon layer from the metal substrate. Oxygen intercalation alters the graphene bandstructure significantly by inducing a p-doping of about 600 meV [47].

Silver Intercalated Graphene

Like noble metals in general, also silver is expected to act as a weakly interacting substrate for graphene. In theoretical studies graphene is expected to be physisorbed on the Ag(111) surface and the Dirac cone is expected not to show a bandgap at all [48, 121]. Due to the lack of catalytic activity, the method of choice for the growth of structurally highly perfect graphene on metal substrates, the catalytic decomposition of ethylene, cannot be used in this case. A possible way of obtaining graphene on silver is to use the standard grown gr/Ir(111) and add a layer of silver by evaporation. Afterwards the sample is heated, yielding an intercalation of the silver layer and resulting in the desired monolayer graphene on silver configuration. The decoupling from the Ir(111) substrate can be tuned by choosing the appropriate silver interlayer thickness. Silver intercalation of epitaxial graphene is also proposed for the decoupling of graphene on Ni [48, 121]. An alternative

approach in preparation is presented in Ref. [122], using direct C evaporation from a graphite carbon source. This process also leads to gr/Ag which is experimentally found to be weakly interacting.

Like Ir(111) the Ag(111) surface shows a Shockley-type surface state. It has an onset energy of $E_0 = -75\,\mathrm{meV}$ and is known to persist under 1 ML of several noble gases like Ar, Kr or Xe [123].

In a numerical study graphene on silver is discussed as a substrate in biosensor applications [124].

1.6 Surface States

After having reviewed some fundamental aspects of the 2D electron system of graphene, we turn to another 2D electron system, namely surface states of bulk solids. The presence of a surface has dramatic influence on the electronic states of a solid [59, 125, 126]. In contrast to the choice of periodic boundary conditions leading to Bloch waves with a real momentum **k**, the Schrödinger equation has to be solved with the boundary condition of a free surface. On the one hand the presence of a surface means an interface to the vacuum side, meaning a broken periodicity of the lattice potential in a 3D solid. On the other hand it also means an altering of the remaining periodic lattice potential close to the surface. This is especially valid for broken covalent bonds e.g. in semiconductors.

Connected to the high surface potential, all electronic wavefunctions have to decay exponentially into the vacuum. Since at the solid-vacuum interface the continuity of the wavefunction is postulated as a connection condition, also solutions of the Schrödinger equation which do not describe a meaningful physical behavior within the bulk region are recognized: Now also solutions with imaginary **k** momentum values become meaningful, which grow exponentially inside the bulk towards the surface but are now connected to the exponential decay at the interface, see Fig. 1.4. This situation corresponds to a locally enhanced probability density at the surface. In the framework of the nearly free electron approximation these states are referred to as (Shockley-)surface states, appearing predominantly in metals and small bandgap semiconductors. Surface states which are mathematically obtained by a pure tight-binding model with strongly perturbed surface potential (e.g. in d-electrons of transition metals, semiconductors, insulators) are referred to as Tamm-states [125]. Both types of surface states form two dimensional electron gases (parabolic dispersion) at the surface:

$$E(k) = E_0 + \frac{\hbar^2 k^2}{2m^\star} \tag{1.8}$$

with $m^\star$ the effective mass.

It can be shown that in the case of semiconductors and insulators these states are energetically always located within the bandgap [126], in the case of metals in the projected bulk band gap [59]. Therefore, at appropriate population surface states can basically act as conducting states at the surface of bulk semiconductors or insulators, sometimes appearing in rare combinations of physical properties like the spin-polarized surface state in the ferromagnetic semiconductor EuO observed by our group [128]. However, their existence is fragile with respect to the specific structure of the surface in the sense of local potentials.

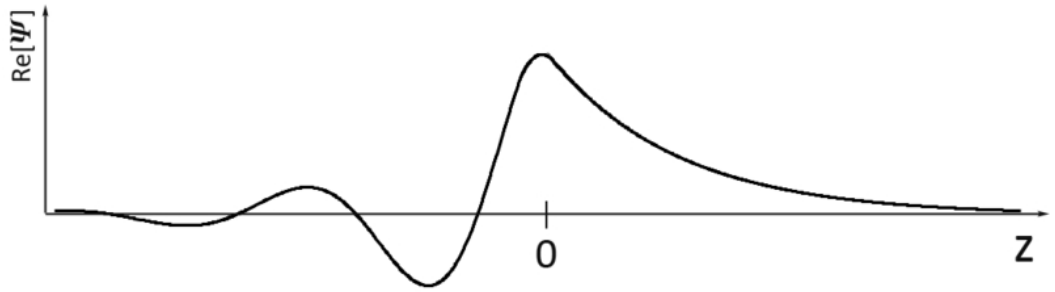

Figure 1.4: Solution of the Schrödinger equation for states localized at the surface: The real part Ψ exponentially decays both into the bulk and the vacuum. The value $z = 0$ determines the surface [127].

Adsorbates at the surface might cause a saturation of unsaturated bonds and therefore a bandgap in the surface state spectrum or even a vanishing of the surface states, killing a surface conductivity. Surface states which are degenerate with bulk states are called surface resonances. In sum, at the solid vacuum interface three types of electronic states in the occupied spectrum exist [57]:

- Bloch-bulk states which are delimited by the surface and therefore decay exponentially into the vacuum.
- Pure surface states, which decay exponentially into both the bulk and the vacuum and are located at the surface only.
- Surface resonances with a high amplitude at the surface and a reduced amplitude within the bulk as a Bloch-wave.

Image Potential States

In contrast to the occupied spectrum of surface states discussed before, image potential states describe the unoccupied high energy spectrum of surface states, existing in an attractive image charge Coulomb potential between the Fermi level E_F and the vacuum level $E_\mathrm{F} + \Phi$ (with Φ the local work function), as depicted in Fig.1.5. Perpendicular to the surface they feature a hydrogen-like spectrum (characterized by a quantum number n) which converges to $E_\mathrm{F} + \Phi$ [130], parallel to it a two dimensional electron gas (2DEG) forms with a continuous distribution of parallel momentum k for the case of extended systems. States $\Psi^{(n)}(k)$ with energies $E^{(n)}(k)$ result. In STM, IPSs appear as peaks in the local density of states (LDOS) measured while retracting the tip from the surface.

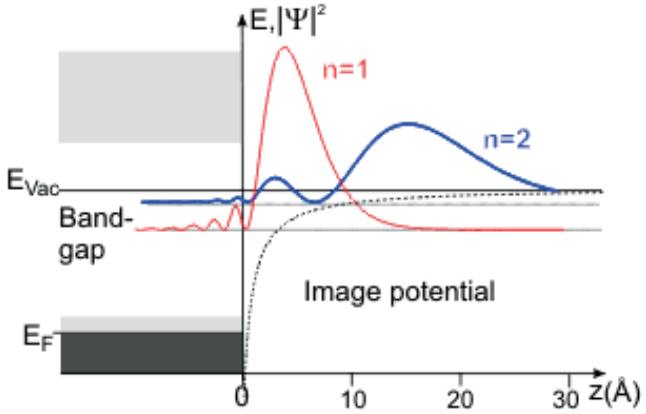

Figure 1.5: Schematic depiction of the $n = 1$ and $n = 2$ IPS wavefunctions, energetically residing in the projected bulk band gap. With increasing n, the weight of the wavefunction moves further away from the surface (see z scale). Reprinted from [129].

As they are Stark-shifted due to the electric field between the tip and the sample [131] they are often referred to as field emission resonances. Fig.1.6 depicts the influence of the

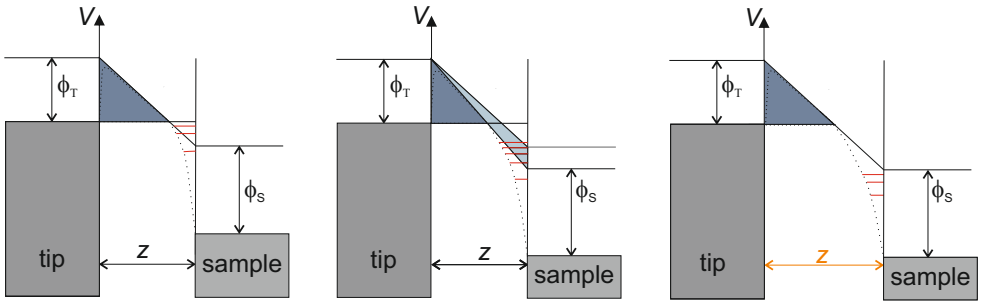

Figure 1.6: Compensating the Stark shift within one voltage sweep in constant current mode: Comparison of the effective tunneling barrier for different bias voltage and tip-sample distance. See text for detailed discussion.

constant current mode on measuring IPS in $\mathrm{d}I/\mathrm{d}V$ point spectroscopy: From left to right the sketch depicts the potentials of the tip and the sample (gray boxes) which are spatially separated by a distance z. Adding the workfunctions of the tip and the sample Φ_T and Φ_S, one obtains the triangular tunneling barrier which area can be controlled by the bias voltage (potential difference). The effective tunneling barrier is colored dark blue, the area is relevant for the tunneling probability. For the case of IPS, a Coulomb potential is added (dashed line). The IPS spectrum is sketched by red lines in the Coulomb potential. In the

center image, the same situation is plotted for the case of an increased bias voltage (in this example by lowering the sample potential). The area of the effective tunneling barrier is reduced, increasing the tunneling probability and thus the tunneling current. At the same time the potential for the IPS is broadened, changing the IPS spectrum by reducing the energetic distance of neighboring states. In constant current mode the distance z is consequently increased in order to restore the initial area of the effective tunneling barrier (right picture). This is accompanied with restoring the initial width of the potential for the IPS, restoring the initial spectrum in the sense of energy splitting. The absolute positions in energy are not conserved. This process is important in the continuous increase of V_{bias} in a constant current point spectroscopy voltage ramp with active feedback as it is used in Chap. 7.

Surface states play an important role in the framework of this thesis as they compete with Dirac electrons in the LDOS of epitaxial graphene systems and therefor affect our investigations on quantum confinement on GQDs (see Chap. 4 and Chap. 6). Image potential states on GQDs are investigated in Chap. 7.

1.7 Quantum Confinement of Electrons

Quantum confinement of electrons describes the altering of a materials electronic system by reduced dimensionality in the order of the electronic wavelength. The most prominent experimental example is the real space imaging of the electrons of a 2D electron gas confined to a ring of iron atoms on Cu(111), imaged by scanning tunneling microscopy [132, 133]. Intensive investigations of the outstanding electronic and optical properties of 0D structures have been performed in the field of semiconductor quantum dots [134]. Low dimensional electron systems are supposed to have potential application in quantum computing [135] and opto-electrical applications (e.g. solar cells [136–138]) while being already available in upscalable processes [139].

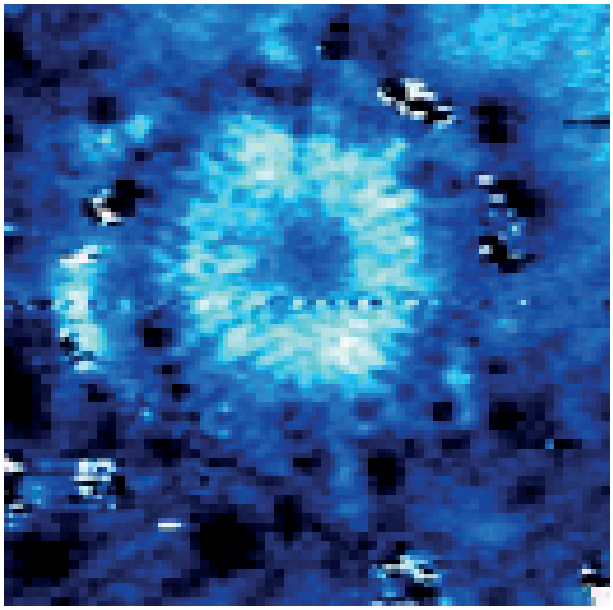

Figure 1.7: Electron confinement pattern as observed on an oxygen intercalated GQD on Ir(111) by STS. Compare (1,1) in Fig. 1.8.

In most cases reduced spatial dimensionality is connected to a rise of the potential energy at the boundary of a nanostructure, creating a local minimum inside which in this case is commonly referred to as a quantum well. A direct consequence is the localization of initially free electrons of a metallic band in a standing wave pattern risen by the scattering of electronic waves on the opposing walls of the quantum well and subsequent quantum mechanical interference as it is well known from the particle-in-a-box problem [140]. The example of a cylindrical potential well is presented as an excerpt of the master thesis of

Wouter Jolie [141] in Chap. A, a plot of the six lowest energy Bessel eigenstates in this geometry is presented in Fig. 1.8.

The confinement is accompanied by a lift of the states of a metallic band, giving rise to discrete atom-like states (characterized by a set of quantum numbers). This is due to the fact that at least for an infinite potential outside the well the wavefunction has to vanish at the boundary, implying that only discrete values for the momentum k are allowed. Therefore, the discretization in energy and momentum is a clear quantum size effect, providing two main parameters for tuning the confinement character of a quantum well, namely its width and the strength of the potential at its boundaries. Whereby the latter one is tuned by doping [142].

A quantitative description of electron confinement is given by mainly two different models: At first the perturbation of the density of states by screening the presence of the potential well, which is referred to as the Friedel oscillation picture [143]. Second the more qualitative, but more simple single electron model, assuming a single electron wave being backscattered from a hard wall potential well and subsequent interference [132]. The latter model can be modified by adding the possibility of inelastic scattering (soft wall), leading to a more quantitative description [144].

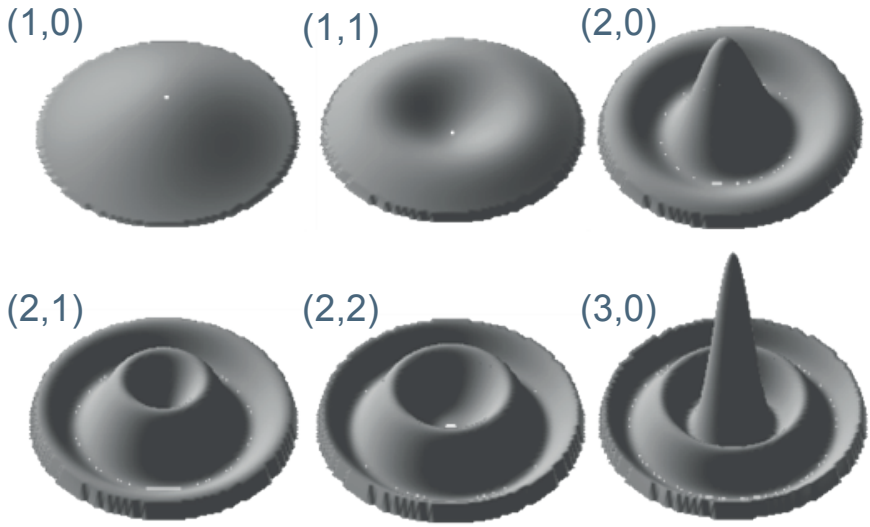

Figure 1.8: The first six confined states (Bessel eigenstates) (m,l) for an infinite cylindrical potential well. Compare Fig. 1.7, Fig. 4.8, Fig. 6.8, and Fig. 7.5.

For the case of graphene, *'confinement can be produced either by etching, by the reduced dimensions of the graphene crystallites or by the application of gate potentials (here Klein tunneling poses strong limitations on the use of such a method)'* [145]. For confining Dirac electrons on extended graphene, the use of inhomogeneous magnetic fields is proposed

[146]. The experimental observation of quantum confinement on nanopatterned graphene was first reported in Ref. [147].

Confinement on GQDs on Ir(111) is described in Refs. [110–113]. However, aiming at a proof for the observation of a confinement of graphene's linear dispersing Dirac electrons, these publications were challenged by [112], stating that the observations were mainly due to a confinement of Ir(111) surface states below the GQDs. In Chap. 6 we show that the problem of unclear assignment of the observed confinement structures on epitaxial GQDs is fixed by suppressing these surface states [1]. In Chap. 7 we demonstrate the first observation of confined high energy surface states in a tunable quantum well [2].

Though there are hints that confinement of Dirac particles differs from the one of Schroedinger electrons [148, 149], our system can be approached by a simple model [110, 111, 113]: For an analytical treatment and the determination of the wave vector k belonging to a state with specific E we approximate a GQD with an area A as an infinite cylindrical well with radius $r = \sqrt{A/\pi}$ [150]. In this case, the eigenstates in polar coordinates (ρ,ϕ) are given by

$$\Psi_{m,l} \propto J_l(k_{m,l}\rho)e^{\pm il\phi}, \tag{1.9}$$

where J_l is the spherical Bessel function of the first kind with order l [132]. Details on the Bessel functions are provided in A.3. The continuous distribution of k breaks down into discrete values $k_{m,l}$. Due to the confinement, $\Psi_{m,l}$ must have a node for $\rho = r$, leading to the condition

$$k_{m,l}r = z_{m,l} \tag{1.10}$$

with $z_{m,l}$ the m-th zero of J_l, i.e., the eigenstates can be characterized by quantum numbers m and l, hence $\Psi_{m,l}$ or (m,l) in shortened notation. The momentum $k_{m,l}$ of a given state (m,l) observed at an energy E can thus be calculated via

$$k_{m,l} = z_{m,l}/r = z_{m,l}\sqrt{\pi/A}. \tag{1.11}$$

The energies of the eigenstates are given by

$$E_{m,l} = E_0 + (\hbar^2\pi/2) \cdot z_{m,l}^2/(A \cdot m^\star), \tag{1.12}$$

with E_0 the energy of the state on extended graphene and $m^\star$ the effective electron mass. For $r \to \infty$, this equation converges to the dispersion relation of free electrons, see Sec. A.1.

Due to the long spin coherence time in graphene, a discussion of a potential use of GQDs in quantum computing was started by Trauzettel et al. [21]. Recently it has been shown that also plasmons can be confined in graphene nanostructures [151, 152].
Quantum confinement is the basic concept for most of the results presented in this thesis, see Chap. 4, Chap. 5, Chap. 6 and Chap. 7.

1.8 Electron Scattering Processes Observed by STM

In everyday life we are surrounded by many macroscopic examples of particle scattering, like light scattering at dust particles or photons scattering at the edge of a slit, showing diffraction and interference effects. In normal direction to a scatterer the translational symmetry is broken while it is conserved in the parallel direction. Here, scattering processes are closely related to Noether's theorem. It implies that the momentum is only conserved in the parallel direction (e.g. to a slit) while it is not conserved in the normal direction, requiring a momentum transfer.

Thinking about scattering of electrons at atomic size point defects or nanostructures like a surface step, of course quantum mechanics in solid state systems comes into play. The setting should be described by scatterers as perturbations of the density of states (DOS), since the DOS involves all necessary concepts for a realistic picture of the material's electronic structure. Therefore the picture of a single electron wave scattering at a defect and forming a standing wave by interfering with a reflected version of itself is often an oversimplified one. It does not take into account the presence of the bulk electrons, nor that there is a pronounced difference between LDOS and $\mathrm{d}I/\mathrm{d}V$ in the vicinity of perturbations: This issue becomes of vital importance when deriving a surface state dispersion from STS measurements, like in the pioneering work of Crommie et al. on Cu and of Hasegawa and Avouris on Au [153, 154]. Here a significant deviation from the dispersion relations measured by PES showed up, due to the oscillations in the *total* density of states connected to a screening of the impurity, which are commonly referred to as Friedel oscillations [143]. In STS data analysis these Friedel oscillations are considered by either adding an oscillating surface potential term [153] or considering an oscillating background in the $\mathrm{d}I/\mathrm{d}V$ signal like in the detailed description by Hörmandinger [155].

In terms of scattering observations, $\mathrm{d}I/\mathrm{d}V$ is found to reproduce the LDOS oscillations best in constant height mode and far away from a scattering site [155]. This means some contradiction to the experimental reality since at least the latter collides with the fact that the oscillations experience a quite strong damping (e.g. by electron phonon coupling). The Friedel contribution becomes more severe the larger the energy range $E - E_\mathrm{F}$ gets, but is still present in spectroscopic constant energy mapping since the Lock-in technique also involves the energy range provided by voltage modulation. In the latter case and in case of using very low voltage (few mV) STM topographs, the observed oscillations are sometimes referred to as energy resolved Friedel oscillations, e.g. in Ref. [156].

Great efforts have been made to find successful ways of recovering the true LDOS from the $\mathrm{d}I/\mathrm{d}V$ signal [157, 158], not all of them are suitable for large STS data sets since they can be quite expensive in terms of time consumption. A very convenient way of analyzing scattering effects in STM is the use of Fourier transformed $\mathrm{d}I/\mathrm{d}V$ maps, as this technique provides direct access to the k-space [156]. In general, systems with isotropic Fermi surfaces which are not dominated by many-body effects [159] only show the $q(E) = 2k(E)$ scattering vector in form of isotropic scattering, resulting in a circle with radius $k(E)$ in Fourier transformed STM (FT-STM) imaging. Despite all popular hand-waving explanations, this is a direct consequence of a singularity in the derivative of the Lindhart susceptibility, which probably is the most simple mathematical reflection of the Friedel screening concept [160]. The connection between the dominant scattering vector and the shape of the Fermi surface has also experimentally been confirmed for the anisotropic case [161]. If more than one quantum number is envolved, this approach is not suitable anymore and has to be substituted by T-matrix calculations [160].

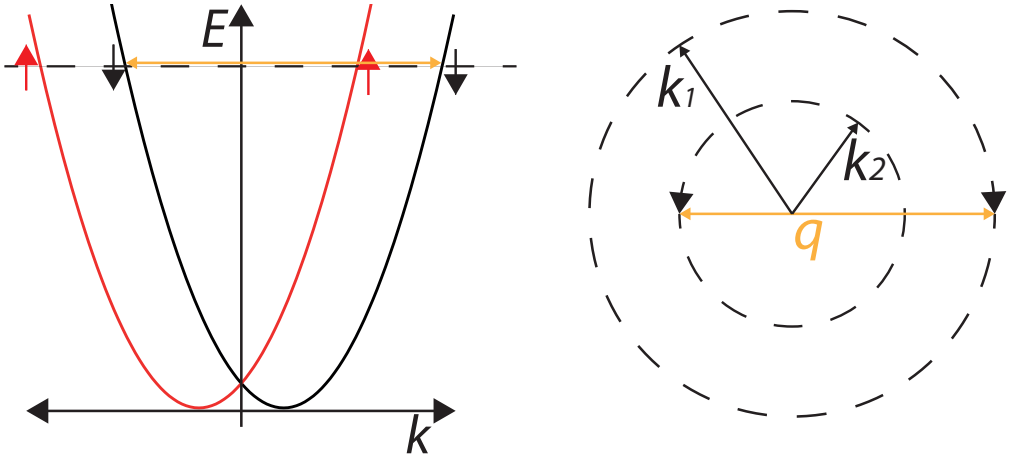

Figure 1.9: Sketch of the Rashba split of a metallic surface state. The parabolic dispersion is split into two branches for both spin directions. The spin direction is always orthogonal to the momentum vector k. Due to spin conservation scattering is only possible from one constant energy contour to the other one (indicated by orange arrow), yielding a scattering vector $q = k_1 + k_2$.

A general issue in STS is the imaging of spin-split surface states, like for example the Rashba split surface state of Ir(111). Here the parabolic dispersion of the surface state is split in k due to spin-orbit interaction, leading to a parabolic dispersion for each spin orientation which both are displaced in k. Since for Rashba split states the spin orientation is always orthogonal to the k direction, in a constant energy cut the split corresponds to

two circular shaped constant energy contours with each of them populated by a single spin species rotating clockwise and counter clockwise around the contour, respectively (see Fig. 1.9). Due to spin conservation, scattering is only allowed between the two circles, but not within one circle. In STS this leads to the fact that only the scattering vector $q = k_1 + k_2$ from one circle to the other is observed, which means that the two Rashba states are indistinguishable in STM [162], unlike e.g. in spin-polarized ARPES [163].

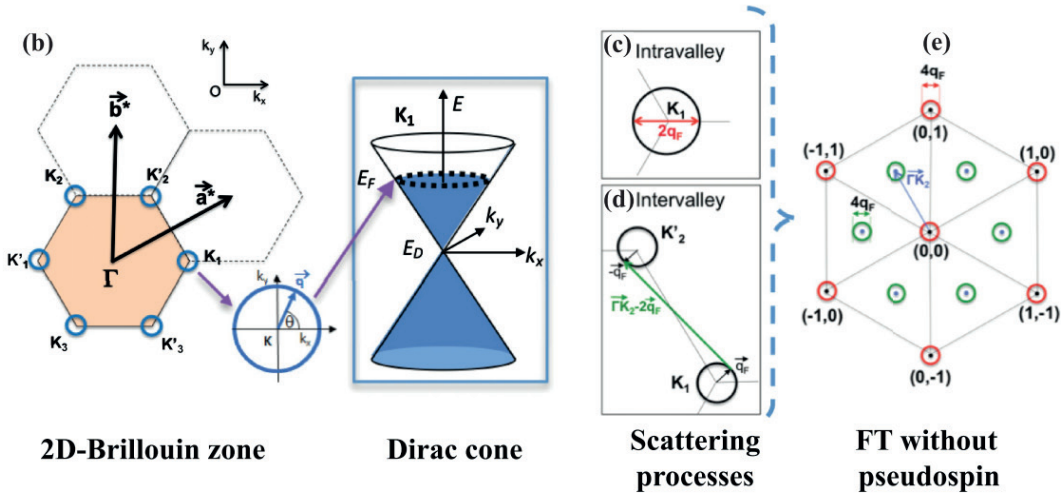

Figure 1.10: Schematic depiction of the two characteristic scattering processes in graphene for the example of n-doping, neglecting pseudospin. Reprinted figure with permission from [164]. Copyright 2012 by the American Physical Society.

For graphene the special shape of the constant energy contours in reciprocal space reveals two basic types of electron scattering from atomic sized defects depicted in Fig. 1.10: First, the intervalley scattering process connects states from neighboring K points ("valleys") and thus different sublattices. Second, intravalley scattering connects states of the same Dirac cone. In STS these mechanisms result in characteristic patterns in FT-STM spectroscopic maps [85, 164–168]. The imaging in Fig. 1.10 is simplified, as it does not take into account the role of pseudospin, which has a high impact on the characteristic patterns discussed in very detail in Ref. [164]. The most important consequences are the absence of the intravalley feature at the Γ-point in zero order and its appearance in first order, as well as an altering of the $(\sqrt{3} \times \sqrt{3})\,\mathrm{R30°}$ circular features from intervalley scattering. The observation of the characteristic scattering processes in graphene in experimental investigations acts as an indicator for the degree of decoupling of the carbon layer in epitaxial graphene (intercalation) compounds.

1.9 Imaging Graphene in STM

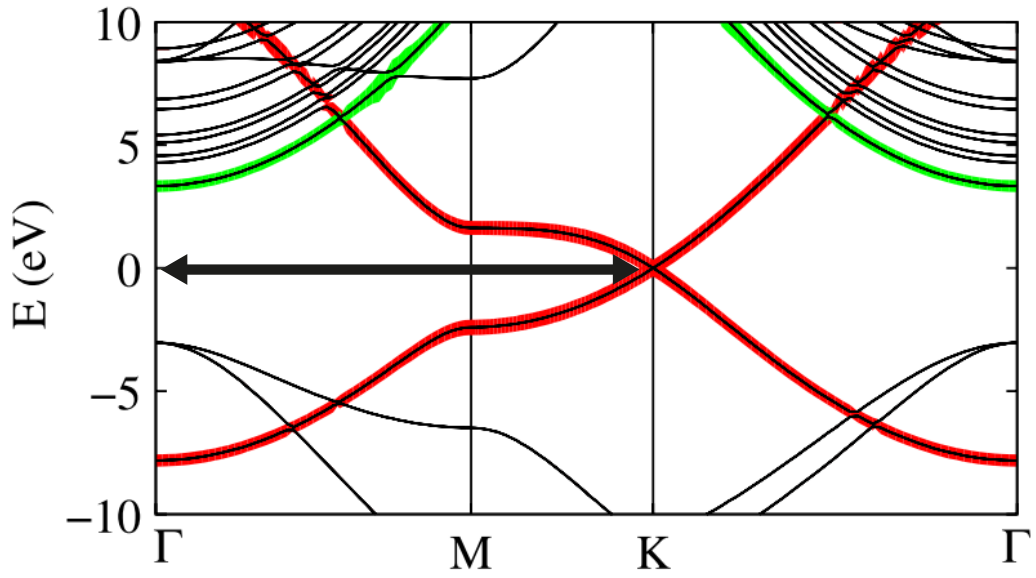

Figure 1.11: Black arrow indicates momentum transfer in the tunneling process. Reprinted figure with permission from [169]. Copyright 2008 by the American Physical Society.

STM imaging of graphene is widely reported in literature for many different substrates. However, if it is not grown or transferred on an insulating substrate (like e.g. SiC) with a defined and wide bandgap, it is not that clear from a naive point of view why graphene on a metallic substrate can be imaged at all by the means of STM. The reason for this remark is based on a combination of the typical tunneling process and the bandstructure of graphene: Most of the tunneling electrons leaving or entering an s-orbital [61] shaped tip (depending on positive or negative bias) have a vanishing surface parallel momentum which means in reciprocal space entering at the Γ point of the first Brillouin zone. Looking at graphene's bandstructure, it is obvious that within an energy range of $\approx 8.5\,\mathrm{eV}$ graphene does not provide any states at the Γ point which could be involved in the tunneling process [92]. This means that all STM imaging obtained in this energy window has to rely on the substrate density of states. Especially, imaging is not predominantly based on Dirac electrons located the K points. Instead, the graphene on metal topography obtained in STM seems to be more like a masking or altering of the metal LDOS by graphene's own LDOS. In contrast, for heavily involving graphene's Dirac electrons, a parallel momentum transfer to the tunneling electrons as indicated in Fig. 1.11 is required. In consequence

the contribution to the tunneling density of states (TDOS, e.g. [169]) measured in STM decreases [170]:

$$\mathrm{TDOS} = \mathrm{LDOS} \cdot \exp(-z_0 \lambda^{-1}), \tag{1.13}$$

with

$$\lambda^{-1} = 2\sqrt{2m_e\Phi/\hbar^2 + k_{m,l}^2} \tag{1.14}$$

and $k_{m,l}$ the surface parallel momentum and Φ the local workfunction.
As described in Refs. [169, 170], a parallel momentum might be provided by surface phonons. While the presence or absence of a momentum transfer and therefore the specific LDOS character might be of minor importance for topographic imaging, it becomes a central argument in the discussion of STS data. This involves questions like the visibility of a Dirac signature in STS point spectra or preferred states in the tunneling process in Chap. 7 [2].

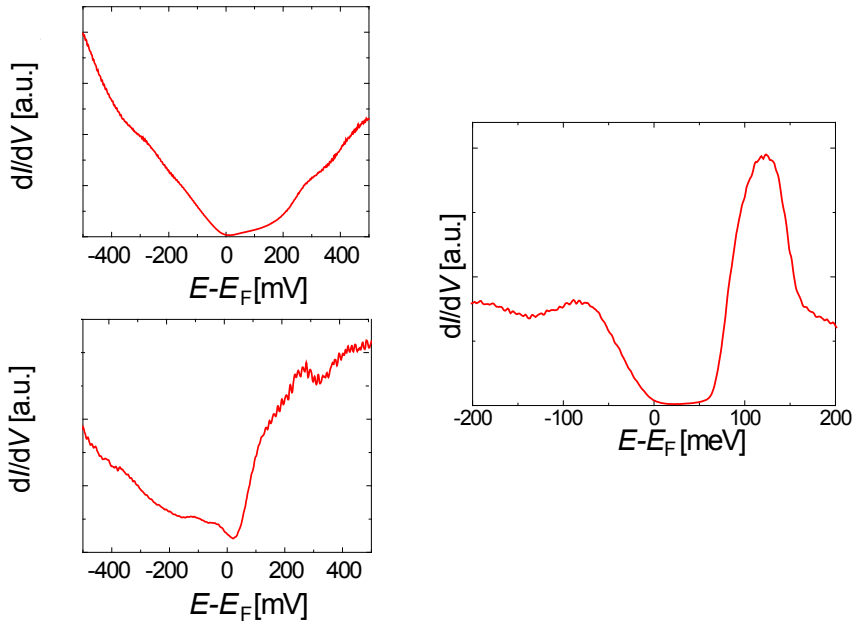

Figure 1.12: Types of commonly observed STS point spectra observed on gr/Ir(111), showing different shape at E_F.

In STS spectra phonon-mediated tunneling appears as a pronounced (pseudo-)gap at E_F, since the phonon mediation starts opening a further tunneling channel only at a certain phonon excitation energy [20, 170]. Although this mechanism seems to resemble the argumentation provided in Chap. 1.1 for IETS, Wehling et al. point out that it is not

limited to an inelastic character (dynamic phonons), since the giant enhancement of I only relies on the intermixing of Dirac electrons with nearly-free states at Γ [169]. The latter one is already provided by small corrugations of the graphene layer [169].
Although the considerations mentioned above seem to be quite plausible, in other literature the need for a momentum transfer is challenged by an argument based on the uncertainty principle: Considering an atomically sharp tip, the $k_{||}$ available within the uncertainty is already sufficient to reach the K-points [171]. However, this does not include an appropriate estimate for the tunneling probability dependence on $k_{||}$. This means that even if it is possible to reach the K points by uncertainty, it is still unclear why the tunneling probability to graphene should reach or exceed the one to the substrate. In other words the tunneling electron's median $k_{||}$ still remains unknown.

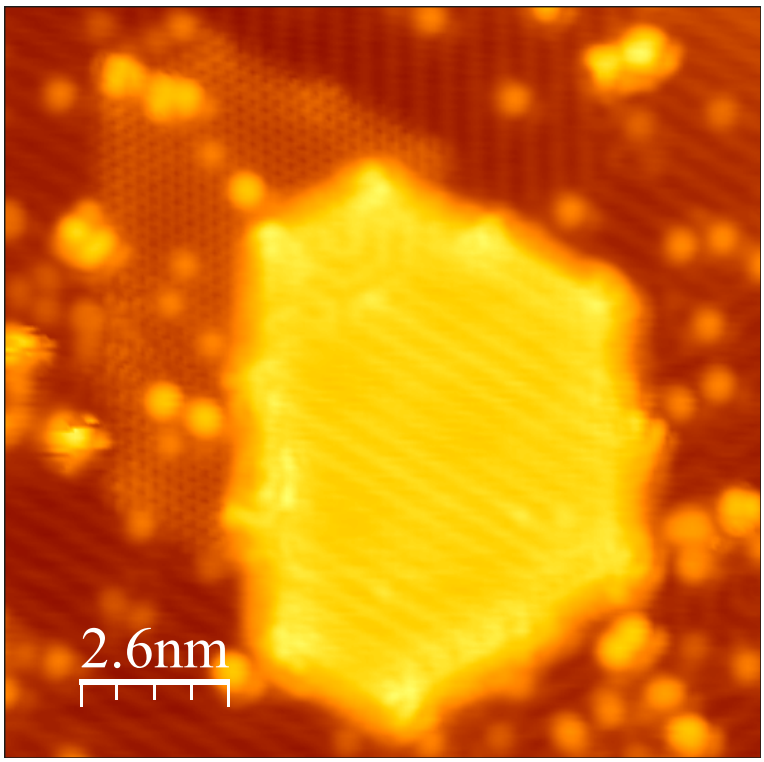

Figure 1.13: Constant current STM topographic image of an oxygen intercalated GQD on Ir(111), size $(13\,\mathrm{nm})^2$, imaged with an accidentally (useful) microscopical double tip.

The considerations on momentum transfer vary if the tip orbital differs from the s-orbital shape. Other tip orbital geometries might have a much larger tunneling probability to the K points [172] and therefore do not require a large momentum transfer to access the Dirac points. In general, tips generating a low density of states around $0\,\mathrm{V}$ are considered to be

less substrate sensitive compared to the ones generating V-shaped spectra, which usually accompany metal-like surfaces and are therefore more substrate sensitive in the gr/metal systems. Examples for both types of spectra obtained with microscopically different STM tips are shown in Fig. 1.12.

An accidental finding is shown in Fig. 1.13, showing a double tip imaging of an oxygen intercalated GQD on Ir(111). One of the tip atoms being active in the tunneling process is sensitive to the K points, imaging the carbon structure of the GQD, while the second one is sensitive to the oxygen superstructure. This observation nicely uncovers the different need for momentum transfer depending on the tip geometry within a single image.

CHAPTER 2

Experimental Setup

The STM/STS measurements presented in this work have all been performed with a low temperature STM (LT-STM) in ultra high vacuum (UHV) at 5.5 K. The setup is a commercially available system of SPS-CreaTec Fischer GmbH. It is based on a setup originally developed at Freie Universität Berlin, which is described in very detail in Ref. [173]. Therefore, this chapter is focused on a dense overview. All relevant customization and modification concerning our individual setup and details of the devices are described in Refs. [120, 174].

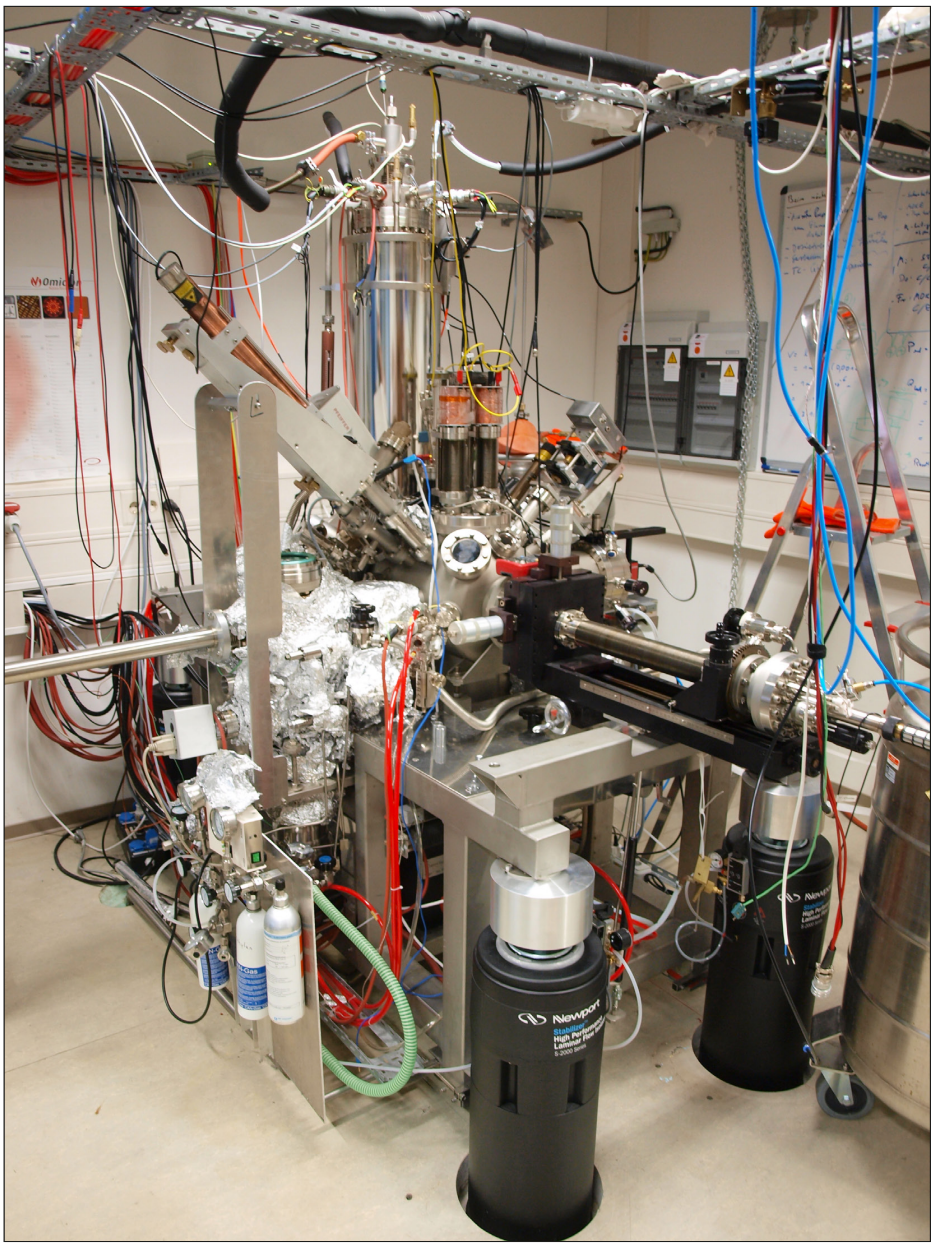

Figure 2.1: Picture of the LT-STM setup.

The setup consists of a UHV double chamber (in the following referred to as two main chambers) and a load lock chamber, which are separated by gate valves, respectively. Samples and STM-tips can be transferred between the load lock and the preparation chamber with a simple manipulator. In the preparation chamber they can be grabbed with the main manipulator, which provides three translational and one rotational degree of freedom. The preparation chamber is used for the in-situ cleaning, preparation and storage of the samples and additional STM-tips. In addition, non-STM measurement techniques like LEED, MOKE and mass spectrometry can be performed in the preparation chamber. The STM chamber is equipped with a helium bath cryostat, enabling STM and STS measurements at low temperature.

2.1 Ultra High Vacuum

STM measurements aim at the investigation of defined surfaces. Therefore, the quality of the sample surface heavily depends on the quality of the vacuum pressure inside the chamber. UHV is generated by a three stage pumping process. The load-lock and the preparation chamber are equipped with a prepump[1] and a turbo molecular pump (TMP), respectively. With the valves to the turbo pumps closed the main chamber's UHV is maintained by combined ion getter/Ti-sublimation pumps[2] in the preparation and the STM chamber, respectively. Ti sublimation is activated in both main chambers in a scheduled process every 24 (preparation chamber) and 48 (STM chamber) hours. The minimal base pressure of the preparation chamber achieved was $8.5 \cdot 10^{-11}$ mbar. The pressure can be lowered by about a factor of two by cooling the Ti-evaporation cladding with liquid nitrogen.

During sample preparation generally both TMPs are running, for STM measurements they are switched off in order to avoid vibrational disturbance of the measurement signal. The rotational flange of the manipulator means a small leak, which is compensated by a two-stage differential pumping system via the load lock. Therefore, pumping the manipulator needs a sufficient vacuum (lower than $5.0 \cdot 10^{-9}$ mbar) in the load-lock. This means that during long lasting measurements (a few weeks) the manipulator cannot be pumped, therefore showing enhanced leakage to the preparation chamber.

[1] load-lock: oil-free membrane pump; preparation chamber: rotary pump Pfeiffer HiPace 300
[2] Gamma Vacuum TiTan 300TV

The pressure measurements are performed by Bayard-Alpert hot-cathode ionization gauges in both the STM and the preparation chamber, in the load-lock a combined instrument with Bayard-Alpert and Pirani gauges is used[3] (covering the whole pressure range).

The minimal base pressure in the STM chamber is the high 10^{-11} mbar regime at room temperature and reaches $\approx 10^{-13}$ mbar if the cryostat is cooled to minimal temperature with liquid helium [173], enabling measurements on the same surface for weeks (cryostat walls act as a cold trap).

2.2 Low Temperature

Measurements in the low temperature regime provide ideal conditions for STM and STS measurements. According to the Wigner-Polanyi equation the desorption rate of gas molecules attached to surfaces inside the chamber exponentially decreases with low temperatures, thus leading to a significant improvement in the background pressure which enables measurements for a few weeks without repreparing the sample.

Low temperatures reduce the mobility of tip and surface atoms. Simultaneous cooling of the sample and the STM tip creates a temperature equilibrium and therefore reduces the thermal drift, providing stable tunneling conditions for many hours. This is necessary for point spectroscopy measurements where the tip has to stay in a stable lateral position and also in a defined tip-sample distance without feedback-loop up to a few minutes.

The STM is mounted in contact with a liquid helium bath cryostat. By using a reverse biased Zener diode, the STM can be continuously heated to room temperature. The bath cryostat consists of an outer cryostat with a capacity of 15 l liquid nitrogen and an inner one with a capacity of 4 l liquid helium. The inner cryostat can also be filled up with liquid nitrogen instead of liquid helium if the very low temperatures are not needed. The outlet of the liquid helium filled part is connected to a recovery line to the institute's helium liquifier. The temperature measurement is performed by two diodes, which are connected to the STM upper plate and the cryostat, respectively. The two diode voltages are permanently recorded by the STM electronics.

The minimal values $T_{\mathrm{Kryo}} = 4.4\,\mathrm{K}$ and $T_{\mathrm{STM}} = 5.5\,\mathrm{K}$ are obtained when the Bayard-Alpert pressure gauge in the STM chamber is switched off.

[3] Vacom Atmion

2.3 Damping of External Excitations

In order to eliminate the influence of external excitations on the imaging quality, a maximum of decoupling from typical mechanical and electrical excitations is required. In the case of the LT-STM setup, this is achieved by a two stage mechanical vibration isolation, consisting of the chassis resting on four laminar flow dampers with active relevelling decoupling the setup from (low-frequency) vibrations of the building and an additional internal damping for high-frequency mechanical excitations.

The internal damping is realized by both mounting the STM with three thin springs under the liquid helium cryostat and by using a permanent magnetic field for an eddy current brake.

Electromagnetic influences are reduced by using short coaxial cabling (BNC) and by the vacuum chamber itself acting as a Faraday cage in connection with an appropriate ground. During measurements, the Faraday cage effect of the chamber is supported by using metallic cover panels at the windows of the STM chamber. The possibility of using the Createc PSTMAFM software for an analysis of the real time excitation spectrum is described in Chap. B.

2.4 Scanning Tunneling Microscope

The STM is mounted under the LHe bath cryostat and is realized in form of a Besocke-beetle-type [175]. For the sample transfer the STM is pulled down by a cable control and fixed on a ground plate which is in good thermal contact with the cryostat. During measurements the STM hangs freely at the springs under the cryostat as described above. By applying periodic high voltage pulses, the three outer piezo actuators are moved in such a way that the thrust ring starts a rotational motion (slip-stick motion). The thrust ring is equipped with three ramps with a height of $\approx 0.7\,\mathrm{mm}$, therefore the rotation makes the STM tip move in vertical direction in a macroscopical manner. This motion leads to a coarse approach of the tip to the sample until the tunneling contact is reached.

As soon as the tunneling contact is established, the tip is moved by the central piezo only, in both the lateral (scanning) and the vertical direction (height profile). This configuration has been used for all measurements comprised by this work.

In principle the lateral movement can also be performed by the outer three piezo actuators with the advantage of decoupling the vertical and the lateral motions. A disadvantage is

the fact that scanning with the outer piezos means moving the whole thrust ring, therefore moving quite a high mass which reduces the maximum scanning speed.
All measurements presented in this work were performed by a homemade tungsten tip, which was electrochemically etched from a wire in NaOH. Details of the etching process and the resulting microscopical tip shapes are discussed in Ref. [174].

CHAPTER 3

Experimental Procedures

In the following the typical preparation routines of the samples used for this work are explained in very detail. Most of them connect to those developed and frequently used in other work of our group. Especially the preparation of gr/Ir(111) is a standard routine already described in Ref. [29]. All sample preparations for this work were carried out in-situ on a home built electron beam sample holder, which uses the electron emission from a hot filament on high negative potential to heat the grounded metal sample by electron bombardment. Details of the sample holder are described in Refs. [120, 174]. All preparation routines in this chapter describe the standard routines. In case, deviating parameters are indicated and discussed in the specific chapter on results. A further section describes the tools involved in data acquisition and processing.

3.1 Sample Preparation

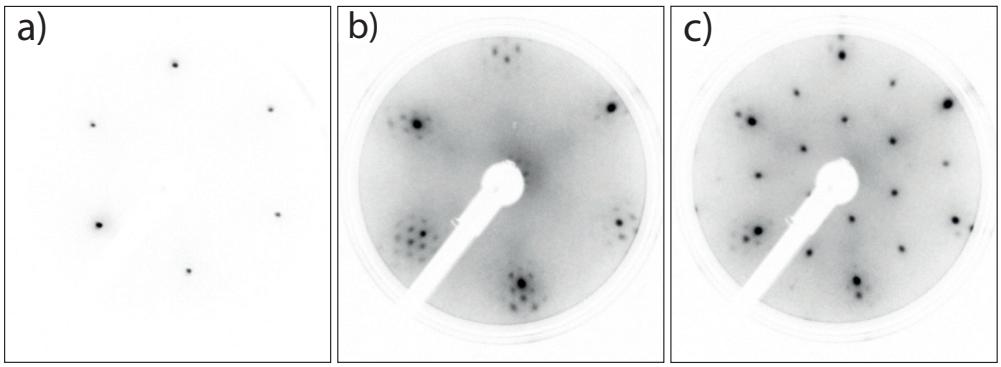

Figure 3.1: LEED documentation of a gr/O/Ir(111) sample preparation routine (contrast inverted). (a) LEED image of Ir(111) after cycles of Ar^+ ion bombardment and annealing at 1450 K at a primary electron energy of $E = 123.5$ eV. (b) LEED image after preparation of GQDs on Ir(111) by one TPG cycle with heating at 1220 K at an electron energy $E = 107.6$ eV. (c) LEED image after oxygen intercalation of GQDs by exposing the sample shown in (b) to 750 L of molecular oxygen at $T = 433$ K, imaged at an electron energy $E = 107.6$ eV.

Ir(111)

The common in-situ preparation of clean Ir(111) surfaces is performed in UHV by two to three cycles of bombardment of a monocrystal surface with Ar^+ ions with an energy of 1.5 keV at room temperature under normal incidence (sputtering) and subsequent annealing at 1450 K for a maximum duration of 30 s. Typical sputtering parameters for a metal crystal in regular use are $t = 20$ min, $p = 1.6 \cdot 10^{-4}$ mbar Ar pressure in the ion gun ($p = 6.0 \cdot 10^{-7}$ mbar in the preparation chamber) and a compensating current of $-3\,\mu$A between ground and the sample. The differentially pumped ion gun was operated with $I_{\text{fil emis}} = 10$ mA and $I_{\text{emis ion}} \approx 20\,\mu$A. The typical parameters for electron beam heating of the sample were $I_{\text{Filament}} = 1.78$ A, $U_{\text{HV}} = -1250$ V and $I_{\text{emis}} \approx 30$ mA.
The background pressure of the preparation chamber is lowest with the manipulator cooled by liquid helium, using it as a cryo pump [see Sec. 2.2]. This implies the use of Ne instead of Ar as the sputtering gas, since Ne is the only noble gas with higher atomic mass than helium that does not condense at 25 K (condensed sputter gas molecules would cause a significant increase of the chamber's base pressure when warming up). Since the sputtering

yield is lowered for Ne compared to Ar, in general Ne sputtering is limited to sample preparations which require extremely clean surfaces.

Most of the residual adsorbates after the surface preparation can be attributed to evaporation from the sample environment during the annealing process and to segregation from the Ir bulk. The annealing step is performed as fast as possible in order to prevent enhanced evaporation from sample surroundings like the sample holder and manipulator parts which are in thermal contact with the sample holder.

Cooling down from the annealing step might cause carbon contained in the Ir bulk to segregate to the surface. Therefore, after the last cycle oxygen firing at 1120 K in an O_2[1] background pressure of $p = 3 \times 10^{-7}$ mbar (corresponding $I_{O_2} = 1.0 \times 10^{-10}$ A at the QMS) for 10 to 20 min removes the contaminates. The typical parameters for electron beam heating of the sample to 1120 K were $I_{\text{Filament}} = 1.78$ A, $U_{\text{HV}} = -400$ V and an electron emission current from the filament to the sample of $I_{\text{emission}} = -18$ mA. In order to keep the temperature constant a temperature controller[2] was used to control the high voltage at the filament. It is important to stop the oxygen exposition before stopping the heating, since otherwise oxygen might adsorb on the sample surface.

After the preparation the surface quality is checked by a LEED measurement, which shows six well defined spots reflecting the Ir(111) surface lattice symmetry as depicted in Fig. 3.1 (a). Half of the spots are brighter than the others, revealing a 3-fold symmetry. This feature is caused by the fact that the *bulk* fcc-lattice of the iridium crystal is 3-fold symmetric. At the particular energy used to obtain the diffraction pattern, the electrons do not only scatter with the first layer at the surface, but penetrate deeper into the crystal.

Graphene on Ir(111)

Closed Monolayer Graphene

Graphene was prepared on top of the clean Ir(111) surface by a two step catalytic decomposition of C_2H_4 (ethylene, IUPAC: ethene). The sample is positioned in front of a pipe-like gas inlet in the direction of normal incidence.

In a first temperature programmed growth step [29] it was exposed to 1×10^{-7} mbar of C_2H_4[3] at room temperature. The dosing was done in a very precise way by using a manually controlled leak valve and measuring the ethylene partial pressure via the quadrupole mass

[1] Messer CANgas Sauerstoff 5.0

[2] Invensys Eurotherm 2404

[3] Messer CANgas Ethylen 3.5

spectrometer (QMS) with a current equivalent of $I_{C_2H_4} = 1.0 \times 10^{-11}$ A. After ethylene dosing the sample was subsequently heated to 1470 K for 30 s.
In a second step the graphene layer was closed by chemical vapor deposition, exposing the sample to 3×10^{-7} mbar C_2H_4 with a current equivalent of $I_{C_2H_4} = 2.0 \times 10^{-11}$ A at the QMS at 1120 K for 10 min. The process is self-limited to the growth of exactly one monolayer of graphene [29].
After the preparation the surface quality was checked in a LEED measurement, which after a successful preparation showed six well defined spots reflecting the Ir(111) lattice symmetry and the characteristic satellite spots centered around the carbon lattice spots caused by the moiré superstructure of gr/Ir(111) [91] as exemplarily shown in Fig. 3.1 (b) for only 0.2 ML coverage.

Graphene Quantum Dots

The preparation of graphene quantum dots includes the TPG step only. The average size of the GQDs was controlled by the temperature of the heating step according to [29], the overall coverage by the number of TPG cycles. One step approximately yields a coverage of ≈ 0.22 ML. More than two TPG cycles tend to result in a surface with a high impurity concentration on the pristine Ir(111) areas. Due to the reduced coverage, checking the success of a GQD preparation by spatially averaging techniques like LEED or ARPES can be difficult. However, in order to observe quantum-size effects on GQDs, low coverage and small sized ones are preferred, since a small size enhances the separation in energy of confined electronic states.

Oxygen Intercalation

Oxygen intercalation under GQDs was achieved following the routine described in Ref. [51] by exposing an as prepared GQDs/Ir(111) sample to 750 L of molecular oxygen[4] at temperatures of 433 K (Chap. 5) and 450 K (Chap. 6), with the temperature manually controlled using the sample holder filament current only (without applying high voltage to the filament). The dosage exceeds the saturation coverage by more than one order of magnitude [176, 177].
The sample was positioned in front of a gas inlet pipe in the direction of normal incidence. The dosage was achieved via a molecular oxygen background pressure which was measured as a partial pressure equivalent to $I_{O_2} = 9.8 \cdot 10^{-8}\, A_{QMS}$ at the QMS for $t = 100$ s and

[4] Messer CANgas Sauerstoff 5.0

using a manually controlled leak valve. The gas inlet pipe enhances the local O_2 pressure at the sample surface by a factor of 19.5 ± 6.0 with respect to the O_2 background pressure [174].
After oxygen exposure, many new spots occur in the LEED pattern, see Fig. 3.1 (c). Note that the image was recorded at the same electron energy as Fig. 3.1 (b), keeping the reciprocal lattice constants in the same scale.
The inner spots with half the length of the Ir(111) reciprocal lattice vectors are attributed to oxygen. They are well visible compared to the carbon lattice of the GQDs, since oxygen covers the entire iridium surface, and correspond to three rotated p(2 × 1)-superstructure domains. Details of the oxygen on Ir(111) and oxygen under graphene on Ir(111) morphology are discussed in Sec. 5.1 and Chap. 6.

Silver Intercalation

Silver intercalation was achieved by exposing an as prepared GQDs/Ir(111) sample to vaporized silver and subsequent heating. Silver was evaporated from a molybdenum crucible filled with Ag pieces cut from a high-purity wire in a four pocket electron beam evaporator with a flux monitor and an ion trap[5].
Typical parameters during the evaporation were an evaporator filament current of $I_{\mathrm{Fil}} = 3.3\,\mathrm{A}$, a voltage of $U_{\mathrm{HV}} = +1090\,\mathrm{V}$ at the crucible, an electron emission current between the filament and the crucible of $I_{\mathrm{emis}} = 6.5\,\mathrm{mA}$ and a flux monitor current of $I_{\mathrm{flux}} \approx 15\,\mathrm{nA}$. The Ag layer was deposited at room temperature with a rate checked before with a microbalance[6] over approximately one hour. The deposition rate ρ corresponds to a coverage in ML by the following considerations:
Silver shows a face-centered cubic (fcc) lattice structure with a lattice constant of $a = 4.085\,\text{Å}$, thus the (111) lattice plane distance is $d_{(111)} = a/\sqrt{3} = 2.358\,\text{Å}$. STM imaging of thick layers reveals a Ag/Ir(111) surface texture with a surface lattice constant close to the value of bulk Ag(111) (see Chap. 4). Therefore, we obtain the number of monolayers N directly by the rate ρ:

$$N = \frac{\rho \times t}{d_{(111)}} \tag{3.1}$$

In order to serve as a substrate for graphene, 15 ML of silver were deposited on top of a GQD/Ir(111) sample prepared as described above with one TPG cycle yielding a graphene coverage of ≈ 22 %. With the evaporator parameters $I_{\mathrm{fil}} = 3.3$ A, $U_{\mathrm{HV}} = 1160$ V and

[5] Specs EBE-4
[6] Sycon STM-100/MF, Sycon VSO-100

$I_{\text{emis}} = 6.40\,\text{mA}$ and $I_{\text{flux}} = 15$ nA, we obtained a rate of $R = 0.575$ Å/min. In our setup the quartz micro balance is not perpendicular orientated to the evaporator and hence not the total flux is measured. However, by aligning the sample perpendicular to the evaporator the required period of evaporation t is reduced by a factor of $\cos 48^\circ \approx 2/3$, yielding $t = 60\,\text{min}$ for 15 ML.
In order to intercalate the whole 15 ML under the graphene nanostructures, we heated the as prepared Ag/gr/Ir(111) surface as high as possible. The upper heating temperature limit is given by the desorption temperature of silver on iridium, which starts around 900 K [178]. In Ref. [179] the authors even claim that silver has a pronounced threshold character, since it does not desorb for $T < 1000$ K, but leads to a silver-free surface in less than 5 s at a temperature of 1300 K. In view of this background, the temperature was set to $T = 750$ K for 20 minutes.

3.2 Data Acquisition and Analysis

All STM/STS data was acquired by the software *PSTMAFM* by SPS Createc Fischer GmbH. This software is the PC interface of the STM electronics and therefore used for the direct control of the STM. For most of the constant energy spectroscopic mapping, a script written in *Pascal* by Christoph Boguschewski was used in order to record a set of images comprising topography and $\mathrm{d}I/\mathrm{d}V$ at multiple energies one after the other. Spatial STM/STS data analysis was performed by the image processing software suites *Nanotec Electronica WSxM* [180] and *Image Metrology SPIP*. They were used to subtract background from the images/scan lines in order to allow further processing like Fourier transformation in FFT algorithm or the determination of height profiles, spatial spectroscopic cross sections, and height distributions as well as lateral distance measurements. These programs were also used to adjust the image contrast and appropriate color code for representation. Point spectroscopy data was processed using *Additive OriginPro 8.6* and *9.0*, as well as *Microsoft Excel 2007* and *Casa Software CasaXPS*. They were also used to generate different representations of the data like e.g. matrix plots. Mathematical models were calculated using the *Waterloo Maple 13* CAS package.

PART II

Results

CHAPTER 4

Graphene Quantum Dots on Silver

The experiments described in this chapter were planned by Carsten Busse, Wouter Jolie and myself. The sample preparations were performed by Wouter Jolie and myself. The STM measurements and data analysis were performed by Wouter Jolie and myself. Several paragraphs and the figures of this chapter are adopted within their meaning or literally taken from the work of Wouter Jolie in the course of his Master project under my advice [141]. The results were obtained with important contributions by Carsten Busse and Thomas Michely. Some of the results presented here are part of the manuscript ***Tuning the Electronic Properties of Graphene Quantum Dots with Silver*** which is currently in preparation [52].

In this chapter we present the first study on Graphene Quantum Dots (GQDs) on silver (gr/Ag). In STS we identify the Shockley-type surface state of Ag(111) and find its onset energy shifted by strain in Ag/Ir(111). We study its behavior in the presence of graphene and discuss its role in the observation of Dirac electron confinement on GQDs. Finally we show that the surface state is suppressed in 1 ML of Ag on Ir(111) under GQDs.

In order to reduce the graphene-substrate interaction compared to gr/Ir(111), we consider silver as a potentially useful substrate (see Chap. 1.5). Details on graphene and gr/Ag are discussed in Chap. 1. Aiming for a decoupling of the electronic Dirac system of graphene, we investigate the LDOS of GQD/Ag/Ir(111) with an interlayer thickness of 15 ML by means of STS. Thick layers avoid complicated and potentially not well defined surface structures, especially in view of the fact that thin layers of Ag/Ir(111) tend to form surface alloys [181].
Since studies on Dirac electron confinement on GQD/Ir(111) are quite challenging due to the competing surface states [112], we concentrate on the behavior of the silver surface state in the presence of graphene and analyze finite-size effects on the LDOS of GQDs/Ag.

4.1 Morphology

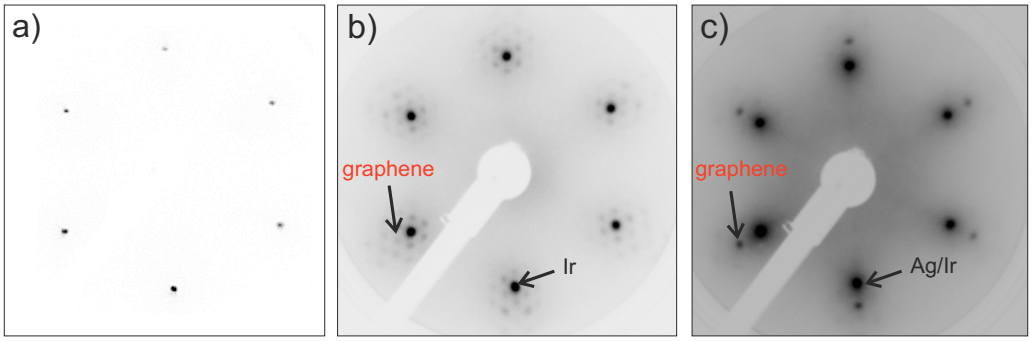

Figure 4.1: LEED pattern (contrast inverted) from (a) Ir(111), (b) Ir(111) covered with graphene and (c) Ag/Ir(111) covered with graphene (primary electron energies $E = 118.6\,\text{eV}$, $143.5\,\text{eV}$, $143.5\,\text{eV}$ from left to right). Reprinted with modifications from [141].

Fig. 4.1 shows a series of LEED images of the preparation process of a 15 ML thick epitaxial Ag layer on Ir(111) following the routine described in Sec. 3.1. The subfigures (a) and (b) show the diffraction patterns obtained after major steps of the process, namely (a) of the clean Ir(111) surface and (b) after the preparation of GQDs on Ir(111). In (c), the LEED pattern of the resulting surface after silver deposition and heating is presented. The patterns in (b) and (c), obtained at an electron energy of $E = 143.5$ eV, differ from each other in the sense of an enlarged distance between graphene and substrate spots. Since the bulk lattice constant of silver ($a_{3D} = 4.09$ Å[182]) is larger compared to the one of iridium ($a_{3D} = 3.84$ Å[182]), it shows a smaller lattice in reciprocal space, matching

Fig. 4.1. The observations in LEED act as a clear evidence for a successful preparation, changing the graphene support from iridium to silver. The graphene moiré spots are only faintly visible after Ag intercalation, which is most probably a consequence of the smaller corrugation of the carbon layer on the silver substrate. This finding is a first experimental hint that graphene on silver is a weakly interacting system [183].

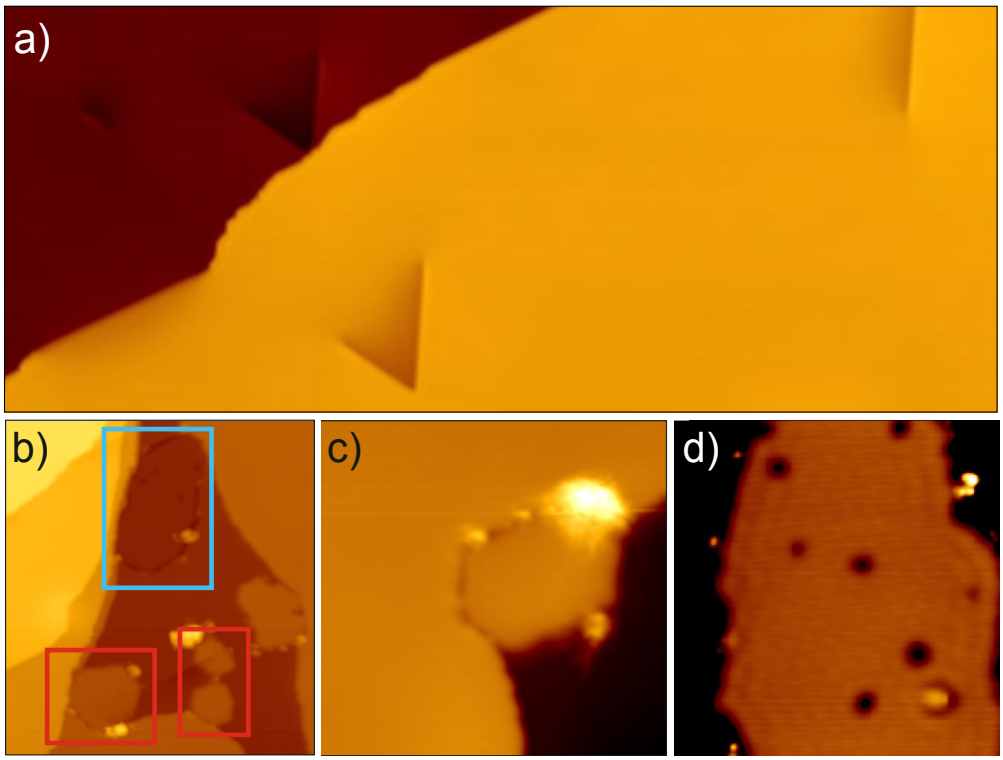

Figure 4.2: (a) STM topographic image of Ag/Ir(111), revealing triangular defects ($I = 1$ nA, $U = 0.5$ V, image size 90×37 nm^2). (b),(c) STM images showing different kinds of GQDs (blue and red boxes) and (d) graphene on Ag/Ir(111); parameters (b) $I = 0.2$ nA, $U = 0.5$ V, image size 80×85 nm^2; (c) $I = 0.2$ nA, $U = 1$ V, image size 33×32 nm^2; (d) $I = 0.2$ nA, $U = 0.5$ V, image size 30×25 nm^2. Reprinted with modifications from [141].

Fig. 4.2 (a) shows an STM topograph of a surface area on the 15 ML thick Ag layer on Ir(111) which is free of graphene. The surface obviously is not completely relaxed: Many misalignments are found on the sample, together with pronounced triangular defects, which is related to the heating duration used for preparation. Another effect of this deficiency is the fact that the film thickness varies spatially across the sample so that the interaction of iridium with the the topmost silver layer or even with graphene might still be present on several spots.

This is directly observed in STM images, since the clean silver surface exhibits different kinds of reconstructions at areas of low coverage (not shown). In the following, we restrict ourselves to areas without any reconstruction, since our study aims at a suppressed graphene-iridium interaction.
Most of the quite rare GQDs on the surface are located at silver step edges, as displayed in Fig. 4.2 (b), (c). It is possible that they find their way to the surface via these step edges, instead of directly going through the relaxed silver lattice. However, it is known from other experiments that at temperatures high enough for the GQDs to become mobile at the surface, a preference to bind at the step edges of the substrate is observed, reducing the binding energy of the GQD boundary. Parts of graphene get damaged on their way to the surface, resulting in a porous structure of the carbon layers [see Fig. 4.2 (d)]. Only small GQDs pass through the silver film without substantial damage.
However, the biggest disadvantage of the preparation procedure is that places, where graphene found its way to the surface, are accompanied by unknown adsorbates from the silver layers underneath, too [see Fig. 4.2 (b)]. Due to the low temperatures compared to the annealing temperatures of the Ir(111) surface preparation, they resist desorption into the vacuum. If the adsorbates are located in close vicinity or directly on GQDs, they may disturb the properties of graphene's electronic system, providing an additional scattering potential for charge carriers. We identify three different types of graphene areas on the silver surface:

- GQDs embedded in Ag/Ir(111), see Fig. 4.2 (b) with blue box
- GQDs on Ag/Ir(111), see Fig. 4.2 (b) with red boxes and (c)
- larger, porous graphene areas on Ag/Ir(111), see Fig. 4.2 (d).

Since we are dealing with 15 ML of silver, GQDs on top and those ones embedded in the uppermost layer should have similar properties concerning the interaction with the iridium substrate. The larger, imperfect graphene layers are used to probe basic properties of graphene like its moiré periodicity and the Dirac energy shift following the substrate change, while investigations on GQDs focus on confinement.
In the following, the moiré periodicity of graphene on Ag will be calculated in order to obtain the lattice constants of graphene and silver in our system. According to [184] we obtain:

$$\frac{2\pi}{a_{\mathrm{m}}} = \Delta k = k_{\mathrm{gr}} - k_{\mathrm{Ag/Ir(111)}} = \frac{2\pi}{a_{\mathrm{gr}}} - \frac{2\pi}{a_{\mathrm{Ag/Ir(111)}}}. \tag{4.1}$$

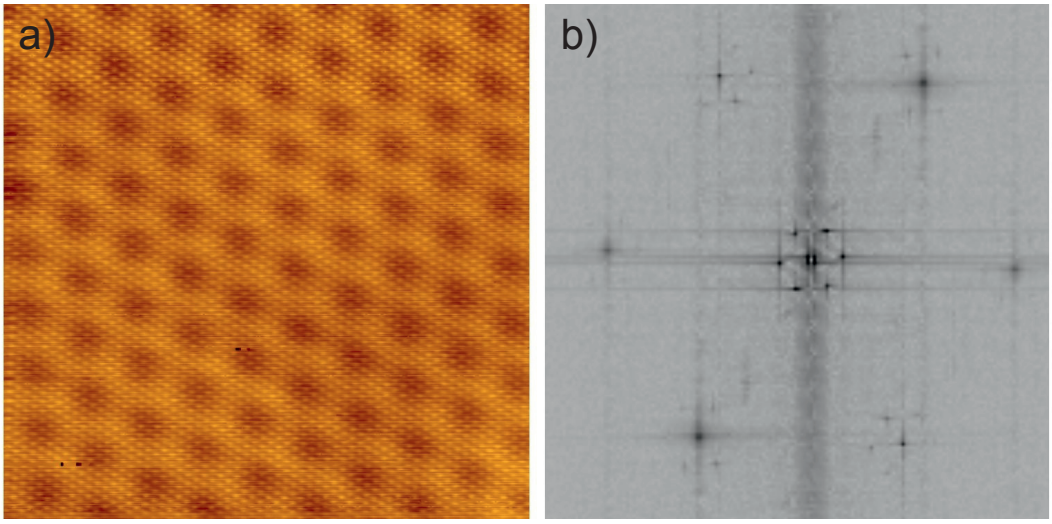

Figure 4.3: (a) Atomic resolution of gr/Ag/Ir(111) ($I = 1$ nA, $U = 0.2$ V, image size 14×14 nm^2). (b) Fourier transform of (a), revealing carbon lattice spots of graphene and satellite spots of the moiré superstructure. Reprinted with modifications from [141].

In Fig. 4.3 (a) we show an atomically resolved STM topograph of gr/Ag/Ir(111). We obtain the lattice constants of graphene and the moiré superstructure by a FT of Fig. 4.3 (a) as presented in (b). The large hexagon arises from graphene, the smaller one in the center of the image from the moiré superstructure. Due to the symmetry of the lattice, three pairs of reciprocal vectors are analyzed, leading to six values for the lattice constant of both graphene and its moiré. Here, the standard deviation is used to get the error of the measurement. The first row of Table 4.1 reveals the calculated values. The values given in brackets correspond to the error in the last significant digit.

Table 4.1: Lattice constants of the moiré superstructure for gr/Ag/Ir(111), freestanding graphene and Ag as determined from Fig. 4.3 (b). Literature values are given for reference.

Method	a_{m} [Å]	a_{gr} [Å]	a_{Ag} [Å]
FT [Fig. 4.3 (b)]	16.3(2)	2.50(1)	
freestanding/bulk	16.8 [Eq. 4.1]	2.465 [185]	2.89 [182]

Using Eq. 4.1 with the lattice constants of freestanding graphene ($a_{\mathrm{gr}} = 2.465$ Å) and the bulk Ag(111) surface ($a_{\mathrm{Ag}} = 2.89$ Å) we expect $a_{\mathrm{m}} = 16.8$ Å [186]. However, the lattice constant $a_{\mathrm{m}} = 16.3(2)$ Å obtained by FT is much smaller. For the graphene lattice

constant, FT yields $a_{\mathrm{gr}} = 2.50(1)$ Å, only slightly deviating from the literature value for freestanding graphene (see Tab. 4.1).
In view of these findings, the strong deviation in a_{m} can be explained by the periodicity of Ag/Ir(111) deviating from the value of a pure Ag(111) surface in literature. Therefore, strain seems to play a role as in the case of silver on silicon reported in Ref. [187]. In this publication the substrate still induces a strain of 1 % in a 50 Å silver film. We rewrite Eq. 4.1 and calculate the lattice periodicity of silver:

$$a_{\mathrm{Ag/Ir(111)}} = \frac{1}{\frac{1}{a_{\mathrm{gr}}} - \frac{1}{a_{\mathrm{m}}}} = \frac{1}{\frac{1}{2.50\text{Å}} - \frac{1}{16.3\text{Å}}} = 2.95\,\text{Å}. \tag{4.2}$$

By error propagation $\Delta a_{\mathrm{Ag/Ir(111)}} = \sqrt{\left(\frac{\partial a_{\mathrm{Ag/Ir(111)}}}{\partial a_{\mathrm{gr}}}\Delta a_{\mathrm{gr}}\right)^2 + \left(\frac{\partial a_{\mathrm{Ag/Ir(111)}}}{\partial a_{\mathrm{m}}}\Delta a_{\mathrm{m}}\right)^2}$ we obtain $\Delta a_{\mathrm{Ag/Ir(111)}} = 0.02$ Å, thus $a_{\mathrm{Ag/Ir(111)}} = (2.95 \pm 0.02)$ Å.
The value of a_{Ag} is used to compute the strain:

$$\epsilon = \frac{\Delta a_{\mathrm{Ag}}}{a_{\mathrm{Ag}}} = \frac{a_{\mathrm{Ag/Ir(111)}} - a_{\mathrm{Ag}}}{a_{\mathrm{Ag}}}. \tag{4.3}$$

with a_{Ag} the literature value for a pure Ag(111) surface.
Thus, the minimum/maximum strain is in the range of $\epsilon = 1.5..2.9$ %, given by the combinations of the extremal values of $\Delta a_{\mathrm{gr}} = \pm 0.01$ Å and $\Delta a_{\mathrm{m}} = \pm 0.2$ Å (see Tab. 4.1). Our errors in the lattice constants as determined by FT and standard deviation are quite small compared to the errors reported in literature for e.g. the very precise measurement of a_{m} of gr/Ir(111) yielding $\Delta a_{\mathrm{m}} = \pm 0.4$ Å (here the substrate lattice constant is precisely known) [184]. Assuming larger errors ($\Delta a_{\mathrm{gr}} = \pm 0.03$ Å and $\Delta a_{\mathrm{m}} = \pm 0.4$ Å) in the FT lattice constants, the minimum/maximum strain is in the range of $\epsilon = 0.3..4.1$ %.
Note that the value computed for the silver periodicity can be assumed to remain constant with and without graphene on top. Graphene will not influence the spacing between the neighboring silver atoms, a common assumption for systems with a weak interaction between graphene and its substrate [184].

4.2 The Ag(111) Surface State

In this section the surface state of Ag/Ir(111) is analyzed on both silver and graphene covered areas of the surface. In order to improve the reliability of the STS spectra, a defined tip is prepared before every single measurement by dipping the initial tungsten wire

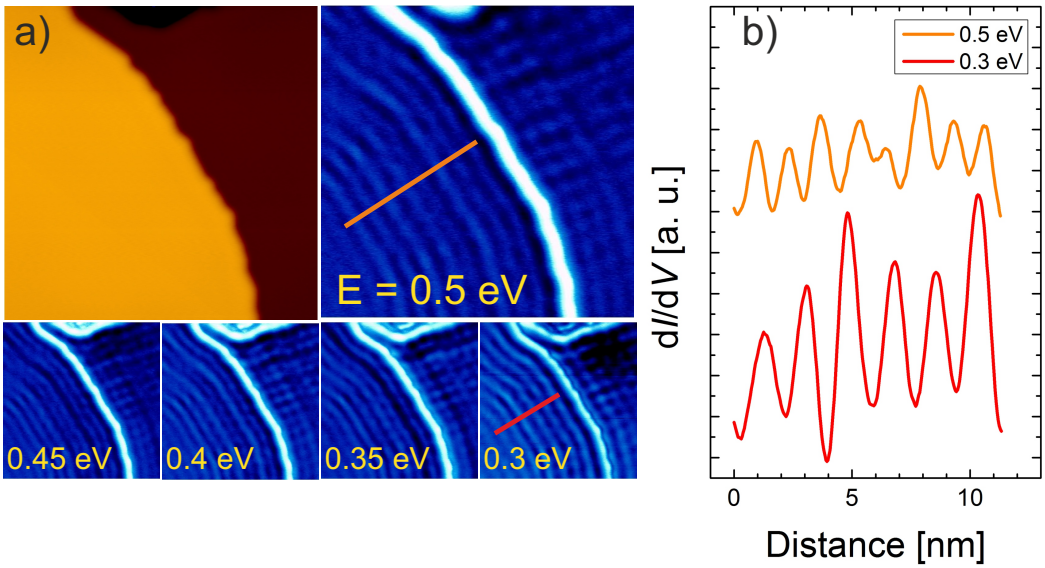

Figure 4.4: (a) STM topograph showing step edges of Ag/Ir(111) ($I = 0.1$ nA, $U = 0.45$ V, image size 22×22 nm^2), and several dI/dV-maps (blue). (b) Line profile across energy resolved Friedel oscillations at $E = 0.5$ eV and $E = 0.3$ eV, revealing a change in the wavelength with energy. Both lines are marked in the respective STS-maps. The profiles have been stacked for clarity. Reprinted from [141].

into the silver substrate. Hereby we exploit the featureless DOS of Ag, a great advantage of this sample system.

In Fig. 4.4 (a), a topographic image is shown together with several constant energy dI/dV-maps of the LDOS. In these maps the wave pattern of the scattered surface state is clearly visible. On the upper terrace scattering at the descending step edge is detected, resulting in a wave pattern normal to the edge. On the lower terrace two edges located close to each other produce wave trains in different directions, causing an interference pattern by superposition.

Fig. 4.4 (b) exemplarily shows two spatial lineprofiles in the spectroscopic maps for different energies, indicating a change in wavelength with E. The patterns result from an interference between an incoming and outgoing wave. The resulting wave vector is given by the relation $k = \frac{\pi}{\lambda}$. By mapping the silver surface at various energies and extracting the k-values out of each map, one obtains the dispersion relation shown in Fig. 4.5, together with a quadratic fit according to the expected dispersion of the Shockley-type Ag(111) surface state as with pure Ag(111). The error in k is negligible, while the error of E is approximately 0.02 eV according to the lower limit of the experimental resolution (Eq. 1.1). The best fitting values for E_0 and $m^\star$ are typed in the figure. Although the matching quadratic fit confirms the

Shockley-type character of the Ag/Ir(111) surface state with respect to effective masses, the surface state onset E_0 is shifted towards a higher energy, from -0.075 eV to 0.011 eV when compared to Ag(111).

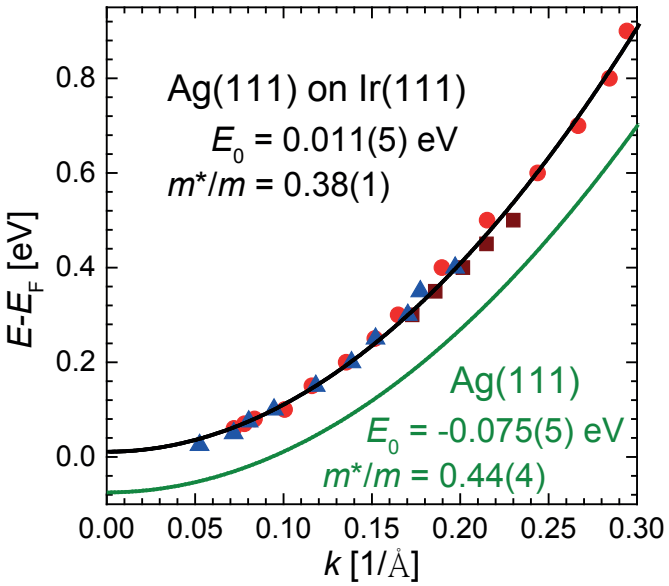

Figure 4.5: Dispersion extracted from three different areas on Ag/Ir(111). Black line: parabolic band of best fit parameters (black numbers). Green colored dispersion: Expected dispersion for Ag(111), computed with (green colored) parameters [188]. The brown rectangular data points correspond to maps of Fig. 4.4. Reprinted with modifications from [141].

To explain the shift of the surface state band, a model calculated for silver on Si(111)-(7×7) is taken into account [187]. There a similar shift of the surface state band is reported and attributed to a net strain in the lattice of the thin silver film, since hybridization effects between silver and the substrate cannot explain the perturbation of the band [189]. The strain lifts the bulk band located at lower energies than the surface state, changing the entire projected bulk band gap. This influences the surface state, since it is bound to the gap, preserving the potential that confines it to the surface plane. As a consequence, a shift of the bulk band structure due to strain creates a shift of the surface state band [187]. The strain, which is necessary to shift the state to $E_0 = 0.01$ eV, is about ≈ 0.5 % (see Fig. 3 in Ref. [187]). This value roughly fits to the strain values obtained from our FT analysis (see above).

In STS point spectra E_0 appears as a sharp kink as shown in Fig. 4.6 (b) for a spectrum measured on uncovered silver (black curve). The rapid, exponential decrease with rising energies is the effect of the non-vanishing $k_{||}$ for states with energies higher than E_0, increasing the exponential decay and thus damping the detected signal of the DOS. The evaluation of the kink yields an independent value of $E_0 = 0.05(3)$ eV, slightly above the one measured by mapping the energy resolved Friedel oscillations evaluated above. Its error is in agreement with our experimental resolution. Both values of E_0 agree with each other within their errors.

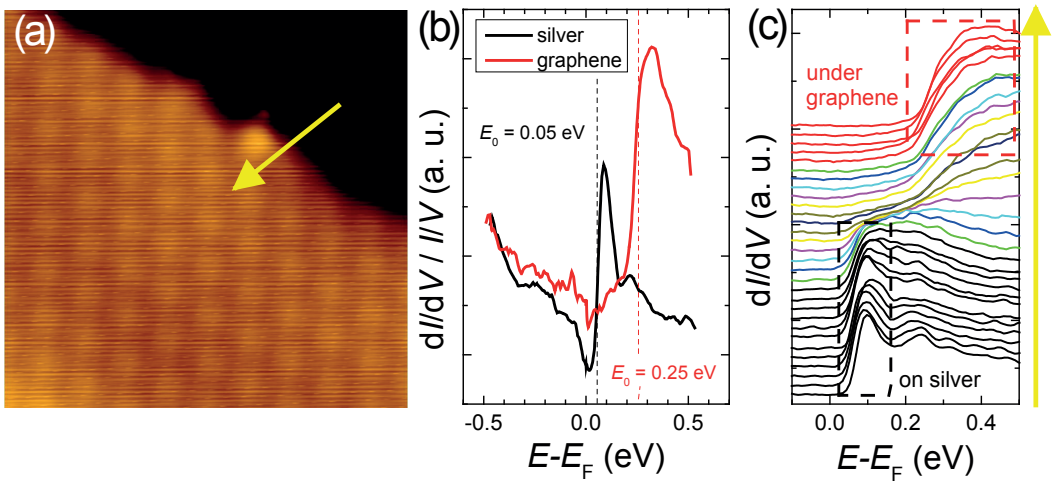

Figure 4.6: (a) STM topograph of Ag/Ir(111) partially covered with gr ($I = 0.4$ nA, $V = 0.2$ V, size $14 \times 14\,\mathrm{nm}^2$). Yellow line indicates the path of the tip for (c). (b) Two normalized spectra (number 4 and 27 from the set) revealing the shift of the surface state located under graphene ($I_{\mathrm{stab}} = 0.081$ nA, $V_{\mathrm{stab}} = 0.5$ V, averaged over 2 spectra). Dashed lines denote energies used to extract E_0. (c) 30 STS-spectra along the yellow line in (a), from Ag/Ir(111) (black) to gr/Ag/Ir(111) (red). The dashed rectangles enclose the signal attributed to the surface state. Reprinted from [141].

In the following we study the effect of graphene on the surface state by a set of 30 dI/dV-point spectra along a line, starting on the silver surface and ending on a graphene flake, see Fig. 4.6 (a,c). The graphene area is easily identified by the pronounced moiré superstructure. Since it is not possible to normalize all individual spectra probably due to the low current, the non-normalized dI/dV-signals are plotted with an additional offset. Beginning at the bottom of the plot, the kink of the surface state is seen near E_{F} [black spectra in Fig. 4.6 (c)]. Approaching the border of graphene, this signal vanishes smoothly (rainbow), indicating that at the border between graphene and silver the surface state is destroyed. After passing the border, the band reappears in the spectra persisting under the graphene layer, yet shifted towards higher E_0 (red spectra). Note that the missing normalization affects the shape of the spectra. This is getting more important at higher energies, which is obvious by comparing Figs. 4.6 (b) and (c). Though the shapes of the surface state on silver looks similar, the unnormalized signal detected under graphene is much broader and does not decrease with increasing energy. Only with a proper normalization the real shape of the DOS is obtained, decaying exponentially with increasing $k_{||}$.

To get more quantitative, the 4th and 27th spectrum of the set are plotted in Fig. 4.6 (b). The red spectrum on graphene demonstrates that E_0 is shifted by approximately +0.325 eV with respect to Ag(111), which is +0.2 eV with respect to the uncovered Ag/Ir(111) (black curve). This shift is comparable to the shift of the Ir(111) surface state under graphene [117]. It has almost the same size and sign. These similarities are due to the equivalent change of the boundary conditions for both surface states, changing from vacuum to graphene interface.

4.3 Dirac Feature of Graphene on Silver

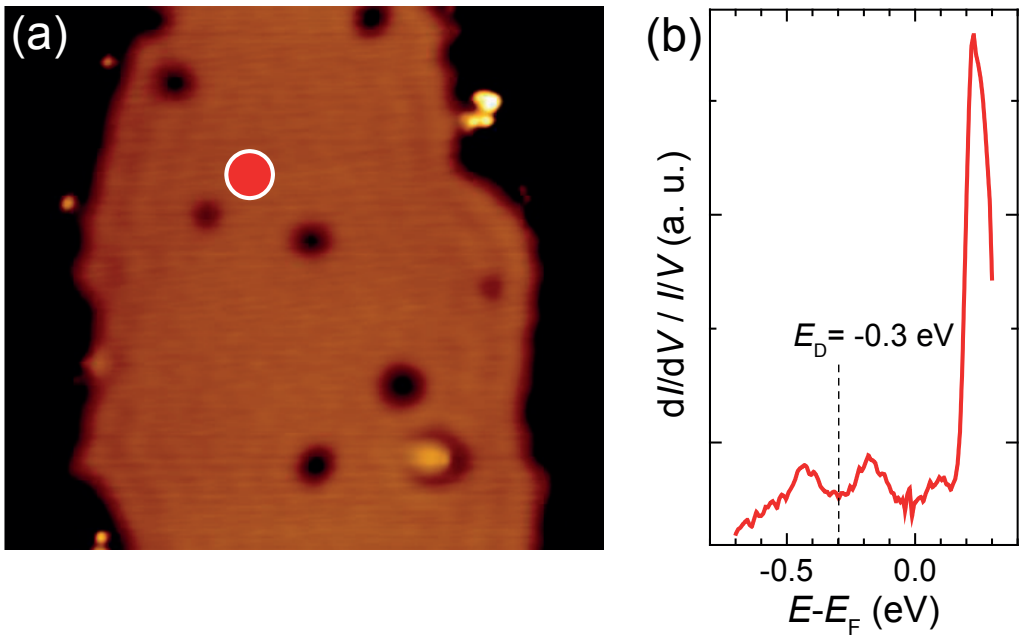

Figure 4.7: (a) STM topograph of graphene with a red circle indicating the place of the spectrum shown in (b) ($I = 0.2$ nA, $U = 0.5$ V, image size 30×25 nm^2). (b) STS spectrum revealing the shifted E_0 of the silver surface state and a dip at the Dirac energy E_D. The dotted line indicates the energy where E_D has been read out ($I_\mathrm{stab} = 0.2$ nA, $V_\mathrm{stab} = 0.3$ V, averaged over 2 spectra). Reprinted from [141].

In the recorded STS spectra, the surface state is always very prominent on and next to graphene, making it difficult to probe weaker signals arising from the DOS of graphene. These signals are weaker because accessing the Dirac states located at the K-point of the first BZ requires higher $k_{||}$ and therefore possesses a lower tunneling probability in STS. Nevertheless, a solution to obtain a fingerprint of the LDOS of graphene is to use a higher stabilizing current, reducing the distance for the graphene electrons to tunnel

into the tip or vice versa. With this, it is possible to probe E_D of gr/Ag. E_D is needed to determine the doping level and hence the dispersion relation of gr/Ag. Theoretical calculations estimate E_D in the range of -0.4 to -0.3 eV [48, 121], thus far away from the band of the silver surface state under graphene.

In Fig. 4.7(b), a normalized dI/dV-spectrum measured on a graphene area is plotted. The graphene area, together with a red mark revealing the probing place, is presented in Fig. 4.7(a). In the spectrum, a high signal arising from the surface state is present at positive bias voltage. It is located at a high E_0, since the entire band is shifted under graphene (see above). In the negative energy range a dip appears, indicating a linear increase and decrease of the LDOS. We attribute the minimum of the dip at $E_D = -0.3$ eV to the n-doped Dirac energy of gr/Ag. Hence, the lowest value postulated by theory matches our finding.

The feature, which allows us to read out E_D, is not as prominent as the kink of the surface state, because of the reasons mentioned above, but comparable to other STS works [190–192]. In our measurements, features like the dip in Fig. 4.7(b) were absent outside graphene, in any analyzed spectrum.

Before discussing confined states on GQDs, a résumé of the last two sections is given in Tab. 4.2, listing all extracted and additionally needed parameters of the surface state under graphene side-by-side with the values of gr/Ag. The value of E_D is rather hard to obtain,

Table 4.2: Parameters of the Ag(111) surface state under and of the Dirac electrons in graphene. Reprinted from [141].

E_0 (under graphene) [eV]	m^*/m	E_D [eV]	v_F [10^6 m/s]
0.25(7)	0.42(6)	$-0.30(5)$	1

thus a (high) estimation of the error of 0.05 eV is made. For the velocity of the Dirac electrons in graphene the value for freestanding graphene is used [91]. The effective mass of silver is stated to stay constant when putting graphene on top of it, a rough estimation, but valid for graphene on Ir(111). Its error is set to match both known values of $m^\star$ with their error bars.

4.4 Confinement on Graphene Quantum Dots on Silver

In the following we describe confinement patterns observed on GQDs/Ag by STS. The results from the discussions above help to identify the specific origin of the charge carriers involved in the confinement process.

Compared to extended surface areas with free electrons, reduced spatial extent induces a discretization of energy and momentum (see Sec. 1.7). In STS, we observe spatial LDOS variations by measuring $\mathrm{d}I/\mathrm{d}V$-spectra across and next to a GQD, as shown in Fig. 4.8 (b). In the center of a GQD [Fig. 4.8 (a)] we do not only observe the already discussed shift of E_0 under graphene, but an additional pronounced feature in the LDOS at 0.37 eV marked by a blue line. The linewidth reflects the experimental resolution in energy (see Eq. 1.1). Constant energy spatial mapping of this feature [Fig. 4.8 (c)] reveals the dedicated spatial LDOS structure of the (2,0) Bessel eigenstate on the lower GQD at 0.37 eV. It has a high intensity in the center of the GQD, where the spectrum has been recorded. With the same technique, the upper GQD is evaluated. The maps, recorded at the energies of additional maxima in further spectra (not shown), are shown in Fig. 4.8 (c)-(d). They reveal the (1,0) and (3,0) eigenstates of the upper GQD.

To analyze our data quantitatively we treat the GQDs as infinite, cylindrical potential wells (see Sec. 1.7). The potential can be explained by the difference in the local work function Φ between GQD and substrate, a step edge dipole [59] like in Fig. 4.9 (a) or structural features that affect the binding situation. For the upper GQD in Fig. 4.8 (b), a circle is drawn with a dashed line to indicate the area used in the model. In this case, the deviation from the real shape of the GQD is very small, improving the quality of the computed k. Note that both values, E and k, are evaluated independently: The energy E is obtained via $\mathrm{d}I/\mathrm{d}V$-mapping and k is investigated via the area of the nanostructure and the appropriate spherical Bessel function (see Sec. 1.7):

$$k = \frac{z}{\sqrt{\frac{A}{\pi}}}. \tag{4.4}$$

The number of maxima of a confined electronic state increases with energy. In conclusion, when a GQD is mapped at high energies, patterns similar to energy resolved Friedel oscillations are observed (see Fig. 4.9). At low energies, a standing wave pattern similar to a Bessel function is observed. With increasing E, the patterns get more and more complex, making it possible to directly read out their wavelength in real space. For small

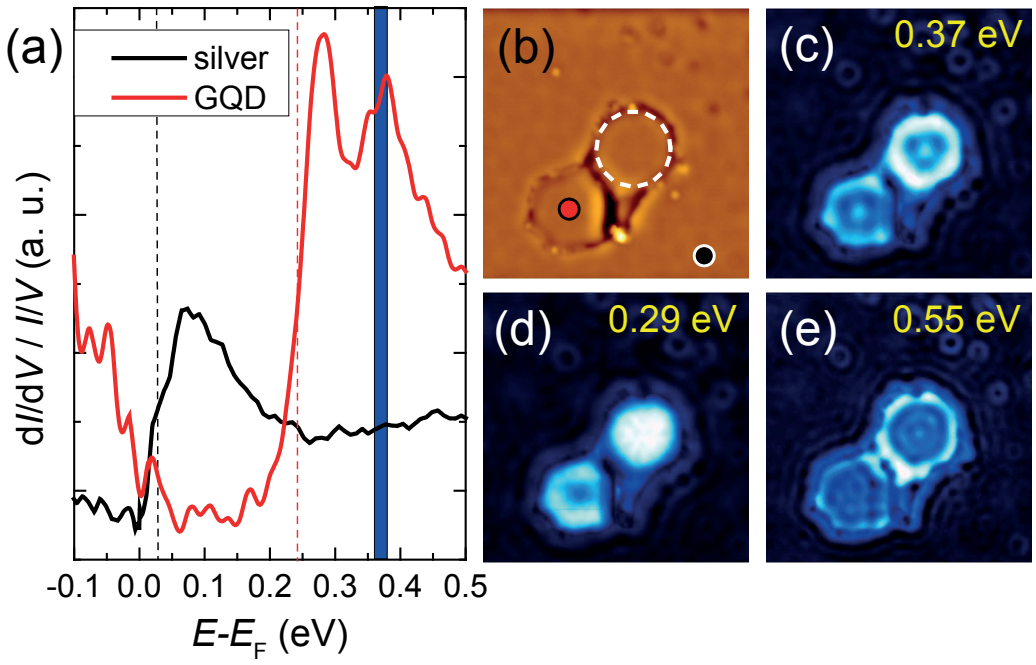

Figure 4.8: Confined states on two GQDs embedded in Ag/Ir(111): (a) Two $\mathrm{d}I/\mathrm{d}V$-spectra recorded on silver (black) and on the lower GQD (red) ($I_{\mathrm{stab}} = 0.1$ nA, $V_{\mathrm{stab}} = 0.8$ V, averaged over two spectra). The kinks of the surface state under and next to graphene are visualized by the dashed lines. On the GQD, a new maximum appears due to a confined state. (b) Topographic image of the GQD with two (small) circles indicating the sites of the measured spectra and one (big) dashed circle illustrating the approximation of the theoretical model ($I = 0.1$ nA, $V = 0.5$ V, image size 28×28 nm^2). (c) STS-map recorded at the energy highlighted in blue in (a) near the maxima. The width of the line corresponds to the error in energy. The map reveals a confined (2,0) state. (d)-(e) STS-maps related to the upper GQD, recording its (1,0) and (3,0) states. Compare Fig. 1.8. Reprinted from [141].

energies, the model is taken into account, while for high energies, the wavelength is used to compute k. For the latter, a pair of λ is evaluated to estimate the error of k. On top of that, the effect of a GQD with a shape far away from a circle is demonstrated. The result are standing wave solutions housing the symmetry of the GQD, a property which cannot be described by our simple model.

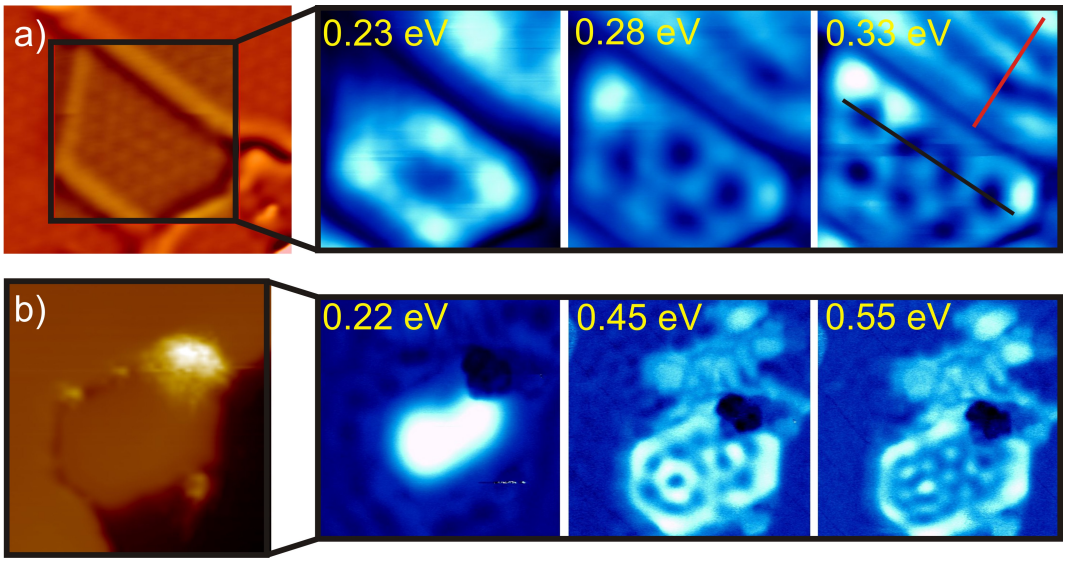

Figure 4.9: (a) A GQD surrounded by step edges ($I = 0.5$ nA, $V = 0.2$ V, image size 22×19 nm^2). A standing wave pattern is observed on the GQD, while energy resolved Friedel oscillations are recorded on the upper, larger graphene terrace. The two lines drawn in the right STS-image are evaluated in Fig. 4.10 (a). (b) Standing wave solutions recorded on a GQD, which are unaffected by the adsorbates on the GQD ($I = 0.2$ nA, $V = 1$ V, image size 20×20 nm^2). Reprinted from [141].

Fig. 4.10 (b) illustrates the result of the E and k analysis in form of a dispersion relation. The error of E has been increased to include the effect of a voltage drop. The Shockley-type surface state of silver is expected to show a parabolic dispersion while graphene's Dirac electrons are expected to disperse linearly. Thus, the data is fitted with both a quadratic and a linear function in order to identify the origin of the confined state. All fitting parameters are summarized in Tab. 4.3.

The fit clearly reveals the silver surface state as the origin of the confinement patterns. The curves represent the expected dispersions for the Shockley surface state (parabolic) and Dirac electrons (linear), computed using the parameters analyzed in the previous sections. Note that the data obtained from the real space analysis deviates slightly from the dispersion obtained by the Bessel eigenstate model because it does not allow for a finite size energy shift (the terraces are large in the sense of GQDs, but not really extended).

Table 4.3: A summary of the parameters extracted from the dispersion relation, compared with values obtained in the previous sections. Reprinted from [141].

	E_0 [eV]	m^*/m	E_D [eV]	v_F [10^6 m/s]
expected values	0.25(7)	0.42(6)	−0.30(5)	1
confinement analysis	0.23(3)	0.44(7)	0.11(4)	0.33(5)

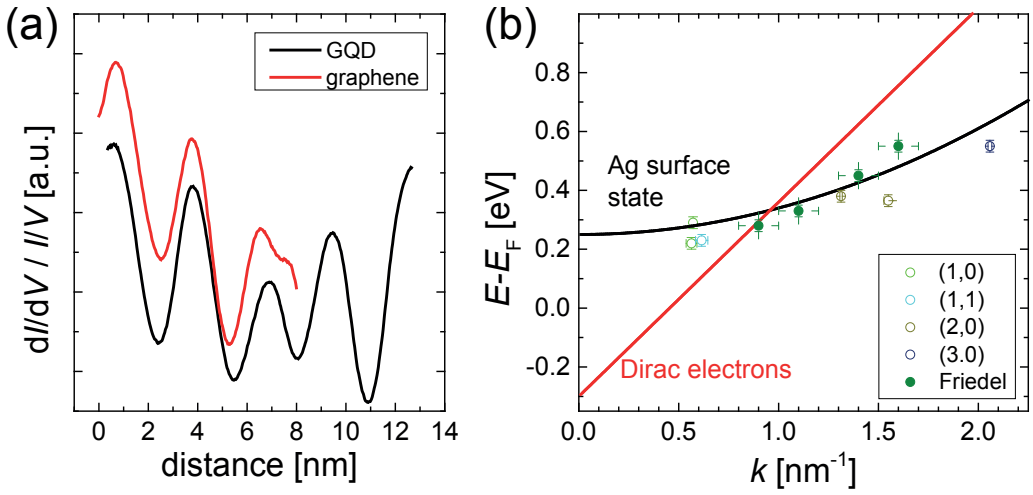

Figure 4.10: (a) Comparison of the LDOS modulation of the two lines drawn in Fig. 4.9 (a). (b) Dispersion relation extracted from the confined states and energy resolved Friedel oscillations obtained on GQDs, together with the expected bands for the surface state (black) and Dirac electrons (red). Reprinted from [141].

This result is not unexpected, since there are several hints that the detected states arise from the silver underneath the GQD: First, the signal of the surface state is always the most prominent feature in the STS spectra, masking the signal of the Dirac electrons. If both states are confined at the same place, the standing wave pattern of the surface state will be easier to detect. Second, all confined states are in the energy range of the surface state. No standing wave patterns were observed at energies lower than 0.2 eV, especially near E_D (negative energies). Third, the wavelength directly extracted from the GQD in Fig. 4.9 (b) is almost equal to the wavelength of the energy resolved Friedel oscillations on the terrace located above the GQD, see Fig. 4.10 (a). The terrace is also covered by graphene but large compared to GQDs and hence do not induce confined states described by Bessel functions. This point is illustrated in Fig. 4.10 (a), showing the equality of the wavelength on both terraces. Having the same wavelength at a certain energy results in equal dispersion relations. Fourth, the confined states are not disturbed by adsorbates eventually laying on top of the GQD [Fig. 4.9(b)].

4.5 Suppressing the Silver Surface State

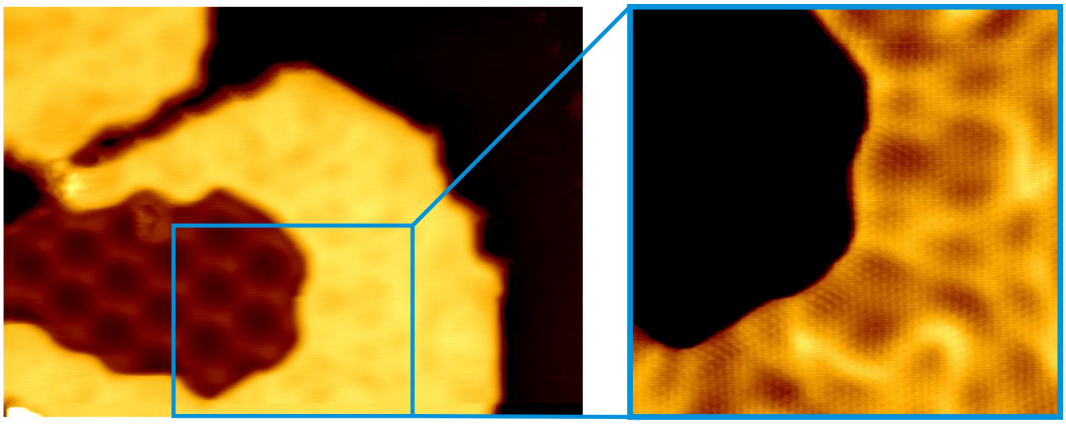

Figure 4.11: Atomic resolution on a partially Ag intercalated GQD, revealing the periodic moiré superstructure without and aperiodic corrugation with intercalated Ag ($I = 0.09$ nA, $V = 0.4$ V, image size 28×20 nm^2). Reprinted from [141].

In this chapter we show that the Ag surface state is suppressed in 1 ML Ag under GQDs. Before discussing the spectroscopic signatures, we give a short introduction to the sample preparation.

After cleaning the sample, GQDs are prepared in the standard way (see Sec. 3.1). The amount of evaporated Ag was restricted to 3 ML. The parameters used to adsorb silver on the sample are listed in the following table:

I_{fil} [A]	U_{HV} [kV]	I_{emis} [mA]	I_{flux} [nA]	R [Å/min]
3.3	1.09	6.5	$15 - 16$	0.5

First, the sample was heated for 3 minutes to 935 K. This temperature is just slightly above the temperature needed to desorb silver. In a second quick heating step T was enhanced to $T = 1125$ K. This results in partially monolayer intercalated GQDs as shown in Fig. 4.11. The partially intercalated GQD areas show a complicated aperiodic substructure.

To probe the LDOS under and next to the partially intercalated GQD, a set of 30 $\mathrm{d}I/\mathrm{d}V$-spectra is recorded over the border of a partially intercalated GQD [inset of Fig. 4.12 (a), orange line].

In Fig. 4.12 (a), the first and last spectra of the set are evaluated. At E_{F}, a divergence in both signals occurred after normalization. However, since it masks only a small energy range, from -0.045 eV to 0.045 eV in (a) and -0.05 eV to 0.06 eV in the whole set, this

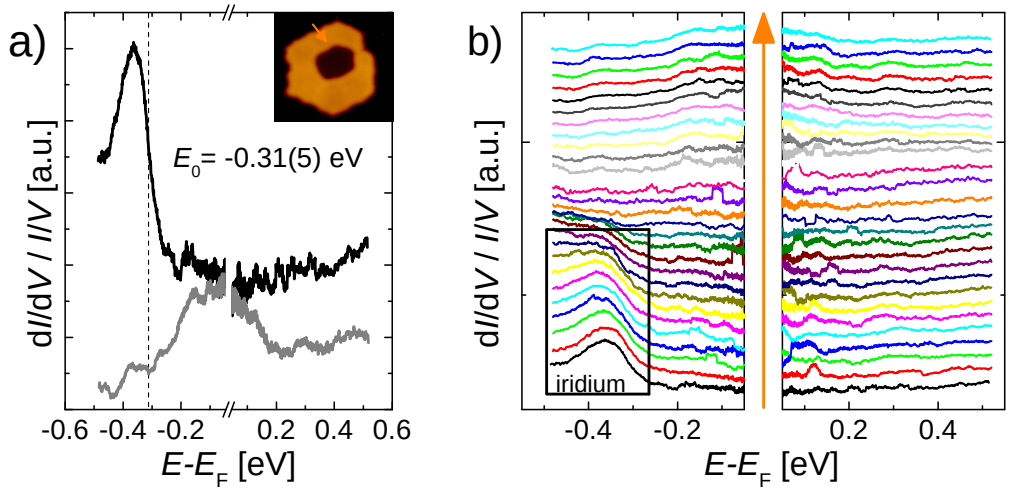

Figure 4.12: 30 point spectra revealing the suppression of the surface states on silver intercalated GQDs: (a) First (black) and last (gray) spectrum of the set recorded along the path marked with a orange line on the STM image in the inset ($I_{\mathrm{stab}} = 0.03$ nA, $V_{\mathrm{stab}} = 0.5$ V, averaged over 4 spectra, image size 17.5×17.5 nm^2). The dashed line marks the initial state energy of the Ir(111) surface state. (b) The whole set shows only a surface state feature next to graphene, enclosed by a rectangle. No surface state is found on silver intercalated GQDs. The spectra are cut around $E = 0$ to eliminate normalization artifacts. Reprinted from [141].

artifact is neglected. Note that the appearance of possible surface states induces a feature visible in a wide energy range, much larger than the masked range in the spectra.

On the Ir substrate (black line), the Shockley surface state band forms at negative energies with $E_0 = -0.31$ eV and in good agreement with the ARPES value [117]. The prominent raise in the DOS evolves towards negative energies is due to the change of sign in the effective mass compared to silver. The tip used to measure the set is sensitive to states at the Γ-point, since the Ir surface state dominates the whole spectrum on the substrate. Thus, if a Shockley surface state exists under the intercalated GQD, it is probed by the tip. On top of the GQD, the shape of the spectrum changes. First, the Ir surface state is absent [gray spectrum in Fig. 4.12 (a)]. Hence, it does not persist under silver covered by graphene. Second, the surface state of silver does not appear at all. Despite the large energy range, only a background arising from the metallic surface is present.

Now the whole set of spectra plotted in Fig. 4.12(b) is analyzed. At the bottom the Ir surface state is visible, enclosed with a black rectangle. At this point, the tip is still probing Ir. Approaching the border of the GQD, the surface state feature decreases, until it vanishes completely. In the second part of the spectra the tip is located on top of the

GQD. Here no significant feature persisting over several spectra can be deduced. The same behavior is observed for positive energies. There no features at all appear or disappear smoothly over several spectra. Hence, the surface states of Ir(111) and Ag(111) are absent under silver intercalated GQDs.

It is supposable that the suppression of the surface states originates from the aperiodic pattern observed on silver intercalated GQDs (see Fig. 4.11). This pattern is accompanied by an aperiodic potential, affecting the periodic potential at the surface needed to create surface states and finally leading to a suppression [193, 194].

4.6 Conclusion

Summarizing our results, for the first time we could study the properties of the Shockley-type surface state on a 15 ML silver film on Ir(111) in the presence of graphene. The Ag film shows clear hints at the presence of strain which is due to a remaining influence of the iridium substrate. As a consequence E_0 is shifted by a small amount to higher energies in accordance with observations already discussed in literature for similar systems.

The presence of graphene does affect the silver surface state more significantly: First, due to weak interaction between Ag an the C atoms, the surface state is preserved at all. This finding is similar to observations of the Ir surface state in gr/Ir(111) [117], which is even present after exposing the sample to ambient conditions. Second, the change in E_0 by the presence of graphene on top is more pronounced, providing an additional shift of $+0.2\,\mathrm{eV}$ with respect to the strain induced value.

STS point spectra reveal a Dirac feature of n-doped gr/Ag in accordance with theoretical predictions and energetically well separated from E_0 which enables the observation at all.

The analysis of confinement patterns on GQDs on Ag by means of STS reveals the Ag surface state as being trapped under the nanostructures, yielding an independent value of the shift in E_0. Dirac electron confinement remains unobserved on this sample.

From the experimental point of view this outcome is not surprising, since the feature of the surface state dominates the STS spectra. This is because of the vanishing $k_{||}$ of the lowest energy levels of its band, evolving at the Γ-point. To get a signature of Dirac electrons, one has to enhance the current, diminishing the stability of the tip. Nevertheless, graphene properties like its Dirac feature in the DOS can be probed, even though they are masked by the much more intense Ag surface state.

A way to cancel the contributions of the silver surface state under graphene is to suppress the entire band, leaving a flat background in the spectrum and hence making it possible

to probe graphene properties only. We show that this can be achieved by decreasing the thickness of the silver layer down to 1 ML, increasing the iridium-silver interaction [141]. However, no confinement of Dirac electrons was observed in this system up to now. This is most probably due to the complicated structure of 1 ML Ag under GQDs on Ir(111) [141].

CHAPTER 5

Charge Effects on Oxygen Intercalated Graphene Nanostructures on Ir(111)

Motivated by the results in Ref. [51], the experiment presented in this chapter was planned by Carsten Busse and myself. The first sample preparation was performed by myself with support by Sven Runte and Jürgen Klinkhammer at the LT-STM setup. Parts of the data analysis were performed within the Bachelor project of Christoph Boguschewski under my advice. The measurements were extended on a second preparation performed by Wouter Jolie under my advice with support by Sven Runte. Wouter Jolie also extended the data analysis of both preparations. The experimental results were discussed with Carsten Busse, Thomas Michely, Wouter Jolie, Antonio Martínez Galera and Achim Rosch.

In an STM and STS study, we investigate oxygen on Ir(111) and oxygen intercalated GQDs on Ir(111). We discover new oxygen superstructures on iridium under graphene and observe two different kinds of charge effects in the GQDs' local density of states. For one of them, in a first approach we draw a connection to the effect of tip induced band bending.

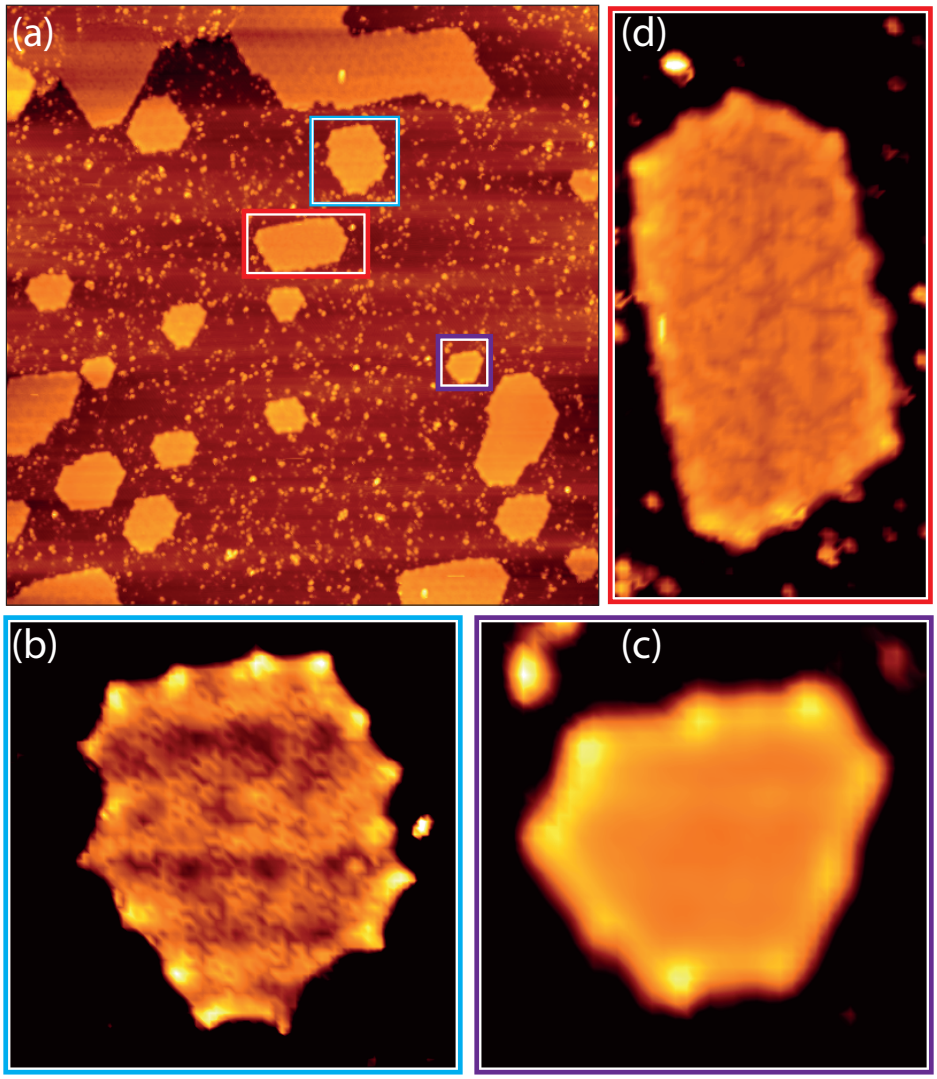

Figure 5.1: (a) Large scale overview on GQDs on Ir(111) after exposing a gr/Ir(111) sample to 750 L of molecular oxygen at $T = 433\,\mathrm{K}$, image size $110.0 \times 110.0\,\mathrm{nm}^2$, $U_{\mathrm{bias}} = 700\,\mathrm{mV}$; (b) Enlarged region of the overview, GQD with $(\sqrt{3} \times \sqrt{3})\,\mathrm{R30}^\circ$ O/Ir(111) superstructure under gr, image size $15.1 \times 15.1\,\mathrm{nm}^2$; (c) Enlarged region of the overview, structureless GQD, image size $8.2 \times 8.2\,\mathrm{nm}^2$; (d) Enlarged region of the overview (rotated), GQD with aperiodic oxygen superstructure, image size $12.0 \times 22.6\,\mathrm{nm}^2$.

Systems with reduced dimensionality enable studies on single electron effects in real space. The most prominent example probably is the coulomb blockade effect, which has been first observed in small tunnel junctions [195]. Based on charging nanostructures like for

example clusters, it even paves the way for studying single electron effects in the ionization of single molecules [196–198].

This chapter deals with the investigation of local structural and electronic features in oxygen intercalated gr/Ir(111). Details on graphene and gr/O/Ir(111) are described in Chap. 1. In this system, we find strong energy dependent LDOS features which were resolved in both point spectroscopy and spatial constant energy mapping and are most probably attributed to single electron charge effects. We describe two different kinds of these features which are associated with certain features in the GQDs' topography, respectively.

Apart from these electronic features we describe new O/Ir(111) superstructures discovered under the carbon layer: Intercalation at $T = 433\,\mathrm{K}$ yields a variety of different intercalation structures. Fig. 5.1 (a) shows a large scale STM topograph with a large distribution of differently sized GQDs on Ir(111) after exposition to 750 L of molecular oxygen at $T = 433\,\mathrm{K}$. Three characteristic islands are highlighted by boxes in blue, violet, and red. Fig. 5.1 (b) exemplarily shows the predominant $(\sqrt{3} \times \sqrt{3})\,\mathrm{R}30^\circ$ intercalation superstructure on the sample. Apart from this we observe completely structureless, probably non-intercalated GQDs [Fig. 5.1 (c)] and ones with a clearly visible, but aperiodic structure [Fig. 5.1 (d)]. These findings are remarkable, as they present the first real space observation of oxygen superstructures on Ir(111) deviating from the standard (2×1) superstructure with respect to iridium which is present where graphene is absent and is widely reported in literature [see Fig. 5.2 (c)].

Latest ARPES investigations on this system also report on the observation of the (2×1) superstructure under graphene, although dealing with a different graphene coverage and discussing evidence for intermediate phases before reaching the saturation coverage [47, 51]. In our case the fact that we are dealing with small graphene patches which are known to be more difficult to intercalate [51] most probably draws a direct connection to the observation of both intermediate and saturated phases.

5.1 Morphology

In this section the oxygen on Ir(111) superstructures under GQDs are discussed in detail. For the measurements under discussion here, a GQD/Ir(111) sample prepared by one TPG cycle (yielding a graphene coverage of ≈ 22 %) was exposed to 750 L of molecular oxygen at a sample temperature of $T = 433\,\mathrm{K}$, using a local pressure of $p_{\mathrm{ox\ local}} = 1 \times 10^{-5}\,\mathrm{mbar}$. Details of the preparation are described in Chap. 3.

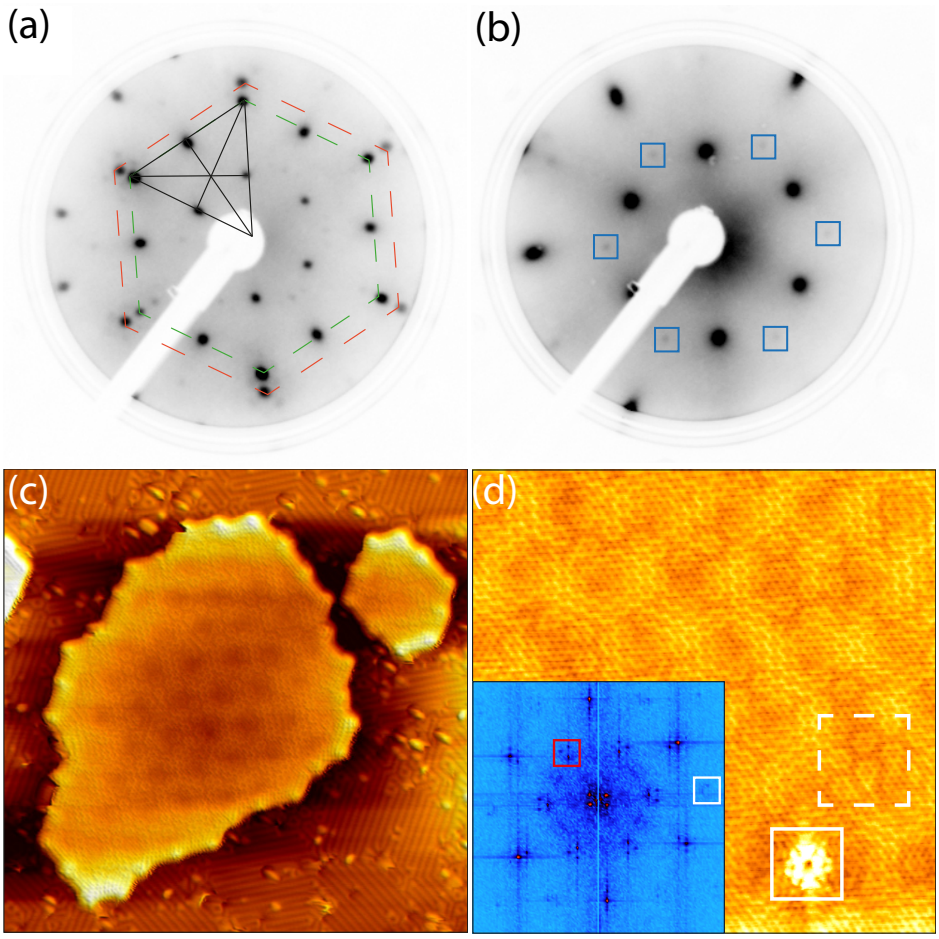

Figure 5.2: (a) and (b) LEED images (contrast inverted) of oxygen intercalated GQDs on Ir(111) prepared by exposing a 0.2 ML gr/Ir(111) sample to 750 L of molecular oxygen, imaged at primary electron energies of $E = 134.7\,\text{eV}$ and $E = 59.1\,\text{eV}$, respectively. Equilateral black triangle in (a) reveals $(\sqrt{3} \times \sqrt{3})\,\text{R}30^\circ$ superstructure spots with respect to Ir(111), also emphasized by blue boxes in (b). (c) STM topographic image of oxygen intercalated GDQs on the sample investigated by LEED [see (a), (b)], image size $29 \times 29\,\text{nm}^2$. (d) STM topographic image of the inner area of the large GQD shown in (c), image size $14 \times 14\,\text{nm}^2$; inset: corresponding FT, colored boxes see text.

Fig. 5.2 (a) shows a LEED measurement performed directly after the preparation process. Being the result of an averaging technique, it does not only contain signatures of the structures related to the intercalated GQDs, but also those related to the oxygen covered

metal substrate surface: Its quite complex overall structure is basically composed of the (2×1) oxygen superstructure on Ir(111) and the carbon lattice spots of graphene.

Referring to the (2×1) oxygen superstructure on Ir(111), due to the symmetry of the lattice, three domains on the surface rotated by 120° with respect to each other are energetically equivalent. The superposition of the three lattices appears as a $p(2 \times 2)$-superstructure with respect to Ir(111) in LEED.

The carbon lattice spots are located close to the first order (1×1) oxygen spots, forming a hexagonal structure of paired spots like in the case of carbon and iridium for gr/Ir(111). Due to the smaller lattice constant of carbon in real space, C spots are identified as the outer ones within the pairs [red dashed line in Fig. 5.2 (a)]. They are surrounded by a faint residual intensity of the moiré superstructure of gr/Ir(111), showing already a reduced interaction of graphene with the metal substrate. In addition to the spots mentioned above, a faint intensity at the $(\sqrt{3} \times \sqrt{3})\,\mathrm{R30}^\circ$ positions with respect to the iridium/oxygen lattice can be noticed. One of the spots is exemplarily identified by an equilateral triangle drawn into the LEED image [see Fig. 5.2 (a)]. The structure is also observed at different electron energy in Fig. 5.2 (b) with the $(\sqrt{3} \times \sqrt{3})\,\mathrm{R30}^\circ$ spots marked by blue boxes. Thus, a $(\sqrt{3} \times \sqrt{3})\,\mathrm{R30}^\circ$ oxygen superstructure with respect to iridium exists on the surface, representing a new structural phase in addition to the (2×1) superstructure which is realized on the metal substrate outside the nanostructures [see Fig. 5.2 (c)].

STM topographic images corresponding to the LEED measurements presented in Fig. 5.2 (a) and (b) are shown in Fig. 5.2 (c) and (d). Subfigure (d) is an enlarged topograph of the inner part of the large GQD in (c). Fig. 5.2 (c) clearly shows the three rotational domains of the (2×1) oxygen superstructure on the iridium surface outside the GQDs in real space. This observation correlates with the dominance of (2×1) in the LEED images since 80% of the surface consist of oxygen covered Ir(111). Numerous adsorbates of unknown origin are predominantly located at the phase boundaries of the rotated (2×1) domains [see Fig. 5.2 (c)].

Referring to the $(\sqrt{3} \times \sqrt{3})\,\mathrm{R30}^\circ$ superstructure, Fig. 5.2 (c) and Fig. 5.2 (d) unambiguously demonstrate that the newly observed superstructure is related to the presence of graphene. Fig. 5.2 (c) shows the complex structure which is typically observed on top of the intercalated GQDs. It is a coexistence of three single (super-)structures [see Fig. 5.2 (d)], namely the honeycomb carbon lattice as the smallest structure, the moiré superstructure present in form of the largest periodicity and the $(\sqrt{3} \times \sqrt{3})\,\mathrm{R30}^\circ$ oxygen superstructure on Ir(111) under graphene.

In fact, oxygen forms an even more complex superstructure. Its density under the carbon areas seems to be inhomogeneous. A careful look at the large GQD in Fig. 5.2 (c) reveals not only the mentioned $(\sqrt{3} \times \sqrt{3})\,\mathrm{R30}^\circ$ superstructure as well as rare patches of (2×1), but also traces of a $(2\sqrt{3} \times 2\sqrt{3})\,\mathrm{R30}^\circ$ superstructure [see Fig. 5.2 (d), dashed white box]. The latter was identified in detailed studies on the superstructures in our group [199]. Especially the inner part of the large GQD in Fig. 5.2 (c) is predominantly covered by the $(2\sqrt{3} \times 2\sqrt{3})\,\mathrm{R30}^\circ$ superstructure. Both the (2×1) and the $(2\sqrt{3} \times 2\sqrt{3})\,\mathrm{R30}^\circ$ structure correspond to a coverage of 0.5 ML, in contrast to $(\sqrt{3} \times \sqrt{3})\,\mathrm{R30}^\circ$ which corresponds to a coverage of 0.33 ML. Note that in the STM topograph oxygen appears dark on the iridium surface which can be deduced from the fact that otherwise the rare (2×2) patches would not fit to the expected oxygen density.

A Fourier Transform of the topography data in Fig. 5.2 (d) is shown in the inset. Comparing the result with the LEED image in Fig. 5.2 (a), the vital differences are grounded on the local character of the FT-STM data (averaging over the size of an STM image) in contrast to the technique of LEED which averages over much larger areas on the surface: It is obvious that the FT does not show a pronounced signature of a (2×1) superstructure, since this phase is rare on the specific GQD as mentioned above. Apart from that, it shows the graphene lattice spots surrounded by moiré satellites which are also observed in LEED. In the FT, the moiré satellites are also present in zero order at the image center.

A very interesting observation in the FT is the presence of a group of three spots at the $(\sqrt{3} \times \sqrt{3})\,\mathrm{R30}^\circ$ positions compared to the faint single spots observed in LEED [see inset Fig. 5.2 (d), red box]. The distance between the three spots fits to the moiré distance. Up to now, we do not have an explanation for the fact that in the FT there are only three instead of six moiré spots visible at the $(\sqrt{3} \times \sqrt{3})\,\mathrm{R30}^\circ$ positions. The observation of a moiré superstructure associated with the $(\sqrt{3} \times \sqrt{3})\,\mathrm{R30}^\circ$ oxygen superstructure under graphene seems to be quite puzzling because it is neither observed in LEED nor is it likely that the oxygen atoms, which are bound to the iridium substrate, interact with graphene's moiré superstructure. Therefore, we attribute their existence to the specific imaging mechanism in STM:

Most likely we observe an imprinting of the $(\sqrt{3} \times \sqrt{3})\,\mathrm{R30}^\circ$ oxygen superstructure into graphene's LDOS which is still altered by the moiré potential. In STM imaging this corresponds to a modulation (multiplication) of graphene's LDOS with the oxygen LDOS underneath and the moiré potential. In FT-STM this corresponds to folding the LDOSs of graphene and oxygen with the moiré potential. This interpretation agrees with the absence of the satellite spots in LEED: This is due to the averaging nature in connection

with the low graphene coverage, preventing a sufficient resolution in view of the fact that the $(\sqrt{3} \times \sqrt{3})\,\mathrm{R30}^\circ$ spots are very faint in LEED at all. Thus, the absence of satellite spots in LEED hints at the fact that in STM the oxygen layer under graphene is imaged indirectly via the altering of graphene's LDOS. In other words: Unlike in rare cases of other graphene systems [e.g. gr/Cu(111)], in our system the carbon layer is not transparent in STM imaging. The $(2\sqrt{3} \times 2\sqrt{3})\,\mathrm{R30}^\circ$ patches in Fig. 5.2 (c) discussed above are too small to appear in the corresponding FT.

An interesting detail is given by the defect visible in the bottom part of Fig. 5.2 (d) (large solid white box). On decoupled graphene electrons tend to create typical patterns of intervalley scattering at point defects [164]. This is exactly what is observed here in form of the two faint circles which are visible in the FT on both the left and the right side of the image [see inset of Fig. 5.2 (d), small white box]. Their location corresponds to second order $(\sqrt{3} \times \sqrt{3})\,\mathrm{R30}^\circ$ positions with respect to the carbon lattice. This acts as a further hint at the reduced substrate interaction.

The altering of graphene's electronic structure by the new oxygen phases is hard to judge for the local scale. However, for the $(\sqrt{3} \times \sqrt{3})\,\mathrm{R30}^\circ$ phase we estimate a doping level of $\Delta E_D \approx 0.3\,\mathrm{eV}$ by interpolating from $\Delta E_D = 0.6\,\mathrm{eV}$ for a saturation coverage of 0.6 ML [2]. The predominant superstructures in oxygen intercalated graphene heavily depend on the sample temperature and the applied molecular oxygen pressure during the intercalation. While the dependence on temperature was already observed and a dependence on the graphene nanostructure size was supposed within the framework of this work (compare Chap. 6), this topic was recently studied systematically by my colleagues Antonio Martínez Galera and Felix Huttmann [199].

5.2 Observation of Charge Effects

During spectroscopy measurements on oxygen intercalated GQDs we observed an increased LDOS on the intercalated GQDs. The observations can be separated into two different types, related to the edges and the surface of the GQDs, respectively.

Edge Related Charge Effect

In a first step the edge associated feature is described. A very high intensity in the $\mathrm{d}I/\mathrm{d}V$ signal is found right at the edges of the islands. These features are well visible in the inset of Fig. 5.3, which shows a $\mathrm{d}I/\mathrm{d}V$ map of a region of differently sized oxygen intercalated GQDs surrounded by the oxygen covered Ir(111) surface in a color code corresponding to

low (black) and high (white) LDOS. All edges of the islands possess bright boundaries, therefore indicating a high LDOS. In the following we refer to this LDOS feature as type A. The mere existence of the feature obviously does not depend on the island size. A cross section (black curve) reveals the massively enhanced LDOS at the borders even more clearly [Fig. 5.3], its direction is drawn into the inset (yellow line). The slope of the feature is steeper inside the island compared to the outer boundary where it resembles a kind of decay.

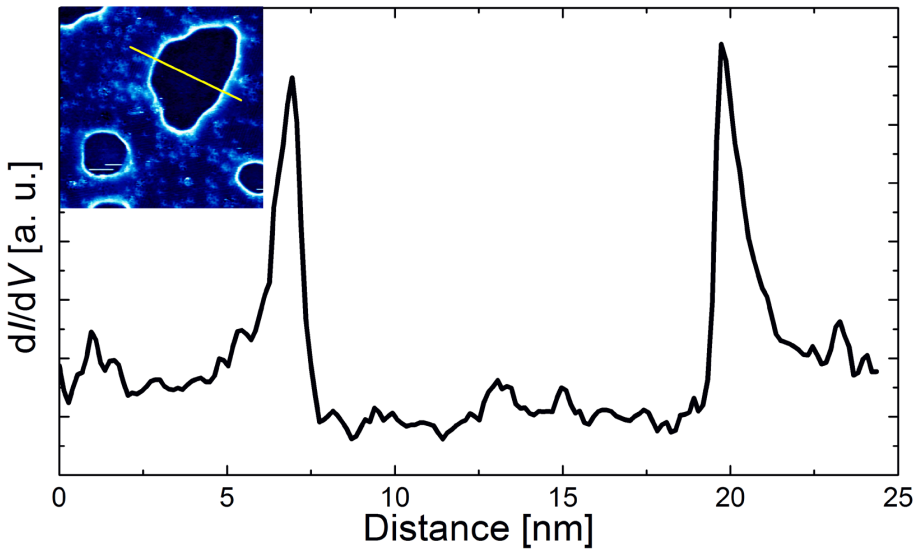

Figure 5.3: Type A LDOS features. Black: Cross section in the dI/dV constant energy map of an O intercalated GQD/Ir(111) shown in inset, following the direction of the yellow line. The substrate surface is covered by an O superstructure.

In a next step we investigate the energy dependence of this feature in a set of spatial dI/dV maps at constant energies in the region mapped in the inset of Fig. 5.3. In order to emphasize the spatial behavior of the spectroscopic feature relative to the GQD topography Fig. 5.4 shows the sum of an STM topograph and the dI/dV map at constant energy, respectively. The color code represents low LDOS (blue) to high LDOS (red). Starting with the lowest energy of 200 meV, the sum shows features of high LDOS inside the island topographies, resembling the shape of the border contours. With increasing energy the radius of these features increases, approaching the boundaries of the islands. A careful look reveals that in an energy range between 480 eV and 560 eV both the LDOS and the topographic contour coincide.

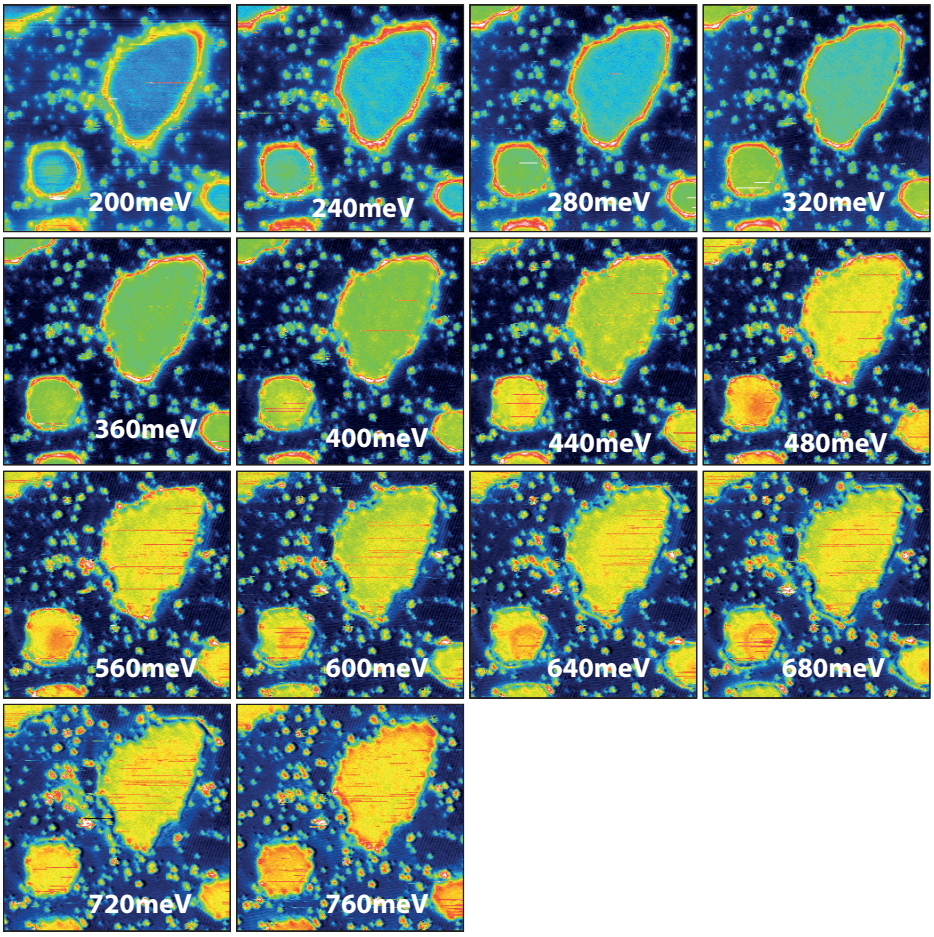

Figure 5.4: Sum of topography and simultaneously recorded constant energy $\mathrm{d}I/\mathrm{d}V$ maps; image sizes $35 \times 35\,\mathrm{nm}^2$, $I_{\mathrm{stab}} = 50\,\mathrm{pA}$, scanning speed 21 Å/s.

Increasing the energy even more, the LDOS contour moves outside the GQDs representing a kind of spill-out. Note that the absolute intensity is hard to interpret, since the topography signal is proportional to the energy integrated density of states between E_F and E, thus leading to significantly increased intensity just by using higher energies. In the sum of course this behavior is added to the pristine constant energy spectroscopy data. The GQD on the bottom left of the images shows an additional energy dependent behavior by having signatures of increased LDOS at its center in addition to the contour connected to the boundary. This observation is discussed in the second part of this chapter.

A quantitative analysis reveals that the radial evolution of the LDOS contour is described best by the quantity $(R_{\mathrm{s}} - R_{\mathrm{t}})/R_{\mathrm{t}}$, with R_{s} the radius of the spectroscopic contours and R_{t} the radius of the GQDs in topography as extracted manually from line profiles in the

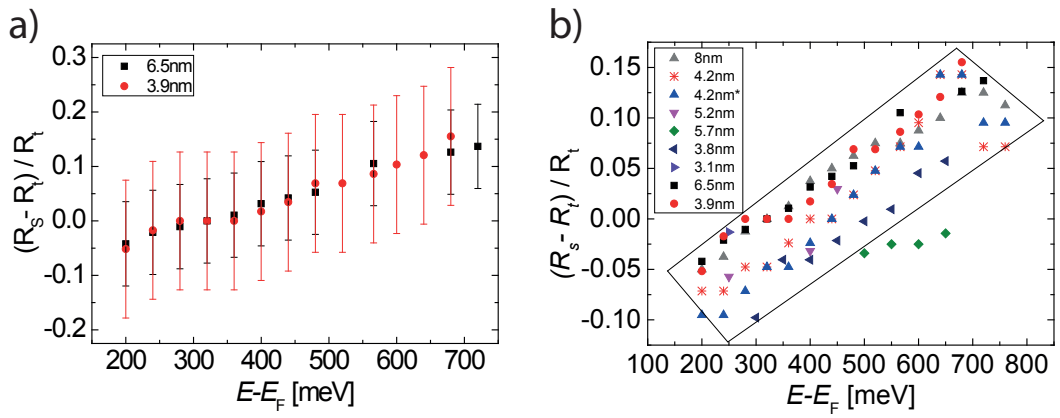

Figure 5.5: (a) Data analysis of the type A LDOS feature for two oxygen intercalated GQDs presented in Fig. 5.4: Normalized difference in radius versus energy $(R_\mathrm{s} - R_\mathrm{t})/R_\mathrm{t}(E - E_\mathrm{F})$, with R_s the averaged minimum and maximum radii of the spectroscopic contours and R_t the equivalent quantity of the GQDs' topography. Bars indicating the error in radius according to $(R_\mathrm{max} - R_\mathrm{min})/2$ for R_s and R_t, respectively. (b) Quantitative analysis of the type A LDOS effect for differently sized oxygen intercalated GQDs, including the data in (a): Normalized difference in radius versus energy $(R_\mathrm{s} - R_\mathrm{t})/R_\mathrm{t}(E - E_\mathrm{F})$, with R_s the radius of the spectroscopic contours and R_t the radius of the GQDs in topography.

spatial mapping and topographic data, respectively. The radius corresponds to the average of the largest and the smallest diameters of the typically non-circular islands, the error to $(R_\mathrm{max} - R_\mathrm{min})/2$ for R_s and R_t, respectively. Thus, the error is quite large since the islands are not really circular shaped. Corresponding plots are shown in Fig. 5.5. They suggest a linear dependence and due to $(R_\mathrm{s} - R_\mathrm{t})/R_\mathrm{t}$ reject a dependence on the area. This is important since spatial confinement structures are associated with the island size [2, 150]. A further detail is presented in Fig. 5.6. It shows a set of GQDs with a pronounced LDOS intensity at all boundaries in a $\mathrm{d}I/\mathrm{d}V$ map at $E - E_\mathrm{F} = -100\,\mathrm{meV}$ [Fig. 5.6 (b)], similar to the observations in Fig. 5.4. Two neighboring GQDs at the image center demonstrate that the LDOS feature is absent when the distance between neighboring GQDs is too close. This observation acts as a hint at the oxygen-carbon interface playing a decisive role in the emergence of the increased density of states at the GQD edges since the small channel between the neighboring GQDs might not be covered by the regular oxygen structure.

Thinking of edge effects in graphene the edge state proposed in theory [9] comes into mind. However, though being a distinct feature of graphene's edges, the broad energy range covered by the feature under discussion here does not fit to the range expected for

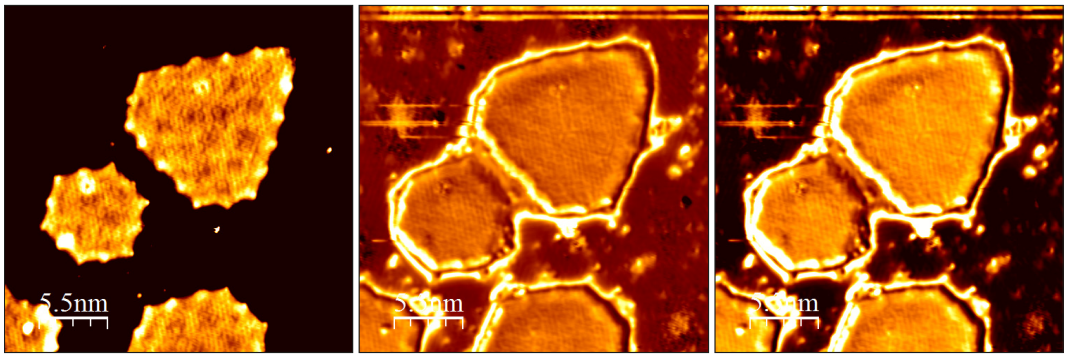

Figure 5.6: Type A LDOS features on a set of GQDs, image sizes $27.5 \times 27.5\,\mathrm{nm}^2$, $V_{\mathrm{bias}} = -100\,\mathrm{mV}$. (a) STM topograph in constant current mode, (b) $\mathrm{d}I/\mathrm{d}V$ at $E - E_{\mathrm{F}} = -100\,\mathrm{meV}$, (c) merged image (a)+(b).

the graphene edge state [200, 201]. In addition the observed spill-out character of the LDOS with a radius larger than the radius of the topography does not correspond to the expected behavior. Another option could be the presence of dangling bonds at the GQDs' edges which after intercalation should be detached from the metal substrate. However, following the intercalation process involving the detachment of the islands' borders with partly Ir bound and partly H-terminated C atoms [118, 183] by dissociated oxygen and subsequent intercalation reduces the probability to end up with dangling C-bonds in view of the presence of H and atomic O. Therefore, we assign our findings to edge effects related to the lateral one dimensional carbon-oxygen interface, providing a certain kind of 1D state associated with the presence of graphene but different from the graphene edge state related to graphene's Dirac system.

Area Related Charge Effect

As mentioned above these observations are not the only ones. A further feature, which was frequently observed in the LDOS of oxygen intercalated GQDs, is given by spot-like areas of highly increased LDOS which open up to circular structures on the area of the GQDs with increasing energy. In the following, we refer to this LDOS feature as type B. An example is presented in Fig. 5.7. It shows a series of $\mathrm{d}I/\mathrm{d}V$ constant energy maps on a $97.7\,\mathrm{nm}^2$ sized oxygen intercalated GQD on Ir(111) in an energy range between 309 meV and 756 meV and demonstrates the emergence of the circular feature and increasing radius with rising energy. For the energy range of 367 to 531 meV the feature vanishes.
Increasing the energy even more it reappears, starting with the spot-like shape again. On the top left of the figure both a corresponding STM topograph and a FT of the inner

area of the GQD topography under investigation are presented. An FT clearly shows the presence of $(\sqrt{3} \times \sqrt{3})\,\mathrm{R30}^\circ$ spots associated with the oxygen superstructure discussed in the first sections of this chapter (see small red box in FT). This is the proof of successful intercalation of the GQD. Right next to two of the $(\sqrt{3} \times \sqrt{3})\,\mathrm{R30}^\circ$ superstructure spots the FT shows two circular features in diagonal direction (see red box). These are features of intervalley scattering since they are not located on the same position as the $(\sqrt{3} \times \sqrt{3})\,\mathrm{R30}^\circ$ superstructure spots (which are with respect to iridium). However, due to the bad statistics on the small length scale of GQDs their mean existence is not sufficient to gain fruitful interpretations from them.

The evolution of the LDOS feature in Fig. 5.7 exhibits a parabolic dependence of the energy $E - E_\mathrm{F}$ on the diameter d of the circular feature, as depicted in Fig. 5.8 (c) by two parabolic fits for both the first and the second appearance, respectively. This finding reminds of a harmonic oscillator potential.

The $\mathrm{d}I/\mathrm{d}V$ maps reveal an asymmetry of the high LDOS intensity with respect to the topography of the island as the LDOS feature is spatially shifted off center to the left (see Fig. 5.7). In Fig. 5.8 (a) a corresponding matrix plot of 50 $\mathrm{d}I/\mathrm{d}V$ point spectra on a line across the same GQD shown in Fig. 5.7 reveals the energy dependence of the feature in even more detail. The color code indicates low LDOS (blue) and high LDOS (red). The matrix plot emphasizes the dependence of the peak energy on the specific place on top of the island. Isoenergy cuts in the matrix plot resemble radial cuts in the constant energy maps in Fig. 5.7. The existence of a second state is hardly visible in Fig. 5.8 (a) due to a reduced LDOS intensity compared to the first one at lower energies. Therefore, in Fig. 5.8 (b) we show an example spectrum out of the matrix plot spectra which clearly possesses two well separated peaks.

Further observations of this type of charge effect were made, but with only one charging within the investigated energy range. Some of these results obtained by constant energy mapping and point spectroscopy on a line are presented in Figs. 5.9 and 5.10, respectively. The evaluation of the $\mathrm{d}I/\mathrm{d}V$ maps in Fig. 5.9 reveals the parabolic $E(d)$ dependence even more clearly. The onset energy differs from both values obtained by the parabolic fits in Fig. 5.8 (c). Fig. 5.10 (b) shows a set of 30 normalized $\mathrm{d}I/\mathrm{d}V$ spectra across a line on a further oxygen intercalated GQD [see white arrow in Fig. 5.10 (a)]. Here a corresponding matrix plot again supports the parabolic dependence in a very convincing manner [see Fig. 5.10 (b)].

We assign the type B feature to a charge effect, as similar LDOS structures are reported for the impurity charging in alkali doped C_{60} [196], Mn acceptors in InAs [197] and GaAs

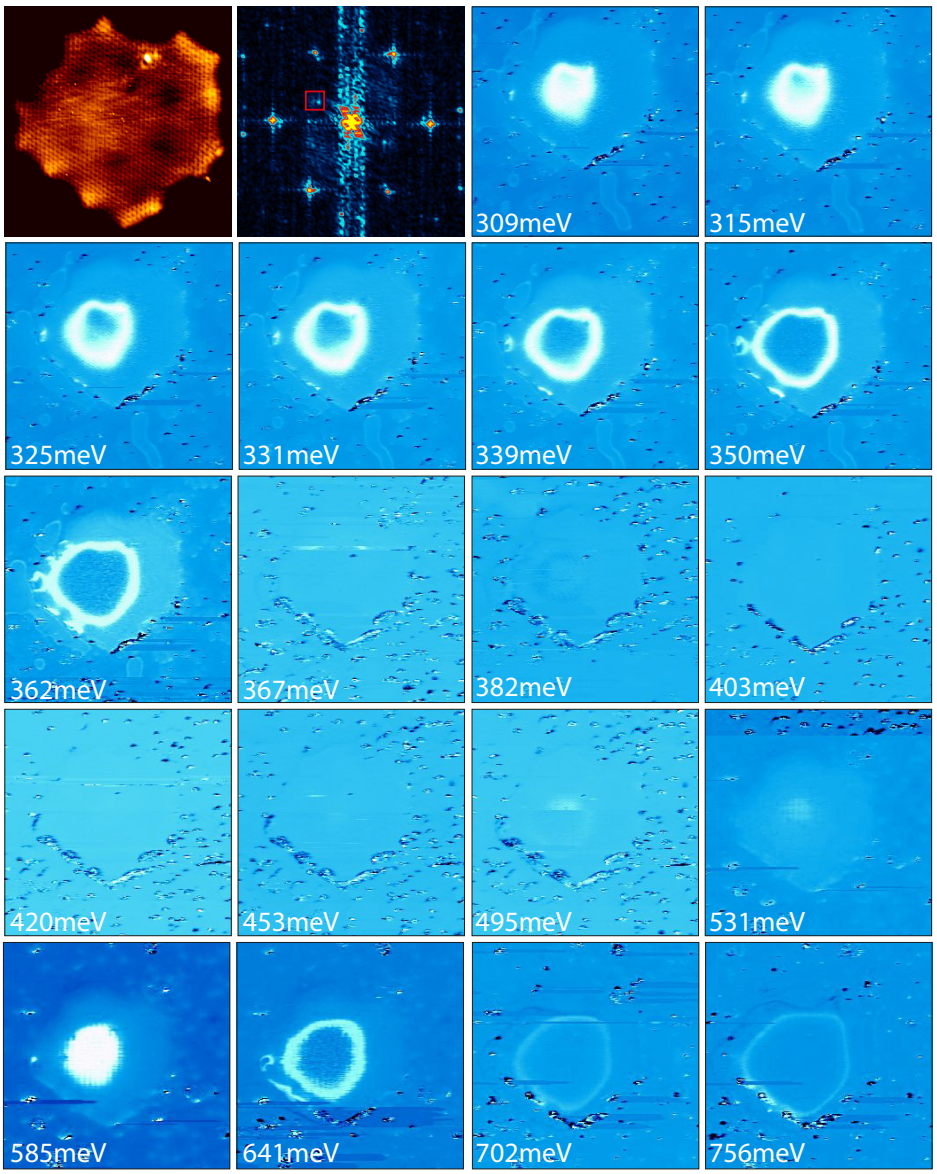

Figure 5.7: LDOS feature type B on an 97.7 nm^2 sized oxygen intercalated GQD on Ir(111). Top left: STM topographic image at $U_{\text{bias}} = 309\,\text{mV}$ and FT corresponding to inner part of the GQD topography, a red box exemplarily emphasizes one of the $(\sqrt{3} \times \sqrt{3})\,\text{R}30°$ superstructure spots. From upper right to bottom: blue colored $\text{d}I/\text{d}V$ maps at constant energies $E - E_F$, $I_{\text{stab}} = 0.1\,\text{nA}$.

[202, 203] and the ionization of Co adatoms on graphene surfaces [198, 204]. The vanishing and reappearance of our feature might be interpreted as a the creation of a new (second) single electron charge state. Although a definite assignment remains difficult, it is most

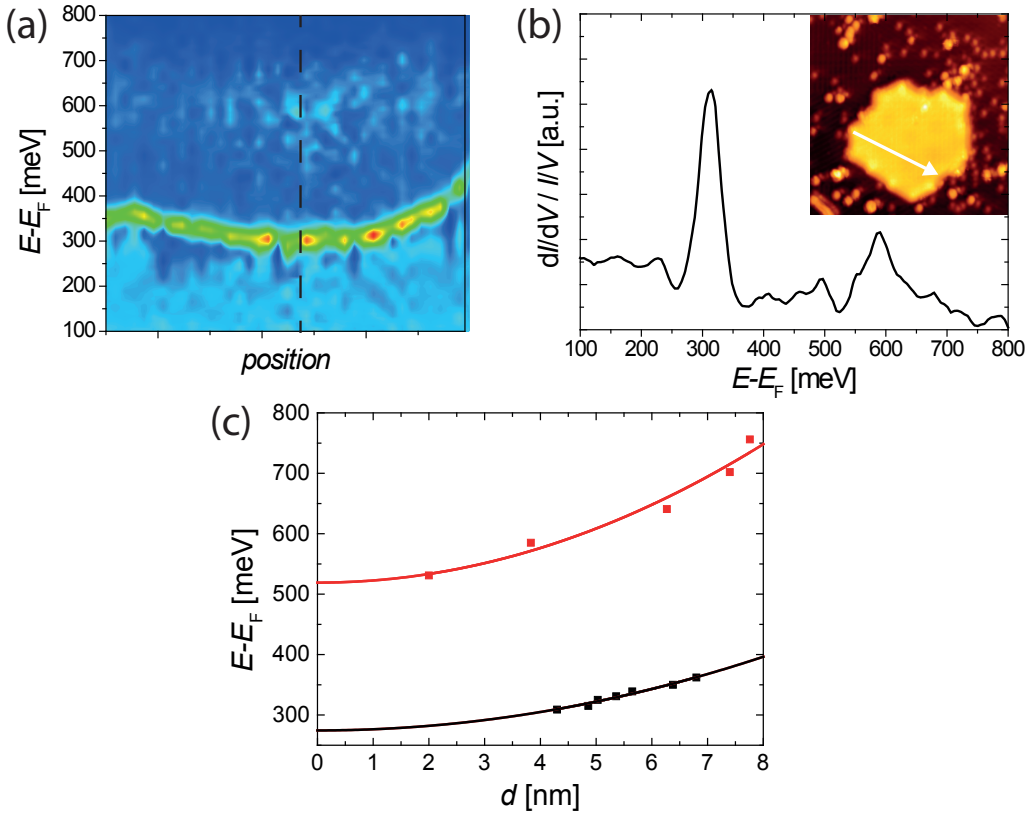

Figure 5.8: LDOS effect type B on a 97.7 nm^2 oxygen intercalated GQD on Ir(111), see corresponding spatial LDOS maps in Fig. 5.7. (a) dI/dV matrix plot of 50 normalized dI/dV point spectra on a line across the GQD shown Fig. 5.7 and in the inset of (b); $U_{\mathrm{stab}} = 756\,\mathrm{meV}$, $I_{\mathrm{stab}} = 0.1\,\mathrm{nA}$. (b) Example of a normalized dI/dV spectrum used for the matrix plot, see dashed black line in (a); inset: STM topographic image, white arrow indicating the direction of the point spectra line shown in (a). (c) Energy depending on diameter $E(d)$ of the LDOS features in Fig. 5.7, for the first and second appearance.

probable that the GQD itself is charged by the electrons from the tunneling process rather than e.g. single atoms of the oxygen layer below the carbon layer. This interpretation is supported by our knowledge of the high degree of decoupling of the oxygen intercalated graphene layer discussed in Sec. 1.5.

In a first attempt we approach a more detailed interpretation of the type B charge effects by assigning them to tip induced charging as discussed by Brar et al. in Ref. [198] for Co adatoms on back-gated graphene/SiO_2. The ring-like structures are explained by a tip induced ionization radius [196]. It is based on the effect of pushing defect states pass E_{F} by a tip induced band bending caused by the electric field connected to the bias voltage

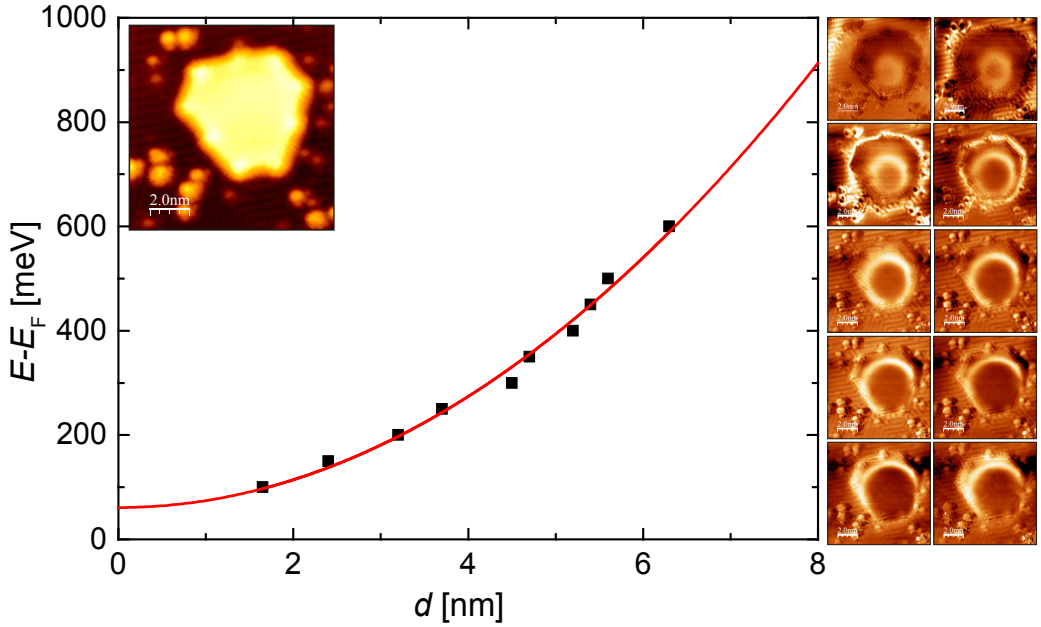

Figure 5.9: LDOS effect type B on a 30.0 nm^2 sized oxygen intercalated GQD on Ir(111). Right: spatial LDOS maps with increasing energy from top left to bottom right, $I_{\mathrm{stab}} = 80\,\mathrm{pA}$, $E - E_{\mathrm{F}}$ see left. Left: $E(d)$ with parabolic fit $E(d) = E_0 + \alpha d^2$ for the energies of the maps presented on the right; inset: STM topograph at $V_{\mathrm{stab}} = 450\,\mathrm{mV}$, $I_{\mathrm{stab}} = 80\,\mathrm{pA}$.

applied in STM. The effect of band bending is strongly correlated with the ability of the sample to efficiently screen the tip electric field. Therefore, there are basically no band bending effects observed on metal surfaces due to their high charge carrier density, but in a very pronounced way for semiconductor surfaces [205].

In the case of Brar et al., the tip induced band bending pushes Co-graphene hybrid states through E_{F}, producing charging and discharging of these defect states. In a charge capacitance model the authors calculate the shift $\Delta\mu$ in chemical potential of the graphene layer depending on the applied bias voltage V_{b} and the backgate voltage V_{gate}.

In Fig. 5.11 we adapt this model to our situation. In our case we are dealing with oxygen intercalated GQDs on Ir(111). Since our graphene does not possess a tunable backgate but deals with the presence of the oxygen layer, we calculate a V_{gate} equivalent quantity by the charge transfer per graphene unit cell n_e provided by the oxygen induced p-doping, using values obtained from a DFT calculation [172]:

$$V_{\mathrm{gate}} = \frac{n_e}{a_{\mathrm{c}}}\frac{d_2}{\epsilon_r\epsilon_0} = \frac{0.004e}{2.45\,\text{Å}^2\,\sin\,60^\circ}\frac{3.96\,\text{Å}}{1.22\epsilon_0} = 0.4\,\mathrm{V} \tag{5.1}$$

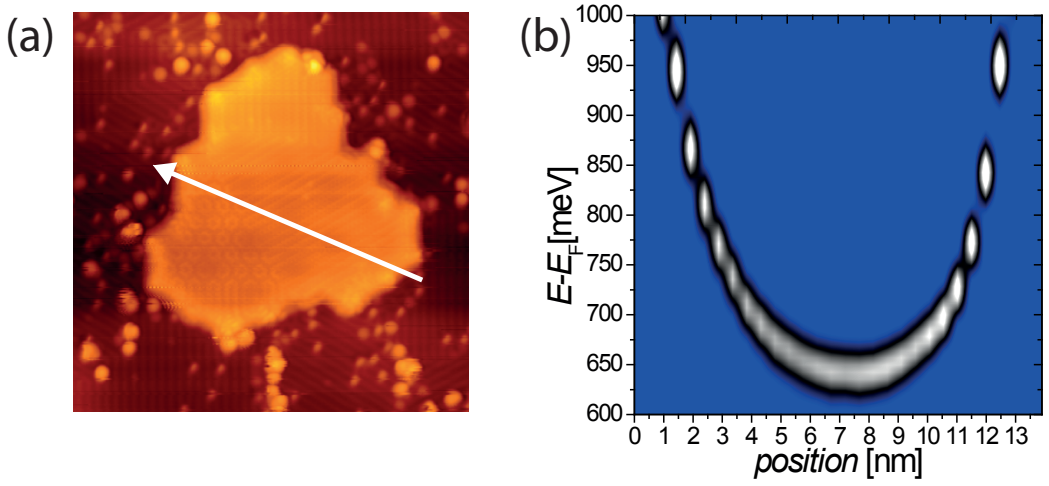

Figure 5.10: LDOS effect type B on a 134 nm^2 sized oxygen intercalated GQD on Ir(111). (a) STM topograph; image size 20.0 nm^2, $I_{\mathrm{stab}} = 0.1$ nA, $V_{\mathrm{stab}} = 1$ V. (b) $(\mathrm{d}I/\mathrm{d}V) / (I/V)$ matrix plot of 30 $\mathrm{d}I/\mathrm{d}V$ point spectra on the line across the GQD shown in (a) (see white arrow); $V_{\mathrm{stab}} = 1$ V, $I_{\mathrm{stab}} = 0.1$ nA.

with a_{c} the lattice constant of graphene, ϵ_r the dielectric constant of the oxygen layer (see below) and d_2 the distance between graphene and the Ir(111) substrate as observed in XSW experiments [120]. According to Ref. [205], the shift in the chemical potential can be calculated using

$$e\phi_{tip} = -eV_b + \Delta\Phi_{tip-gr} \tag{5.2}$$

$$e\phi_{gate} = -eV_{gate} + \Delta\Phi_{gate-gr} \tag{5.3}$$

$$\Delta\mu = -e\phi_Q \tag{5.4}$$

and

$$V_{\mathrm{b}} = \frac{d_1}{d_2}\frac{\epsilon_i}{\epsilon_0}\left(-V_{gate} + \frac{\Delta\Phi_{\mathrm{gate-gr}}}{e}\right) - \left(1 + \frac{d_1}{d_2}\frac{\epsilon_i}{\epsilon_0}\right)\frac{\Delta\mu}{e} \tag{5.5}$$

$$- \frac{d_1 e^3}{\epsilon_0(\hbar v_F)^2\pi}\frac{\Delta\mu}{e}\left|-\frac{\delta\mu}{e}\right| + \frac{\Delta\Phi_{\mathrm{tip-gr}}}{e} \tag{5.6}$$

$$= \frac{9\times10^{-10}}{3.96\times10^{-10}}1.22(-0.4+1.19) - \left(1 + \frac{9\times10^{-10}}{3.96\times10^{-10}}1.22\right)\frac{\Delta\mu}{e} \tag{5.7}$$

$$- \frac{9\times10^{-10}\times(1.6\times10^{-19})^3}{8.85\times10^{-12}\times(1.05\times10^{-34}\times1\times10^6)^2\times\pi}\frac{\Delta\mu}{e}\left|-\frac{\delta\mu}{e}\right| + 0. \tag{5.8}$$

The whole set of parameters entering the calculations is summarized in Tab. 5.1.

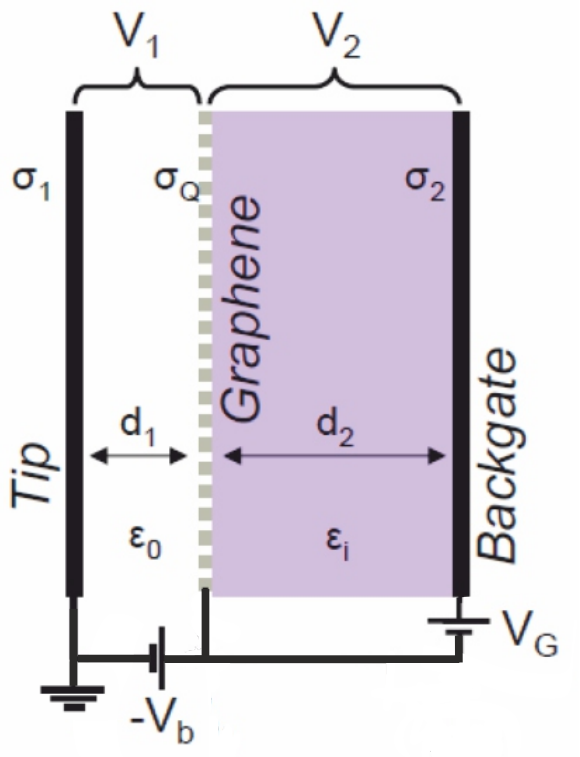

Figure 5.11: Capacitor model adapted from Ref. [198] and changed to our geometry with fixed backgate voltage. Modified figure reprinted by permission from Macmillan Publishers Ltd: Nature Physics [198] (supplementary information), copyright 2010.

Table 5.1: Summary of values entering the calculation of $\Delta\mu$.

quantity	**value**
d_1	9Å[198]
d_2	3.96Å[120]
$\hbar$	1.05×10^{-34} J s
ϵ_0	8.85×10^{-12} $\frac{\text{As}}{\text{Vm}}$
ϵ_i	$1.22 \times \epsilon_0$ [206]
Φ_{gr}	4.6 eV
$\Phi_{\text{tip}} = \Phi_W$	4.6 eV
$\Phi_{\text{gate}} = \Phi_{Ir}$	4.6 eV
$\Delta\Phi_{\text{gate-gr}}$	1.19 eV
$\Delta\Phi_{\text{tip-gr}}$	0 eV
V_{gate}	0.4 V

With d_1 the tip-sample distance (capacitor tip/sample), d_2 the distance between graphene and the Ir(111) substrate as observed in XSW experiments [120], ϵ_i the dielectric constant of the oxygen layer as approximated by a literature value for liquid oxygen under high pressure with the same density as observed for our superstructure [206], Φ_{gr} the workfunction of graphene, Φ_{tip} the workfunction of the tungsten STM tip, Φ_{gate} the workfunction of the backgate (here our Ir substrate) and V_{gate} the backgate voltage as calculated via charge transfer in Eq. 5.1.

We plot $\Delta\mu$ versus the applied tip bias voltage V_{b} and obtain the curve shown in Fig. 5.12 (a). While in the case of Co on graphene [205] the relevant energy scale is given by pushing the Co-graphene hybrid states through E_F, we have to think about a comparable scale in our system. Since it turns out by DFT calculations presented in Chap. 6 of this thesis that the oxygen layer forms oxygen-iridium hybrid states which do not interact with the carbon layer, we are missing an equivalent DOS feature in our system. In addition we do not observe structural defects in STM topographs which are related to the LDOS features, neither in the carbon layer, nor underneath it (see e.g. STM topograph in Fig. 5.7). Despite it is impossible to completely rule out a charging of defect sites which remain unobserved in STM, we stick to our measurements and assume a structurally intact graphene layer. Instead of hybrid structures in the graphene bandstructure brought up by defects, we

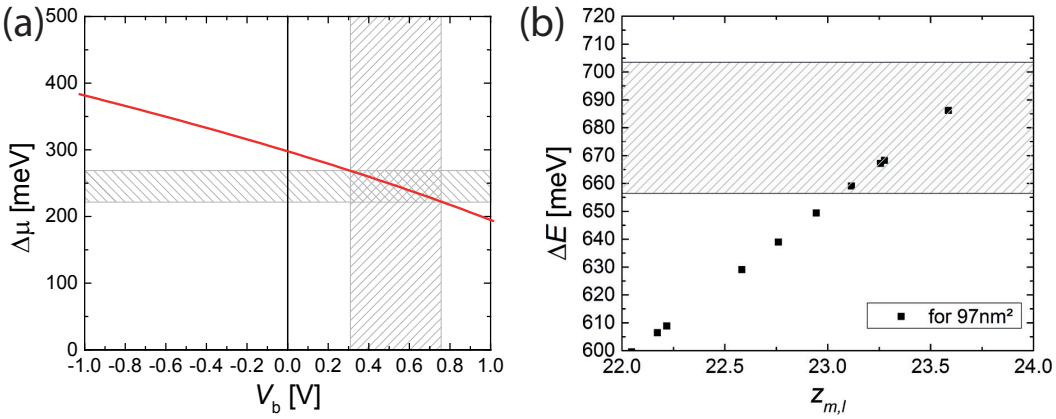

Figure 5.12: (a) Shift in $\Delta\mu$ depending on bias voltage V_{b}; shaded area: parameter range corresponding to Fig. 5.7. (b) Energy shift of electronic states at E_{F} by spatial confinement on a 97.7 nm sized oxygen intercalated GQD, depending on the value of the Bessel function zeroes $z_{m,l}$, see Ref. [207].

remember the fundamental difference of our system compared to [205], namely the reduced dimensionality in form of quantum dots. Therefore, we check the occurring energy splitting in the graphene spectrum when it is discretized by finite size (see Sec. 1.7) and compare it

to the available shift in $\Delta\mu$ induced by band bending as calculated above. In addition we have to focus on those states which are close to E_{F}.

Comparing the energy scales, we refer to the example at hand in Fig. 5.7. As indicated by the shaded areas in Fig. 5.12 (a), the calculated shift in $\Delta\mu$ for the energy range of 309..756 meV amounts to $\Delta\mu = 47$ meV. Taking a look at Fig. 5.12 (b), the shaded area corresponds to exactly 47 meV in energy range and indeed includes several (high order) Bessel eigenstates with an absolute energy shift by confinement larger than the doping level of 680 meV [1]. The values of $z_{m,l}$ in Fig. 5.12 (b) are related to specific states (m,l) via the table provided in Ref. [207]. This basically means two aspects, namely, first, there are several high order Bessel eigenstates causing a confinement shift of states close to E_{F} larger than the doping level. This is required to push states pass E_{F} by band bending as described in Ref. [205]. Second, some neighboring Bessel eigenstates are contained in the energy range of $\Delta\mu = 47$ meV. Note that those of the high order Bessel states with $l = 0$ resemble a sharp concentration of LDOS at the center of the islands, resembling a localized spatial feature comparable to a structural defect site. In sum, from the energy scales point of view it is possible to sweep few Bessel eigenstates of the GQD pass E_{F} by tip induced band bending.

Answering the question why there are exactly two chargings observed in the energy range of Fig. 5.7 remains tough, since on the one hand the shift in $\Delta\mu$ depends on numerous parameters (see Tab. 5.1) and on the other hand the Bessel eigenstates do not possess equidistant spacing in energy. Taken together pushing two eigenstates pass E_{F} in the energy range of Fig. 5.7 seems to be reasonable.

An alternative approach is based on the fact that the uncertainty in $\Delta\mu$ is even larger when tip shape influences are taken into account, too. If we assume a $\Delta\mu$ increased by one order of magnitude due to a differently shaped tip, there is no need to concentrate on Bessel states with an absolute energy shift of 680 meV anymore. Low order states which have a larger energy spacing could already provide the desired energy scale.

The fact that the observed circle of increased LDOS is always more or less centered on the islands could be due to the electric potential associated with the boundary as it is known from the observation of confinement in the framework of this work (see Chap. 6 and Chap. 7). This boundary potential could focus the charge accumulation in the center of the GQDs and could also explain moderate off-centering effects since the GQDs are not perfectly symmetric.

Maybe further experiments can clarify the interpretation given here, although the task of excluding a charging of (hidden) defect sites under the carbon layer (e.g. in the oxygen layer) remains tough.

5.3 Conclusion

In this chapter we report on the first high-resolution STM/STS investigations of the local topographic and electronic properties of oxygen intercalated GQDs on Ir(111). For the intercalation parameters of 750 L oxygen at $T = 433\,\mathrm{K}$ we observe a coexistence of three different superstructures of atomic oxygen adsorbed to the Ir(111) substrate under graphene: (2×1), $(\sqrt{3} \times \sqrt{3})\,\mathrm{R30}^\circ$, and $(2\sqrt{3} \times 2\sqrt{3})\,\mathrm{R30}^\circ$. In addition also non intercalated and aperiodic superstructures exist under GQDs. We have hints that the dominating superstructures are determined by the oxygen pressure and temperature used in the intercalation process, further investigations on this topic are in progress [199]. Very weak moiré spots in LEED and a faint signal from intervalley scattering in FT-STM indicate a reduced substrate interaction.

Concerning the electronic structure, we observed pronounced features in the LDOS of oxygen intercalated GQDs related to the edges (A) and the area of the GQDs (B). We attribute both LDOS features to charge effects either in the GQD/oxygen interface line (A) and/or of laterally confined states (B). The latter type is characterized by a parabolic $E(d)$ dependence, resembling a harmonic oscillator potential. In a first approach, we apply the tip induced band bending model described in Ref. [20] to our situation. The role of spatially and energetically localized features in our case is assumed by high-order eigenstates of the discretized energy spectrum generated by the finite size of our nanostructures. The variable backgate in our case is substituted by the fixed chemical gating provided by the oxygen layer underneath graphene. With these modifications, the model provides similar energy scales for the shift of the chemical potential and our experimental observations.

Perspective investigations have to reveal details of the oxygen/iridium interface in order to approach a mechanism for the type A features. This should include both STM measurements, e.g. IETS can reveal characteristic vibrational modes, and theoretical calculations. Concerning the type B feature, a remaining task is to understand the origin of the parabolic $E(d)$ dependence and to rule out charging of single atoms or defect sites in the oxygen layer underneath graphene by further topographic STM imaging focused on this aspect.

CHAPTER 6

Dirac Electron Confinement on Graphene Quantum Dots

The STM experiments were planned by Wouter Jolie, Carsten Busse and myself. Sample preparation was performed by Wouter Jolie under my advice and with support by Sven Runte. Ulrike Schröder and Timm Gerber contributed with hints concerning the intercalation process. STM measurements were performed by Wouter Jolie and myself. Data analysis was done by Wouter Jolie and myself. The ARPES measurements were performed at Institut za Fiziku (Zagreb) by Marin Petrović, Marko Kralj and myself. The DFT calculations were performed by Nicolae Atodiresei, Vasile Caciuc and Stefan Blügel at Peter Grünberg Institut (PGI) and Institute for Advanced Simulation (IAS) at Forschungszentrum Jülich and JARA. Several paragraphs of this chapter are adopted within their meaning or literally taken from the manuscript ***Dirac Electron Confinement on Graphene Quantum Dots*** *[1] by Wouter Jolie, FC, Marin Petrović, Nicolae Atodiresei, Vasile Caciuc, Stefan Blügel, Marko Kralj, Thomas Michely, and Carsten Busse and from further work of Wouter Jolie [141]. This work is supported by DFG through SFB 608, the projects Bu2197/2-1, INST 2156/514-1, the Bonn-Cologne Graduate School of Physics and Astronomy, and DAAD-MZOS via the project "Electrons in two dimensions".*

In view of experimental difficulties related to the presence of metallic surface states under the carbon layer for both the Ag and Ir substrates, we present an experimental advancement towards a system where the surface state is efficiently suppressed. This is achieved by oxygen adsorption on the free Ir areas and intercalation under the GQDs. By the means of STS, we present the first unambiguous observation of Dirac electron confinement on graphene quantum dots. We analyze the confined electronic states with a relativistic particle-in-a-box model and calculate a linear dispersion relation which matches the results of a complementary ARPES study. Related to recent results reported in literature [47, 51, 192], the observations are confirmed in a DFT study, which additionally to the benefit for the observation of Dirac confinement provides universal insight into the decoupling capabilities of oxygen as an intercalant.

As already briefly mentioned in Sec. 1.7, recent STS studies showed that graphene nanostructures epitaxially grown on Ir(111) are able to confine electronic states [110, 111, 113]. Although it is tempting to assign these states to the Dirac electrons of graphene, several issues are puzzling: In Ref. [110] the size-dependent energies of the first and second eigenstate were attributed to the characteristic linear dispersion relation with a Fermi velocity of $v_F = 10^6$ m/s in agreement with ARPES-studies for extended graphene on Ir(111) [92], whereas substantially lower values of $v_F \approx 0.6 \times 10^6$ m/s are deduced in Refs. [111] and [113]. In addition, for the latter studies a slight n-doping of graphene is found, in contrast to the p-doping established for extended graphene [91]. To make things worse, the most recent study [112] questions the assignment of these states to the Dirac electrons, but rather explains them by a confined surface state of Ir(111), namely the S_0 state at the Γ-point which even persists underneath graphene [114, 117]. This hypothesis was also put forward in Ref. [110] for the case of large islands. In Fig. 6.1 we give a graphical comparison of the results of the above mentioned literature. The results of the existing literature [110–113] can be compared when the data are analyzed in a standardized way. Therefore we applied an approximation to the shape of the eigenstates as Bessel-functions to all of them (compare Fig. 1.8).

The islands and states represented by the data points in Fig. 3 (h) of Ref. [110] were re-evaluated using the procedure described below: Their size together with the quantum numbers of the observed state allows to calculate k, the tunneling voltage at which the given state is observed defines E [208]. These data are shown in Fig. 6.1 using black squares. Note that the states named $n = 0$ and $n = 1$ in Ref. [110] are (1,0) and (1,1) in our notation.

For the case of Ref. [111], Fig. 3 (a) contains data of the STM sample bias where state S [corresponding to (1,0) in our notation] is observed vs. island area. As in the evaluation of our data (see below), we can derive k when we know the area and the state, the energy is determined by the bias voltage. The result is shown in Fig. 6.1 using green upward pointing triangles.

Ref. [113] already presents the data in the standard form (Fig. 4), we have copied these values into our graph as blue downward pointing triangles.

Finally, we also converted the peak position vs. $(\text{diameter})^{-2}$ plot in Fig. 3 (e) from Ref. [112] into $E(k)$ using the Bessel-type analysis and display the resulting values using orange diamonds.

For comparison, we also include dispersion relations determined for the extended system as determined by angular resolved photoemission. The black line is $E(k)$ for the Dirac

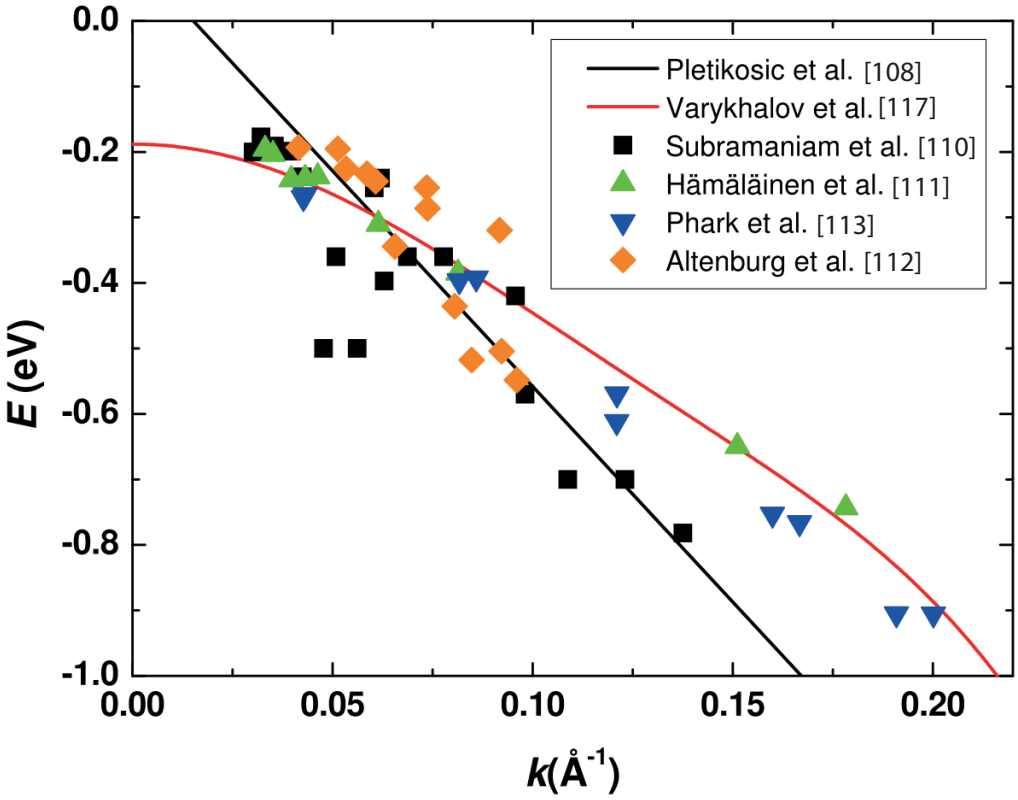

Figure 6.1: Overview of existing data. Lines represent ARPES measurements on extended systems, the symbols represent data on small graphene islands.

electrons in graphene using $E_D = 0.1$ eV for the position of the Dirac point and $v_F = 10^6$ m/s for the Fermi velocity [92, 108]. The red line is the Ir(111) S_0 surface state underneath graphene [117]. It is obtained by fitting a polynomial up to order $n = 8$ using only even n to both branches of the ARPES-data. Scattering can only take place within the same branch as spin conservation has to be obeyed [162], therefore only one common parabola results.

It is obvious that based on this data alone it is not possible to attribute any of the experiments clearly to the Dirac electrons or the Ir(111) surface state. This can also be quantified by calculating the root-mean-square deviation of all four data sets with respect to the two models, see Tab. 6.1.

One can conclude that the coexistence of the Dirac state of graphene and the surface state of Ir(111) does not allow an unambiguous assignment of the experimentally observed states.

At first sight it may seem surprising that it is not possible to clearly distinguish between Dirac electrons at the K-points with a linear dispersion and a Rashba-split parabolic surface state with negative effective mass [117]. The reasons for this are that (i) the

Table 6.1: Root mean square deviation of the published data from the two conflicting explanations (see supplemental material in Ref. [1])

Reference	ΔE_{S_0} (eV)	$\Delta E_{\mathrm{Dirac}}$ (eV)
Subramaniam et al. [110]	0.120	0.108
Hämäläinen et al. [111]	0.018	0.147
Phark et al. [113]	0.047	0.173
Altenburg et al. [112]	0.079	0.075

standing wave patterns observed in STM are only determined by the differences between in- and outgoing waves and are in consequence insensitive to the absolute values of the k-vectors involved, (ii) the Rashba-splitting is averaged out in STM observations [162] because scattering is only allowed between states with the same spin quantum number, and (iii) the curvature of the parabolic S_0 is rather low in the analyzed range of energies (in fact, just fitting a line to the spin-averaged S_0 in the range between 0.05 Å^{-1} and 0.20 Å^{-1} yields $v_{\mathrm{F}} = 0.6 \times 10^6$ m/s, disturbingly close to the values determined in Refs. [111] and [113]).

The most clear-cut way to resolve this situation is to prepare a system where the surface states of Ir(111) are absent. In this chapter we demonstrate that this goal can be achieved using a further property of the system presented in the preceding chapter: Oxygen present between the carbon sheet and the substrate [47, 51] destroys the surface states. This leaves Dirac electrons as the only explanation for the eigenstates we observe.

6.1 Morphology

The sample preparation followed the steps described for the GQD preparation and oxygen intercalation in Chap. 3. For graphene growth, we applied one TPG cycle, adsorbing ethylene with a subsequent heating step at $1285 - 1420$ K and yielding a graphene coverage of ≈ 22 %. The temperature is lower compared to the one used for the gr/Ag/Ir(111) experiment (see Chap. 4), reducing the average size of the GQDs [29]. This leads to GQDs with sizes where sufficiently separated discrete states are expected. In addition, it results in a wide k-range in the dispersion relation that can be compared with the band of graphene. Deviating from the preceding chapter on new oxygen superstructures and charge effects, for the oxygen intercalation experiments described in this chapter we decided to use a slightly enhanced intercalation temperature of 450 K instead of 433 K in order to reduce the number of non-intercalated islands and the appearance of aperiodic superstructures

(compare to Chap. 5). To ensure a decent quality of our sample, the three preparation

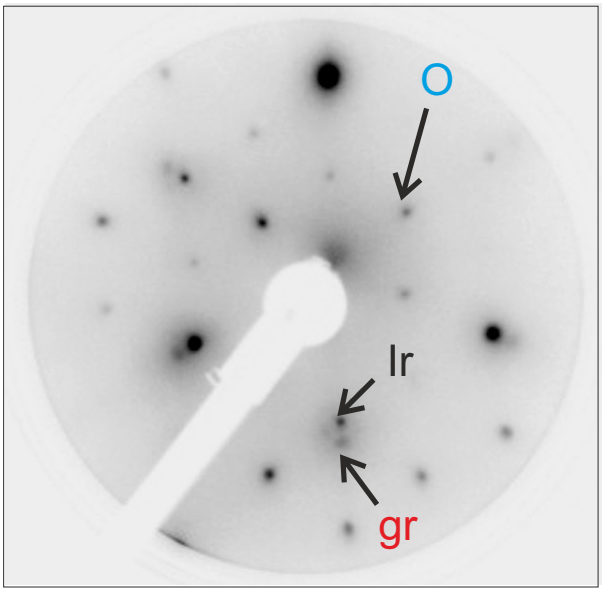

Figure 6.2: LEED pattern (contrast inverted and enhanced) at primary electron energy $E = 154.5$ eV obtained from GQDs on Ir(111) after oxygen intercalation at $T = 450$ K. The arrows indicate graphene (gr), iridium (Ir) and oxygen (O) spots.

steps of cleaning iridium, growing GQDs and intercalating oxygen were checked in a LEED measurement after each step, respectively. The LEED image of the resulting surface recorded at an energy $E = 154.5$ eV is shown in Fig. 6.2. The oxygen signatures visible in LEED after subsequent oxygen intercalation are identical to the findings already discussed in Secs. 3.1 and 5.1 for the 433 K intercalation apart from the fact that the $(\sqrt{3} \times \sqrt{3})R30°$-superstructure is completely absent.

STM topographic images of the surface are shown in Fig. 6.3. GQDs (bright) of different size and shape are visible. Next to graphene, oxygen rows form three p(2×1)-domains on the Ir(111) surface [Fig. 6.3 (b)], connecting to the superstructure visible in LEED (see Fig. 6.2) and already discussed in Sec. 5.1. Decorated structural phase boundaries are observed as also already mentioned for the 433 K preparation.

On most of the GQDs, the same p(2×1)-superstructure is visible, see Fig. 6.3 (c). This proves that oxygen is intercalated between graphene and Ir(111). However, in some cases an additional phase arises, as it is observed on the GQD in Fig. 6.3 (c) (see inset): This is the $(2\sqrt{3} \times 2\sqrt{3})R30°$-superstructure already known from Sec. 5.1. However, for the temperature $T = 450$ K used here, the p(2×1)-phase dominates under the GQDs. This is supported by the fact that the $(2\sqrt{3} \times 2\sqrt{3})R30°$-superstructure is completely absent in LEED (see Fig. 6.2).

Thus, although only a moderate difference of $\Delta T = 17$ K, the increase in temperature during the intercalation step changed the oxygen superstructures on iridium under graphene

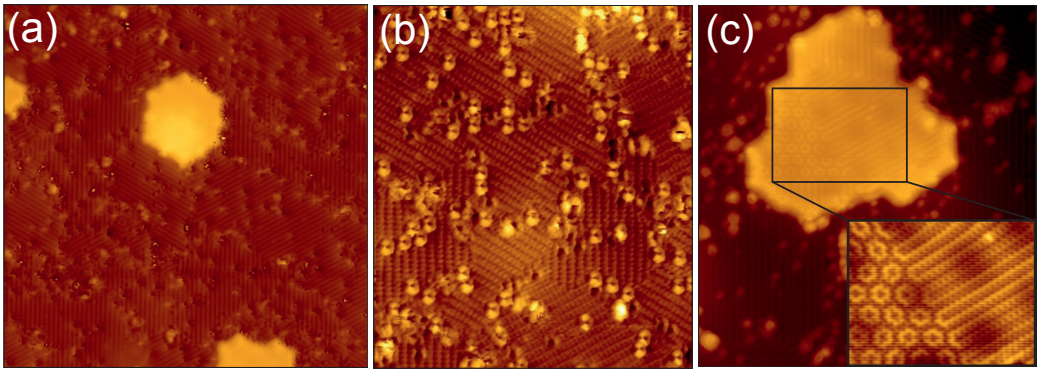

Figure 6.3: (a) STM topographs of the surface, showing the oxygen superstructure on Ir(111) and GQDs ($I = 0.31$ nA, $V = 0.8$ V, image size $38 \times 38\text{nm}^2$). (b) Atomic resolution on oxygen (2×1) superstructure on Ir(111) ($I = 0.5$ nA, $V = 0.7$ V, image size 18×21 nm^2). (c) Oxygen intercalated GQD ($I = 0.28$ nA, $V = 1$ V, image size 24×28 nm^2, inset: atomic resolution). Reprinted with modifications from [141].

in such a way that the $(\sqrt{3} \times \sqrt{3})\,\text{R}30^\circ$ superstructure was absent, still leaving patches of the $(2\sqrt{3} \times 2\sqrt{3})\,\text{R}30^\circ$ and the dominating (2×1) superstructure [see inset of Fig. 6.3 (c), compare to Sec. 5.1]. The number of non-intercalated islands was significantly reduced compared to the preparation used in Chap. 5. Aperiodic superstructures were not observed at all.

Sample for ARPES

Deviating from the preparation routine just outlined for STM, for the ARPES measurements we used six TPG cycles followed by CVD, using ethylene with $p = 10^{-7}$ mbar at 1120 K for five minutes, leading to nearly full coverage. Thereby we (i) obtain a high photoemission intensity from graphene and (ii) achieve a low density of graphene step edges which are known to scatter Ir surface states and thus reduce their photoemission intensity [92]. To achieve oxygen intercalation, also this sample was exposed to more than 750 L of O_2 at $T \geqslant 450$ K, exceeding the amount for saturation coverage by more than an order of magnitude [51].

6.2 Suppressing the Iridium Surface State

The global bandstructure of gr/Ir(111) and gr/O/Ir(111) is determined using ARPES, see Fig. 6.4. ARPES measurements were performed at 150 K in a UHV setup with a base

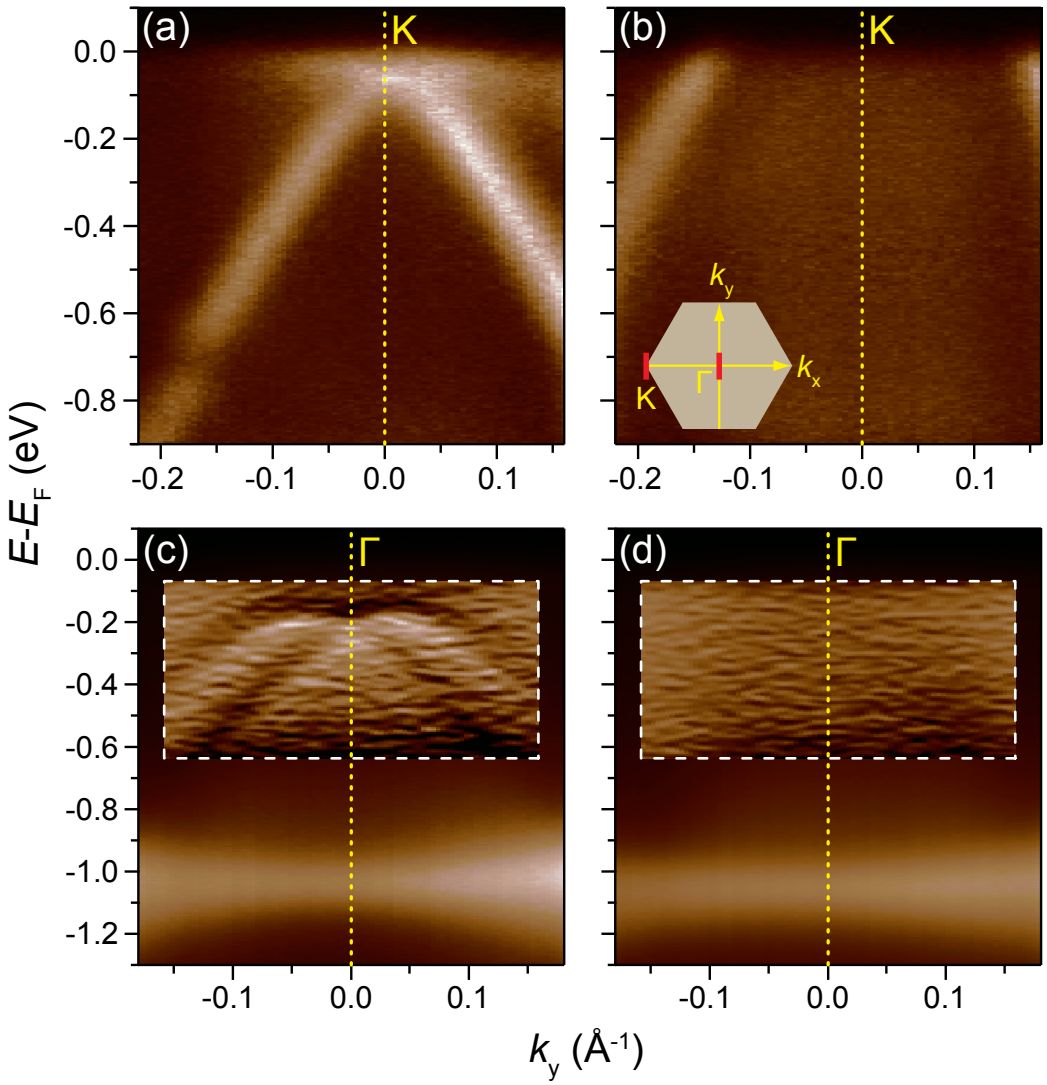

Figure 6.4: ARPES spectra of graphene on Ir(111) before (left) and after (right) oxygen intercalation: (a)→(b) K-point: The Dirac cone of graphene shifts to higher energies due to p-doping. (c)→(d) Γ-point: The Rashba-split Shockley surface state is visible before oxygen intercalation, but not afterwards. For better visibility, the derivative of the photoemission intensity is shown in (c) and (d), i.e. the data appears as illuminated from below with the bright states casting dark shadows.

pressure lower than 5×10^{-10} mbar. A helium discharge lamp ($\hbar\omega = 21.2$ eV) was used for excitation and a Scienta SES 100 analyzer (25 meV energy resolution, 0.2° angular resolution) for data acquisition.

We determined the spectra in a direction perpendicular to Γ-K. For pristine gr/Ir(111), the characteristic linear dispersion of graphene at the K-point is observed, as it is well known from other experiments [91, 92] [Fig. 6.4 (a)]. At the Γ-point, the Rashba-split

parabolic Ir(111) surface state S_0 with negative effective mass is visible [Fig. 6.4 (c)], in agreement with [117]. After oxygen intercalation, the Dirac cone is shifted up in energy [Fig. 6.4 (b)]. This shift is caused by the intercalated oxygen, which induces p-doping in graphene [47]. The surface state S_0 is completely suppressed [Fig. 6.4 (d)]. In addition, there is no indication of the S_1 state at the K-point [91] after intercalation.

Fig. 6.5 shows an additional ARPES-result: In contrast to the preparation described above, here six TPG cycles without subsequent CVD were used, as the presence of many graphene edges is not as critical for the electronic states of graphene as it is for the Ir surface states. These results were obtained in a different experimental geometry, namely *in* ΓK-direction [see inset of Fig. 6.5], thus allowing us to cover an extended k-range of the Dirac cone. We determined the relation $E(k)$ by first fitting the peak positions (single Lorentzian) of individual momentum distribution curves (MDCs) of the left branch of the Dirac cone and then fitting the linear function $E(k) = E_\mathrm{D} - \hbar v_\mathrm{F} q$ to these peak positions in the energy range between -1 and -0.2 eV. In this range a reliable fit was possible, avoiding disturbances as the electron-phonon coupling kink (near to E_F) or π-band intensity variations (below -1 eV). We obtained the location of the Dirac point $E_\mathrm{D} = (0.68 \pm 0.05)$ eV and the Fermi velocity $v_\mathrm{F} = (1.03 \pm 0.01) \times 10^6$ m/s.

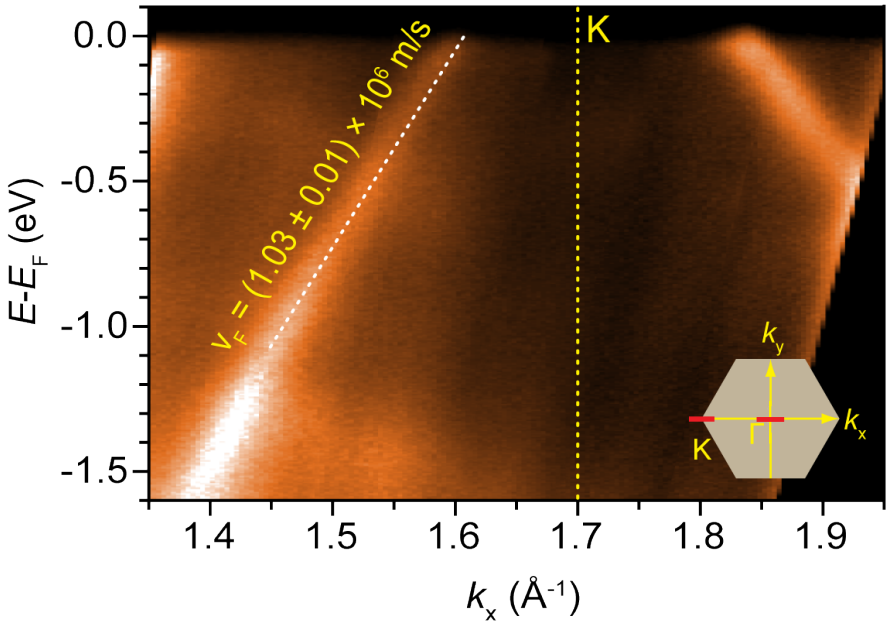

Figure 6.5: (a) ARPES spectra of gr/O/Ir(111) at the K point acquired in the direction parallel to ΓK (see inset). The dispersion relation resulting from the fit is marked by the white dotted line. Inset: Experimental geometry.

6.3 Density Functional Theory

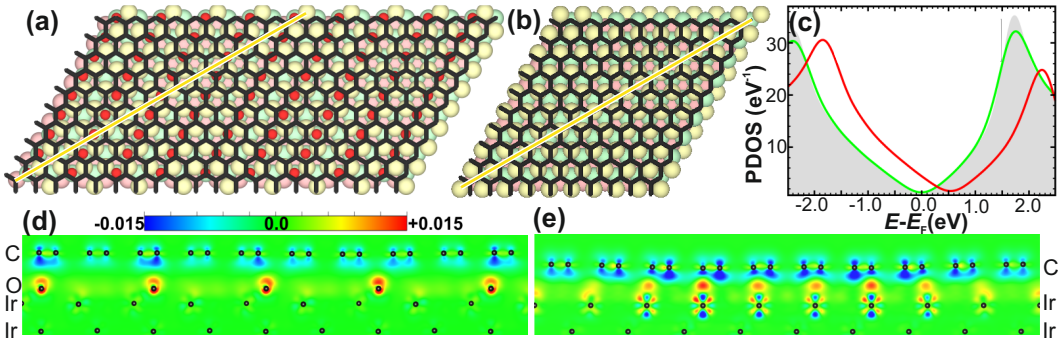

Figure 6.6: (a) Top view of gr/O/Ir(111) [(20×10)gr/(9×9)O/(18×9)Ir(111)]. (b) Top view of gr/Ir(111) [(10×10)gr/(9×9)Ir(111)]. (c) Projected density of states (PDOS) in states/eV of the graphene π-like orbitals. Gray area: Freestanding graphene, green line: freestanding graphene with the same shape as found for gr/O/Ir(111), red line: gr/O/Ir(111). (d) Charge density difference upon adsorption for gr/O/Ir(111) through a plane marked by the bright line in (a) (see color bar, negative values denote charge depletion, unit is eÅ^{-3}). (e) Same as (d) for gr/Ir(111).

Our first principles calculations have been performed in the framework of the density functional theory (DFT) [209, 210] as implemented in the VASP code [211, 212]. In particular, we employed the projector augmented plane-wave (PAW) method [213] to describe the interaction between the valence electrons and the atomic cores and used the Perdew-Burke-Ernzerhof (PBE) exchange-correlation functional [214]. To overcome the inability of this functional to describe the long-range nonlocal correlation effects responsible for the van der Waals interaction we considered the semiempirical DFT-D2 method in our theoretical study [215]. The gr/O/Ir(111) system was modeled by a large realistic supercell consisting of 1129 atoms. To obtain accurate results the plane wave cut-off energy was set to 500 eV.

The main outcome of our calculations is summarized in Fig. 6.6. Subfigure (a) shows the supercell, containing (20×10) unit cells of graphene adsorbed on (9×9)O/(18×9)Ir(111). For comparison, we also show the pristine gr/Ir(111) [Fig. 6.6 (b), note that here the supercell is smaller]. The average binding distance between graphene and Ir(111) is $\bar{h} = 4.23$ Å [see also Fig. 6.6 (d)], which is larger than without O [$\bar{h} = 3.41$ Å, Fig. 6.6 (e) and Ref. [17]]. The peak-to-peak corrugation drops from $\Delta h = 0.35$ Å without O to $\Delta h = 0.19$ Å for intercalated O. Fig. 6.6 (c) shows the PDOS of the graphene π orbitals: Ideal (i.e planar and freestanding) graphene is shown as the area filled gray. At the

Fermi energy the characteristic dip due to the Dirac point is visible. Also for freestanding graphene in the slightly corrugated geometry as found for gr/O/Ir(111) (green line) the overall shape is preserved and the Dirac point coincides with the Fermi energy. However, the adsorption of graphene on O/Ir(111) (red line) leads to a charge transfer and the Dirac cone is shifted to $E_{\mathrm{D}} = 0.55$ eV, in good agreement with our ARPES experiments (see Fig. 6.4). The charge density difference plot [Fig. 6.6 (d)] reveals the origin of this doping: Charge is transferred from the C $\pi-$orbitals into the O/Ir(111) interface states. Note that no charge accumulation between C and O or Ir atoms takes place which implies that no chemical bonds are formed. This is in contrast to gr/Ir(111) where at the fcc and hcp sites weak polar local covalent bonds are formed, see Fig. 6.6 (e) and Ref. [17]. Taken together, the enlarged distance as well as the absence of hybridization between the graphene and the metal substrate indicate efficient decoupling.

6.4 Scanning Tunneling Spectroscopy

For STS, we use the lock-in technique with a frequency in the range of $850 - 950$ Hz and a modulation amplitude of $4 - 10$ mV, resulting in a lower limit of the experimental resolution of $\Delta E \leqslant 0.02$ eV with $V_{\mathrm{mod}} \leqslant 10$ mV (see Eq. 1.1).

STM reveals the presence of oxygen intercalated GQDs of varying shape (hexagons, truncated hexagons, irregular polygons) and size [216]. An STM topograph of an individual slightly triangular GQD is shown in Fig. 6.7 (b) (top left). Point spectra [Fig. 6.7 (a)] are recorded at the locations indicated by the differently shaded dots in Fig. 6.7 (b). Pronounced peaks are visible in the spectra which we attribute to the discrete energies of the first three eigenstates on the graphene flake. The intensity of a given state varies with the location on the GQD of the spectra. This is most obvious in the images mapping the LDOS in Fig. 6.7 (b) at energies approximately at the peak energies [indicated by blue vertical lines in Fig. 6.7 (a)]. The characteristic standing wave patterns of confined states are visible.

To determine the wave vector k belonging to a state with specific E we approximate a GQD with an area A as an infinite cylindrical well as described in Sec. 1.7. For example, the states in Fig. 6.7 (a) are (1,0) at 0.075 eV, (1,1) at -0.150 eV, and (2,0) at -0.425 eV (compare Fig. 1.8).

We obtained $E(k)$ via the identification of individual states either by mapping them at energies determined in point spectra [as for the example given in Fig. 6.7 (a) and (b)] or from maps at closely spaced equidistant energies. We use this spacing as the maximum

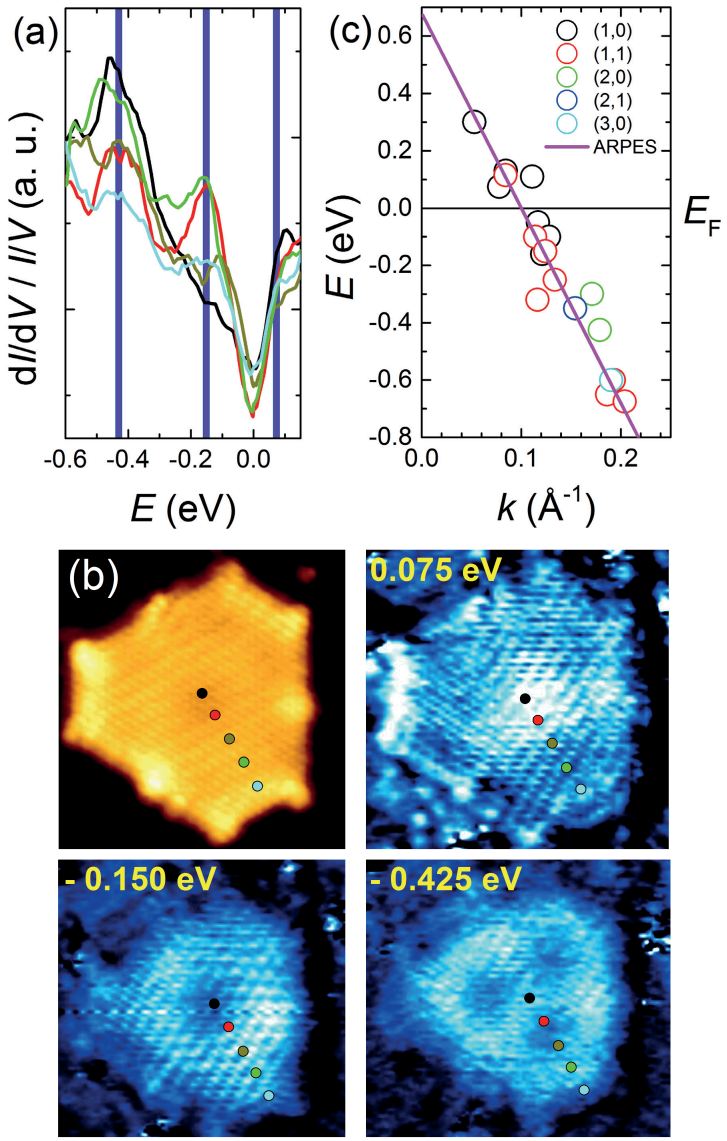

Figure 6.7: Confined states on a GQD: (a) dI/dV-spectra recorded on graphene, revealing the energies of the confined states (stabilizing parameters are $I_{\mathrm{stab}} = 0.4$ nA, $V_{\mathrm{stab}} = 0.6$ V). (b) Topographic ($I = 0.1$ nA, $V = -0.150$ V, image size 75×77 Å^2) and spectroscopic images of the GQD, the later measured at the three energies highlighted by three blue vertical lines in the spectra in (a), where the width of the lines corresponds to the experimental error evaluated above. The differently shaded dots indicate where the spectra were detected. (c) $E(k)$ resulting from the analysis of the confined states compared with the dispersion relation around the K-point found in ARPES. The size of the dots is to the full width at half maximum of the corresponding peaks. A potential error of k due to our simplified model is neglected.

error $\Delta E = \pm 0.05$ eV, which is comparable to the FWHM of our $\mathrm{d}I/\mathrm{d}V$-spectra, see Fig. 6.7 (a), and not much larger than the lower limit of our experimental resolution. The enhanced broadening can arise from a finite (instead of infinite) potential well or Dirac-specific effects like Zitterbewegung [185]. All the confined states evaluated are shown in Fig. 6.8. The resulting relation $E(k)$ [Fig. 6.7 (c)] with $E_\mathrm{D} = (0.64 \pm 0.07)\,\mathrm{eV}$ and $v_\mathrm{F} = (0.96 \pm 0.07) \times 10^6$ m/s fits remarkably well to the dispersion relation of the Dirac states determined by ARPES. It is also interesting to note that v_F is almost equal to the value for freestanding graphene, a strong indication for the decoupling of graphene as a consequence of the chosen intercalant [47].

The effective decoupling of graphene from the metal surface by the intercalated layer of oxygen has further consequences: In Fig. 6.9 (a) we compare point spectra taken on top of a GQD and next to it. The exact locations of the spectra are shown in the inset of the figure. On the GQD a pronounced dip in the density of states around 0.6 eV is observed which we attribute to the vanishing DOS at the Dirac point of graphene. This feature was never observed on non-intercalated graphene on Ir(111) which we explain by the dominant contribution of the states at the Γ-point from the metal in close proximity as compared with the states of graphene at the K-points that are furthermore suppressed by the large transfer of parallel momentum in the tunneling process [170].

Finally, we compare a topographic image of a GQD [Fig. 6.9 (b)] and its Fourier transform [Fig. 6.9 (c)] with the simultaneously acquired $\mathrm{d}I/\mathrm{d}V$-map at $E = -0.150$ eV [Fig. 6.9 (d)] and the corresponding FT [Fig. 6.9 (e)]. In Fig. 6.9 (c) several periodicities reveal themselves as peaks: The outermost spots (enclosed by circles) stem from the graphene lattice, while the two inner spots (enclosed by squares) are caused by one rotational domain of oxygen in a (2×1)-structure with respect to Ir(111) underneath graphene [see Fig. 6.3 (b) and Fig. 6.6 (a)]. In the FT of the spectroscopic image [Fig. 6.9 (e)] additional features appear, namely rings (enclosed by diamonds) centered at the $(\sqrt{3} \times \sqrt{3})R30°$-position (with respect to graphene), which in consequence have to be of electronic rather than structural origin. Specifically, this feature is markedly different from the crystallographic peaks observed for the case of graphene intercalated with oxygen in a $(\sqrt{3} \times \sqrt{3})R30°$ superstructure [2]. Following previous studies, we propose that these rings arise from intervalley scattering between neighboring valleys around K and K' [85, 164]. We speculate that the respective scatterers in our case are the edges of the GQDs. For the diameter of the ring one expects $d(E) = 4k(E)$ [164]. We superimposed a dashed white circle with the expected diameter based on $E(k)$ as determined using ARPES with one of the rings in Fig. 6.9 (e). The agreement confirms our interpretation. The rings are most pronounced for scattering

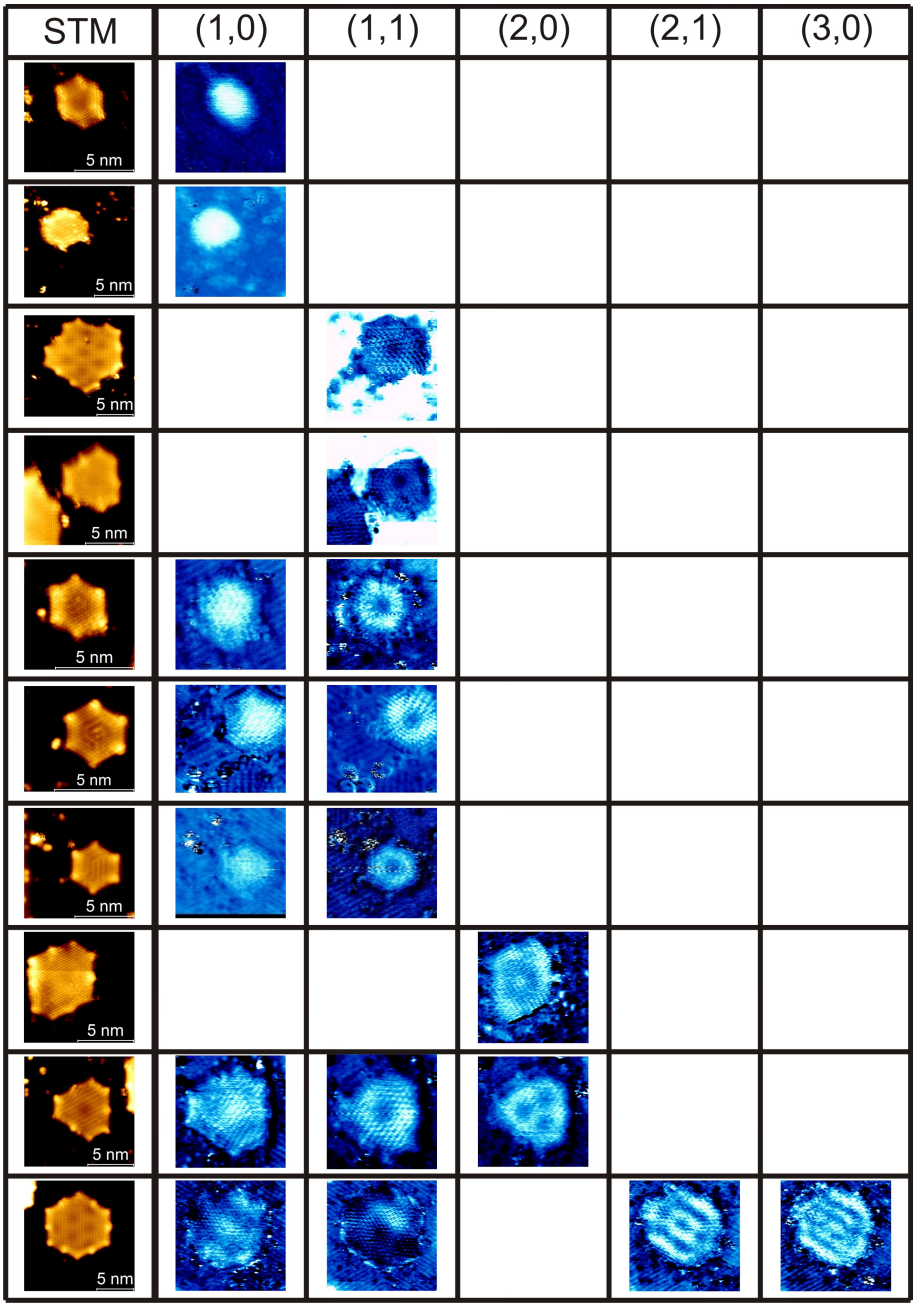

Figure 6.8: Summary of all confined states mapped on oxygen intercalated GQDs on Ir(111) (colored blue) in a matrix assigning them to the specific Bessel eigenstates (m,l) of our model, side-by-side with a corresponding STM topograph. Compare Fig. 1.8.

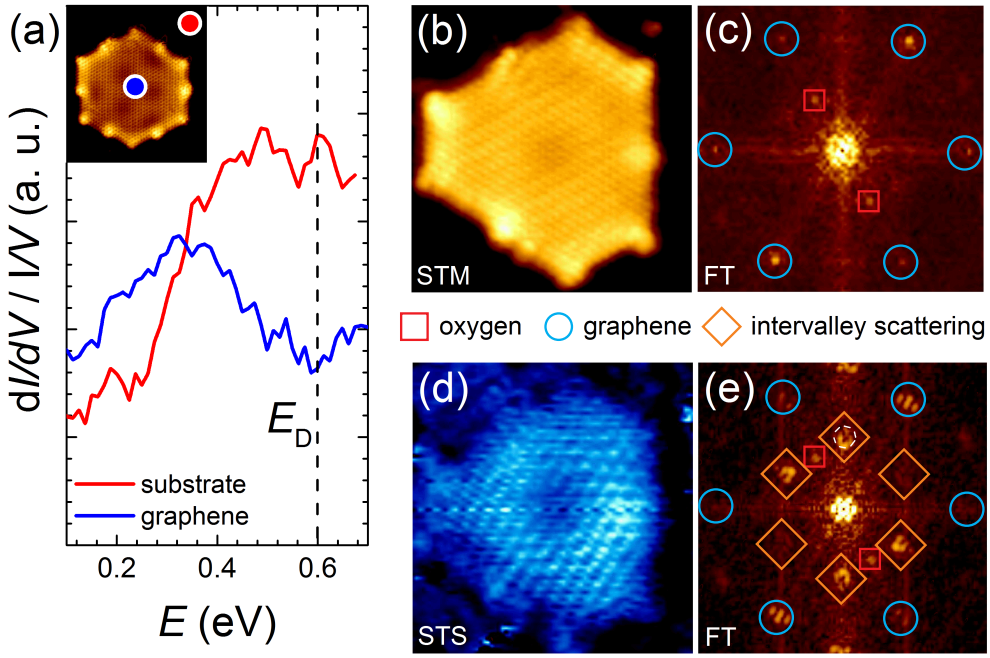

Figure 6.9: (a) dI/dV-spectra taken on the substrate (red) and on the GDQ (blue) as shown in the inset (I = 0.5 nA, V = 0.7 V, image size 110 × 120 Å^2): On the graphene a dip is visible at ≈ 0.6 eV, which is absent on the substrate (stabilizing parameters are I_{stab} = 0.05 nA, V_{stab} = 0.7 V). b) Same STM image as in Fig. 6.7 (b). (c) FT of (b), revealing the periodicities of graphene (enclosed by circles) and the intercalated oxygen rows forming a (2 × 1)-structure (enclosed by squares). (d) Same dI/dV-map of the (1,1) state as shown in Fig. 6.7 (b). (e) FT of (d) containing additional features (enclosed by diamonds) arising from intervalley scattering.

processes perpendicular to the oxygen rows, which can be a hint at the underlying scattering mechanism. However, also the shape of the island is asymmetric, which may also induce intensity differences. Again, these electronic features are properties of decoupled graphene only and were never found for gr/Ir(111) without intercalated oxygen.

6.5 Conclusion

Concerning the morphology of the STM sample, increasing the sample temperature during intercalation by ΔT = 17 K compared to the preparation discussed in Chap. 5 reduced the number of non-intercalated islands and generated a clear dominance of the (2 × 1) oxygen superstructure on iridium under graphene.

On such GQDs we have extracted a linear dispersion relation with parameters matching those of Dirac electrons in oxygen intercalated graphene as determined by ARPES. As the iridium surface states are destroyed by the presence of oxygen, their contribution can be completely excluded. DFT calculations reveal two interesting aspects: First, the oxygen does not form covalent bonds with the carbon layer. Second, the oxygen forms a O-Ir hybrid state. These findings are of general interest for judging the capabilities of oxygen as an intercalant in future research.
In consequence, the states observed by us are the first unambiguous realization of confined Dirac electrons. Our study thus resolves the ambiguity of previous work and in consequence provides the first clear-cut demonstration of confinement of Dirac states. Furthermore, we observe the presence of intervalley scattering and a dip in the LDOS located at the Dirac point. The fact that all these effects are present underlines that intercalated oxygen renders graphene quasi-freestanding.

CHAPTER 7

A Quantum Corral without a Fence

The experiments discussed in this chapter were motivated by Marko Kralj and planned by Carsten Busse and myself. The samples were prepared by myself with support by Sven Runte and Jürgen Klinkhammer. The data analysis was performed by myself with support by Carsten Busse. Several paragraphs and the figures of this chapter are adopted within their meaning or literally taken from the publication ***Mapping Image Potential States on Graphene Quantum Dots*** *[2]. This work is supported by DFG through SFB 608, the projects Bu2197/2-1, INST 2156/514-1, and the Bonn-Cologne Graduate School of Physics and Astronomy, the EU through the project GRENADA, and DAAD-MZOS via the project "Electrons in two dimensions".*

The image of electrons enclosed in a quantum corral taken with a scanning tunneling microscope (STM) by Eigler and coworkers 20 years ago [132] has become a scientific visual icon standing for quantum confinement. To stay in the metaphor, our work now demonstrates that the structural fence is not even needed: Energetic 'hot' electrons are confined in a quantum well where the bottom is formed by GQDs/Ir(111), whereas the walls are formed by a force field. In more detail, the 'hot' electrons are free-electron-like image potential states (IPSs) and the field is generated by an electrostatic potential in form of a difference in local work function at the boundary of the GQDs. The spectrum depends on the size of the nanostructure as well as on the spatial position on top, indicating lateral confinement. Analysis of the substructure of the first state by constant energy spatial mapping of the LDOS reveals characteristic patterns of confined states. The most pronounced state is not the ground state, but an excited state with a favorable combination of the local density of states and parallel momentum transfer in the tunneling process. The electrostatic potential is tuned by chemical gating, tuning the confining potential by changing the local work function. Our experimental determination of this work function allows us to deduce the associated shift of the Dirac point.

Confinement of electrons in nanostructures leads to quantum size effects as a size-dependent electronic structure and atom-like states (characterized by a set of quantum numbers), see Sec. 1.7. Recently, first experiments regarding the confinement of image potential states (IPSs) using the spatial resolution of the scanning tunneling microscope (STM) have been performed [217–222], transcending pioneering studies based on two photon photoemission (2PPE) [223, 224].

Confinement effects for IPSs can be induced by nanostructures fulfilling four conditions: (i) the corresponding potential well must have a sufficient depth given by the difference in local workfunction Φ inside (Φ_{in}) and outside (Φ_{out}) of the nanostructure ($\Delta\Phi = \Phi_{\mathrm{out}} - \Phi_{\mathrm{in}}$) [218], (ii) a well-defined shape, (iii) an established preparation that allows us to adjust the size in a wide range, and (iv) stability under the high STM bias voltage V. Whereas previous work provides fascinating first insights into quantum size effects, no study yet matches all four conditions:

For Co islands on Au(111) a first hint at size-dependent energies is visible [219]. However, the size variation was less than an order of magnitude. Atom-like patterns have been observed above stacking-fault tetrahedra on Ag(111) [221], still $\Delta\Phi$ is so small that the resulting weak confinement only acts on the IPSs lowest in energy. The system NaCl on metal is promising as it shows a large $\Delta\Phi$. However, up to now there is no established method to tune the size of islands with a well-defined shape over a wide range [225, 226]. In consequence, in these experiments electron confinement has not been observed yet. Strong confinement is found for islands of alkali metals on Cu(100) [222]. In this case, the atomic structure of the islands is unclear, the size cannot be varied, and the clusters are not entirely stable during the measurement. An intriguing feature is the coupling between the IPSs on neighboring nanostructures to molecule-like states [219, 222, 227].

IPSs on graphene (gr) are of special interest: On fundamental grounds they share a common origin with the interlayer state of graphite and superatomic states of fullerenes [115, 227]. As a consequence of graphene's 2D character, a splitting into $\Psi^{(n^+)}$ and $\Psi^{(n^-)}$ has been predicted for free-standing [115] and observed for epitaxial graphene weakly coupled to SiC [116, 228]. However, for the more strongly interacting gr/Ru(0001) this specific splitting was not observed as the presence of the substrate destroys the 2D character [229, 230]. Still, the energy of the lowest IPS splits due to the strong corrugation of the carbon sheet which allows a large probability density also between graphene and the substrate. In the system under investigation here, 2PPE could demonstrate parabolic IPSs in the large band gap of the Ir substrate [114]. Neither the energetic splitting due to the 2D character nor

due to corrugation were observed. Note that in Refs. [115] and [116] a shortened notation is used, e.g. 1^+ for $\Psi^{(1^+)}$.

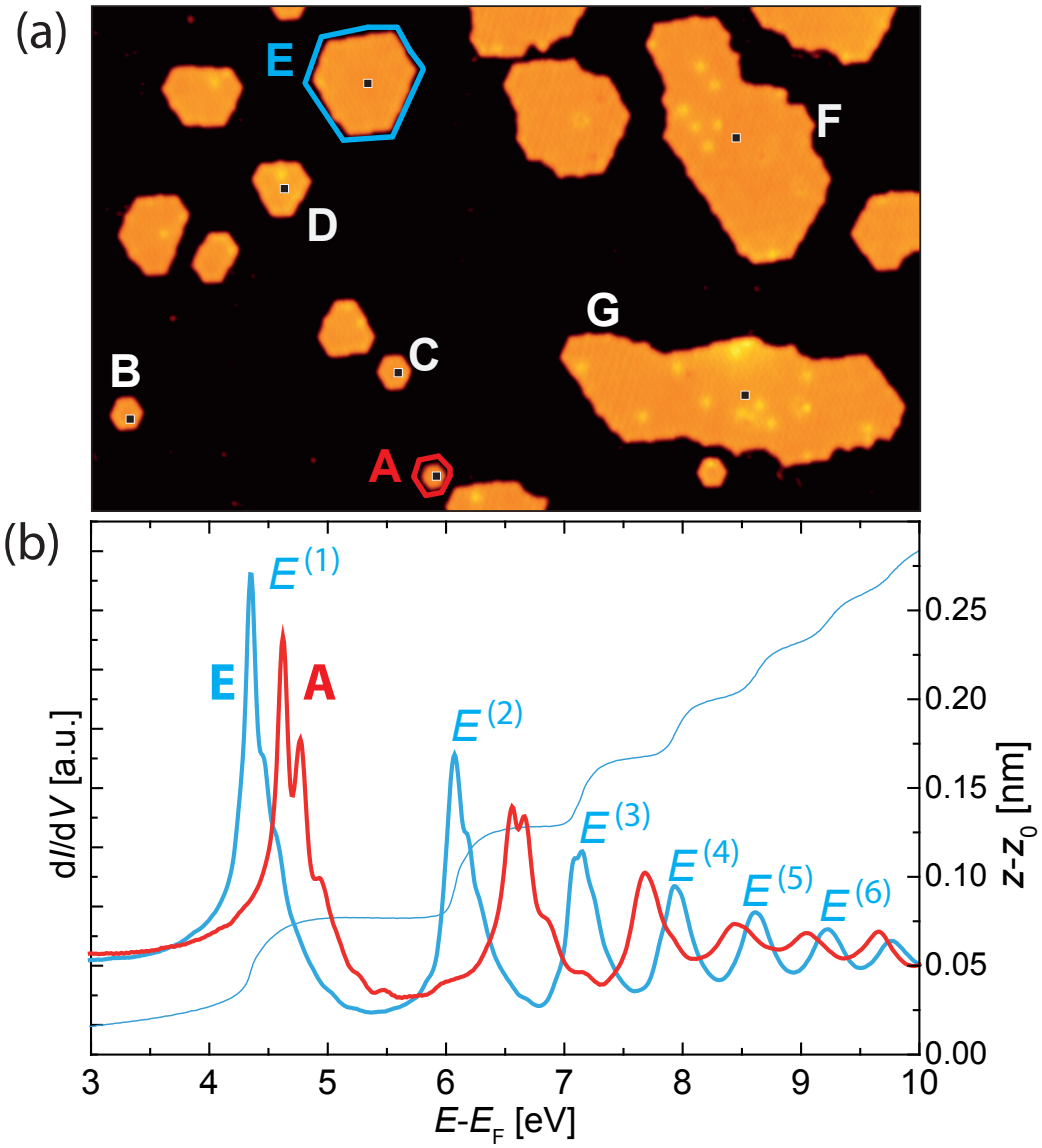

Figure 7.1: (a) Set of GQDs on Ir(111) [some labeled (A)-(G) with increasing area in a range of $A = 7.5..378\,\mathrm{nm}^2$]; image width 90 nm, $V = 1$V, $I = 0.2$nA. (b) $\mathrm{d}I/\mathrm{d}V$ spectra on GQDs (A) and (E); $V_{\mathrm{stab}} = 1\,\mathrm{V}$, $I_{\mathrm{stab}} = 0.2\,\mathrm{nA}$; thin (blue) line: simultaneously recorded $z(V)$ on (E).

We demonstrate that confinement of IPSs can be observed in GQDs on Ir(111). Furthermore, both the width and the depth of the confining potential well can be tuned. The GQDs fulfill all conditions outlined above: (i) A large $\Delta\Phi = \Phi_{\mathrm{Ir}} - \Phi_{\mathrm{gr}} = (5.79 \pm 0.10)$ eV –

(4.65 ± 0.10) eV $= (1.1 \pm 0.1)$ eV [114]. Beyond that, $\Delta\Phi$ can be tuned: The intercalation of electron acceptors (as, e.g., O [51]) between the carbon sheet and its substrate leads to a depletion of charge density in graphene's π system, which in turn shifts the Dirac point E_D to higher energies [47], and vice versa for donors. Assuming that the band structure is rigidly pinned to $E_\mathrm{F} + \Phi$ [231], the work function of intercalated graphene is given by $\Phi_\mathrm{gr/x} = E_\mathrm{D} + \Phi_\mathrm{gr}$, allowing us to change the depth of the potential well by doping. (ii) The GQDs have a well-defined polygonal shape which can be determined with atomic precision [110]. (iii) The GQDs have a size tunable from less than 10 nm^2 to electronically equivalent to infinite [29]. (iv) The system is stable also for high V due to the strong C-C bonds as well as the good conductivity.

Fullerenes [227] and carbon nanotubes [219] can be viewed as extreme cases of confinement. However, for such systems a tuning of the size over orders of magnitude is impossible and the curved geometry gives a new character to the now strongly hybridized states.

The sample was prepared in the standard growth process with an TPG heating temperature of 1270 K as described in Chap. 3, yielding a graphene coverage of $\approx$ 22 %. IPSs are investigated by measuring the differential conductivity in form of both $\mathrm{d}I/\mathrm{d}V(E - E_\mathrm{F})$ point spectra and constant energy maps in constant current mode (stabilization values V_stab, I_stab) with active feedback loop using the lock-in technique ($f = 1.317$ kHz, $V_\mathrm{mod} = 14$ mV) which together with the sample temperature of 5.3 K leads to an energy resolution of $\delta E = 25$ meV [67]. Feedback is important as moving the tip in the z direction during point spectroscopy compensates for the Stark shift within one measurement as depicted in Fig. 1.6. Tip traces $z(V)$ were recorded parallel to the spectra [see Fig. 7.1 (b)].

7.1 Size Dependent Shift of Image Potential States

Figure 7.1 (a) shows GQDs with sizes from less than 10 nm^2 up to 378 nm^2 [29], covering a range of a factor of almost 40. The $\mathrm{d}I/\mathrm{d}V$-spectra taken with the same microscopical tip [232] at the center of the GQDs labeled in Fig. 7.1 (a) show very pronounced features [Fig. 7.1 (b)]. We attribute the discrete peaks to the energies $E^{(n)}$ of the sequence of IPSs with order n = 1,2,.... These energies are down shifted with respect to pristine Ir(111) due to the significantly smaller Φ. The spectra on the differently sized GQDs are also shifted with respect to each other by as much as $\Delta E \approx 0.67$ eV between the largest and the smallest GQD for both $E^{(2)}$ and $E^{(3)}$. Under our experimental conditions, such a large difference cannot be due to a variation of the Stark shift.

The electric field causing this shift depends in a complex way on the distance z from the surface (unless a very large tip radius is assumed), governed by the bias voltage V and the distance z_0 between the tip and the sample. As these quantities are slightly different for the same IPS measured on different islands, one could speculate that these states are Stark-shifted in a different way, making a quantitative analysis impossible.

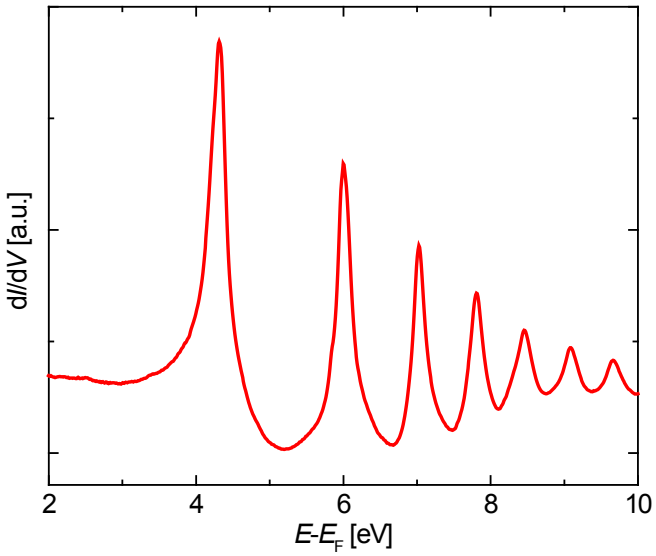

Figure 7.2: $\mathrm{d}I/\mathrm{d}V$ point spectrum on the $A = 378\,\mathrm{nm}^2$ GQD (G) in Fig. 7.1 (a); $V_{\mathrm{stab}} = 1\,\mathrm{V}$, $I_{\mathrm{stab}} = 0.2\,\mathrm{nA}$.

We assess the contribution of the Stark effect by performing I_{stab}- and thus z_0-dependent measurements of $E^{(2)}$ on pristine Ir(111). We approximate the field by assuming a simple capacitor model with $F = U/z_0$ [217]. Increasing I_{stab} from 0.2 nA to 0.3 nA changes the field by $\Delta F = 0.87\,\mathrm{V/nm}$. At the same time $E^{(2)}$ changes by $\Delta E \simeq 40\,\mathrm{mV}$. In the size-dependent measurements on GQDs, the field changes by almost the same value $\Delta F = 0.90\,\mathrm{V/nm}$ for the measurements of $E^{(2)}$ between the smallest and the largest GQDs under the assumption of $z_0 = 0.5\,\mathrm{nm}$ for $I_{\mathrm{stab}} = 0.2$ nA. The observed shift in the energy of this state between two states, however, is $\Delta E \simeq 670\,\mathrm{mV}$ and thus more than an order of magnitude larger compared to the Stark shift measured above, proving that the energy shift is indeed dominated by confinement effects.

In addition to the size-dependence of the peak energy, the individual peaks show a clear substructure, especially the ones for the smaller islands [Fig. 7.1 (b) red line]. This is in contrast to the smooth peaks observed for extended systems (see Fig. 7.2).

A dependence of the energy of the electronic states $\Psi_{m,l}^{(n)}$ (see Sec. 1.6) on the size of the system as well as the occurrence of discrete eigenstates evidenced by the peak substructure are clear fingerprints of lateral quantum confinement. We use the model outlined in Sec. 1.7 and approximate our hexagonal GQDs by an infinite cylindrical potential well with radius r (area A) [150]. Radial cuts through the normalized probability density $\Psi_{m,l}^{(n)*}\Psi_{m,l}^{(n)}$ of

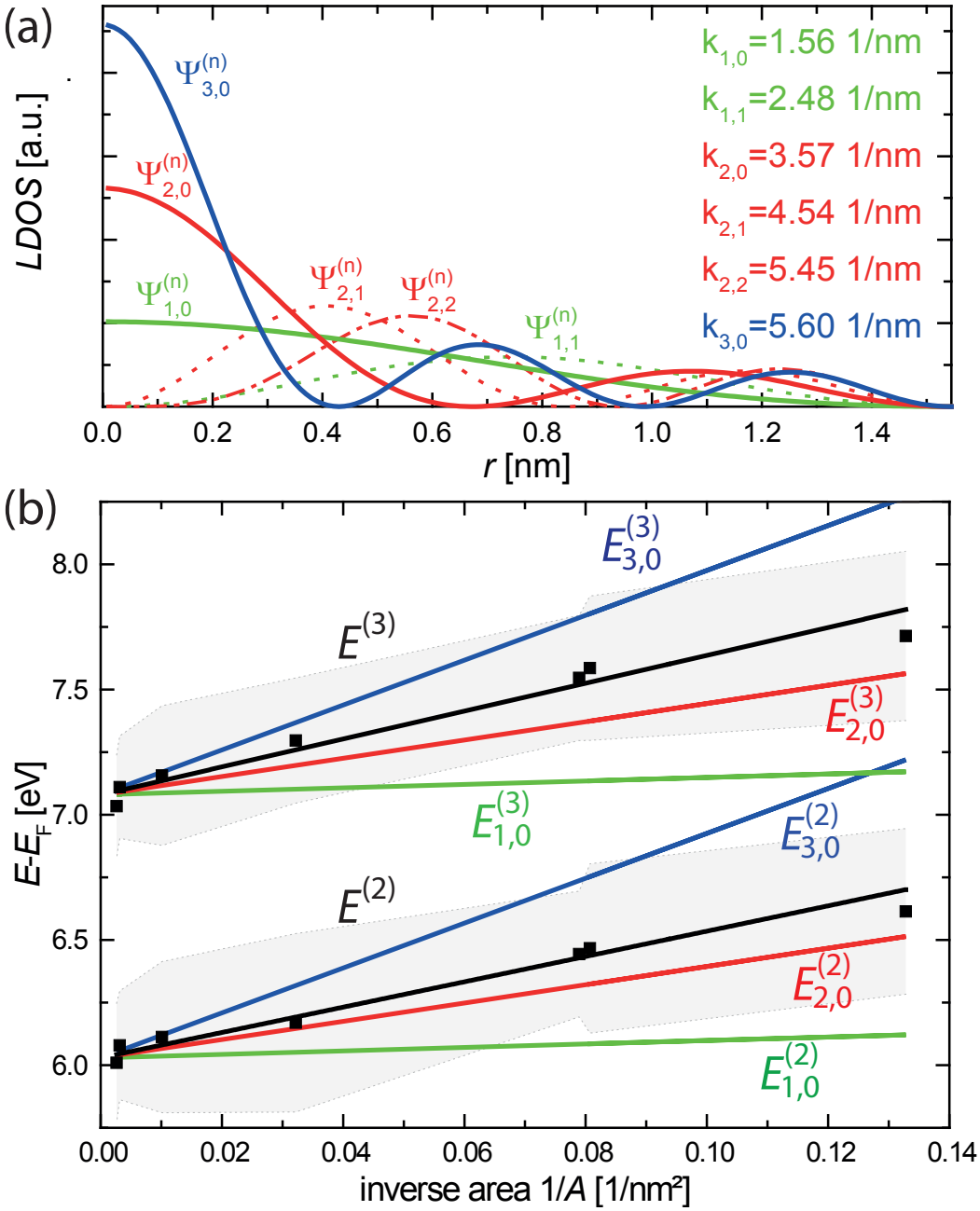

Figure 7.3: (a) Normalized LDOS (LDOS divided by integrated LDOS over the whole GQD area) and $k_{m,l}$ for a model island with $A = 7.5$ nm^2, i.e. $r_0 = 1.545$ nm (right border of the plot), i.e. radial cuts through Bessel figures shown in Fig. 1.8. (b) $E^{(2)}$ and $E^{(3)}$ depending on inverse area, measured on (A)-(G) in Fig. 7.1 (a) with parameters from Fig. 7.1 (b); peak FWHM (gray shading) and linear fits (black lines); calculated energies $E^{(n)}_{m,l}$, see labels.

the first six eigenstates are shown in Fig. 7.3 (a). This plot can be used to explain the substructure of the peaks in Fig. 7.1 (b): A spectrum taken at a point r will pick up LDOS from several states at the respective $E_{m,l}^{(n)}$. Note that even though we took all spectra in the center of the islands ($r = 0$), especially for the case of small dots a contribution of states with $l \neq 0$ has to be expected since the spatial resolution decreases when the tip-sample distance z_0 is no longer small with respect to r. The 2D structures of the model eigenstates are depicted in Fig. 1.8.

We fitted the spectra obtained on the set in Fig. 7.1 (a) phenomenologically by a sequence of n Voigt functions, representing a convolution of Gaussian and Lorentzian. Figure 7.3 (b) shows the position of the peaks $E^{(n)}$ for $n = 2{,}3$ (black squares) and their full width at half maximum (FWHM, gray shading) versus A^{-1} for the whole set of GQDs shown in Fig. 7.1 (a). The state $n = 1$ is disregarded as it is still strongly influenced by the substrate [233]. We compare a linear fit to the data (black lines) with the expected behavior for $E_{m,l}^{(n)}$ ($m^* \approx m_e$ [114]), focusing on states with non-vanishing amplitude at the center of the GQD $l = 0$ [labeled lines in Fig. 7.3 (b)] as we have measured the spectra at $r = 0$ [see Fig. 7.1 (a)]. The values $E_0^{(n)}$ for the calculated energies have been obtained from the y-axis intercept of the linear fit to the peak positions versus inverse area [see black lines in Fig. 7.3 (b)]. The energies $E_{m,l}^{(n)}$ are calculated according to Eq. 1.12 (see Sec. 1.7). Since for the case of small islands, the state with $m = 2$ and $l = 0$ is the only one with its maximum within the FWHM, the data obviously fit best to $\Psi_{2,0}^{(n)}$, both for $n = 2$ and $n = 3$.

This is surprising as this is not the ground state. The physical reason for the observed width of the peaks (gray shading) is complex: Each peak is a superposition of several closely spaced and overlapping subpeaks of different intensities. Each of these subpeaks is broadened due to the finite lifetime of the electrons in the given state and due to the limited experimental resolution [114]. The only meaningful error that we could give for the position of the fitted peak is the uncertainty in the fitting process, which is smaller than the symbol size of the experimental data points in Fig. 7.3 (b). Furthermore, the fitted linear dependence is in reasonable agreement with the expected behavior of this state. Hence, we come to the conclusion that the state with $m = 2$ and $l = 0$ is the dominating contribution to the peaks we observe.

7.2 Preferred State in the Tunneling Process

In a naive picture the dominating state should be the one with the highest tunneling probability and therefore closely related to the respective local density of states at the

center of the GQD. However, the dominance of $\Psi_{2,0}^{(n)}$ cannot be explained by the LDOS at the center of the GQD, as this quantity increases with m for $l = 0$ [see Fig. 7.3 (a)]. The normalized probability density in Fig. 7.3 (a) has been calculated for a model GQD with $r_0 = 1.545\,\mathrm{nm}$ according to

$$norm.\,LDOS\,\Psi_{m,l}^{(n)} = \frac{J_l\left(\frac{z_{m,l}}{r_0}\sqrt{x^2+y^2}\right)^2}{\int_{x,y}^{x^2+y^2<r_0} J_l\left(\frac{z_{m,l}}{r_0}\sqrt{x^2+y^2}\right)^2 dxdy}$$

with $x^2 + y^2 < 1.545$. For a correct interpretation, one has to take into account that tunneling is most probable for electrons with vanishing k, since most of the electrons leaving the tip do not possess a momentum parallel to the sample surface. However, for the electrons confined above the GQDs, the surface parallel $k_{m,l}$ increases with m [see Fig. 7.3 (a)], making them less accessible for STS. In consequence, whereas the LDOS in the center increases with the order of the state, the contribution to the tunneling density of states (TDOS, e.g. [169]) measured in STM decreases in analogy to Sec. 1.9, using $k_{m,l} = z_{m,l}/r$ ($z_{m,l}$ the m-th zero of J_l, see Sec. 1.7).

For the model island with $A = 7.5\,\mathrm{nm}^2$ it follows that $\Psi_{2,0}^{(n)}$ dominates for $0.36\ \mathrm{nm} < z_0 < 1.04\ \mathrm{nm}$, which is a reasonable range for our experiment. Please see Fig. 7.4 for a detailed overview on this topic. We propose that the decrease in peak intensity of confined states observed earlier [234] could also be explained by less probable tunneling due to increased k instead of an *ad hoc* assumption of a peak broadening increasing with energy.

Nevertheless, it is important to note that for high n a broadening in principle is observed due to the finite bulk band gap. This allows IPS electrons to decay into bulk states when those E_n crossing the top edge of the projected bulk band gap are degenerate with bulk states. The resulting shorter lifetime in these IPSs then translates into broadened peaks [235].

Note that the biggest GQD ($378\,\mathrm{nm}^2$) in the set under discussion in Fig. 7.1 is, within the framework of our experiment, equivalent to extended graphene, since the expected energy difference between neighboring states, e.g. $\Psi_{1,0}^{(n)}$ and $\Psi_{2,0}^{(n)}$ for such a large island is already as small as 2.8 meV and therefore below the limit of our experimental resolution of 25 meV mentioned above. Hence, with respect to the kind of experiment performed here, the largest islands studied are indistinguishable from an infinite graphene layer with a continuum of states. Furthermore, even on fundamental grounds our largest islands are equivalent for infinite graphene: The lifetime of the image potential states confined to the graphene islands cannot be greater than the lifetime of the corresponding states on extended graphene. In this case, the lifetime was determined as 114 fs for($n = 2$

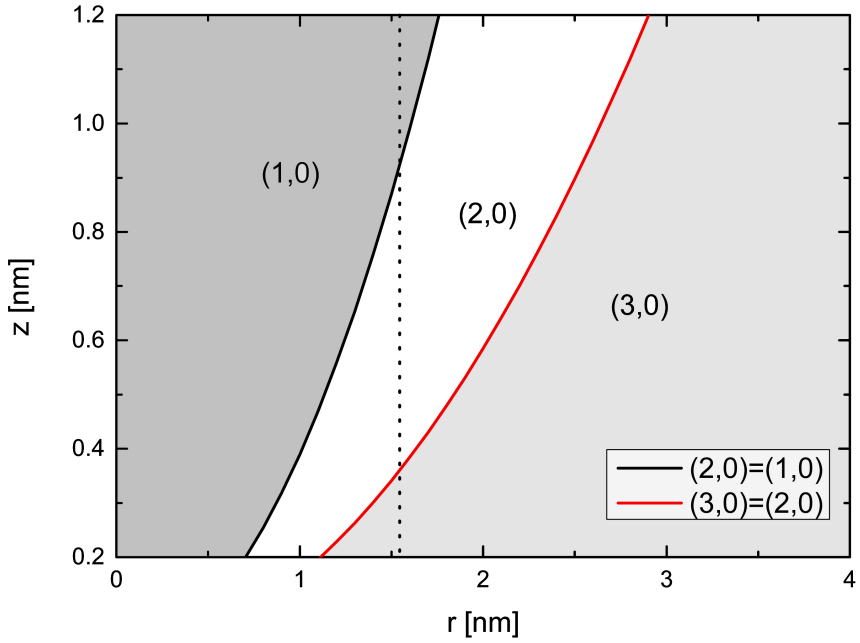

Figure 7.4: TDOS (Sec. 1.9) diagram displaying the preferred IPS state in the tunneling process considering the required momentum transfer depending on radius of the GQD r and the tip-sample distance z. Tuples (r,z) with identical TDOS for IPS (1,0) and (2,0) (black line), tuples (r,z) with identical TDOS for IPS (2,0) and (3,0) (red line). Areas in between: sets of tuples with highest TDOS for (1,0), (2,0) and (3,0), respectively. Radius $r_0 = 1.545\,\text{nm}$ of model island discussed in Fig. 7.3 (a) marked by dashed line.

[19]. This leads to a natural linewidth of 2.9 meV, i.e. of the same size as the expected splitting. Hence, even with perfect experimental resolution it would not be possible to resolve the substructure of the peaks on our largest islands. In consequence, we state that our measurements represent the full range from very small islands to infinite graphene.

7.3 Mapping Confined Image Potential States

The spatial modulation of the LDOS can be resolved by $\mathrm{d}I/\mathrm{d}V$ mapping on a hexagonal GQD for $n = 1$ (Fig. 7.5). For higher n, our resolution in space and energy was not sufficient to detect significant spatial variation of the LDOS, which is similar to [221]. The $\mathrm{d}I/\mathrm{d}V$-spectrum [Fig. 7.5 (f)] shows a substructure equivalent to the one in Fig. 7.3 (b), which does not have exactly the same shape due to different experimental parameters

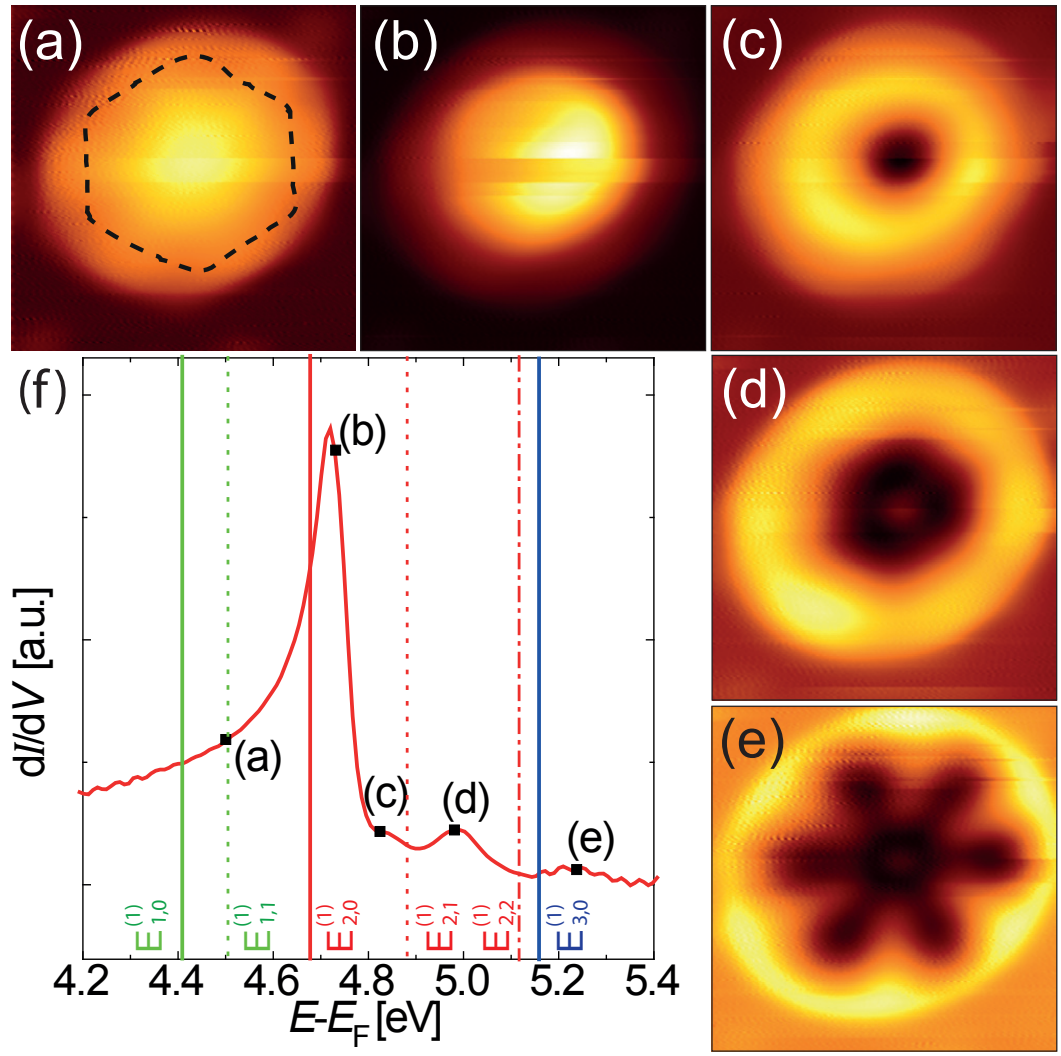

Figure 7.5: (a)-(e) IPS $n = 1$ by 2D constant energy mapping of $\mathrm{d}I/\mathrm{d}V$ on a $A = 11\,\mathrm{nm}^2$ sized GQD. (a)-(e): $E - E_\mathrm{F} = 4.50\,\mathrm{eV}$, $4.73\,\mathrm{eV}$, $4.82\,\mathrm{eV}$, $4.98\,\mathrm{eV}$, $5.22\,\mathrm{eV}$; $I = 0.2\,\mathrm{nA}$; image width: all $5.7\,\mathrm{nm}$; dashed line in (a): topography contour at $E - E_\mathrm{F} = 0.2\,\mathrm{eV}$. (f) $\mathrm{d}I/\mathrm{d}V(E - E_F)$ spectrum of $n = 1$ with energies of maps (a)-(e) (black squares), $E^{(1)}_{m,l}$ indicated by solid (dashed) lines for $l = 0$ ($l \neq 0$); $E^{(1)}_0$ from $n = 1$ fit intercept of the data also used for $E^{(2,3)}_0$ in Fig. 7.3 (b). Compare Fig. 1.8.

(including tip shape). Again, the maximum corresponds to $E_{2,0}^{(1)}$. The maps at selected energies can again be understood on the basis of Fig. 7.3 (a):

The state shown in Fig. 7.5(a) shows a broad maximum resembling $\Psi_{1,0}^{(n)}$ (b) is more peaked in the center like $\Psi_{2,0}^{(n)}$, and (c) and (d) have vanishing intensity in the center like $\Psi_{2,1}^{(n)}$. Strictly speaking, however, the patterns we observe are not pure states, but a superposition of several neighboring states. Note that in Figs. 7.5 (d) and (e) the breaking of the cylindrical symmetry by the hexagonal shape of the GQD becomes evident. Similar patterns have been observed on GQDs as a result of the confinement of low energy occupied states [110–113]. Finally, the inversion of contrast in Fig. 7.5 (e) indicates that the LDOS at this energy is dominated by Ir IPSs, drawing our attention to the interaction of the IPS-2DEGs above graphene and Ir(111).

Fig. 7.6 shows a matrix plot of the $\mathrm{d}I/\mathrm{d}V(E - E_F)$ data of a series of 80 point spectra measured on a line across a perfectly hexagonal GQD [inset of Fig. 7.6], including the boundary regions between Φ_{Ir} and Φ_{gr}. $E^{(n)}$ is decreased on the GQD with respect to Ir(111) due to the lowered Φ. For the boundary region itself, note that the first state shows an abrupt, all higher orders a more continuous way of change. Regarding this observation, both a spill-out of the confined gr-IPSs and a penetration of Ir-IPSs into the area over the GQD should be considered [219]. On this view Fig. 7.6 indicates a suppressed interaction for $n = 1$ and interacting IPS-2DEGs of the GQD and the surrounding substrate for $n > 1$. The pronounced fine structure of $n = 1$ is again due to the shift through the dominant states (m,l) with energy. It can be inferred from Fig. 7.3 (b) that for small GQDs the energy region of visible confinement states extends up to the next IPS. The complex structure found for high n is probably due to an interpenetration of Ir and graphene IPSs or results from a change in the most dominating state for high values of V and z_0 or a combination of both.

In Fig. 7.7 (a) we show a plot of the FWHM of $\mathrm{d}I/\mathrm{d}\,V$ peaks of low ($n = 2$) and high ($n = 5$) order states versus the inverse area of the GQDs presented in Fig. 7.1 (a). FWHM and energies were determined by fitting the experimental data with one Gaussian component per peak. The size effect on the FWHM seems to vanish for high order IPSs. Either the (in reality finite) confinement potential connected to the local work function of the surface does not affect the high order states which reside in some spatial distance to the surface, or this acts as a hint for a tip domination of those states. Furthermore it appears from the plot that n=2 IPSs have a larger absolute FWHM, which might emphasize the expectation of confinement being more effective for the low order IPSs, thus leading to a bigger split in energy as already mentioned above. This picture is also supported by a deviation from

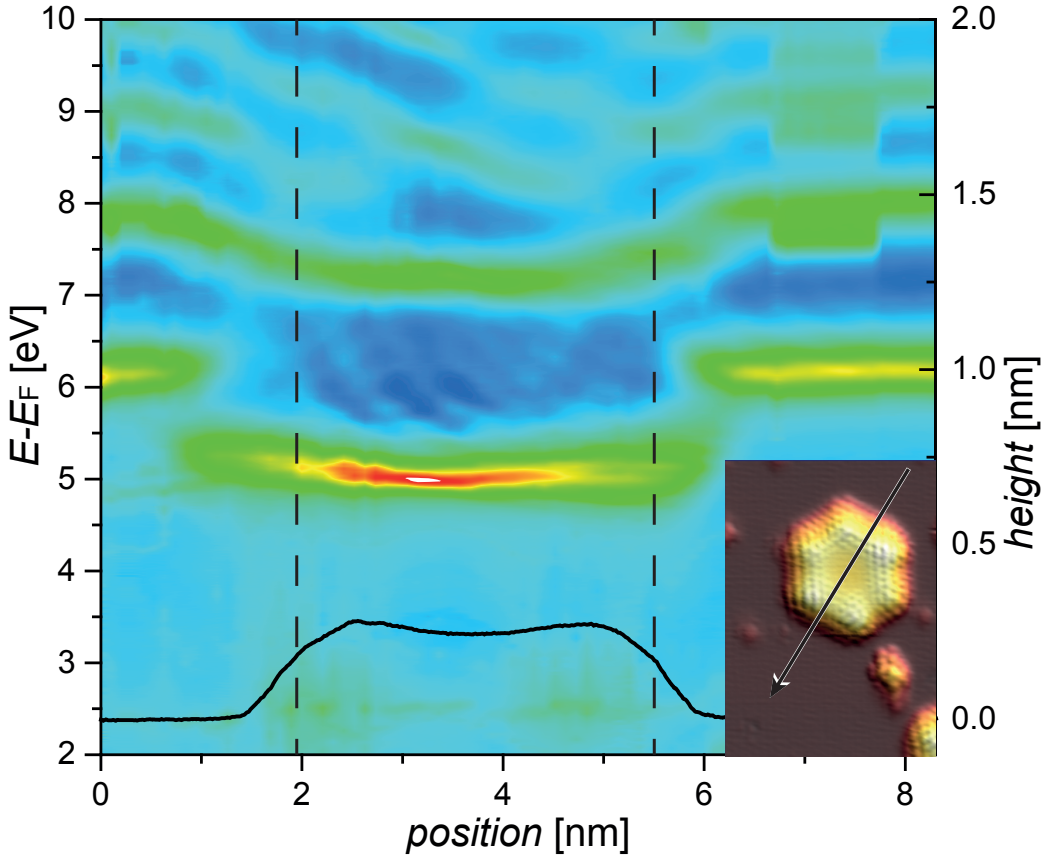

Figure 7.6: $\mathrm{d}I/\mathrm{d}V$ point spectra across an $A = 13\,\mathrm{nm}^2$ GQD on Ir(111) (color scale from blue to red), matrix plot of a series of 80 $\mathrm{d}I\mathrm{d}V$ IPS point spectra in an energy range of $E = 2..10\,\mathrm{eV}$, measured at a setpoint of $I_{\mathrm{stab}} = 4.0 \times 10^{-10}\,\mathrm{A}$ and $V_{\mathrm{stab}} = 710\,\mathrm{mV}$ with a speclength of 120 s and a preamplifier gain of 10^9. Each spectrum consists of 1000 data points and is obtained by the average of five single measurements, with each of them measured in both the back and the forward direction of the voltage ramp; dashed vertical lines indicating border of the GQD; thin black line is a line profile across the topography of the island as indicated in the inset; inset: topography, size $6.8 \times 9.4\,\mathrm{nm}^2$, $V = 712\,\mathrm{mV}$, $I = 0.4\,\mathrm{nA}$.

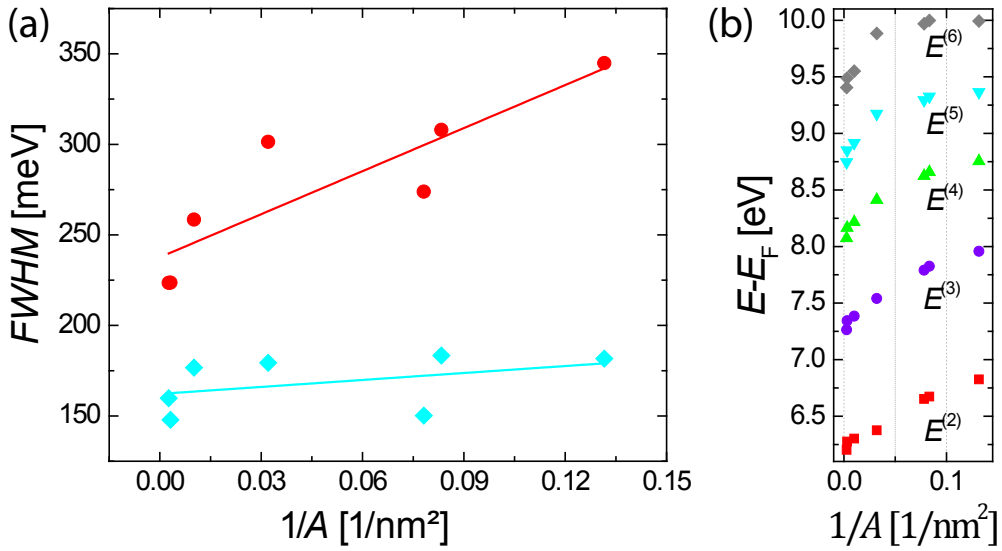

Figure 7.7: (a) FWHM of Gaussian fits to the experimental IPSs peaks for $n = 2$ (red) and $n = 5$ (blue) versus inverse area of the GQDs shown in Fig. 7.1 (a). (b) Corresponding IPSs energy dependence on inverse GQD area for $n = 2..6$ as determined by Gaussian fits (compare $n = 2,3$ already evaluated in Fig. 7.3 (b) using the non-fitted data).

.

the linear dependence on $1/A$ for high order IPS on small GQDs [Fig. 7.7 (b)] compared to the already discussed perfectly linear behavior of the low order states [Fig. 7.3 (b)].

7.4 Tuning the Depth of the Quantum Well

In the following, we will exemplify chemical gating of graphene for the case of O. Exposure of the sample to 750 L of O_2 at 430 K leads to O intercalation for all but the smallest GQDs [51]. In order to demonstrate the effect of intercalation most clearly, we will focus on the largest GQDs which are representative for extended graphene. In the respective STM image [Fig. 7.8 (a)] three superimposed structures can be made out: The graphene honeycomb structure is faintly visible inside the dark depressions. The adsorption of 0.33 ML intercalated O to Ir(111) leads to the pronounced $(\sqrt{3} \times \sqrt{3})$R30° pattern, see also the circled spots in the corresponding Fourier Transform in Fig. 7.8 (b). The large scale pattern (satellite spots in the FT) is due to the moiré structure formed by the incommensurate lattices of graphene and Ir(111) (compare Chap. 5).

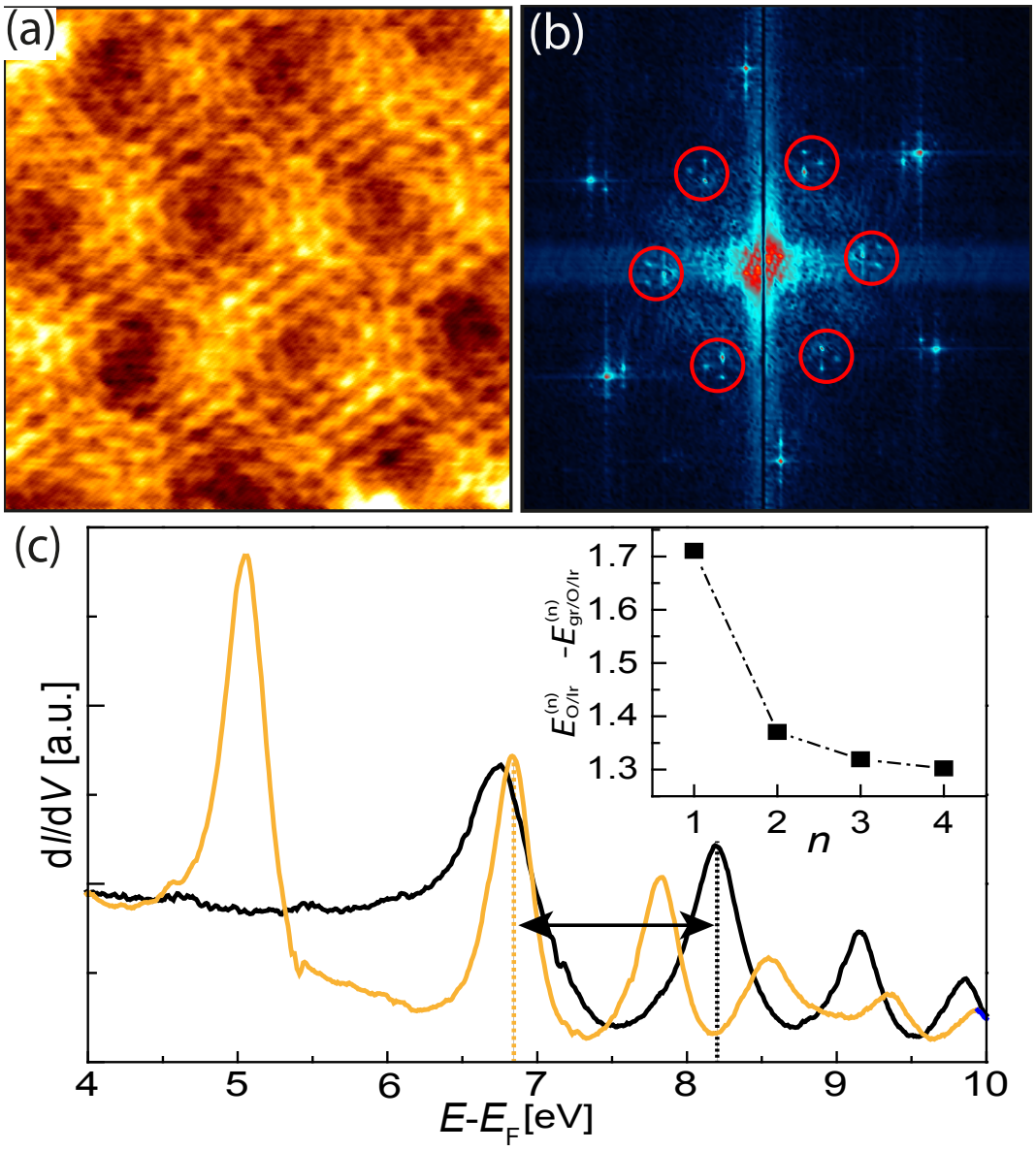

Figure 7.8: (a) Topography: O intercalated GQD, image width 7.6 nm, $V = 110\,\mathrm{mV}$, $I = 0.08\,\mathrm{nA}$; (b) FT-STM of gr/O/Ir(111), circles: $(\sqrt{3} \times \sqrt{3})R30°$-O intercalation superstructure. (c) IPS spectra on gr/O/Ir(111) (yellow) and on O/Ir(111) (black), $\Delta\Phi$ indicated by black arrow; inset: $\Delta E^{(n)} = E^{(n)}_{\mathrm{O/Ir}} - E^{(n)}_{\mathrm{gr/O/Ir}}$.

In Fig. 7.8 (c) we compare spectra on gr/O/Ir (yellow) and on O/Ir(111) (black). We derive $\Delta\Phi = (1.3 \pm 0.1)\,\mathrm{eV}$ from a plot $\Delta E^{(n)} = E^{(n)}_{\mathrm{O/Ir}} - E^{(n)}_{\mathrm{gr/O/Ir}}$ versus n [233]; see inset of Fig. 7.8 (c). Note that, especially for $n = 1$, a large deviation from this value results which is due to the interaction of the lowest IPS with the substrate [233], as already mentioned above. We obtain $\Phi_{\mathrm{gr/O/Ir}} = (5.1 \pm 0.1)\,\mathrm{eV}$, which has to be compared with $\Phi_{\mathrm{gr/Ir}} = (4.7 \pm 0.1)\,\mathrm{eV}$ [114, 236].

According to [231], we deduce $\Delta E_{\mathrm{D}} = E_{\mathrm{D,gr/O/Ir}} - E_{\mathrm{D,gr/Ir}} = \Phi_{\mathrm{gr/O/Ir}} - \Phi_{\mathrm{gr/Ir}} = (0.4 \pm 0.1)\,\mathrm{eV}$. This nicely agrees with $\Delta E_{\mathrm{D}} = 0.3\,\mathrm{eV}$ implied by a recent photoemission study [47] (linearly interpolated using $\Delta E_{\mathrm{D}} = 0.6\,\mathrm{eV}$ for 0.6 ML). In consequence, our determination of the local work function provides direct access to E_{D}, which is often hard to determine by other methods. As an example, for gr/Ir(111) the LDOS determined from STS does not show a pronounced dip at E_{D} [118]. A determination of E_{D} via Φ can be especially useful for mapping the doping level in inhomogeneous graphene systems.

In Fig. 7.9 a matrix plot of a series of 100 $\mathrm{d}I/\mathrm{d}V$ IPS point spectra across an oxygen intercalated GQD in an energy range of $E = 2..10\,\mathrm{eV}$ is presented, measured at a setpoint of $I_{\mathrm{stab}} = 8.0 \times 10^{-11}\,\mathrm{A}$ and $V_{\mathrm{stab}} = 500\,\mathrm{mV}$ with a speclength of 180s and a preamplifier gain of 10^9. Each spectrum consists of 1000 data points and is obtained by the average of three single measurements, with each of them measured in both the back and the forward direction of the voltage ramp. Noticeable is the much more abrupt change in $E^{(n)}_{m,l}$ with position, which is now, comparing to Fig. 7.6, visible not only for $n = 1$ but also for $n = 2$. This is due to the reduced interaction between the Ir- and the gr-2DEGs by separating them by a higher potential barrier. The states $n \geqslant 3$ still show mutual interaction, indicating that intercalation obviously can be used as a tool to tune the decay length of the electronic wave functions at a potential barrier on the local scale.

It should be mentioned that the oxygen intercalated island in Fig. 7.9 is by a factor of 10 larger than the non-intercalated one in Fig. 7.6, which means a reduced energy shift by confinement in Fig. 7.9. This size difference alone should lead to a shift of, e.g., $E^{(2)}_{(2,0)}$ by $\Delta E^{(2)}_{(2,0)} = 0.251\,\mathrm{eV}$. However, the observed shift (relative to the substrate) is $\Delta E^{(2)}_{(2,0)} = 0.591\,\mathrm{eV}$, showing that the increased confinement potential is the dominant effect. Note that it is not possible to measure on very small GQDs in the intercalated case, as small graphene GQDs tend to resist intercalation [51].

Considering the findings for the FWHM, the peak position dependence on area and the influence of the tuned barrier, we obtain the idea of low order IPS being well confined on the nanostructures, showing little interaction with states outside the potential well and high order ones exhibiting a much more complex behavior. For high order states the

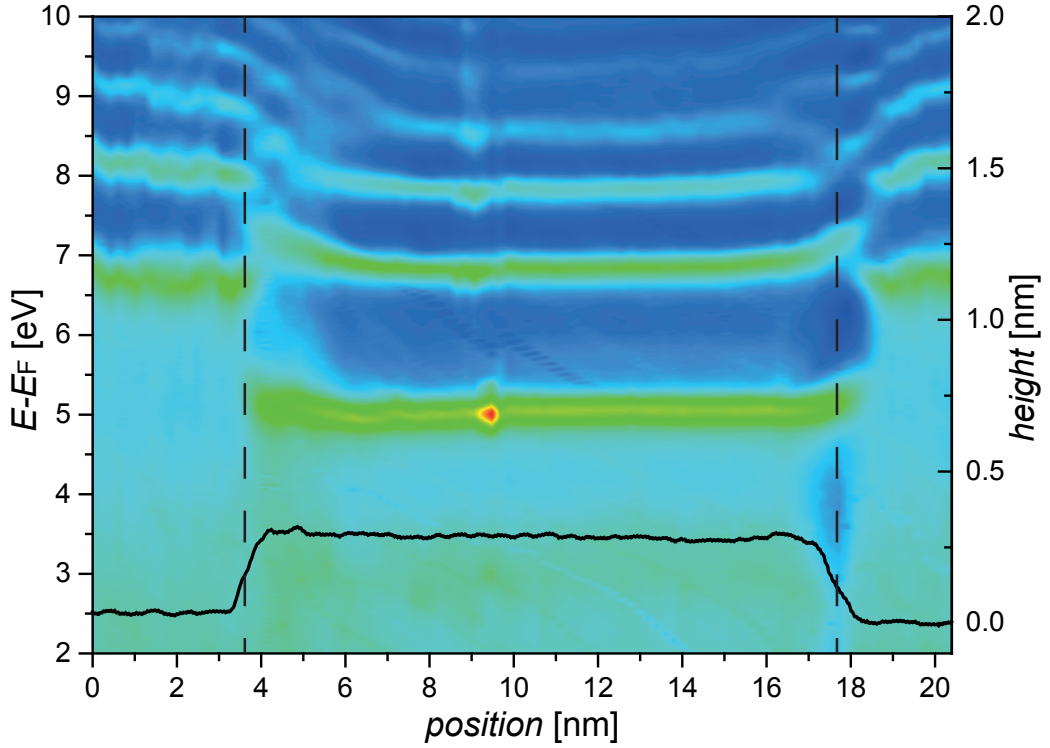

Figure 7.9: IPS spectrum in one spatial dimension, measured across an $A = 125\,\mathrm{nm}^2$ sized oxygen intercalated GQD on Ir(111). Matrix plot of a series of 100 $\mathrm{d}I/\mathrm{d}V$ point spectra in an energy range of $E = 2..10\,\mathrm{eV}$, measured at a setpoint of $I_{\mathrm{stab}} = 8.0 \times 10^{-11}\,\mathrm{A}$ and $V_{\mathrm{stab}} = 500\,\mathrm{mV}$ with a speclength of 180 s and a preamplifier gain of 10^9. Each spectrum consists of 1000 data points and is obtained by the averaging three single measurements, with each of them measured in both the back and the forward direction of the voltage ramp; inset: topography, size $27.5 \times 16.7\,\mathrm{nm}^2$, $V = 0.5\,\mathrm{V}$, $I = 0.08\,\mathrm{nA}$.

situation may be better described by disturbed (small islands) and undisturbed states (large islands). High order states are far way from the surface, almost exceeding the typical decay length of the confinement potential into the vacuum, thus in case of small structures transforming the potential well into an effective finite barrier.

7.5 Conclusion

Summing up our results, the large difference in work function between graphene and Ir(111), the well-defined shape of the nanostructures as well as their large size variation and high stability enabled us to demonstrate confinement effects of IPSs. We have shown that the energy spectrum depends on the size of the GQDs and evolves into a series of atom-like states, which is dominated by a state other than the ground state due to an interplay of density of states and parallel momentum transfer in the tunneling process. Intercalating extended graphene with an electron acceptor introduces an additional degree of freedom as this allows tuning of the local workfunction Φ. Tuning Φ enables control over the interaction of the IPS-2DEG of the GQDs with the one of the substrate.
The determination of Φ allows us to deduce the local doping level E_{D}. This is of vital importance for studies on inhomogeneous graphene intercalation compounds. Our findings open new possibilities for the study of quantum size effects as GQDs are a very flexible building material for nanostructures.
Although the emergence of new states by IPSs hybridization does not play a role in the system at hand (see above), it might play an important role when it comes to stacked graphene structures as proposed and studied by the Manchester group [4], leading to pronounced contributions to the transport processes in such systems. Such states could behave in a similar way as the ones studied by us.
In principle, further experimental work and support from theory could make a deconvolution of the substructure peaks possible and therefore allow a study of the lifetime of confined IPSs, which we propose as future work.

CHAPTER 8

Inelastic Electron Tunneling Spectroscopy on Graphene Quantum Dots

The experiment presented in this chapter was planned by Carsten Busse and myself. All experimental work discussed in this chapter was carried out by myself at the LT-STM setup, including both data acquisition and analysis. The results were discussed with Carsten Busse.

After having explored the lateral electronic structure of intercalated and non-intercalated GQDs, we now turn to a sometimes neglected part of nanostructured graphene. This chapter deals with STM-IETS investigations (Sec. 1.1) of the boundary region of GQDs on Ir(111).

In theoretical studies free-standing graphene edges are predicted to possess spin-polarized edge-states [9]. Recently, the existence of magnetic edge states has even been discussed for epitaxial graphene on copper, gold and silver, while it is absent on Ir(111) [118, 183]. Especially the edge state of H-terminated edges of graphene on gold is supposed to be magnetic [183]. Graphene edge states have experimentally been observed in STM for the case of nanoribbons on Ru(0001) [237]. Since in the case of epitaxial graphene the existence of magnetic edge states or the existence of edge states at all heavily depends on the hybridization behavior of the boundary, there is a strong need for local techniques which are able to determine the specific edge termination. Especially the edge termination of GQDs on Ir(111) has been under discussion for quite a while [118, 238]. In STM, addressing the edges can be quite challenging, since this region is governed by structural (topographic height), electronic (change in local workfunction) and chemical (bonds) peculiarities. In the following a route to approach the edge termination will be outlined, making use of the advanced technique of inelastic electron tunneling spectroscopy (IETS) described in Sec. 1.1.

8.1 Probing the Edge

For the experiment discussed here, GQDs have been prepared in the standard way by catalytic decomposition of ethylene on Ir(111) in one TPG step, yielding a graphene coverage of ≈ 22 % (see Sec. 3.1).

A typical result is shown in Fig. 8.1, presenting two $\mathrm{d}^2I/\mathrm{d}V^2$ point spectra on the $325\,\mathrm{nm}^2$ sized GQD in Fig. 8.2 (b). They were obtained by averaging two single curves obtained from forth and backward application of the point spectroscopy voltage ramp, respectively. Since the time constant of the lock-in amplifier was chosen too large, before averaging the spectra of the two directions were moved on top of each other, moving by the same value in opposite directions.

The black curve in Fig. 8.1, taken at the place marked by a black dot on the GQD in Fig. 8.2 (a), does not show any symmetry with respect to Fermi energy, which excludes the present features to be associated with vibrational excitations described in Sec. 1.1. In contrast, the red curve in Fig. 8.1 [red dot in Fig. 8.2 (a)] shows a clearly antisymmetric feature at $E = \pm(125 \pm 38)\,\mathrm{meV}$, which we in consequence assign to a vibrational excitation of the GQD boundary by electrons of the tunneling process (see Sec. 1.1). The error in energy (gray shaded areas in Fig. 8.1) is given by the experimental resolution (see Sec. 1.1). The vibrational excitation energy at the edge of the GQD is characteristic for the element

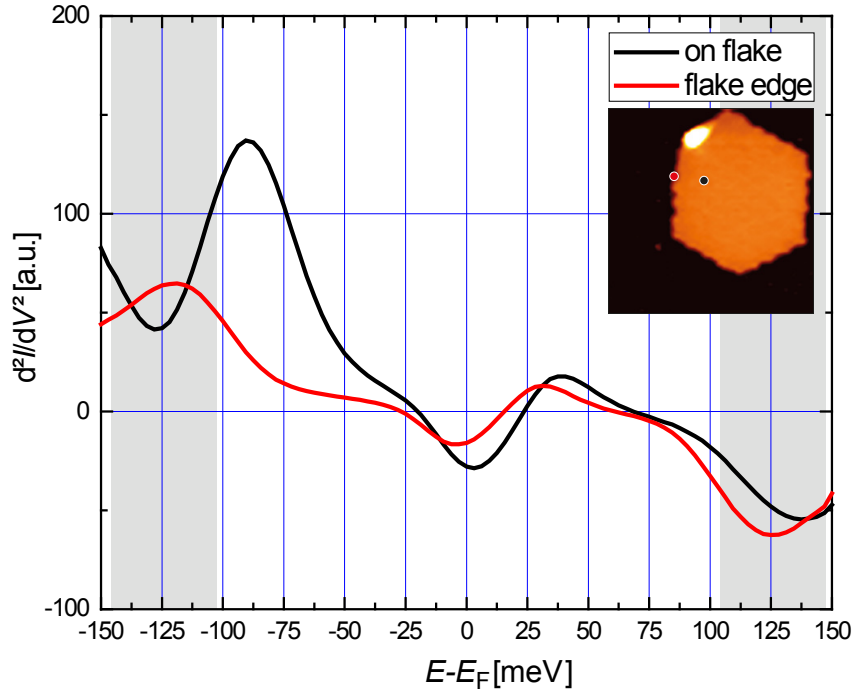

Figure 8.1: $\mathrm{d}^2I/\mathrm{d}V^2$ point spectra on the GQD shown in Fig. 8.2 (a), measured at the edge (red curve) and on top of the nanostructure (black curve); $I_{\mathrm{stab}} = 0.4\,\mathrm{nA}$, $U_{\mathrm{stab}} = 150\,\mathrm{mV}$, $t = 120\,\mathrm{s}$, preamplifier gain 10^8; gray shaded areas indicate experimental resolution; inset: STM topograph, image size $27.5 \times 27.5\ \mathrm{nm}^2$. Colored dots correspond to $\mathrm{d}^2I/\mathrm{d}V^2$ point spectra.

specific binding character and the observed excitation energy of $E = \pm(125 \pm 18)\,\mathrm{meV}$ is in a reasonable range for e.g. C-H excitations [78, 239, 240].

The presence of a vibrational boundary mode is also supported by the corresponding spatial $\mathrm{d}^2I/\mathrm{d}V^2$ mapping at the excitation energy on the same $325\,\mathrm{nm}^2$ sized GQD/Ir(111) probed in Fig. 8.1. The mapping in Fig. 8.2 (b) was performed at an energy close to the $E = \pm(125 \pm 18)\,\mathrm{meV}$ provided by point spectroscopy. During the measurements the final value of the point spectroscopy was not available due to the need for further processing of the raw data as mentioned above. The raw data of Fig. 8.1 indicated an excitation energy of $E = -119\,\mathrm{meV}$. Despite that, the map in Fig. 8.2 (b) clearly shows a boundary associated vibrational excitation.

Surprisingly, also the moiré pattern of gr/Ir(111) shows up in the $\mathrm{d}^2I/\mathrm{d}V^2$ data [91], see Fig. 8.2 (b). This observation could act as a support for the findings in reported in Ref. [17], discussing the spatially varying binding character between graphene and the Ir(111) substrate, which should also be reflected in different modes of vibrational excitations.

However, the point spectra needed to identify the required symmetry with respect to Fermi energy do not possess the necessary resolution to support such an interpretation on the basis of the data at hand.
The small dots outside the GQD [Fig. 8.2 (b)] are supposed to have been created during the preparation process and might be identified as non-dissociated hydrocarbons. However, their presence does not compromise the validity of the arguments given here since they do not influence the edges of the GQDs.
In Fig. 8.2 (c) and Fig. 8.2 (d) we show a measurement similar to the one presented in Fig. 8.2 (a) and Fig. 8.2 (b). It also shows two GQDs on Ir(111), sized 53 nm^2 and 6 nm^2. However, although the $\mathrm{d}^2I/\mathrm{d}V^2$ imaging quality is worse due to an unstable tip, the measurement clearly shows the reproducibility and reliability of our investigation since both of the GQDs show an enhanced $\mathrm{d}^2I/\mathrm{d}V^2$ signal at $E = -120\,\mathrm{mV}$. The fact that two GQDs varying in size by almost one order of magnitude are both showing the enhanced signal at the same energy suggests that the character of edge termination does not depend on the GQD size.

8.2 Conclusion

We present a promising way to probe the edge termination of GQDs on Ir(111), using STM-IETS to detect vibrational modes characteristic for the boundary bonds. The observed excitation energy is in a reasonable range for C-H excitations [78, 239, 240]. To make a definite assignment, further investigations and especially DFT calculations providing values for possible vibrational excitations of gr-Ir bonds are needed. The experiment should be repeated with a reduced bias voltage modulation amplitude in order to improve the low experimental resolution of 36 meV.
A possible perspective for further experiments could be the growth of GQDs by catalytic decomposition of C_2D_4. By using deuterium the termination of the edges should provide a clearly different excitation energy in STM-IETS compared to the hydrogen used in the experiment described here [241]. Also the lateral C-Ir binding character could be a goal of further investigation in STM-IETS experiments in view of a possible moiré dependency.

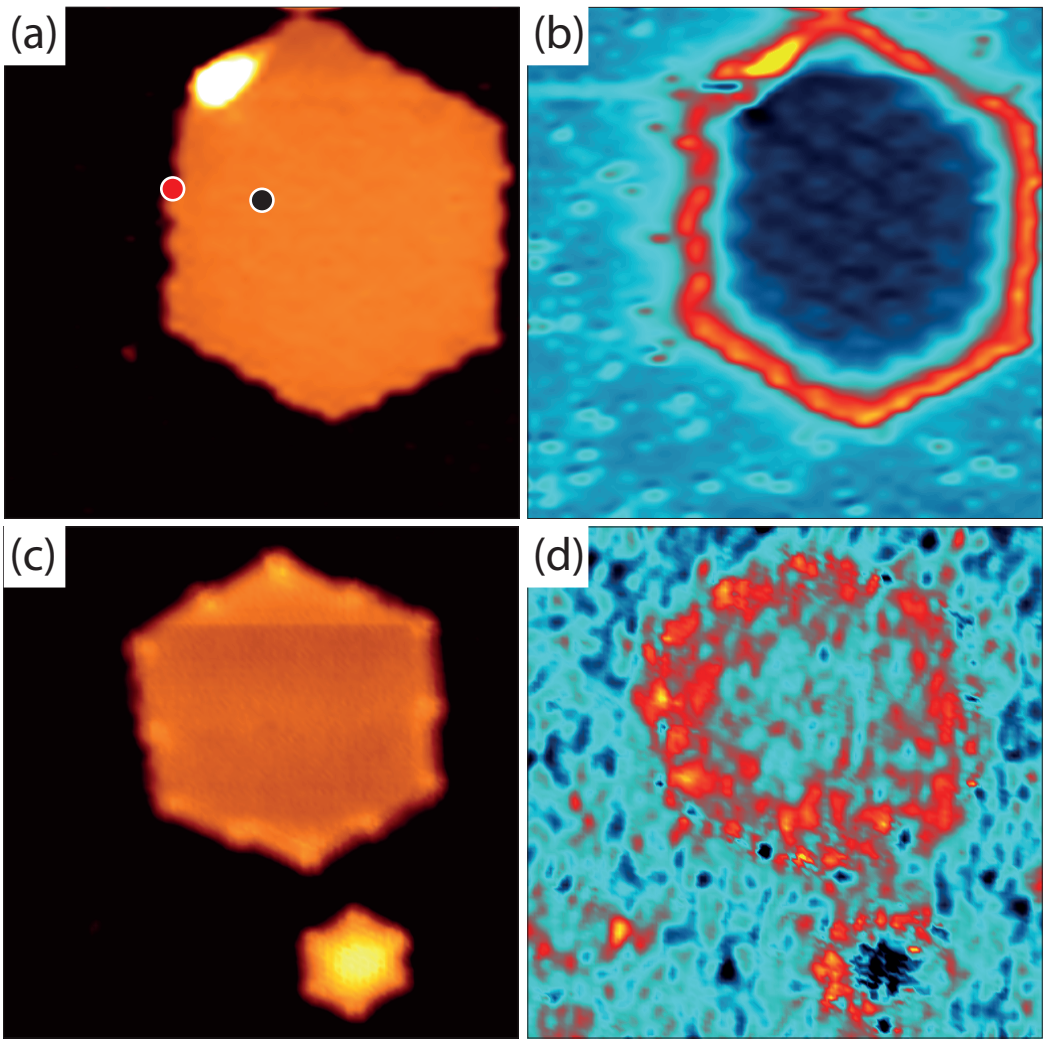

Figure 8.2: (a) Constant current topographic image of a 325 nm^2 sized GQD/Ir(111), image size 27.5 × 27.5 nm^2. Colored dots corresponding to colors of d^2I/dV^2 point spectra in Fig. 8.1. (b) simultaneously to (a) recorded d^2I/dV^2 spectroscopy map of the same area, measured at 5 K; setpoint $I_{\mathrm{stab}} = 4.0 \times 10^{-10}$ A, $U_{\mathrm{stab}} = -119$ mV with 64 × 64 pixels, scanning speed 79 s/line, preamplifier gain of 10^8; lock-in amp. parameters: time const. 300 ms, $V_{\mathrm{mod}} = 20$ mV, mod. frequency 323.1 Hz, sensitivity 100 mV, harm 2; DSP feedback: integrator -0.72, P-gain 1.0; (c) Constant current topographic image of two GQDs/Ir(111), image size 13.8 × 13.8 nm^2. (d) simultaneously to (c) recorded d^2I/dV^2 spectroscopy map of same area, measured at 5 K, setpoint $I_{\mathrm{stab}} = 1.6 \times 10^{-9}$ A, $U_{\mathrm{stab}} = -120$ mV, 128 × 128 pixels, scanning speed 115 s/line, preamplifier gain 10^8.

CHAPTER 9

Metallic State at 1D Defects in Epitaxial Graphene on Ir(111)

The experiment described in this chapter was planned by Carsten Busse and myself. The sample was prepared by myself with support by Sven Runte. Data acquisition and analysis were performed by myself. Concerning the interpretation Carsten Busse, Thomas Michely, Tim O. Wehling, Achim Rosch and Eran Sela made contributions.

This chapter reports on the observation of metallic states arising at substrate step edges and structural phase boundaries in gr/Ir(111) by the means of STS. The results are the first spectroscopic results for this kind of states first mentioned in Ref. [242].

STM investigations on non-intercalated closed layer epitaxial graphene include observations like the Dirac cone feature in point spectroscopy [1], the interlayer state (and thus substrate dependency of image potential states [227, 229]), scattering from defects [164], the influence of moiré structures on graphene's electronic properties [243] and many more.
Defects in extended graphene, especially grain boundaries, are of vital importance on the route towards applications. In a large scale production process, graphene usually has a polycrystalline character. The concentration of grain boundaries plays a crucial role in transport, since the electron transmission at these defects can be significantly suppressed [244]. However, one dimensional defects can also host metallic states with potential application in nanoelectronics when the defects are generated in a controlled way [242].
After we have discussed the high impact of reduced dimensionality on the electronic spectrum of graphene in form of GQDs, in this chapter findings for distinct regions of a closed layer of gr/Ir(111) are presented, namely those which are disturbed by the presence of step edges and structural phase boundaries. In gr/Ni one dimensional defects at structural phase boundaries are able to induce local states which form a metallic wire along the defects and are a kind of self-doping of graphene [242]. For the case of gr/Ir(111), we investigate the LDOS perpendicular to the 1D defects and study the effect of different kinds of 1D defects on the presence of metallic states.

9.1 Step Edge

All results presented in this chapter relate to STM and STS measurements on a closed monolayer of epitaxial gr/Ir(111) prepared in the combined TPG/CVD process described in Sec. 3.1.
Figure 9.1 (a) shows an STM topograph of a closed graphene layer at an iridium step edge. It comprises the pronounced moiré structure as well as defects in the graphene lattice and faint atomic resolution. Three specific places on the surface are marked by colored squares, indicating places on the lower (red) and the upper (blue) terrace, respectively, and one right at the step edge (black).
The corresponding $\mathrm{d}I/\mathrm{d}V$ point spectra in an energy range of $\pm 500\,\mathrm{mV}$ with respect to Fermi energy are shown in Fig. 9.1 (b), yielding a severe difference in shape between the two places on top of the terraces and at the step edge. Note that graphene on iridium is known to be only slightly p-doped by approximately 80 meV (Sec. 1.4), leaving the investigated energy range still quite symmetric also with respect to the Dirac point. The spectra on the

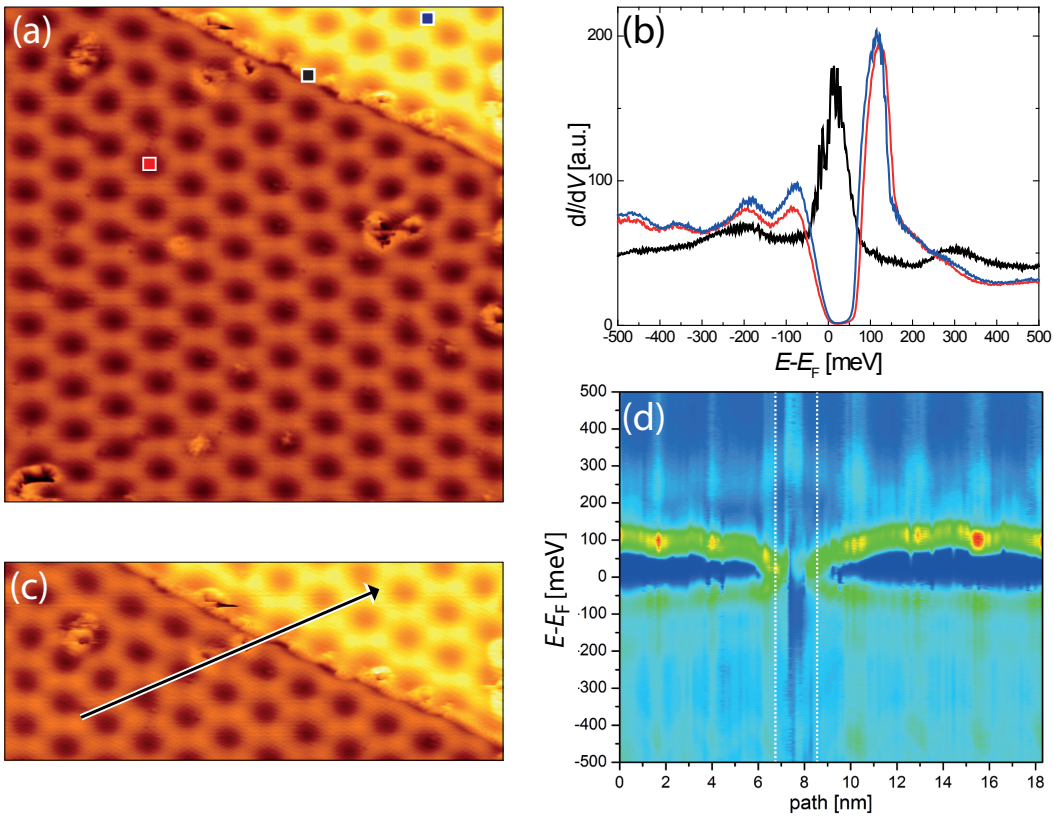

Figure 9.1: (a) STM topograph, size $27.5 \times 27.5\,\mathrm{nm}^2$, colored squares indicate location of point spectra shown in (b). (b) three $\mathrm{d}I/\mathrm{d}V$ IPS point spectra in an energy range of $E = -500..500\,\mathrm{meV}$, measured at a setpoint of $I_{\mathrm{stab}} = 3.0 \times 10^{-8}\,\mathrm{A}$ and $V_{\mathrm{stab}} = 500\,\mathrm{mV}$ in period of 120s and with preamplifier gain of 10^8. Each spectrum with 1024 data points and obtained by averaging back and the forward direction of voltage ramp. (c) STM topograph, size $27.5 \times 11.0\,\mathrm{nm}^2$, black arrow indicating an 18.3 nm path of 120 point spectra in (d) Matrix plot of a series of 120 $\mathrm{d}I/\mathrm{d}V$ point spectra in a range of $E = -500..500\,\mathrm{meV}$, measured at setpoint $I_{\mathrm{stab}} = 3.0\,\mathrm{nA}$, $V_{\mathrm{stab}} = 500\,\mathrm{mV}$ in period of 120s and with preamplifier gain 10^8. Each spectrum with 1024 data points and obtained by averaging two single measurements, each of them with both the back and the forward direction of voltage ramp; dashed white lines indicate width of metallic feature.

terraces [Fig. 9.1 (b); red, blue] do not show any density of states at Fermi energy which of course would not be the case for a situation where the tip is sensitive to the metallic substrate. Therefore, we assign the observed spectra to phonon assisted inelastic tunneling [169, 170] or at least to a tip shape which is expected to be quite sensitive to the graphene band structure. Both spectra coincide very well which emphasizes the stability of the tip.

In contrast, the spectrum shows a metallic character in form of a peaked shape exactly at E_F on top of the step edge [Fig. 9.1 (b), black curve].

With this special character of the step edge LDOS in mind we also attribute the sharp structure of the step edge in topographic imaging [Fig. 9.1 (a)] to the extraordinary sensitivity of the tip to metallic states at the edge. In Fig. 9.1 (b) the graphene layer over

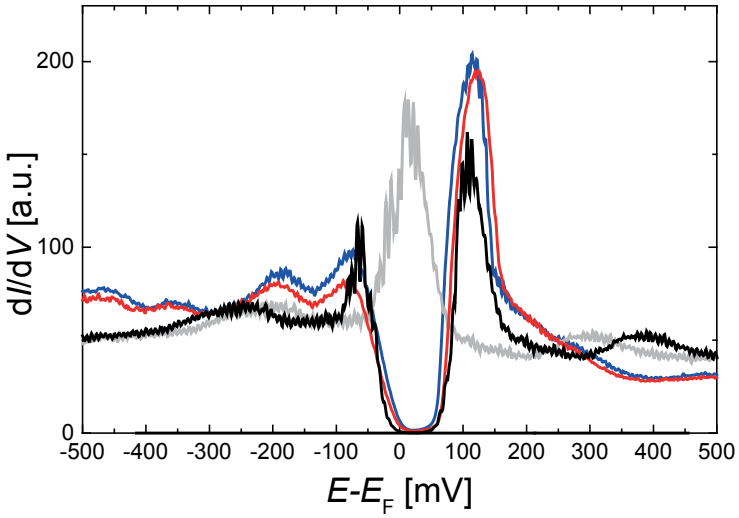

Figure 9.2: Replotting Fig. 9.1 (b) with an artificially generated gap in the black spectrum at the step edge with $E_G = 130\,\text{meV}$ as calculated in Ref. [169]. The original position of the black curve (as measured) is shown in gray.

the Ir step in Fig. 9.1 (a) is shown again, but with an arrow indicating a path of 120 $\mathrm{d}I/\mathrm{d}V$ point spectra on a line of 18.3 nm in length, which means measuring the point spectra in a 1.5 Å distance, respectively. In order to get a good access to this vast amount of data, the spectra are presented in Fig. 9.1 (d) in form of a matrix plot, with the color code indicating the $\mathrm{d}I/\mathrm{d}V$ signal from low (blue) to high (red) intensity. Each spectrum consists of two averaged single measurements, each of them with both voltage ramp directions. They have been measured with a preamplifier gain of 10^8 and a speclength of 120 s at a setpoint of $I_{\text{stab}} = 3.0\,\text{nA}$ and $V_{\text{stab}} = 500\,\text{mV}$. The matrix plot clearly shows that the change between the gapped and the peaked character at Fermi energy of the spectra at the step edge is a rather continuous one:

The two peaks at negative and positive energy which limit the gapped energy range move closer together with approaching the substrate step edge, smoothly reducing the gap and finally resulting in the peaked shape shown in Fig. 9.1 (b) (black curve). Two dashed white colored lines in Fig. 9.1 (d) indicate the spatial width of the metallic feature by a distance

of $\approx 1.9\,\mathrm{nm}$. This value is similar to the width of a metallic nanowire reported in Ref. [242] for a one dimensional defect produced by a structural phase boundary.

In addition to this puzzling behavior, in Fig. 9.1 (d) additional structures appear with a spatial periodicity of approximately 2.5 nm at roughly $E = \{-450; -200; +250\}\,\mathrm{meV}$. Also both the negative and the positive branch of the gap limiting peak structure seem to possess an intensity modulation with the same spatial periodicity. The observed periodicity is most probably connected to the moiré superstructure [see Fig. 9.1 (a)], giving rise to additional peaks depending on the specific spatial position. Note that the Fermi energy peak [Fig. 9.1 (b) black] is not well visible in the matrix plot in Fig. 9.1 (d). This is due to the fact that the matrix plot contrast has to be adjusted to the much higher intensities of the gap limiting peak structure.

An interesting finding is revealed by generating an artificial gap in the data obtained at the step edge [black curve in Fig. 9.1 (b)] as it is expected for phonon-mediated inelastic tunneling: In Fig. 9.2 we insert a gap of $E_G = 130\,\mathrm{meV}$ according to [169] and include an asymmetry with respect to E_F due to the experimental issue of a voltage drop by about 20 mV. We recalculate the negative $E - E_\mathrm{F}$ branch of the spectrum using a shift of -45 meV in energy and a sigmoidal smoothening at the gap, plotting $\mathrm{dI/dV'_{-}} = 1/(1 + \exp(\alpha(\mathrm{V'_{bias}} + 45))) \times \mathrm{dI/dV_{meas.}}$ versus $V'_\mathrm{bias} = V_{\mathrm{bias\,meas.}} - 45\,\mathrm{mV}$. The positive $E - E_\mathrm{F}$ branch is consistently recalculated using a shift of +85 meV in energy and plotting $\mathrm{dI/dV'_{+}} = 1/(1 + \exp(-\alpha(\mathrm{U'_{bias}} - 85))) \times \mathrm{dI/dV_{meas.}}$ against $V'_\mathrm{bias} = V_{\mathrm{bias\,meas.}} + 85\,\mathrm{mV}$. For both branches we used $\alpha = 0.1$.

The artificial gap coincides quite well with the measured ones on top of the terraces (blue and red curves in Fig. 9.2). This supports the interpretation of the gapped structure at E_F for the spectra on the terraces as being caused by phonon-mediated inelastic tunneling [170]. Furthermore, the presence of the step edge closes the inelastic gap, either by a sheer dominance of the TDOS by the metallic state at the Γ point [242], changing the preferred states in the tunneling process, or by the changed geometry of tip and sample. In any case the defect breaks the translational symmetry and therefore the momentum of the tunneling electron is not conserved at all.

Up to now, the origin of the pronounced peaks limiting the gap in the spectra located on the terraces remains unknown.

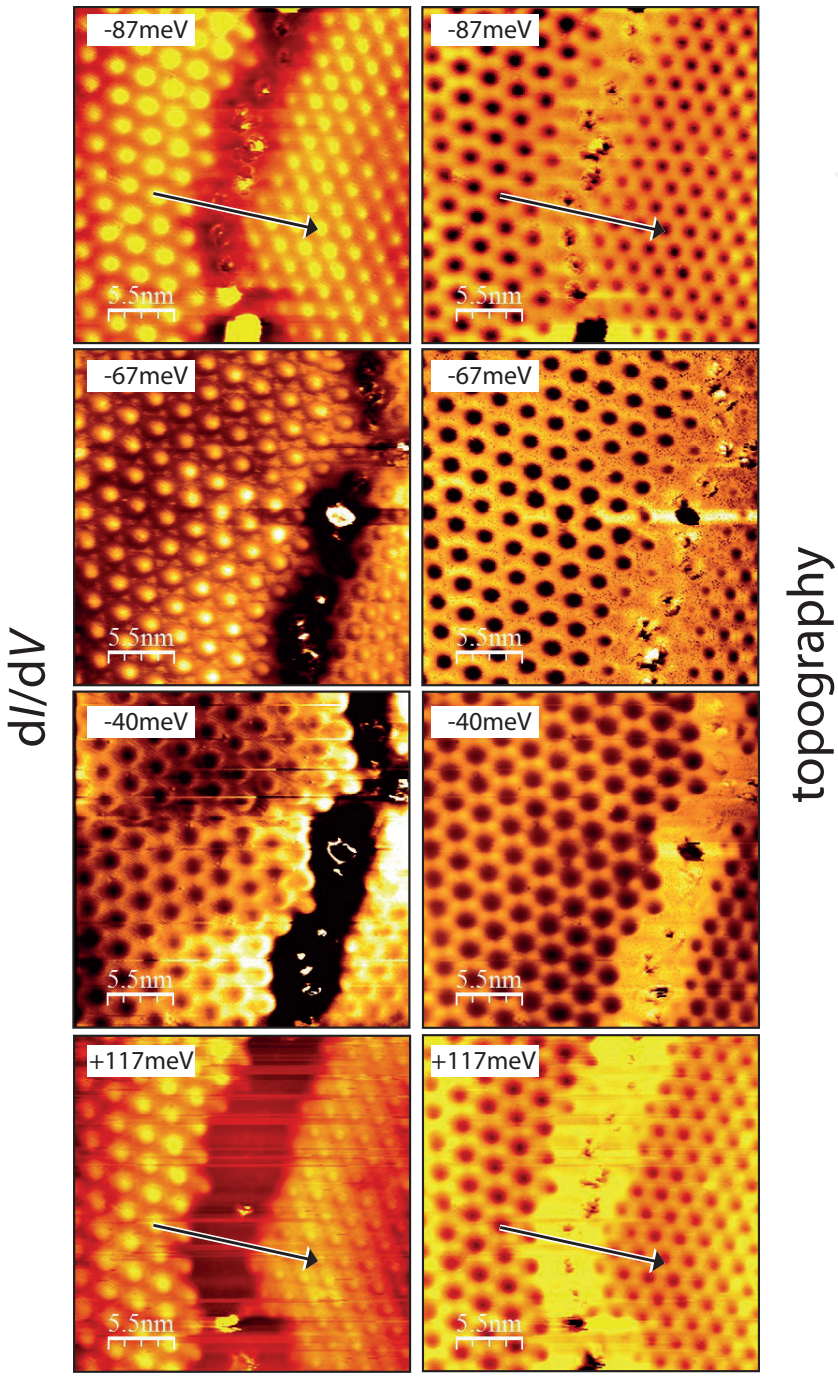

Figure 9.3: Spatial distribution of the gap limiting peaks (compare with Fig. 9.4); spectroscopic maps (left) with simultaneously recorded STM topographs (right), size $27.5 \times 27.5\,\mathrm{nm}^2$; $I_{\mathrm{stab}} = 1\,\mathrm{nA}$; black arrows indicate line of the point spectra presented in Fig. 9.4.

9.2 Structural Phase Boundary

The metallic state was also observed on another topographically distinct region, namely a structural phase boundary separating two different rotational domains of graphene [see Fig. 9.3]. The left region of the images shows a graphene area with a moiré superstructure periodicity of 2.47 nm, the right one an area with a moiré superstructure periodicity of 2.00 nm. In the figure, constant energy $\mathrm{d}I/\mathrm{d}V$ maps are presented side-by-side with the corresponding simultaneously recorded STM topographs. The $\mathrm{d}I/\mathrm{d}V$ maps reveal the spatial distribution of those states which contribute to the borders of the gapped energy range in the local density of states. They comprise the left ($E-E_\mathrm{F} = \{-87; -67; -40\}$ meV) and the right boundary ($E - E_\mathrm{F} = +117$ meV) of the gap (see Fig. 9.4) and emphasize the sensitivity to (undisturbed) graphene states outside the gap since the phase boundary shows a low LDOS signal for these energies. In contrast, the STM topographic images show no depletion at the phase boundary due to the fact that here all states between E_F and $E = e \cdot V_\mathrm{bias}$ contribute to the signal and thus especially the metallic wire appears in low voltage topographic imaging (see $V = +117$ mV topograph in Fig. 9.3) [242].

In addition, the maps resemble a pronounced contrast inversion of the moiré with respect to the corresponding STM topography [245]. The matrix plot in Fig. 9.4 reveals a behavior similar to the observations discussed in Fig. 9.1 (d) for the substrate step. It consists of a series of 60 $\mathrm{d}I/\mathrm{d}V$ point spectra in an energy range of $E = -500..500$ meV, measured at a setpoint of $I_\mathrm{stab} = 3.0 \times 10^{-9}$ A and $V_\mathrm{stab} = 700$ mV with a speclength of 60 s and a preamplifier gain of 10^8. Each spectrum consists of 1024 data points and is obtained by averaging the back and the forward direction of the voltage ramp. The neighboring topograph indicates the place where the spectra have been measured, with the black arrow indicating the length and the direction of the path perpendicular across the phase boundary.

Also for the case of the boundary region of neighboring rotational domains the two gap limiting peaks move closer together, close the gap (dark blue) and merge into a single peak right at Fermi energy. Moving away from the boundary to the neighboring domain, they separate again and resemble the initial gap size. We determine the width of the metallic wire to ≈ 1.6 nm (dashed white lines in Fig. 9.4), resembling the value determined in Ref. [242] and in accordance with our value obtained at the step edge (see above). Also in this case the whole spectrum seems to be modified by a certain spatial periodicity, but in contrast to the observation at the step edge the typical length scale is now much smaller than both moiré periodicities in the topography.

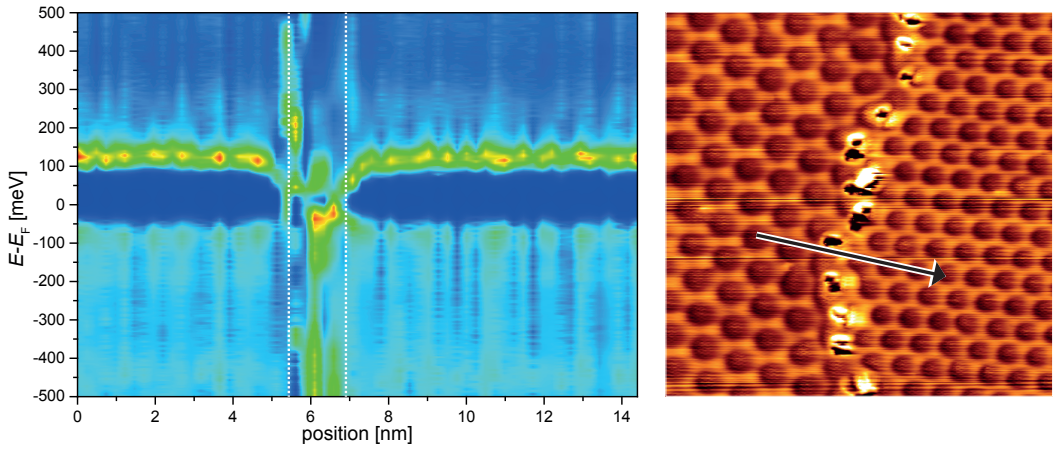

Figure 9.4: Left: Matrix plot of a series of 60 $\mathrm{d}I/\mathrm{d}V$ IPS point spectra in an energy range of $E = -500..500\,\mathrm{meV}$, measured at a setpoint of $I_{\mathrm{stab}} = 3.0 \times 10^{-9}\,\mathrm{A}$ and $V_{\mathrm{stab}} = 700\,\mathrm{mV}$ with a speclength of 60 s and a preamplifier gain of 10^8. Color code from blue (low $\mathrm{d}I/\mathrm{d}V$ signal) to red (high $\mathrm{d}I/\mathrm{d}V$ signal). Each spectrum consists of 1024 data points and is obtained by averaging the back and the forward direction of the voltage ramp; dashed white lines indicate width of the metallic wire. Right: STM topograph, image size $27.5 \times 27.5\,\mathrm{nm}^2$, $V_{\mathrm{bias}} = 700\,\mathrm{mV}$; black arrow indicating a 14.4 nm path of the 60 point spectra.

Apart from the mechanism proposed in Ref. [242], we made some effort to consider further possible origin of these stunning features in the locally altered closed layer graphene. Though still resisting a final understanding, the features could be associated with strain in the carbon layer, which should exist both at the step edge and the structural phase boundary of rotated domains [246–248]. Strain in graphene is known to induce large pseudo-magnetic fields [246, 247, 249].

9.3 Conclusion

We observed metallic wires in the LDOS at one dimensional defects of a closed monolayer of graphene on Ir(111). Based on a microscopical tip which in spectroscopy shows a gapped LDOS at the Fermi level usually attributed to phonon-mediated tunneling, we find the gap vanishing on one dimensional defects in graphene in form of (i) a step edge of the substrate or (ii) a structural phase boundary of the graphene layer. Introducing an artificial gap to the metallic state in the order of one theoretically expected in phonon assisted inelastic tunneling resembles the naturally gapped shapes with pronounced peaks

at the gap borders observed far away from the one dimensional defect. Our findings share similarities with the proposed metallic nanowires in one dimensional defects in gr/Ni [242]. The origin of the strong peaks limiting our gapped spectra remains unknown.
Questions arise concerning the homogeneity of the observed state along the defect lines. This requires further STS measurements, mapping the wires in 2D. Our findings might be related to the question of electron transport across 1D defects since the presence of metallic wires should significantly influence the transmission in perpendicular direction.

CHAPTER 10

Summary and Outlook

10.1 Summary

The work on GQDs provides a variety of new insight into exciting new physics by exploiting the opportunities of a model system which is highly tunable in spatial, chemical and electronic parameters. We could reveal several new aspects in the sense of both structural and electronic properties, using the unique local capabilities of scanning tunneling spectroscopy.

With the aim of restoring properties of free-standing graphene in an epitaxial system and observing clear fingerprints of Dirac electrons, we investigated two possible intercalants in order to decouple graphene from the Ir(111) substrate. First, our interest focused on silver. We report on the first study of the local properties of the Shockley-type silver surface state on a 15 ML film on Ir(111) in the presence of graphene on top. The Ag/Ir(111) film shows clear hints at the presence of strain due to a remaining influence of the iridium substrate, shifting the surface state onset by a small amount to higher energies in accordance with observations already discussed in literature for similar systems. The presence of graphene changes the silver surface state more significantly: Though being preserved at all, the change in the surface state onset energy by the presence of graphene on top provides an additional shift of +0.2 eV with respect to the strain induced value. STS point spectra reveal a Dirac feature of n-doped gr/Ag in accordance with theoretical predictions, energetically well separated from the silver surface state onset. The analysis of confinement patterns on GQDs/Ag by means of STS reveals the silver surface state as being trapped under the nanostructures.

In consequence, we approached the intermixing of graphene and substrate LDOS by canceling the unwanted substrate contributions in form of surface states. For the case of Ag, this can be achieved by decreasing the thickness of the silver layer down to only 1 ML, increasing the iridium-silver interaction [141]. However, although locally showing Dirac features in STS point spectra, due to a complicated morphology up to now no confinement of Dirac electrons was observed in this system [141].

A very successful way for achieving the suppression of metallic surface states was paved by us using oxygen as an intercalant. Apart from clear signatures in STS, the efficient decoupling of graphene and the suppression of the surface states by the presence of oxygen are confirmed by DFT and ARPES, respectively.

For the first time we report on high-resolution STM/STS investigations on the local topographic and electronic properties on oxygen intercalated GQDs. We observed three different superstructures of atomic oxygen adsorbed to the Ir(111) surface under graphene:

(2×1), $(\sqrt{3} \times \sqrt{3})\,\mathrm{R30}^\circ$, and $(2\sqrt{3} \times 2\sqrt{3})\,\mathrm{R30}^\circ$. Concerning the electronic structure, we observed pronounced features in the LDOS of oxygen intercalated GQDs related to the edges (i) and the area of the GQDs (ii). We attribute both features to charge effects in the GQD/oxygen interface line (i) and a single-electron effect connected to the charging of discrete confined states by tip-induced band bending (ii).

We used this sample system to unambiguously demonstrate the possibility of confining Dirac electrons to GQDs for the first time, surpassing experimental difficulties of recent studies reported in literature [1]. Here we have extracted a linear dispersion relation with parameters matching those of Dirac electrons in oxygen intercalated graphene as determined by ARPES. Furthermore, we observe the presence of intervalley scattering and a dip in the LDOS located at the Dirac point. A complementary DFT study yields the absence of covalent bonds of graphene towards the oxygen layer underneath. In sum the presence of all these effects underlines that intercalated oxygen renders graphene quasi-freestanding.

In addition, we extended our investigations to the unoccupied surface state spectrum at high energies, namely image potential states [2]. The large difference in work function between graphene and Ir(111), the well-defined shape of the nanostructures as well as their large size variation and high stability enabled us to demonstrate confinement effects of IPSs. We have shown that the energy spectrum depends on the size of the GQDs and evolves into a series of atom-like states, which is dominated by a state other than the ground state due to an interplay of density of states and parallel momentum transfer in the tunneling process. Intercalating extended graphene with an electron acceptor introduces an additional degree of freedom as this allows a tuning of the local workfunction. The determination of this work function allows us to deduce the local doping level E_D.

Up to now STS studies mainly concentrate on the surface of GQDs. Since the boundary plays a crucial role in terms of both topography and electronic properties (as it provides the confining potential), we turned our interest to the edges and present a promising way to probe the binding situation at the boundary. Here we use inelastic electron tunneling spectroscopy to detect vibrational modes as fingerprints of the boundary bonds. We found a distinct excitation energy which is in a reasonable range for C-H excitations [78, 239, 240].

Finally, reduced dimensionality is not the only way of shaping graphene's electronic system on the local scale, as we observed in form of an unconventional feature in the LDOS on a closed monolayer of graphene on Ir(111). Based on a microscopical tip, which in STS shows a gapped LDOS at the Fermi level usually attributed to phonon-mediated tunneling,

we find this gap vanishing on areas where the graphene is disturbed by (i) step edges of the substrate or (ii) structural phase boundaries of the graphene layer. Our findings resemble the emergence of metallic nanowires in one dimensional defects in gr/Ni [242].

10.2 Outlook

Our findings open new possibilities for studies on quantum size effects as graphene is a very flexible building material for nanostructures [2]. Concerning the investigation of laterally confined electronic states, there are various methods on how to prepare rationally designed architectures: Graphene can be cut by STM lithography [250], allowing complicated well geometries. A clever choice of the hydrocarbon precursor leads to the formation of superperiodic structures [251] which may give rise to backfolding of bands. One can envision that it is possible to move GQDs with an STM tip, allowing exact studies of the interaction of neighboring quantum wells. Such structures would resemble a diatomic molecule, where the participating quantum wells can even have different energy levels due to a variation in size or in doping.

For the case of gr/O/Ir(111) these considerations can be applied quite directly, whereas in the case of gr/Ag/Ir(111) more experiments are needed to find an appropriate way of decoupling GQDs and suppress the LDOS disturbance by the presence of the silver surface state. The parameter space of temperature, duration of heating and Ag layer thickness still leaves a chance to succeed in this task.

For gr/O/Ir(111) further analysis on the dominating O superstructures on Ir(111) is in progress, a manuscript is already in preparation. The interpretation of the charge effects remains challenging, a possible approach is given by further STM experiments which focuses on the presence of structural defects on areally charged GQDs in order to rule out a charging of single atoms or atomic defect sites in the oxygen layer.

Concerning the investigations on the GQD edges by STM-IETS, we propose further experiments with adjusted tunneling parameters and better experimental resolution to make a definite assignment to certain vibrational modes. Also DFT calculations in order to obtain values for hypothetical vibrational excitations of gr-Ir bonds are highly desirable. A possible perspective for further experiments could be the growth of GQDs by CVD/TPG with C_2D_4. Deuterium terminated edges are expected to provide a different excitation energy in STM-IETS compared to hydrogen termination [241].

PART III

Appendix

APPENDIX A

Details on Results

The appendix provides relevant details on discussions in the main chapters, e.g. additional calculations and supplemental results. Furthermore, technical details on scanning tunneling spectroscopy with the LT-STM setup are provided.

A.1 Fundamentals

Particle in a Cylindrical Box

This section was elaborated by Wouter Jolie in Ref. [141]. In the framework of this thesis it acts as an easy-to-access background information.
A simplified model to illustrate the physics of trapped electrons is the famous *particle-in-a-box* problem. For simplicity, the free electron with mass m is captured in a cylindrical box with an impenetrable wall at its border $\tilde{R}$. Mathematically, this is described by a potential $V(r)$ defined as

$$V(r) = \begin{cases} 0 & \text{if r} < \tilde{\text{R}} \\ \infty & \text{if r} \geqslant \tilde{\text{R}}. \end{cases} \tag{A.1}$$

The Schrödinger equation, in polar coordinates, can be written as

$$\begin{aligned} &\hat{H}\psi = E\psi \\ &\quad \Leftrightarrow -\frac{\hbar^2}{2m}\left(\frac{\partial^2}{\partial r^2} + \frac{1}{r}\frac{\partial}{\partial r} + \frac{1}{r^2}\frac{\partial^2}{\partial \theta^2}\right)\psi(\mathtt{r},\ \theta) = E\psi(\mathtt{r},\ \theta). \end{aligned} \tag{A.2}$$

By using a product ansatz, $\psi(r,\ \theta) = R(r)\cdot Y(\theta)$, the equation can be separated into two:

$$\begin{aligned} \frac{d^2 Y_{\mathrm{m_l}}(\theta)}{d\theta^2} &= -m_{\mathrm{l}}^2 Y_{\mathrm{m_l}}(\theta) \\ \frac{d^2 R(r)}{dr^2} + \frac{1}{r}\frac{dR(r)}{dr} - \frac{m_{\mathrm{l}}^2}{r^2}R(r) &= -k^2 R(r) \end{aligned} \tag{A.3}$$

with $k = \sqrt{2mE/\hbar^2}$.
The first equation has the solution

$$Y_{\mathrm{m_l}}(\theta) = \frac{1}{\sqrt{2\pi}} e^{im_{\mathrm{l}}\theta} \tag{A.4}$$

and with the requirement $Y_{\mathrm{m_l}}(\theta) = Y_{\mathrm{m_l}}(\theta + 2\pi)$, we get a quantized $m_{\mathrm{l}} = 0,\ \pm 1,\ \pm 2,\ ...$. The second equation can be rewritten with $z = kr$:

$$\frac{d^2 R(z)}{dz^2} + \frac{1}{z}\frac{dR(z)}{dz} + \left(1 - \frac{m_{\mathrm{l}}^2}{z^2}\right)R(z) = 0. \tag{A.5}$$

This differential equation is known as *Bessel differential equation*. Because m_l is an integer and the wave function should be finite at the origin ($r = 0$), the Bessel functions of the first kind are taken into account. These can be written (with $\Gamma(x)$ being the gamma function) in a Taylor series expansion around $r = 0$ [252]:

$$R_{\mathrm{m_l}}(z) = \sum_{\nu} \frac{(-1)^{\nu}}{\nu!\Gamma(\nu + m_\mathrm{l} + 1)} \cdot \left(\frac{r}{2}\right)^{2\nu + m_\mathrm{l}}. \tag{A.6}$$

The next step is to consider the boundary condition at $r = \tilde{R}$. There the wave function should vanish because of the influence of the infinite potential outside the circle:

$$J_{\mathrm{m_l}}\left(k_{(n,m_\mathrm{l})}\tilde{R}\right) = 0 \Rightarrow E_{(\mathrm{n,m_l})} = \frac{\hbar^2 k^2_{(\mathrm{n,m_l})}}{2m} = \frac{\hbar^2}{2m\tilde{R}^2} z^2_{(\mathrm{n,m_l})}. \tag{A.7}$$

Here n is the n-th zero of the Bessel function. The states and their energy can now be labeled by the two integer quantum numbers (n,m_l). Now that the solutions and energies of the Schrödinger equation are known, one can compute $|\psi|^2$ which is equivalent to $\rho_\mathrm{s}(E)$ in Sec. 1.1. The dependence of θ in $Y_{\mathrm{m_l}}(\theta)$ is purely imaginary, which means that it vanishes when the square of the absolute value is taken. The first six solutions are illustrated in Fig. 1.8.

For the chosen form of the potential well, no θ-dependence is observed. However, a modulation can occur when the shape of the box deviates from a cylinder. In this case, standing wave patterns possessing the symmetry of the border are generated.

Note that the quantum number m_l is linked to $\hat{L}$ (in polar coordinates) via:

$$\begin{aligned} \hat{L}Y_{\mathrm{m_l}}(\theta) &= \frac{\hbar}{i}\frac{\partial}{\partial\theta}Y_{\mathrm{m_l}}(\theta) \\ &= \hbar m_\mathrm{l} Y_{\mathrm{m_l}}(\theta). \end{aligned} \tag{A.8}$$

This leads to the consequence that states with higher $|m_\mathrm{l}|$ have a higher angular momentum, a statement which can be seen in Fig. 1.8: The density moves to the rim with increasing m_l, while at $m_\mathrm{l} = 0$ most of the density is located in the middle of the circle.

Confinement Energies: $r \to \infty$

The cylindrically-symmetric theory described in Sec. 1.7 evolves as follows if the radius goes to infinity:

We look at the energy of the eigenstates in the cylindrically-symmetric model. These are given by

$$E_{m,l}^{(n)} = E_0^{(n)} + \left(\hbar^2 \cdot \pi/2\right) \cdot \frac{z_{m,l}^2}{(A \cdot m^*)} \tag{A.9}$$

For the momentum $k_{m,l}$, we have the condition:

$$\begin{aligned} k_{m,l} \cdot r &= z_{m,l} && \text{(A.10)} \\ k_{m,l} \cdot \sqrt{A/\pi} &= z_{m,l} && \text{(A.11)} \end{aligned}$$

Inserting this in the equation for the eigenstates yields:

$$\begin{aligned} E_{m,l}^{(n)} &= E_0^{(n)} + \left(\hbar^2\pi/2\right) \cdot \left(k_{m,l} \cdot \sqrt{A/\pi}\right)^2 /(A \cdot m^*) && \text{(A.12)} \\ &= E_0^{(n)} + \left(\hbar^2\pi/2\right) \cdot k_{m,l}^2 \cdot A/\left(A \cdot \pi \cdot m^*\right) && \text{(A.13)} \\ &= E_0^{(n)} + \hbar^2 \cdot k_{m,l}^2/(2 \cdot m^*) && \text{(A.14)} \end{aligned}$$

This is the well-known dispersion relation for a free electron with effective mass m^* and an energy offset $E_0^{(n)}$. The size of the island does not enter this equation explicitly; it is also valid when the radius goes to infinity. Now we take a look at the allowed values for $k_{m,l}$ in this case. The condition above ($k_{m,l} \cdot r = z_{m,l}$) does allow all possible values when r goes to infinity. Formally this can be seen as follows: We select a momentum k' and ask whether it fulfills the condition. For large m, the zero of the Bessel function J_0 can be approximated by $z_{m,l} = (m - \frac{1}{4}) \cdot \pi$ [253]. We now look at an island with radius
$r = m \cdot \frac{\pi}{k'}$
Then we have:

$$\begin{aligned} k_{m,l} &= \frac{z_{m,l}}{r} && \text{(A.15)} \\ &= \left(m - \frac{1}{4}\right) \cdot \frac{\pi}{\left(m \cdot \frac{\pi}{k'}\right)} && \text{(A.16)} \\ &= \left(m - \frac{1}{4}\right) \cdot \frac{k'}{m} && \text{(A.17)} \\ &= k' - \frac{k'}{4 \cdot m} && \text{(A.18)} \end{aligned}$$

We now look at the case when m goes to infinity (and thus r goes to infinity) and find:
$k_{m,l} = k'$
This proves that for an infinitely large islands all values of $k_{m,l}$ are allowed. Together with the relation for the energy we thus have a continuum of states with the dispersion relation of the free electron.

A.2 Dirac Electron Confinement on Graphene Quantum Dots

For the sake of completeness, Fig. A.1 shows the same spectra as in Fig. 6.4 (c) and (d) before the contrast enhancement by derivation.

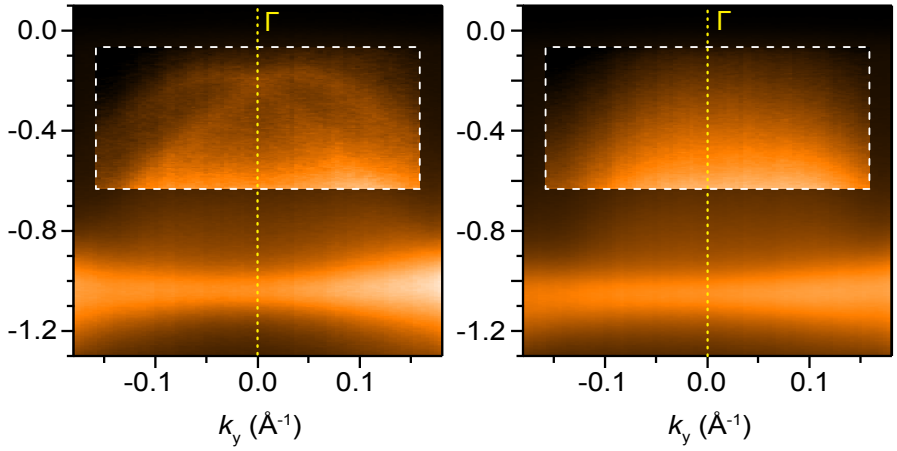

Figure A.1: ARPES spectra of gr/Ir(111) (left) and gr/O/Ir(111) (right) at the K-point acquired in the direction perpendicular to ΓK. Contrast was enhanced inside dashed rectangles in order to optimize the visibility of iridium surface state S_0.

A.3 A Quantum Corral Without a Fence

Bessel Zeroes and Rayleigh's Formula

Table A.1: First mth zeroes $z_{m,l}$ of the lth order Bessel functions of the first kind.

	$m = 1$	$m = 2$	$m = 3$
$l = 0$	2.405	5.520	8.654
$l = 1$	3.832	7.016	8.536
$l = 2$	5.136	8.417	9.969

Starting from the wave equation in spherical coordinates, this problem has a separable solution. The spherical Bessel functions of the first kind belong to the solutions of the radial part (see Sec. A.1). Represented by Rayleigh's Formula [254] they are given by

$$J_l(x) = (x)^l \left(-\frac{1}{x}\frac{d}{dx} \right)^l \frac{sin(x)}{x} \tag{A.19}$$

the first mth zeroes $z_{m,l}$ of the lth order Bessel functions of the first kind are given in Tab. A.1. Further zeroes are provided in Ref. [207].

APPENDIX B

Technical Details on Scanning Tunneling Spectroscopy

Connecting the Lock-In Amplifier (Stanford Research Systems SR830 DSP) with the Createc Electronics

Modulation of Bias Voltage

Establish the following BNC connections:

1. Monitor ADC0 (Createc) - Signal Input A/I (SR830)
2. ADC1 - CH1 Output
3. Mod. In (Createc electronics) - SINE OUT (Lock-in)

Modulation of z-Voltage

1. Monitor DAC0 (Createc electronics) - Signal Input A/I (SR830)
2. ADC1 - CH1 Output
3. z-Mod (HV amplifier) - SINE OUT (Lock-in)

B.1 Preparing a Spectroscopy Measurement

Involved instruments: Createc PSTMAFM software, Createc electronics, SR830 DSP lock-in amplifier. The basics of lock-in amplifying are extensively described in the operating manual of the SR830 Lock-In amplifier.

Time Spectrum

Take a time spectrum (Createc PSTMAFM). Ensure that there is an appropriate background of noise (in the order of 10^{-4} while in contact, 10^{-5} out of contact). If it is not sufficient, prepare the tip. Mechanical, electrical and tip effects are assigned to certain bands in the time spectrum. Find an appropriate modulation frequency in a band of lowest noise in the time spectrum. Typically different ranges in the spectrum are assigned to mechanically or electronic vibrations: 0-1.000 Hz are typically assigned to mechanic vibrations (300-1.000 Hz: e.g. bad sample fixation; 150-300 Hz boiling of LHe/LN2, in connection with increased liquid gas consumption; frequencies 1.000-2.000 Hz are associated with tip vibrations and might improve under tip forming [255]). Electronic noise is difficult to detect as considering special frequency ranges (despite from multiples of net frequency 50 Hz of course), but persists out of tunneling contact. A realtime analysis of the mechanical noise spectrum can be achieved by the use of a device named geophone which is based on the voltage induced by a relative movement of a coil to a permanent magnet. The geophone output can be recorded by one of the STM electronics DAC input connectors. Problems in the interpretation of the time spectrum are often induced by a lack of sample surface quality. Adsorbates from the surface might be gathered by the tip, showing vibrations in the spectrum. Other possibilities of noise analysis are provided by observing the tunneling current in open feedback mode and by measuring $I(z)$ curves. While the first provides obvious qualitative insight into noise problems, the latter can be used to determine the quality of the tunneling connection by expecting I to vary by approximately one order of magnitude while retracting the tip 1 nm in a *reliable* way in multiple subsequent spectra.

Preferences of the Lock-in Amplifier

Pull back the STM tip by setting the tunneling current to $I = 0$ A. Switch the modulation to ON (Createc Electronics). Now configure the Lock-In: Press *Freq* and choose a modulation frequency in the range of $500 - 1400$ Hz. The right choice is a frequency which respects

the results of the time spectrum (mentioned above) and is maximally odd: e.g. 833.1 Hz. This prevents the mod frequency from being a multiple of an external noise frequency in the system (e.g. power line frequency 50 Hz) and thus causing resonances. Please mind the bandwidth of the preamplifier, e.g. Femto DLPCA-200 has a bandwidth of 1.1 kHz in 10^9 gain mode. This means that all *mod* frequencies higher than 1.1 kHz experience a strong signal damping and thus provide only a low $\mathrm{d}I/\mathrm{d}V$ signal.

Press *Ampl* and choose a modulation amplitude in the range of 4 to 30 mV. Low amplitudes require a low noise level but have the best energy resolution! Ensure that there are appropriate values in the *TIME CONSTANT* field of the Lock-in: Typical values are 10 or 30 ms and 12 dB (filter slope, acts like a kind of input gain). Then press *AUTO Gain*. If there is an overload detected in the *Sensitivity* field, lower the Sensitivity value manually. Then press *AUTO Phase* in order to eliminate the phase difference between the input and the reference signal (this maximizes the lock-in output signal). Due to the voltage modulation oscillations of the current exist there, even without being in tunneling contact. These oscillations are caused by capacitive effects in the lines. In order to get rid of these artifacts, press $-90°$. Finally press *AUTO Reserve*.

Restore the tunneling contact by slowly increasing the tunneling current. The phase relation (displayed on channel two) should be rather stable. If this is not the case either the feedback loop still reacts too fast or the tip is in a bad condition.

B.2 Point Spectroscopy

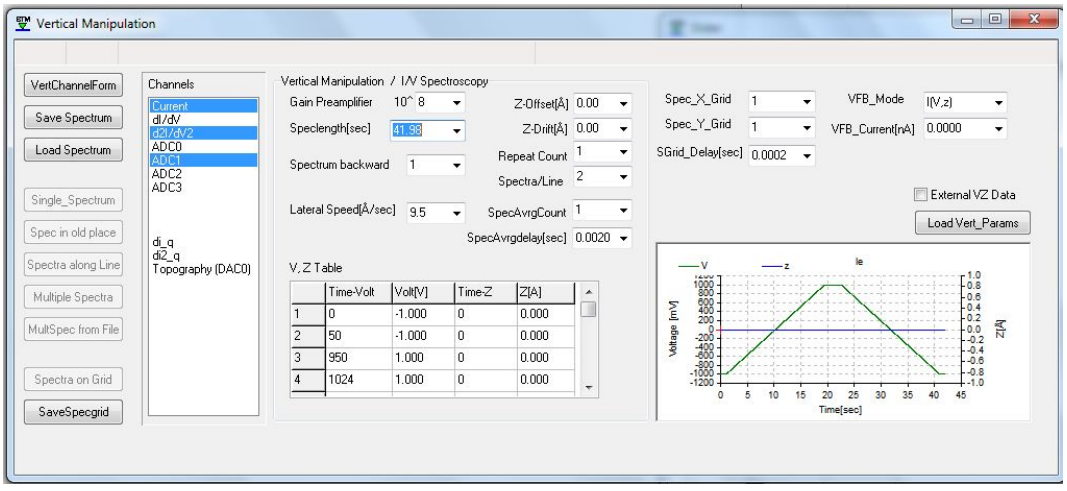

Figure B.1: Vertical Manipulation (VM) menu of the PSTMAFM software.

Point spectra are measured via the *VM mode* (vertical manipulation) of the PSTMAFM software. They require a related topography STM image to be saved in *.VERT* files. So first take a topography image, then measure a point spectrum at a desired position on the image:

1. Choose the spectroscopy mode: parameter *VFB Mode*, standard: $I(V,z)$.

2. Choose the *Speclength*[sec]: this defines the velocity of the variations (e.g. variation of bias voltage in *I(V)* mode).

3. Edit the *V,Z Table* (changes require a double click into a random parameter field to be saved, the saved table is visualized right next to it on the right).

4. Activate the appropriate channels: e.g. the Lock-in output is connected to *ADC1*, it is recommended to activate *Current*, *ADC1*.

5. Set the *Spectrum backward* value to 1.

6. Click on *VertChannelForm*, then select *ADC1* and right click on the plot area, select *Auto Update*.

7. Click on the desire type of spectrum (e.g. *Single Spectrum*).

8. Click on a position in the topography image.

I(V)

Switch *VFB Mode* to $I(V,z)$. Select a position in the topography image by clicking *Single Spectrum* and then clicking on a desired point in the image. The tip moves with the velocity *Lateral Speed*[A/sec] to the selected position (choose a low value to prevent the tip from changing its (orbital) shape on the way to it by interaction with the surface). For the same reason ensure that the feedback loop is sufficiently strong if you perform measurements on positions far away from the center of the first scanline (general resting position). Once arrived, the feedback loop stabilizes the tip position at this point with respect to the voltage and current values chosen in the *Slider* window (stabilization parameters, setpoint). Be aware of the fact that stabilization voltage and current (*Slider* window) define the tip distance and thus orbital overlap. Finally, the variation of the bias voltage according to the entries in the *V,Z Table* starts, with the feedback loop automatically switched off.

I(V) With Closed Feedback

Switch *VFB Mode* to *z(V)*. This mode is recommended when the measurement extends over a wide voltage range. Since the tunneling probability increases significantly with higher voltage, the current signal in open feedback mode quickly exceeds the preamplifier input range (at least in 10^9 and 10^8 gain modes). Closed feedback loop uses a constant current setpoint and thus avoids this problem. But at the same time the $\mathrm{d}I/\mathrm{d}V$ signal now is not only determined by the density of states of tip and sample and the increasing tunneling probability with higher voltage, but also by the varying tip/sample distance, which leads to further complication in data analysis, requiring a deconvolution of the signal and the z(U) influence. Therefore, the data set should always contain a *z(U)* channel. Nevertheless, *I(V)* closed feedback mode is the only way to measure e.g. image potential states. Please note that the shape of the spectra is influenced by the feedback parameters. Usually rather low values for Integrator (e.g. -15) and *P-Gain* (e.g. 15) (DSP flag in *Parameter* window) are best. Of course these values have to be adjusted to the present tunneling conditions.

I(z)

This mode is predestined for work function measurements. Switch *VFB Mode* to *I(V,z)*. In the *V,z Table* use constant voltage and an appropriate z ramp. Mind the fact that positive z-values mean moving towards the sample surface, negative values moving away. Last one is the way of choice for collecting data for work function measurements. Typical values are -3..-10Å.

z(V) and *dz/dV*

We use this mode for measuring image potential states (IPS, also called field emission resonances or Gundlach oscillations). $\mathrm{d}z/\mathrm{d}V$ means modulating the z piezo voltage. Of course this requires quite high modulation voltages, since otherwise the piezo will not react. Using this mode for IPS measurements gives a poor resolution compared to e.g. *I(V)* closed feedback mode.

Calculating the *Speclength* value

In order to ensure a sufficient period of integration, the speclength has to be chosen with respect to the Lock-in *TIME CONSTANT*. Period of integration per measuring point

should be at least one time constant. The number of measuring points is given by the highest *Time-Volt* value in the *V,Z Table*. Please note that the resolution is limited by the modulation voltage and the general noise level. Therefore, in order to prevent a waste of time, the number of measurement points should correspond to the expected resolution: E.g. measuring a voltage range of 1.000 mV with a resolution of 10 mV means that 128 measurement points are sufficient. A sufficient *speclength* in seconds is obtained by min. *speclength*=(*TIME CONSTANT*[ms])x(*Time Volts*)/1000.

Editing the *V,Z Table*

The *V,Z Table* provides two columns for two parameters varying during a spectroscopic measurement: voltage (*Volt[V]*) and distance z (*Z[A]*). *Volt[V]* is varied in the spectroscopy modes $I(V)$ and $z(V)$, *Z[A]* is varied in the mode $I(z)$. Both in the same measurement are usually only varied for tip preparation (discussed below). The time scale of the respective variations is given in units of measuring points (here called *Time-Volts*) which are of course related to time via the *speclength* value. A typical voltage ramp for a point spectrum is shown in the picture above (spectrum backward included). It is recommended to keep the voltage at a constant value for some measuring points in order to enable the feedback loop to stabilize the tip at the desired position in the image (same at maximum/minimum values).

B.3 Constant Energy $\mathrm{d}I/\mathrm{d}V$ Mapping

Constant Current Mode

This is the right mode in the case of the sample not being extremely flat (corrugation > 1 Å). At first perform the steps described above. Choosing the modulation frequency consider the following: On the one hand capacitive effects in general get worse with high modulation frequencies, on the other hand one would like to use a high frequency because it enables the system to perform $\mathrm{d}I/\mathrm{d}V$ maps with stronger feedback (and thus higher scanning speed, minimizing drift effects). An appropriate frequency range is the one mentioned above. Activate the channels *Topography*, *Current* and *ADC1* in *Parameter* window. Adjust the scanning speed in that way that you obtain once the lock-in time constant per pixel. This equals to ***Scanning Speed*** **[s/line] = (*pixels* in X direction)** $\times$ **(*TIME CONSTANT* [ms])/1000**. Choose low values for the feedback. This is

possible due to the low scanning speed and necessary to prevent the feedback from removing the modulation frequency from the signal.

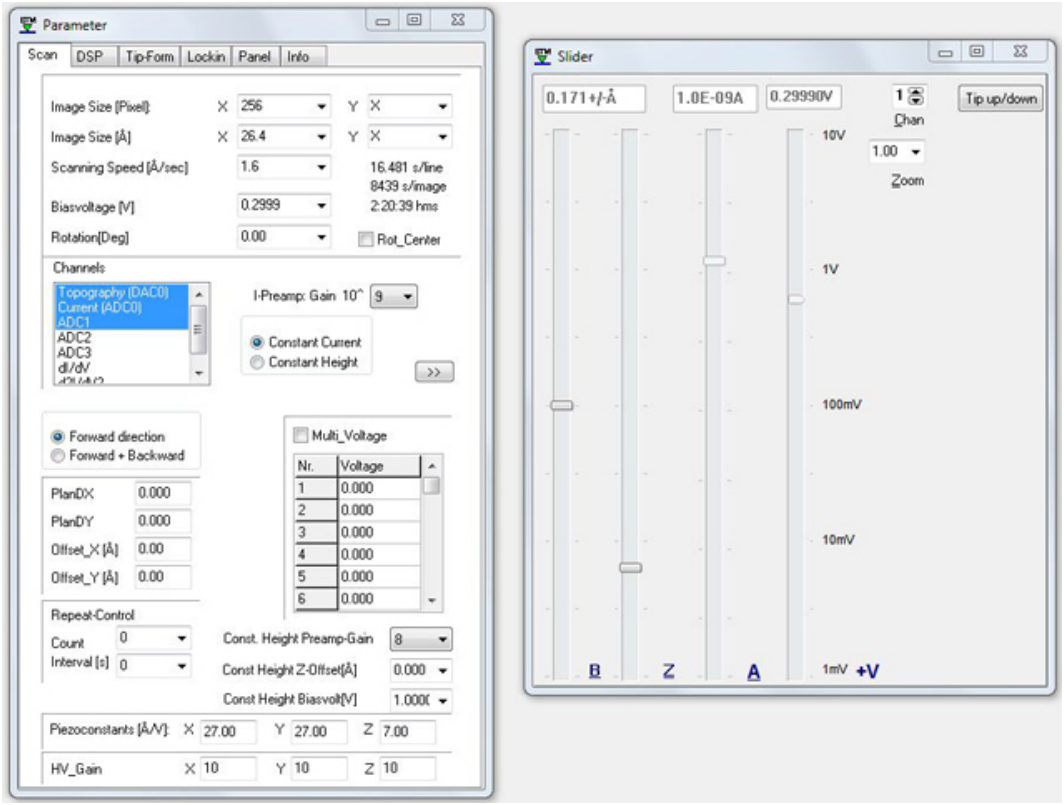

Figure B.2: *Parameter* and *Slider* menu of the *PSTMAFM* software.

Constant Height Mode

Subtract a plane on the structure to be measured by clicking *Pln* and selecting three points in the image. Save the plane by *DSP*, *Set Plan Dx Dy*. Choose the desired parameters in Parameter window, *Scan* flag for *Const. Height Preamp-Gain*, *Const Height Z-Offset* and *Const. Height Biasvolt*[V]. Finally switch to *Constant Height*. This mode can only be used on very flat surface regions (and therefore often small image sizes). Advantage: tip/surface distance is constant, therefore constant orbital overlap, signal only from LDOS variations.

Inelastic Electron Tunneling Spectroscopy

Inelastic Electron Tunneling Spectroscopy (IETS) requires the measurement of the $\mathrm{d}^2I/\mathrm{d}U^2$ signal via the second harmonic of the lock-in signal (chapter 1.1). Therefore, the *harm* button at the lock-in amplifier has to be pressed in order to switch to the value 2. In the

experiments described in the framework of this work, in addition the modulation frequency was reduced to about 300 Hz, the modulation amplitude increased to 20 mV. Up to now it remains unclear, whether this change in parameters was needed because of measuring the second harmonic or because of compensating for an unstable tip.

B.4 Tip Forming with Vertical Manipulation

The *VM* function can be used to perform sophisticated tip forming (in principle the tip forming mode is a simplified case of vertical manipulation). Especially VM mode can be used to carry out multiple tip forming cycles by choosing a certain value of *Repeat Count*. An example of a possible tip forming with 5 cycles is shown below. The entries read as follows: Tip lowers distance by 8 Å(positive z value!), with a 2 V pulse while moving back

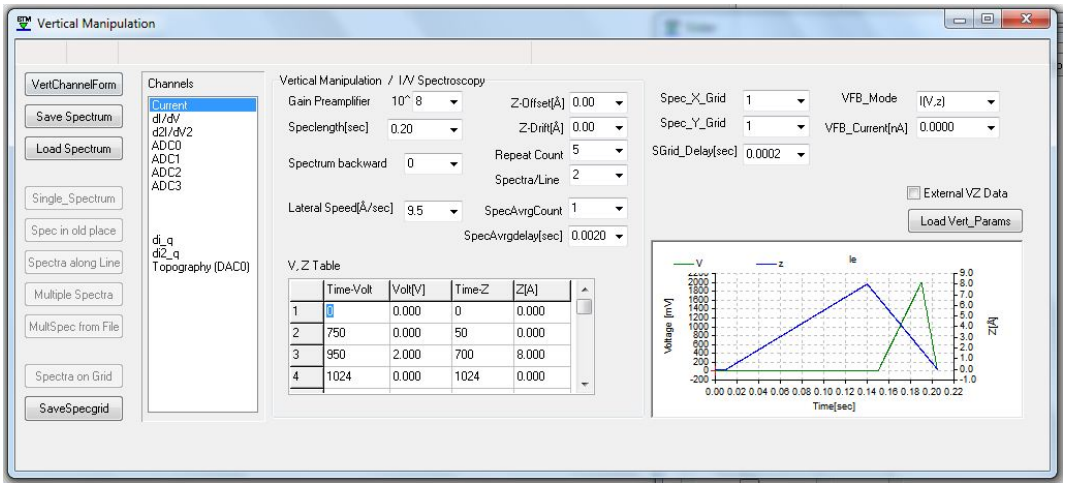

Figure B.3: Vertical Manipulation (VM) menu of the PSTMAFM software.

to the starting position. There are 5 cycles in total, with one cycle taking 0.2 s. In order to prevent the tip from dipping a lot of times (5 in the present example) into the same position, which might be contaminated with dirt blown off the tip during the first cycle, one can think about using the *Spectra along Line* mode of vertical manipulation. This will provide a clean point on the surface for each cycle.

B.5 dI/dV Energy Resolution

The resolution in energy is given by the modulation frequency and the noise level of the involved electronics' outputs and lines. Modulation frequency causes a ΔU of $\Delta U \simeq$

$2U_{mod} \cdot \sqrt{2}$. The signal quality can be improved by the use of a capacitor-input-filter (sometimes referred to as Pi-filter) at the Piezo voltage input connectors: The piezo signal DC voltages always have a small AC component on top as an artifact of HV amplification. This AC component might "talk" to the bias line and spoil the tunneling signal, which is observed as a severe peak broadening in $\mathrm{d}I/\mathrm{d}V$ spectra.

B.6 Problems and Solutions

1. Huge artifacts at start and end point of point spectra: In order to avoid artifacts of preamp switching after starting a spectrum, avoid different values of *Gain Preamplifier* in *VM* mode and *Parameter* menu.

2. **Never switch the modulation ON/OFF while being in tunneling contact (-> Tip Crash)!**

3. Avoid switching on the LHe level meter while in tunneling contact, this might cause a tip change.

APPENDIX C

Acknowledgments

- First I would like to thank **Priv.-Doz. Dr. Carsten Busse** for the opportunity and supervision of my PhD project. In any respect he provided support for technical solutions, planning of experiments and data analysis. Being always available for discussions, apart from numerous scientific topics he introduced me to the field of Fermi Questions on both physics and off-topic.

- I thank **Prof. Dr. Achim Rosch** for serving as a referee of this thesis, being always open for supporting our work with new ideas and teaching me the fundamentals of classical and quantum mechanics during my studies (in a way accessible even for an experimentalist). He also introduced me to graphene in an interesting advanced seminar.

- **Prof. Dr. Thomas Michely** served as my mentor in the BCGS for many years and evoked my interest for surface physics. He gave persistent support of my project with important contributions to both funding and scientific discussions.

- Many thanks to **Wouter Jolie** for his dedicated work on silver and oxygen intercalated graphene. With his efforts during his Master project he paved the way for vast parts of this thesis. I also appreciate his proof-reading efforts, really fruitful discussions and patient guidance through our skydrive data jungle. For a few months we even did not need skype for communication.

- I thank **Dr. Marko Kralj** at Institute za Fiziku for the hospitality during my stays in Zagreb and important input to my work. The latter includes the kick-off of our IPS measurements and important contributions concerning the suppression of metallic surface states. I really enjoyed the trips to Zagreb for measuring ARPES. Especially, I would like to thank **Marin Petrović** and **Iva Srŭt Rakić** for bidding

me welcome and even some really convenient transfers by car (also thanks to **Dr. Mario Rakić**!).

- Special thanks also to our collaborators **Dr. Nicolae Atodiresei**, **Dr. Vasile Caciuc** and **Prof. Dr. Stefan Blügel** from the Peter Grünberg Institut (PGI) and Institute for Advanced Simulation (IAS) at Forschungszentrum Jülich for supporting our research with superior DFT calculations.

- I thank **Prof. Dr. Iván Brihuega** at Universidad Autónoma de Madrid for providing me insight into the details of Scanning Tunneling Spectroscopy and the opportunity of a very interesting three-month stay in Madrid. In this context I also have to thank **Héctor Gonzáles Herrero** and **Bruno De La Torre Cerdeño** for sharing the lab.

- Futher thanks go to the **Bonn-Cologne Graduate School of Physics and Astronomy**, in person **Dr. Petra Neubauer-Günther** and **Dr. Dietmar Weil**, for regular financial support, interesting workshops and funding trips to stimulating conferences like the DPG Spring Meeting 2011, the Capri Spring School on Topological Insulators and especially my visit to the group of Prof. Dr. Iván Brihuega at Universidad Autónoma de Madrid. In this context I thank **Prof. Dr. Hans Kroha** and **Prof. Dr. Moritz Sokolowski** at the University of Bonn for advising my work as mentors during my diploma thesis and PhD project, respectively.

- Special thanks in alphabetical order go to my friends and (former) colleagues **Dr. Jürgen Klinkhammer**, **Dr. Sven Runte** and **Dr. Sebastian Standop** for many discussions, pleasant and efficient teamwork in the LT-STM lab, a really nice atmosphere in the office, proof-reading, table soccer training,... Particularly, I thank Sven for introducing me to a decent work attitude in the lab and Festo to our setup.

- **Ulrike Schröder** and **Dr. Timm Gerber** introduced me to the process of oxygen intercalation, thus enabling important prerequisites for my work.

- **Dr. Antonio Martínez Galera** gave me a warm welcome in Madrid and now, as a Post-Doc in our group, contributed to the understanding of new oxygen superstructures on iridium under graphene.

- I thank **Christoph Boguschewski** for the Python script which he developed during his Bachelor thesis and was frequently used for the work presented in this thesis.

Furthermore I would like to thank all remaining members of our group for the always pleasant atmosphere and fruitful discussions.
Last but not least I thank my family for paving my way and perpetual support in any respect. In particular I thank my **parents** for proof-reading the whole thesis. Especially I thank my wife **Anne** for persistent support, never complaining about me spending hours in front of the PC and always keeping my knowledge on school physics up to date with new projects and experiments (turning our living room into a home lab).

APPENDIX D

Bibliography

[1] W. Jolie, F. Craes, M. Petrović, N. Atodiresei, V. Caciuc, S. Blügel, M. Kralj, T. Michely, and C. Busse: "Dirac Electron Confinement on Graphene Quantum Dots". *Physical Review B* **accepted** (2014). (Cit. on pp. iii, 5, 18, 20, 28, 91, 93, 97, 134, 145, 199).

[2] F. Craes, S. Runte, J. Klinkhammer, M. Kralj, T. Michely, and C. Busse: "Mapping Image Potential States on Graphene Quantum Dots". *Phys. Rev. Lett.* **111** (5 2013), 056804. DOI: 10.1103/PhysRevLett.111.056804. (Cit. on pp. iii, 5, 28, 34, 79, 82, 105, 109, 145, 146, 199).

[3] F. Jona, J. A. Strozier Jr, and W. S. Yang: "Low-energy electron diffraction for surface structure analysis". *Reports on Progress in Physics* **45.5** (1982), 527. (Cit. on p. v).

[4] A. Geim and I. Grigorieva: "Van der Waals heterostructures". *Nature* **499.7459** (2013), 419–425. (Cit. on pp. 3, 126).

[5] K. von Klitzing, G. Dorda, and M. Pepper: "New method for high-accuracy determination of the fine-structure constant based on quantized Hall resistance". *Phys. Rev. Lett.* **45.6** (1980), 494–497. (Cit. on p. 3).

[6] J. G. Bednorz and K. A. Müller: "Possible high T_c superconductivity in the Ba- La- Cu- O system". *Zeitschrift für Physik B Condensed Matter* **64.2** (1986), 189–193. (Cit. on p. 3).

[7] Y. Kamihara, T. Watanabe, M. Hirano, and H. Hosono: "Iron-Based Layered Superconductor La $[O_{1-x}$ $F_x]$ FeAs (x= 0.05-0.12) with $T_c = 26$ K". *Journal of the American Chemical Society* **130.11** (2008), 3296–3297. (Cit. on p. 3).

[8] M. Z. Hasan and C. L. Kane: "Colloquium: Topological insulators". *Rev. Mod. Phys.* **82** (4 Nov. 2010), 3045–3067. DOI: 10.1103/RevModPhys.82.3045. (Cit. on pp. 3, 16).

[9] A. H. Castro Neto, F. Guinea, N. M. R. Peres, K. S. Novoselov, and A. K. Geim: "The electronic properties of graphene". *Rev. Mod. Phys.* **81.1** (Jan. 2009), 109–162. DOI: 10.1103/RevModPhys.81.109. (Cit. on pp. 3, 14, 15, 82, 128).

[10] A. K. Geim and K. S. Novoselov: "The rise of graphene". *Nature Materials* **6.3** (Mar. 2007), 183–191. DOI: 10.1038/nmat1849. (Cit. on pp. 3, 14, 15).

[11] M. D. Stoller, S. Park, Y. Zhu, J. An, and R. S. Ruoff: "Graphene-Based Ultracapacitors". *Nano Letters* **8.10** (2008). PMID: 18788793, 3498–3502. DOI: 10.1021/nl802558y. (Cit. on p. 3).

[12] A. A. Balandin, S. Ghosh, W. Bao, I. Calizo, D. Teweldebrhan, F. Miao, and C. N. Lau: "Superior thermal conductivity of single-layer graphene". *Nano Letters* **8.3** (2008), 902–907. (Cit. on p. 3).

[13] X. Wang, L. Zhi, and K. Müllen: "Transparent, conductive graphene electrodes for dye-sensitized solar cells". *Nano Letters* **8.1** (2008), 323–327. (Cit. on p. 3).

[14] K. S. Kim, Y. Zhao, H. Jang, S. Y. Lee, J. M. Kim, K. S. Kim, J.-H. Ahn, P. Kim, J.-Y. Choi, and B. H. Hong: "Large-scale pattern growth of graphene films for stretchable transparent electrodes". *Nature* **457.7230** (2009), 706–710. (Cit. on p. 3).

[15] C. Lee, X. Wei, J. W. Kysar, and J. Hone: "Measurement of the elastic properties and intrinsic strength of monolayer graphene". *Science* **321.5887** (2008), 385–388. (Cit. on p. 3).

[16] K. S. Novoselov, A. K. Geim, S. V. Morozov, D. Jiang, M. I. Katsnelson, I. Grigorieva, S. V. Dubonos, and A. A. Firsov: "Two-dimensional gas of massless Dirac fermions in graphene". *Nature* **438.7065** (2005), 197–200. (Cit. on p. 3).

[17] C. Busse, P. Lazić, R. Djemour, J. Coraux, T. Gerber, N. Atodiresei, V. Caciuc, R. Brako, A. T. N'Diaye, S. Blügel, J. Zegenhagen, and T. Michely: "Graphene on Ir(111): Physisorption with Chemical Modulation". *Phys. Rev. Lett.* **107** (3 July 2011), 036101. DOI: 10.1103/PhysRevLett.107.036101. (Cit. on pp. 3, 16–18, 102, 103, 129).

[18] A. K. Geim: "Nobel lecture: random walk to graphene". *Reviews of Modern Physics* **83.3** (2011), 851. (Cit. on p. 3).

[19] S. Morozov, K. Novoselov, M. Katsnelson, F Schedin, D. Elias, J. Jaszczak, and A. Geim: "Giant intrinsic carrier mobilities in graphene and its bilayer". *Physical Review Letters* **100.1** (2008), 016602. (Cit. on p. 3).

[20] V. W. Brar, Y. Zhang, Y. Yayon, T. Ohta, J. L. McChesney, A. Bostwick, E. Rotenberg, K. Horn, and M. F. Crommie: "Scanning tunneling spectroscopy of inhomogeneous electronic structure in monolayer and bilayer graphene on SiC". *Appl. Phys. Lett.* **91** (2007), 122102. DOI: 10.1063/1.2771084. (Cit. on pp. 3, 15, 34, 92).

[21] B. Trauzettel, D. V. Bulaev, D. Loss, and G. Burkard: "Spin qubits in graphene quantum dots". *Nat. Phys.* **3.3** (2007), 192. DOI: 10.1038/nphys544. (Cit. on pp. 3, 29).

[22] K. Nakada, M. Fujita, G. Dresselhaus, and M. S. Dresselhaus: "Edge state in graphene ribbons: Nanometer size effect and edge shape dependence". *Phys. Rev. B* **54** (24 1996), 17954–17961. DOI: 10.1103/PhysRevB.54.17954. (Cit. on p. 3).

[23] C. W. J. Beenakker: "Colloquium: Andreev reflection and Klein tunneling in graphene". *Rev. Mod. Phys.* **80** (4 2008), 1337–1354. DOI: 10.1103/RevModPhys.80.1337. (Cit. on pp. 3, 15).

[24] K. S. Novoselov, A. K. Geim, S. V. Morozov, D. Jiang, Y. Zhang, S. V. Dubonos, I. V. Grigorieva, and A. A. Firsov: "Electric Field Effect in Atomically Thin Carbon Films". *Science* **306** (2004), 666. DOI: 10.1126/science.1102896. (Cit. on p. 3).

[25] V. Nicolosi, M. Chhowalla, M. G. Kanatzidis, M. S. Strano, and J. N. Coleman: "Liquid Exfoliation of Layered Materials". *Science* **340.6139** (2013). DOI: 10.1126/science.1226419. (Cit. on p. 3).

[26] C. Busse: "Graphene on metal surfaces". habilitation dissertation. Universität zu Köln, 2011 (cit. on pp. 3, 15–18, 20).

[27] S. Marchini, S. Günther, and J. Wintterlin: "Scanning tunneling microscopy of graphene on Ru(0001)". *Phys. Rev. B* **76** (7 Aug. 2007), 075429. DOI: 10.1103/PhysRevB.76.075429. (Cit. on pp. 3, 16).

[28] T. Ohta, F. E. Gabaly, A. Bostwick, J. L. McChesney, K. V. Emtsev, A. K. Schmid, T. Seyller, K. Horn, and E. Rotenberg: "Morphology of graphene thin film growth on SiC(0001)". *New J. Phys.* **10.2** (2008), 023034. DOI: 10.1088/1367-2630/10/2/023034. (Cit. on p. 3).

[29] J. Coraux, A. T. N'Diaye, M. Engler, C. Busse, D. Wall, N. Buckanie, F.-J. M. zu Heringdorf, R. van Gastel, B. Poelsema, and T. Michely: "Growth of graphene on Ir(111)". *New Journal of Physics* **11.2** (2009), 023006. (Cit. on pp. 3, 43, 45, 46, 97, 113).

[30] K. V. Emtsev, A. Bostwick, K. Horn, J. Jobst, G. L. Kellogg, L. Ley, J. L. McChesney, T. Ohta, S. A. Reshanov, J. Röhrl, E. Rotenberg, A. K. Schmid, D. Waldmann, H. B. Weber, and T. Seyller: "Towards wafer-size graphene layers by atmospheric pressure graphitization of silicon carbide". *Nature Materials* **8.3** (2009), 203–207. DOI: 10.1038/nmat2382. (Cit. on pp. 3, 4).

[31] J. Coraux, A. T. N'Diaye, C. Busse, and T. Michely: "Structural Coherency of Graphene on Ir(111)". *Nano Lett.* **8.2** (2008), 565. DOI: 10.1021/nl0728874. (Cit. on p. 3).

[32] A. J. Martínez-Galera, I. Brihuega, and J. M. Gómez-Rodríguez: "Ethylene Irradiation: A New Route to Grow Graphene on Low Reactivity Metals". *Nano Letters* **11.9** (2011), 3576–3580. DOI: 10.1021/nl201281m. (Cit. on p. 4).

[33] X. Li, W. Cai, J. An, S. Kim, J. Nah, D. Yang, R. Piner, A. Velamakanni, I. Jung, E. Tutuc, S. K. Banerjee, L. Colombo, and R. S. Ruoff: "Large-Area Synthesis of High-Quality and Uniform Graphene Films on Copper Foils". *Science* **324.5932** (2009), 1312–1314. DOI: 10.1126/science.1171245. (Cit. on p. 4).

[34] S. Bae, H. Kim, Y. Lee, X. Xu, J.-S. Park, Y. Zheng, J. Balakrishnan, T. Lei, H. R. Kim, Y. I. Song, Y.-J. Kim, K. S. Kim, B. Özyilmaz, J.-H. Ahn, B. H. Hong, and S. Iijima: "Roll-to-roll production of 30-inch graphene films for transparent electrodes". *Nature Nanotechnology* **5.8** (2010), 574–578. DOI: 10.1038/nnano.2010.132. (Cit. on p. 4).

[35] P. X.-L. Feng: "Nanoelectromechanical systems: Tuning in to a graphene oscillator". *Nature Nanotechnology* **8.12** (2013), 897–898. DOI: 10.1038/nnano.2013.268. (Cit. on p. 4).

[36] F. Schedin, A. K. Geim, S. V. Morozov, E. W. Hill, P. Blake, M. I. Katsnelson, and K. S. Novoselov: "Detection of individual gas molecules adsorbed on graphene". *Nature materials* **6.9** (2007), 652–655. (Cit. on p. 4).

[37] R. Arsat, M. Breedon, M. Shafiei, P. Spizziri, S. Gilje, R. Kaner, K. Kalantar-zadeh, and W. Wlodarski: "Graphene-like nano-sheets for surface acoustic wave gas sensor applications". *Chemical Physics Letters* **467.4** (2009), 344–347. (Cit. on p. 4).

[38] L. Gomez De Arco, Y. Zhang, C. W. Schlenker, K. Ryu, M. E. Thompson, and C. Zhou: "Continuous, highly flexible, and transparent graphene films by chemical vapor deposition for organic photovoltaics". *ACS nano* **4.5** (2010), 2865–2873. (Cit. on p. 4).

[39] Y. Wang, Z. Shi, Y. Huang, Y. Ma, C. Wang, M. Chen, and Y. Chen: "Supercapacitor devices based on graphene materials". *The Journal of Physical Chemistry C* **113.30** (2009), 13103–13107. (Cit. on p. 4).

[40] Y.-M. Lin, K. A. Jenkins, A. Valdes-Garcia, J. P. Small, D. B. Farmer, and P. Avouris: "Operation of graphene transistors at gigahertz frequencies". *Nano Letters* **9.1** (2008), 422–426. (Cit. on p. 4).

[41] M. S. Fuhrer: "Critical Mass in Graphene". *Science* **340.6139** (2013), 1413–1414. DOI: 10.1126/science.1240317. (Cit. on pp. 4, 16).

[42] B. Hunt, J. D. Sanchez-Yamagishi, A. F. Young, M. Yankowitz, B. J. LeRoy, K. Watanabe, T. Taniguchi, P. Moon, M. Koshino, P. Jarillo-Herrero, and R. C. Ashoori: "Massive Dirac Fermions and Hofstadter Butterfly in a van der Waals Heterostructure". *Science* **340.6139** (2013), 1427–1430. DOI: 10.1126/science.1237240. (Cit. on pp. 4, 16).

[43] Y.-M. Lin, K. A. Jenkins, A. Valdes-Garcia, J. P. Small, D. B. Farmer, and P. Avouris: "Operation of Graphene Transistors at Gigahertz Frequencies". *Nano Letters* **9.1** (2009), 422–426. DOI: 10.1021/nl803316h. (Cit. on p. 4).

[44] F. Xia, T. Mueller, Y.-M. Lin, A. Valdes-Garcia, and P. Avouris: "Ultrafast graphene photodetector". *Nature Nanotechnology* **4.12** (2009), 839–843. (Cit. on p. 4).

[45] P. Blake, P. D. Brimicombe, R. R. Nair, T. J. Booth, D. Jiang, F. Schedin, L. A. Ponomarenko, S. V. Morozov, H. F. Gleeson, E. W. Hill, A. K. Geim, and K. S. Novoselov: "Graphene-Based Liquid Crystal Device". *Nano Letters* **8.6** (2008). PMID: 18444691, 1704–1708. DOI: 10.1021/nl080649i. (Cit. on p. 4).

[46] C. R. Dean, A. F. Young, I. Meric, C. Lee, L. Wang, S. Sorgenfrei, K. Watanabe, T. Taniguchi, P. Kim, K. L. Shepard, and J. Hone: "Boron nitride substrates for high-quality graphene electronics". *Nature Nanotechnology* **5.10** (2010), 722–726. DOI: 10.1038/nnano.2010.172. (Cit. on p. 4).

[47] R. Larciprete, S. Ulstrup, P. Lacovig, M. Dalmiglio, M. Bianchi, F. Mazzola, L. Hornekær, F. Orlando, A. Baraldi, P. Hofmann, and S. Lizzit: "Oxygen Switching of the Epitaxial Graphene-Metal Interaction". *ACS Nano* **6** (2012), 9551–9558. DOI: 10.1021/nn302729j. (Cit. on pp. 4, 19, 20, 75, 94, 97, 101, 105, 113, 124).

[48] M. Hasegawa, K. Nishidate, T. Hosokai, and N. Yoshimoto: "Electronic-structure modification of graphene on Ni(111) surface by the intercalation of a noble metal". *Phys. Rev. B* **87** (8 2013), 085439. DOI: 10.1103/PhysRevB.87.085439. (Cit. on pp. 4, 16, 20, 63).

[49] S. Schumacher, D. F. Förster, M. Rösner, T. O. Wehling, and T. Michely: "Strain in Epitaxial Graphene Visualized by Intercalation". *Phys. Rev. Lett.* **110** (8 2013), 086111. DOI: 10.1103/PhysRevLett.110.086111. (Cit. on pp. 4, 19).

[50] S. Schumacher, T. O. Wehling, P. Lazić, S. Runte, D. F. Förster, C. Busse, M. Petrović, M. Kralj, S. Blügel, N. Atodiresei, V. Caciuc, and T. Michely: "The Backside of Graphene: Manipulating Adsorption by Intercalation". *Nano Letters* **13.11** (2013), 5013–5019. DOI: 10.1021/nl402797j. (Cit. on pp. 4, 19).

[51] E. Grånäs, J. Knudsen, U. A. Schröder, T. Gerber, C. Busse, M. A. Arman, K. Schulte, J. N. Andersen, and T. Michely: "Oxygen Intercalation under Graphene on Ir(111): Energetics, Kinetics, and the Role of Graphene Edges". *ACS Nano* **6** (2012), 9951–9963. DOI: 10.1021/nn303548z. (Cit. on pp. 4, 19, 20, 46, 73, 75, 94, 97, 99, 113, 122, 124).

[52] W. Jolie, F. Craes, T. Michely, and C. Busse: "Tuning the Electronic Properties of Graphene Quantum Dots with Silver". *in preparation* (2014). (Cit. on pp. 4, 53, 199).

[53] M. Petrović, I. Šrut-Rakić, S. Runte, C. Busse, J. Sadowski, P. Lazić, I Pletikosić, Z.-H. Pan, M. Milun, P. Pervan, et al.: "The mechanism of caesium intercalation of graphene". *Nat. Comm.* **4** (2013). (Cit. on p. 4).

[54] C. Riedl, C. Coletti, T. Iwasaki, A. A. Zakharov, and U. Starke: "Quasi-free-standing epitaxial graphene on SiC obtained by hydrogen intercalation". *Physical review letters* **103.24** (2009), 246804. (Cit. on p. 4).

[55] A. Grüneis and D. V. Vyalikh: "Tunable hybridization between electronic states of graphene and a metal surface". *Phys. Rev. B* **77** (19 2008), 193401. DOI: 10.1103/PhysRevB.77.193401. (Cit. on p. 4).

[56] C. Herbig, M. Kaiser, N. Bendiab, S. Schumacher, D. F. Förster, J. Coraux, K. Meerholz, T. Michely, and C. Busse: "Mechanical exfoliation of epitaxial graphene on Ir(111) enabled by Br_2 intercalation". *Journal of Physics: Condensed Matter* **24.31** (2012), 314208. (Cit. on pp. 4, 19).

[57] C. J. Chen: *Introduction to Scanning Tunneling Microscopy*. Oxford University Press, 2007 (cit. on pp. 8, 23).

[58] G. Binnig, H. Rohrer, C. Gerber, and E. Weibel: "7 × 7 Reconstruction on Si(111) Resolved in Real Space". *Phys. Rev. Lett.* **50.2** (1983), 120. DOI: 10.1103/PhysRevLett.50.120. (Cit. on p. 8).

[59] K. Oura, V. Lifshits, A. Saranin, A. Zotov, and M. Katayama: *Surface science: an introduction (Advanced texts in physics)*. Springer-Verlag Berlin, Heidelberg, 2003 (cit. on pp. 8, 13, 22, 64).

[60] J. Bardeen: "Tunnelling from a many-particle point of view". *Phys. Rev. Lett.* **6.2** (1961), 57–59. (Cit. on p. 8).

[61] J. Tersoff and D. Hamann: "Theory of the scanning tunneling microscope". *Phys. Rev. B* **31.2** (1985), 805–813. (Cit. on pp. 8, 10, 33).

[62] R. M. Feenstra, J. Stroscio, and A. P. Fein: "Tunneling spectroscopy of the Si(111) 2×1 surface". *Surf. Sci.* **181.1-2** (1987), 295–306. (Cit. on p. 10).

[63] M. A. Reed: "Inelastic electron tunneling spectroscopy". *Materials Today* **11.11** (2008), 46 –50. DOI: http://dx.doi.org/10.1016/S1369-7021(08)70238-4. (Cit. on pp. 10, 11).

[64] R. Temirov: "Studying Complex Metal Molecule Interface with Low Temperature Scanning Tunneling Microscope: From Electronic Structure to Charge Transport". dissertation. Jacobs University Bremen, 2008 (cit. on p. 10).

[65] G. Kichin, C. Wagner, F. S. Tautz, and R. Temirov: "Calibrating atomic-scale force sensors installed at the tip apex of a scanning tunneling microscope". *Phys. Rev. B* **87** (8 2013), 081408. DOI: 10.1103/PhysRevB.87.081408. (Cit. on p. 11).

[66] M. Bode: "Spin-polarized scanning tunnelling microscopy". *Reports on Progress in Physics* **66.4** (2003), 523. (Cit. on p. 11).

[67] M. Morgenstern: "Probing the local density states of dilute electron systems in different dimensions". *Surface Review and Letters* **10.06** (2003), 933–962. DOI: 10.1142/S0218625X0300575X. (Cit. on pp. 11, 113).

[68] B. N. J. Persson and A. Baratoff: "Inelastic electron tunneling from a metal tip: The contribution from resonant processes". *Phys. Rev. Lett.* **59** (3 1987), 339–342. DOI: 10.1103/PhysRevLett.59.339. (Cit. on pp. 11, 12).

[69] C. Jia and X. Guo: "Molecule-electrode interfaces in molecular electronic devices". *Chem. Soc. Rev.* **42** (13 2013), 5642–5660. DOI: 10.1039/C3CS35527F. (Cit. on pp. 11, 12).

[70] J. Langan and P. Hansma: "Can the concentration of surface species be measured with inelastic electron tunneling?" *Surface Science* **52.1** (1975), 211 –216. DOI: http://dx.doi.org/10.1016/0039-6028(75)90020-5. (Cit. on p. 11).

[71] M. Galperin, M. A. Ratner, and A. Nitzan: "Inelastic electron tunneling spectroscopy in molecular junctions: Peaks and dips". *The Journal of Chemical Physics* **121.23** (2004), 11965–11979. DOI: 10.1063/1.1814076. (Cit. on p. 11).

[72] L. Malard, M. Pimenta, G. Dresselhaus, and M. Dresselhaus: "Raman spectroscopy in graphene". *Physics Reports* **473.5-6** (2009), 51–87. DOI: http://dx.doi.org/10.1016/j.physrep.2009.02.003. (Cit. on p. 11).

[73] J. Lambe and R. C. Jaklevic: "Molecular Vibration Spectra by Inelastic Electron Tunneling". *Phys. Rev.* **165** (3 Jan. 1968), 821–832. DOI: 10.1103/PhysRev.165.821. (Cit. on p. 12).

[74] S. Ewert, G. Heiland, H. Lüth, U. Roll, and W. Sander: "Molecular Vibrations in a Polymethine Dye Layer Studied by Inelastic Electron Tunneling Spectroscopy". *physica status solidi (b)* **89.2** (1978), 459–465. DOI: 10.1002/pssb.2220890215. (Cit. on p. 12).

[75] J. R. Hahn, H. J. Lee, and W. Ho: "Electronic Resonance and Symmetry in Single-Molecule Inelastic Electron Tunneling". *Phys. Rev. Lett.* **85** (9 2000), 1914–1917. DOI: 10.1103/PhysRevLett.85.1914. (Cit. on p. 12).

[76] H. Ueba and B. Persson: "Theoretical state-of-the art in adsorbate motions and reactions induced by inelastic tunneling current with STM". *Surface Science* **566-568, Part 1.0** (2004), 1 –12. DOI: http://dx.doi.org/10.1016/j.susc.2004.06.130. (Cit. on p. 12).

[77] L. Vitali, R. Ohmann, K. Kern, A. Garcia-Lekue, T. Frederiksen, D. Sanchez-Portal, and A. Arnau: "Surveying Molecular Vibrations during the Formation of Metal-Molecule Nanocontacts". *Nano Letters* **10.2** (2010), 657–660. DOI: 10.1021/nl903760k. (Cit. on p. 12).

[78] K. Morgenstern: "On the interpretation of IETS spectra of a small organic molecule". *Journal of Physics: Condensed Matter* **23**.**48** (2011), 484007. (Cit. on pp. 12, 129, 130, 145).

[79] W. Ho: *Wilson Ho Group*. `http://www.physics.uci.edu/~wilsonho/wilsonho.html`. 2013 (cit. on p. 12).

[80] A. Damascelli: "Probing the Electronic Structure of Complex Systems by ARPES". *Physica Scripta* **2004**.**T109** (2004), 61. (Cit. on p. 13).

[81] S. Hüfner: *Photoelectron Spectroscopy: Principles and Applications*. Advanced Texts in Physics. Springer, 2003 (cit. on p. 13).

[82] K. Giesen, F. Hage, F. J. Himpsel, H. J. Riess, and W. Steinmann: "Two-photon photoemission via image-potential states". *Phys. Rev. Lett.* **55** (3 1985), 300–303. DOI: `10.1103/PhysRevLett.55.300`. (Cit. on p. 13).

[83] T. Fauster and W. Steinmann: "Two-photon photoemission spectroscopy of image states". *Electromagnetic Waves: Recent Developments in Research* **2** (1995), 347–411. (Cit. on p. 13).

[84] P. R. Wallace: "The Band Theory of Graphite". *Phys. Rev.* **71**.**9** (1947), 622. DOI: `10.1103/PhysRev.71.622`. (Cit. on pp. 14, 15).

[85] G. M. Rutter, J. N. Crain, N. P. Guisinger, T. Li, P. N. First, and J. A. Stroscio: "Scattering and Interference in Epitaxial Graphene". *Science* **317**.**5835** (July 2007), 219–222. DOI: `10.1126/science.1142882`. (Cit. on pp. 15, 32, 105).

[86] Y. Zhang, Y.-W. Tan, H. L. Stormer, and P. Kim: "Experimental observation of the quantum Hall effect and Berry's phase in graphene". *Nature* **7065** (2005), 201–204. DOI: `10.1038/nature04235`. (Cit. on p. 15).

[87] M. Katsnelson: "Zitterbewegung, chirality, and minimal conductivity in graphene". *The European Physical Journal B-Condensed Matter and Complex Systems* **51**.**2** (2006), 157–160. (Cit. on p. 15).

[88] L. Fu: "Topological Crystalline Insulators". *Phys. Rev. Lett.* **106** (10 2011), 106802. DOI: `10.1103/PhysRevLett.106.106802`. (Cit. on p. 16).

[89] T. H. Hsieh, H. Lin, J. Liu, W. Duan, A. Bansil, and L. Fu: "Topological crystalline insulators in the SnTe material class". *Nature Communications* (2013), 982. DOI: `10.1038/ncomms1969`. (Cit. on p. 16).

[90] B. E. Feldman, B. Krauss, J. H. Smet, and A. Yacoby: "Unconventional Sequence of Fractional Quantum Hall States in Suspended Graphene". *Science* **337.6099** (2012), 1196–1199. DOI: 10.1126/science.1224784. (Cit. on p. 16).

[91] I. Pletikosić, M. Kralj, P. Pervan, R. Brako, J. Coraux, A. T. N'Diaye, C. Busse, and T. Michely: "Dirac Cones and Minigaps for Graphene on Ir(111)". *Phys. Rev. Lett.* **102** (5 2009), 056808. DOI: 10.1103/PhysRevLett.102.056808. (Cit. on pp. 16, 46, 63, 95, 100, 101, 129).

[92] M. Kralj, I. Pletikosić, M. Petrović, P. Pervan, M. Milun, A. T. N'Diaye, C. Busse, T. Michely, J. Fujii, and I. Vobornik: "Graphene on Ir(111) characterized by angle-resolved photoemission". *Phys. Rev. B* **84** (7 2011), 075427. DOI: 10.1103/PhysRevB.84.075427. (Cit. on pp. 16, 18, 33, 95, 96, 99, 100).

[93] L. Gao, J. R. Guest, and N. P. Guisinger: "Epitaxial Graphene on Cu(111)". *Nano Letters* **10.9** (2010), 3512–3516. DOI: 10.1021/nl1016706. (Cit. on p. 16).

[94] M. Sicot, P. Leicht, A. Zusan, S. Bouvron, O. Zander, M. Weser, Y. S. Dedkov, K. Horn, and M. Fonin: "Size-Selected Epitaxial Nanoislands Underneath Graphene Moiré on Rh(111)". *ACS Nano* **6.1** (2012), 151–158. DOI: 10.1021/nn203169j. (Cit. on p. 16).

[95] P. Sutter, J. T. Sadowski, and E. Sutter: "Graphene on Pt(111): Growth and substrate interaction". *Phys. Rev. B* **80** (24 2009), 245411. DOI: 10.1103/PhysRevB.80.245411. (Cit. on p. 16).

[96] S. Y. Zhou, G.-H. Gweon, A. V. Fedorov, P. N. First, W. A. de Heer, D.-H. Lee, F. Guinea, A. H. Castro Neto, and A. Lanzara: "Substrate-induced bandgap opening in epitaxial graphene". *Nature Materials* **6.10** (2007), 770–775. DOI: 10.1038/nmat2003. (Cit. on p. 17).

[97] S. Kim, J. Ihm, H. J. Choi, and Y.-W. Son: "Origin of Anomalous Electronic Structures of Epitaxial Graphene on Silicon Carbide". *Phys. Rev. Lett.* **100** (17 2008), 176802. DOI: 10.1103/PhysRevLett.100.176802. (Cit. on p. 17).

[98] G. Giovannetti, P. A. Khomyakov, G. Brocks, P. J. Kelly, and J. van den Brink: "Substrate-induced band gap in graphene on hexagonal boron nitride: Ab initio density functional calculations". *Phys. Rev. B* **76** (7 2007), 073103. DOI: 10.1103/PhysRevB.76.073103. (Cit. on p. 17).

[99] M. Y. Han, B. Özyilmaz, Y. Zhang, and P. Kim: "Energy band-gap engineering of graphene nanoribbons". *Phys. Rev. Lett.* **98.20** (2007), 206805. (Cit. on p. 17).

[100] X. Li, X. Wang, L. Zhang, S. Lee, and H. Dai: "Chemically Derived, Ultrasmooth Graphene Nanoribbon Semiconductors". *Science* **319.5867** (2008), 1229–1232. DOI: 10.1126/science.1150878. (Cit. on p. 17).

[101] E. McCann, D. S. Abergel, and V. I. Fal'ko: "Electrons in bilayer graphene". *Solid State Communications* **143.1–2** (2007), 110 –115. DOI: http://dx.doi.org/10.1016/j.ssc.2007.03.054. (Cit. on p. 17).

[102] E. V. Castro, K. S. Novoselov, S. V. Morozov, N. M. R. Peres, J. M. B. L. dos Santos, J. Nilsson, F. Guinea, A. K. Geim, and A. H. Castro Neto: "Biased Bilayer Graphene: Semiconductor with a Gap Tunable by the Electric Field Effect". *Phys. Rev. Lett.* **99** (21 2007), 216802. DOI: 10.1103/PhysRevLett.99.216802. (Cit. on p. 17).

[103] T. Ohta, A. Bostwick, T. Seyller, K. Horn, and E. Rotenberg: "Controlling the Electronic Structure of Bilayer Graphene". *Science* **313.5789** (2006), 951–954. DOI: 10.1126/science.1130681. (Cit. on p. 17).

[104] T. G. Pedersen, C. Flindt, J. Pedersen, N. A. Mortensen, A.-P. Jauho, and K. Pedersen: "Graphene Antidot Lattices: Designed Defects and Spin Qubits". *Phys. Rev. Lett.* **100** (13 2008), 136804. DOI: 10.1103/PhysRevLett.100.136804. (Cit. on p. 17).

[105] J. Bai, X. Zhong, S. Jiang, Y. Huang, and X. Duan: "Graphene nanomesh". *Nature Nanotechnology* **5.3** (2010), 190–194. DOI: 10.1038/nnano.2010.8. (Cit. on p. 17).

[106] R. Balog, B. Jørgensen, L. Nilsson, M. Andersen, E. Rienks, M. Bianchi, M. Fanetti, E. Lægsgaard, A. Baraldi, S. Lizzit, Z. Sljivancanin, F. Besenbacher, T. G. Hammer B. Pedersen, P. Hofmann, and L. Hornekær: "Bandgap opening in graphene induced by patterned hydrogen adsorption". *Nat. Mater.* **9.4** (2010), 315. DOI: 10.1038/nmat2710. (Cit. on p. 17).

[107] E. Starodub, A. Bostwick, L. Moreschini, S. Nie, F. E. Gabaly, K. F. McCarty, and E. Rotenberg: "In-plane orientation effects on the electronic structure, stability, and Raman scattering of monolayer graphene on Ir(111)". *Phys. Rev. B* **83** (12 2011), 125428. DOI: 10.1103/PhysRevB.83.125428. (Cit. on pp. 17, 18).

[108] I Pletikosić, M Kralj, D Šokčević, R Brako, P Lazić, and P Pervan: "Photoemission and density functional theory study of Ir(111); energy band gap mapping". *J. Phys. Condens. Matter* **22.13** (2010), 135006. DOI: 10.1088/0953-8984/22/13/135006. (Cit. on pp. 17, 18, 96).

[109] S. Standop, O. Lehtinen, C. Herbig, G. Lewes-Malandrakis, F. Craes, J. Kotakoski, T. Michely, A. V. Krasheninnikov, and C. Busse: "Ion Impacts on Graphene/Ir(111): Interface Channeling, Vacancy Funnels, and a Nanomesh". *Nano Letters* **13.5** (2013), 1948–1955. DOI: 10.1021/nl304659n. (Cit. on pp. 17, 19, 199).

[110] D. Subramaniam, F. Libisch, Y. Li, C. Pauly, V. Geringer, R. Reiter, T. Mashoff, M. Liebmann, J. Burgdörfer, C. Busse, T. Michely, R. Mazzarello, M. Pratzer, and M. Morgenstern: "Wave-Function Mapping of Graphene Quantum Dots with Soft Confinement". *Phys. Rev. Lett.* **108** (4 2012), 046801. DOI: 10.1103/PhysRevLett.108.046801. (Cit. on pp. 17, 19, 28, 95, 97, 113, 120).

[111] S. K. Hämäläinen, Z. Sun, M. P. Boneschanscher, A. Uppstu, M. Ijäs, A. Harju, D. Vanmaekelbergh, and P. Liljeroth: "Quantum-Confined Electronic States in Atomically Well-Defined Graphene Nanostructures". *Phys. Rev. Lett.* **107** (23 2011), 236803. DOI: 10.1103/PhysRevLett.107.236803. (Cit. on pp. 17, 28, 95, 97, 120).

[112] S. J. Altenburg, J. Kröger, T. O. Wehling, B. Sachs, A. I. Lichtenstein, and R. Berndt: "Local Gating of an Ir(111) Surface Resonance by Graphene Islands". *Phys. Rev. Lett.* **108** (20 2012), 206805. DOI: 10.1103/PhysRevLett.108.206805. (Cit. on pp. 17, 28, 54, 95, 97, 120).

[113] S.-h. Phark, J. Borme, A. L. Vanegas, M. Corbetta, D. Sander, and J. Kirschner: "Direct Observation of Electron Confinement in Epitaxial Graphene Nanoislands". *ACS Nano* **5.10** (2011), 8162–8166. DOI: 10.1021/nn2028105. (Cit. on pp. 17, 28, 95, 97, 120).

[114] D. Niesner, T. Fauster, J. I. Dadap, N. Zaki, K. R. Knox, P.-C. Yeh, R. Bhandari, R. M. Osgood, M. Petrović, and M. Kralj: "Trapping surface electrons on graphene layers and islands". *Phys. Rev. B* **85** (8 Feb. 2012), 081402. DOI: 10.1103/PhysRevB.85.081402. (Cit. on pp. 17, 18, 95, 111, 113, 116, 124).

[115] V. M. Silkin, J. Zhao, F. Guinea, E. V. Chulkov, P. M. Echenique, and H. Petek: "Image potential states in graphene". *Phys. Rev. B* **80** (12 2009), 121408. DOI: 10.1103/PhysRevB.80.121408. (Cit. on pp. 17, 111, 112, 191).

[116] S. Bose, V. M. Silkin, R. Ohmann, I. Brihuega, L. Vitali, C. H. Michaelis, P. Mallet, J. Y. Veuillen, M. A. Schneider, E. V. Chulkov, P. M. Echenique, and K. Kern: "Image potential states as a quantum probe of graphene interfaces". *New J. Phys.* **12.2** (2010), 023028. (Cit. on pp. 17, 111, 112, 191).

[117] A. Varykhalov, D. Marchenko, M. R. Scholz, E. D. L. Rienks, T. K. Kim, G. Bihlmayer, J. Sanchez-Barriga, and O. Rader: "Ir(111) Surface State with Giant Rashba Splitting Persists under Graphene in Air". *Phys. Rev. Lett.* **108** (2012), 066804. (Cit. on pp. 18, 62, 69, 70, 95, 96, 101).

[118] Y. Li, D. Subramaniam, N. Atodiresei, P. Lazić, V. Caciuc, C. Pauly, A. Georgi, C. Busse, M. Liebmann, S. Blügel, M. Pratzer, M. Morgenstern, and R. Mazzarello: "Absence of Edge States in Covalently Bonded Zigzag Edges of Graphene on Ir(111)". *Advanced Materials* **25**.**14** (2013), 1967–1972. DOI: 10.1002/adma.201204539. (Cit. on pp. 19, 83, 124, 128).

[119] H. Zhang, A. Soon, B. Delley, and C. Stampfl: "Stability, structure, and electronic properties of chemisorbed oxygen and thin surface oxides on Ir(111)". *Phys. Rev. B* **78** (4 2008), 045436. DOI: 10.1103/PhysRevB.78.045436. (Cit. on p. 20).

[120] S. Runte: "Atomic and Electronic Structure of Graphene and Graphene Intercalation Compounds". dissertation. University of Cologne, 2013 (cit. on pp. 20, 37, 43, 88–90).

[121] P. A. Khomyakov, G. Giovannetti, P. C. Rusu, G. Brocks, J. van den Brink, and P. J. Kelly: "First-principles study of the interaction and charge transfer between graphene and metals". *Phys. Rev. B* **79** (19 2009), 195425. DOI: 10.1103/PhysRevB.79.195425. (Cit. on pp. 20, 63).

[122] B. Kiraly, E. V. Iski, A. J. Mannix, B. L. Fisher, M. C. Hersam, and N. P. Guisinger: "Solid-source growth and atomic-scale characterization of graphene on Ag(111)". *Nature Communications* **4** (0), –. DOI: 10.1038/ncomms3804. (Cit. on p. 21).

[123] F. Forster, G. Nicolay, F. Reinert, D. Ehm, S. Schmidt, and S. Hüfner: "Surface and interface states on adsorbate covered noble metal surfaces". *Surf. Sci.* **532** (2003), 160 –165. DOI: http://dx.doi.org/10.1016/S0039-6028(03)00151-1. (Cit. on p. 21).

[124] S. H. Choi, Y. L. Kim, and K. M. Byun: "Graphene-on-silver substrates for sensitive surface plasmon resonance imaging biosensors". *Opt. Express* **19**.**2** (2011), 458–466. DOI: 10.1364/OE.19.000458. (Cit. on p. 21).

[125] A. Zangwill: *Physics at surfaces*. Cambridge University Press, 1988 (cit. on p. 22).

[126] N. W. Ashcroft and N. D. Mermin: *Festkörperphysik*. 2nd ed. Oldenbourg, 2005 (cit. on p. 22).

[127] Wikipedia. https://en.wikipedia.org/wiki/Surface_states. (2014) (cit. on p. 23).

[128] J. Klinkhammer, M. Schlipf, F. Craes, S. Runte, T. Michely, and C. Busse: "Spin-Polarized Surface State in EuO(100)". *Phys. Rev. Lett.* **112** (1 2014), 016803. DOI: 10.1103/PhysRevLett.112.016803. (Cit. on pp. 22, 200).

[129] M. Berlin: *MBI Berlin*. http://www.mbi-berlin.de/de/research/projects/3-01/subprojects/5_spin/IPS/ips.html. 2013 (cit. on p. 24).

[130] P. M. Echenique and J. B. Pendry: "The existence and detection of Rydberg states at surfaces". *J. Phys. C: Solid State Phys.* **11.10** (1978), 2065. (Cit. on p. 23).

[131] S. Crampin: "Lifetimes of Stark-Shifted Image States". *Phys. Rev. Lett.* **95** (4 2005), 046801. DOI: 10.1103/PhysRevLett.95.046801. (Cit. on p. 24).

[132] M. Crommie, C. Lutz, and D. Eigler: "Confinement of Electrons to Quantum Corrals on a Metal Surface". *Science* **262** (1993), 218–220. DOI: 10.1126/science.262.5131.218. (Cit. on pp. 26–28, 110).

[133] M. Crommie, C. Lutz, D. Eigler, and E. Heller: "Quantum interference in 2D atomic-scale structures". *Surface Science* **361-362.0** (1996), 864 –869. DOI: http://dx.doi.org/10.1016/0039-6028(96)00552-3. (Cit. on p. 26).

[134] A. P. Alivisatos: "Semiconductor Clusters, Nanocrystals, and Quantum Dots". *Science* **271.5251** (1996), 933–937. DOI: 10.1126/science.271.5251.933. (Cit. on p. 26).

[135] D. Loss and D. P. DiVincenzo: "Quantum computation with quantum dots". *Phys. Rev. A* **57** (1 Jan. 1998), 120–126. DOI: 10.1103/PhysRevA.57.120. (Cit. on p. 26).

[136] V. M. Aroutiounian, S. Petrosyan, A. Khachatryan, and K. J. Touryan: "Quantum dot solar cells". *Proc. SPIE* **4458** (2001), 38–45. DOI: 10.1117/12.448264. (Cit. on p. 26).

[137] A. J. Nozik: "Quantum dot solar cells". *Physica E: Low-dimensional Systems and Nanostructures* **14.1-2** (2002), 115 –120. DOI: http://dx.doi.org/10.1016/S1386-9477(02)00374-0. (Cit. on p. 26).

[138] P. V. Kamat: "Quantum Dot Solar Cells. Semiconductor Nanocrystals as Light Harvesters". *The Journal of Physical Chemistry C* **112.48** (2008), 18737–18753. DOI: 10.1021/jp806791s. (Cit. on p. 26).

[139] A. M. Jawaid, S. Chattopadhyay, D. J. Wink, L. E. Page, and P. T. Snee: "Cluster-Seeded Synthesis of Doped CdSe:Cu4 Quantum Dots". *ACS Nano* **7.4** (2013), 3190–3197. DOI: 10.1021/nn305697q. (Cit. on p. 26).

[140] R. W. Robinett: "Visualizing the solutions for the circular infinite well in quantum and classical mechanics". *Am. J. Phys.* **64.4** (1996), 440–446. DOI: {10.1119/1.18188}. (Cit. on p. 26).

[141] W. Jolie: "Electronic Properties on and under Graphene Quantum Dots". Master's Thesis. Universität zu Köln, 2013 (cit. on pp. 27, 53–55, 57, 59–63, 65–69, 71, 93, 99, 144, 150).

[142] S. C. Erwin, L. Zu, M. I. Haftel, A. L. Efros, T. A. Kennedy, and D. J. Norris: "Doping semiconductor nanocrystals". *Nature* **7047** (2005), 91–94. DOI: 10.1038/nature03832. (Cit. on p. 27).

[143] J. Friedel: "Metallic alloys". *Il Nuovo Cimento (1955-1965)* **7** (1958), 287–311. (Cit. on pp. 27, 30).

[144] E. J. Heller, M. F. Crommie, C. P. Lutz, and D. M. Eigler: "Scattering and absorption of surface electron waves in quantum corrals". *Nature* **6480** (1994), 464466. DOI: 10.1038/369464a0. (Cit. on p. 27).

[145] N. M. R. Peres, J. N. B. Rodrigues, T. Stauber, and J. M. B. Lopes dos Santos: "Dirac electrons in graphene-based quantum wires and quantum dots". *Journal of Physics: Condensed Matter* **21.34** (2009), 344202. (Cit. on p. 27).

[146] A. De Martino, L. Dell'Anna, and R. Egger: "Magnetic Confinement of Massless Dirac Fermions in Graphene". *Phys. Rev. Lett.* **98** (6 2007), 066802. DOI: 10.1103/PhysRevLett.98.066802. (Cit. on p. 28).

[147] C. Berger, Z. Song, X. Li, X. Wu, N. Brown, C. Naud, D. Mayou, T. Li, J. Hass, A. N. Marchenkov, E. H. Conrad, P. N. First, and W. A. de Heer: "Electronic Confinement and Coherence in Patterned Epitaxial Graphene". *Science* **312.5777** (2006), 1191–1196. DOI: 10.1126/science.1125925. (Cit. on p. 28).

[148] M. V. Berry and R. Mondragon: "Neutrino billiards: time-reversal symmetry-breaking without magnetic fields". *Proceedings of the Royal Society of London. A. Mathematical and Physical Sciences* **412.1842** (1987), 53–74. (Cit. on p. 28).

[149] L. A. Ponomarenko, F. Schedin, M. I. Katsnelson, R. Yang, E. W. Hill, K. S. Novoselov, and A. K. Geim: "Chaotic Dirac Billiard in Graphene Quantum Dots". *Science* **320.5874** (2008), 356–358. DOI: 10.1126/science.1154663. (Cit. on p. 28).

[150] H. Hövel and I. Barke: "Morphology and electronic structure of gold clusters on graphite: Scanning-tunneling techniques and photoemission". *Prog. Surf. Sci.* **81.23** (2006), 53 –111. DOI: 10.1016/j.progsurf.2006.01.002. (Cit. on pp. 28, 82, 114).

[151] J. Chen, M. Badioli, P. Alonso-González, S. Thongrattanasiri, F. Huth, J. Osmond, M. Spasenović, A. Centeno, A. Pesquera, P. Godignon, A. Z. Elorza, N. Camara, F. J. Garcia de Abajo, R. Hillenbrand, and F. H. L. Koppens: "Optical nano-imaging of gate-tunable graphene plasmons". *Nature* **487** (2012), 77–81. (Cit. on p. 29).

[152] Z. Fei, S. Robin, G. O. Andreev, W. Bao, A. S. McLeord, M. Wagner, L. M. Zhang, Z. Zhao, M. Thiemens, G. Dominguez, M. M. Folger, A. H. Castro Neto, C. N. Lau, F. Keilmann, and D. N. Basov: "Gate-tuning of graphene plasmons revealed by infrared nano-imaging". *Nature* **487** (2012), 82–85. (Cit. on p. 29).

[153] Y. Hasegawa and P. Avouris: "Direct observation of standing wave formation at surface steps using scanning tunneling spectroscopy". *Phys. Rev. Lett.* **71.7** (1993), 1071–1074. (Cit. on p. 30).

[154] M. Crommie, C. Lutz, and D. Eigler: "Imaging standing waves in a two-dimensional electron gas". *Nature* (1993). (Cit. on p. 30).

[155] G. Hörmandinger: "Imaging of the Cu(111) surface state in scanning tunneling microscopy". *Phys. Rev. B* **49** (19 1994), 13897–13905. DOI: 10.1103/PhysRevB.49.13897. (Cit. on p. 30).

[156] L. Petersen, P. T. Sprunger, P. Hofmann, E. Lægsgaard, B. G. Briner, M. Doering, H.-P. Rust, A. M. Bradshaw, F. Besenbacher, and E. W. Plummer: "Direct imaging of the two-dimensional Fermi contour: Fourier-transform STM". *Phys. Rev. B* **57.12** (1998), R6858–R6861. (Cit. on pp. 30, 31).

[157] J. Li, W.-D. Schneider, and R. Berndt: "Local density of states from spectroscopic scanning-tunneling-microscope images: Ag(111)". *Phys. Rev. B* **56** (12 Sept. 1997), 7656–7659. DOI: 10.1103/PhysRevB.56.7656. (Cit. on p. 31).

[158] V. A. Ukraintsev: "Data evaluation technique for electron-tunneling spectroscopy". *Phys. Rev. B* **53** (16 1996), 11176–11185. DOI: 10.1103/PhysRevB.53.11176. (Cit. on p. 31).

[159] P. Sprunger, L. Petersen, E. Plummer, E. Lægsgaard, and F. Besenbacher: "Giant Friedel oscillations on the beryllium (0001) surface". *Science* **275.5307** (1997), 1764. (Cit. on p. 31).

[160] L. Simon, C. Bena, F. Vonau, M. Cranney, and D. Aubel: "Fourier-transform scanning tunnelling spectroscopy: the possibility to obtain constant-energy maps and band dispersion using a local measurement". *Journal of Physics D: Applied Physics* **44.46** (2011), 464010. (Cit. on p. 31).

[161] P. Hofmann, B. G. Briner, M. Doering, H.-P. Rust, E. W. Plummer, and A. M. Bradshaw: "Anisotropic Two-Dimensional Friedel Oscillations". *Phys. Rev. Lett.* **79** (2 1997), 265–268. DOI: 10.1103/PhysRevLett.79.265. (Cit. on p. 31).

[162] L. Petersen and P. Hedegård: "A simple tight-binding model of spin-orbit splitting of sp-derived surface states". *Surface Science* **459.1-2** (2000), 49–56. DOI: http://dx.doi.org/10.1016/S0039-6028(00)00441-6. (Cit. on pp. 32, 96, 97).

[163] J. H. Dil: "Spin and angle resolved photoemission on non-magnetic low-dimensional systems". *Journal of Physics: Condensed Matter* **21.40** (2009), 403001. (Cit. on p. 32).

[164] P. Mallet, I. Brihuega, S. Bose, M. M. Ugeda, J. M. Gomez-Rodriguez, K. Kern, and J. Y. Veuillen: "Role of Pseudospin in quasiparticle interferences in epitaxial graphene pprobe by high-resolution scanning tunneling microscopy". *Phys. Rev. B* **86** (2012), 045444. (Cit. on pp. 32, 79, 105, 134).

[165] I. Brihuega, P. Mallet, C. Bena, S. Bose, C. Michaelis, L. Vitali, F. Varchon, L. Magaud, K. Kern, and J. Y. Veuillen: "Quasiparticle Chirality in Epitaxial Graphene Probed at the Nanometer Scale". *Phys. Rev. Lett.* **101** (20 2008), 206802. DOI: 10.1103/PhysRevLett.101.206802. (Cit. on p. 32).

[166] M. M. Ugeda, I. Brihuega, F. Guinea, and J. M. Gómez-Rodríguez: "Missing Atom as a Source of Carbon Magnetism". *Phys. Rev. Lett.* **104** (9 2010), 096804. DOI: 10.1103/PhysRevLett.104.096804. (Cit. on p. 32).

[167] M. M. Ugeda, D. Fernández-Torre, I. Brihuega, P. Pou, A. J. Martínez Galera, R. Pérez, and J. M. Gómez-Rodríguez: "Point Defects on Graphene on Metals". *Phys. Rev. Lett.* **107** (11 2011), 116803. DOI: 10.1103/PhysRevLett.107.116803. (Cit. on p. 32).

[168] A. J. Martínez-Galera, I. Brihuega, and J. M. Gómez-Rodríguez: "Ethylene Irradiation: A New Route to Grow Graphene on Low Reactivity Metals". *Nano Letters* **11.9** (2011), 3576–3580. DOI: 10.1021/nl201281m. (Cit. on p. 32).

[169] T. O. Wehling, I. Grigorenko, A. I. Lichtenstein, and A. V. Balatsky: "Phonon-Mediated Tunneling into Graphene". *Phys. Rev. Lett.* **101** (21 2008), 216803. DOI: 10.1103/PhysRevLett.101.216803. (Cit. on pp. 33–35, 117, 135–137).

[170] Y. Zhang, V. W. Brar, F. Wang, C. Girit, Y. Yayon, M. Panlasigui, A. Zettl, and M. F. Crommie: "Giant phonon-induced conductance in scanning tunnelling spectroscopy of gate-tunable graphene". *Nature Physics* **4.8** (Aug. 2008), 627–630. DOI: {10.1038/nphys1022}. (Cit. on pp. 34, 105, 135, 137).

[171] H. Raza: *Graphene Nanoelectronics*. Springer, 2012 (cit. on p. 35).

[172] Tim O. Wehling, private communication. (cit. on pp. 35, 87).

[173] S. Zöphel: "Der Aufbau eines Tieftemperatur-Rastertunnelmikroskops und Strukturuntersuchungen auf vicinalen Kupferoberflächen". dissertation. Freie Universität Berlin, 2000 (cit. on pp. 37, 40).

[174] J. Klinkhammer: "Electronic Structure and Magnetism of Thin Films of the Ferromagnetic Semiconductor EuO on the Nanometer Scale". dissertation. University of Cologne, 2013 (cit. on pp. 37, 42, 43, 47).

[175] K. Besocke: "An easily operable scanning tunneling microscope". *Surf. Sci.* **181.1-2** (1987), 145–153. (Cit. on p. 41).

[176] D. I. Hagen, B. E. Nieuwenhuys, G. Rovida, and G. A. Somorjai: "Low-energy Electron Diffraction, Auger Electron Spectroscopy, and Thermal Desorption Studies of Chemisorbed CO and O_2 on the (111) and Stepped [6(111)×(100)] Iridium Surfaces". *Surf. Sci.* **57** (1976), 632 –650. DOI: http://dx.doi.org/10.1016/0039-6028(76)90352-6. (Cit. on p. 46).

[177] M Bianchi, D Cassese, A Cavallin, R Comin, F Orlando, L Postregna, E Golfetto, S Lizzit, and A Baraldi: "Surface core level shifts of clean and oxygen covered Ir(111)". *New J. Phys.* **11** (2009), 063002. (Cit. on p. 46).

[178] N. R. Gall, E. V. Rut'kov, and A. Y. Tontegode: "Two Dimensional Graphite Films on Metals and Their Intercalation". *Int. J. Mod. Phys. B* **11** (1997), 1865–1911. DOI: 10.1142/S0217979297000976. (Cit. on p. 48).

[179] N. R. Gall', E. V. Rut'kov, and A. Y. Tontegode: "Interaction of silver atoms with iridium and with a two-dimensional graphite film on iridium: Adsorption, desorption, and dissolution". *Phys. Solid State* **46** (2004), 371–377. DOI: 10.1134/1.1649439. (Cit. on p. 48).

[180] I. Horcas, R. Fernandez, J. M. Gomez-Rodriguez, J. Colchero, J. Gomez-Herrero, and A. M. Baro: "WSXM: A software for scanning probe microscopy and a tool for nanotechnology". *Rev. Sci. Instr.* **78**.**1** (2007). DOI: 10.1063/1.2432410. (Cit. on p. 49).

[181] W. Chen, S. Wang, Y. Tseng, D. Tsai, and J. Tsay: "The formation of a surface alloy for Ag/Ir(111) ultrathin films". *Surface Science* **605**.**23–24** (2011), 2045 –2049. DOI: http://dx.doi.org/10.1016/j.susc.2011.08.002. (Cit. on p. 54).

[182] C. Kittel: *Introduction to Solid State Physics*. John Wiley & Sons, Inc., 1971 (cit. on pp. 54, 57).

[183] Y. Li, W. Zhang, M. Morgenstern, and R. Mazzarello: "Electronic and Magnetic Properties of Zigzag Graphene Nanoribbons on the (111) Surface of Cu, Ag, and Au". *Phys. Rev. Lett.* **110** (21 2013), 216804. DOI: 10.1103/PhysRevLett.110.216804. (Cit. on pp. 55, 83, 128).

[184] A. T. N'Diaye, J. Coraux, T. N. Plasa, C. Busse, and T. Michely: "Structure of epitaxial graphene on Ir(111)". *New Journal of Physics* **10**.**4** (2008), 043033. (Cit. on pp. 56, 58).

[185] N. M. Souza-Neto, D. Haskel, Y.-C. Tseng, and G. Lapertot: "Pressure-Induced Electronic Mixing and Enhancement of Ferromagnetic Ordering in EuX ($X = Te$, Se, S, O) Magnetic Semiconductors". *Phys. Rev. Lett.* **102**.**5** (2009), 057206. DOI: 10.1103/PhysRevLett.102.057206. (Cit. on pp. 57, 105).

[186] M. Pozzo, D. Alfé, P. Lacovig, P. Hofmann, S. Lizzit, and A. Baraldi: "Thermal Expansion of Supported and Freestanding Graphene: Lattice Constant versus Interatomic Distance". *Phys. Rev. Lett.* **106** (13 2011), 135501. DOI: 10.1103/PhysRevLett.106.135501. (Cit. on p. 57).

[187] G. Neuhold and K. Horn: "Depopulation of the Ag(111) Surface State Assigned to Strain in Epitaxial Films". *Phys. Rev. Lett.* **78** (7 1997), 1327–1330. DOI: 10.1103/PhysRevLett.78.1327. (Cit. on pp. 58, 60).

[188] R. Paniago, R. Matzdorf, G. Meister, and A. Goldmann: "Temperature dependence of Shockley-type surface energy bands of Cu(111), Ag(111) and Au(111)". *Surf. Sci.* **336** (1995), 113–122. (Cit. on p. 60).

[189] K. Sawa, Y. Aoki, and H. Hirayama: "Thickness dependence of Shockley-type surface states of Ag (111) ultrathin films on Si (111) 7× 7 substrates". *Physical Review B* **80.3** (2009), 035428. (Cit. on p. 60).

[190] F. Li, G. Parteder, F. Allegretti, C. Franchini, R. Podloucky, S. Surnev, and F. P. Netzer: "Two-dimensional manganese oxide nanolayers on Pd (100): the surface phase diagram". *J. Phys. Condens. Matter* **21** (2009), 134008. (Cit. on p. 63).

[191] Y. Zhang, V. W. Brar, C. Girit, A. Zettl, and M. Crommie: "Origin of spatial charge inhomogeneity in graphene". *Nature Phys.* **5** (2009), 722–726. (Cit. on p. 63).

[192] W.-J. Jang, H. Kim, J. H. Jeon, J. K. Yoon, and S.-J. Kahng: "Recovery and local-variation of Dirac cones in oxygen-intercalated graphene on Ru(0001) studied using scanning tunneling microscopy and spectroscopy". *Phys. Chem. Chem. Phys.* **15** (38 2013), 16019–16023. DOI: 10.1039/C3CP52431K. (Cit. on pp. 63, 94).

[193] E. Bertel and U. Bischler: "One-dimensional surface states on metal surfaces ". *Surf. Sci.* **307-309** (1994), 947 –952. DOI: http://dx.doi.org/10.1016/0039-6028(94)91521-0. (Cit. on p. 70).

[194] R. Fasel, P. Aebi, R. G. Agostino, L. Schlapbach, and J. Osterwalder: "Electronic structure of high-and low-temperature c (2× 2)-Na/Al (001) phases from angle-scanned ultraviolet photoemission". *Physical Review B* **54.8** (1996), 5893. (Cit. on p. 70).

[195] T. A. Fulton and G. J. Dolan: "Observation of single-electron charging effects in small tunnel junctions". *Phys. Rev. Lett.* **59** (1 1987), 109–112. DOI: 10.1103/PhysRevLett.59.109. (Cit. on p. 74).

[196] N. A. Pradhan, N. Liu, C. Silien, and W. Ho: "Atomic Scale Conductance Induced by Single Impurity Charging". *Phys. Rev. Lett.* **94** (7 2005), 076801. DOI: 10.1103/PhysRevLett.94.076801. (Cit. on pp. 75, 84, 86).

[197] F. Marczinowski, J. Wiebe, F. Meier, K. Hashimoto, and R. Wiesendanger: "Effect of charge manipulation on scanning tunneling spectra of single Mn acceptors in InAs". *Phys. Rev. B* **77** (11 Mar. 2008), 115318. DOI: 10.1103/PhysRevB.77.115318. (Cit. on pp. 75, 84).

[198] V. W. Brar, R. Decker, H.-M. Solowan, Y. Wang, L. Maserati, K. T. Chan, H. Lee, O. Girit, A. Zettl, S. G. Louie, M. L. Cohen, and M. F. Crommie: "Gate-controlled ionization and screening of cobalt adatoms on a graphene surface". *Nature Physics* **7**.**1** (2010), 43–47. DOI: 10.1038/nphys1807. (Cit. on pp. 75, 85, 86, 89).

[199] A. J. Martínez-Galera, F. Craes, F. Huttmann, U. A. Schröder, C. Busse, and T. Michely: "Oxygen superstructures on Ir(111)". *in preparation* (2014). (Cit. on pp. 78, 79, 92).

[200] P. Koskinen, S. Malola, and H. Häkkinen: "Evidence for graphene edges beyond zigzag and armchair". *Phys. Rev. B* **80** (7 2009), 073401. DOI: 10.1103/PhysRevB.80.073401. (Cit. on p. 83).

[201] P. Koskinen, S. Malola, and H. Häkkinen: "Self-Passivating Edge Reconstructions of Graphene". *Phys. Rev. Lett.* **101** (11 2008), 115502. DOI: 10.1103/PhysRevLett.101.115502. (Cit. on p. 83).

[202] A. M. Yakunin, A. Y. Silov, P. M. Koenraad, J. H. Wolter, W. Van Roy, J. De Boeck, J.-M. Tang, and M. E. Flatté: "Spatial Structure of an Individual Mn Acceptor in GaAs". *Phys. Rev. Lett.* **92** (21 2004), 216806. DOI: 10.1103/PhysRevLett.92.216806. (Cit. on p. 85).

[203] A. M. Yakunin, A. Y. Silov, P. M. Koenraad, J.-M. Tang, M. E. Flatté, W. V. Roy, J. D. Boeck, and J. H. Wolter: "Spatial Structure of Mn-Mn Acceptor Pairs in GaAs". *Phys. Rev. Lett.* **95** (25 2005), 256402. DOI: 10.1103/PhysRevLett.95.256402. (Cit. on p. 85).

[204] Y. Wang, V. W. Brar, A. V. Shytov, Q. Wu, W. Regan, H.-Z. Tsai, A. Zettl, L. S. Levitov, and M. F. Crommie: *Mapping Dirac quasiparticles near a single Coulomb impurity on graphene*. 2012. DOI: 10.1038/nphys2379 (cit. on p. 85).

[205] V. W. Brar: *Scanning Tunneling Spectroscopy of Graphene and Magnetic Nanostructures*. dissertation, University of California, Berkeley, 2010 (cit. on pp. 87, 88, 90, 91).

[206] B. A. Younglove: "Dielectric constant of compressed gaseous and liquid oxygen". *J. Res. Nat. Bur. Stand. Sec. A: Phys. Ch.* **76A** (1 1971), 37–40. DOI: 10.6028/jres.076A.004. (Cit. on pp. 89, 90).

[207] C. L. Beattie: "Table of First 700 Zeros of Bessel". *BELL SYSTEM TECHNICAL JOURNAL* (1958). (Cit. on pp. 90, 91, 154).

[208] M. Pratzer, M. Morgenstern, private communication. (cit. on p. 95).

[209] P. Hohenberg and W. Kohn: "Inhomogeneous Electron Gas". *Phys. Rev. B* **136** (1964), 864. (Cit. on p. 102).

[210] W. Kohn and L. J. Sham: "Self-Consistent Equations Including Exchange and Correlation Effects". *Phys. Rev.* **140** (1965), A1133. (Cit. on p. 102).

[211] G. Kresse and J. Furthmüller: "Efficient iterative schemes for ab initio total-energy calculations using a plane-wave basis set". *Phys. Rev. B* **54** (1996), 11169. (Cit. on p. 102).

[212] G. Kresse and J. Hafner: "Ab initio molecular-dynamics simulation of the liquid-metal–amorphous-semiconductor transition in germanium". *Phys. Rev. B* **49** (1994), 14251. (Cit. on p. 102).

[213] P. E. Blöchl: "Projector augmented-wave method". *Phys. Rev. B* **50.24** (1994), 17953. DOI: 10.1103/PhysRevB.50.17953. (Cit. on p. 102).

[214] J. P. Perdew, K. Burke, and M. Enzerhof: "Generalized Gradient Approximation Made Simple". *Phys. Rev. Lett.* **77** (1996), 3865. (Cit. on p. 102).

[215] S. Grimme: "Semiempirical GGA-type density functional constructed with a long-range dispersion correction". *J. Comput. Chem.* **27** (2006), 1787. (Cit. on p. 102).

[216] F. Craes, S. Runte, J. Klinkhammer, M. Kralj, T. Michely, and C. Busse: "Mapping Image Potential States on Graphene Quantum Dots". *Phys. Rev. Lett.* **111** (2013), 056804. (Cit. on p. 103).

[217] P. Wahl, M. A. Schneider, L. Diekhöner, R. Vogelgesang, and K. Kern: "Quantum Coherence of Image-Potential States". *Phys. Rev. Lett.* **91** (10 2003), 106802. DOI: 10.1103/PhysRevLett.91.106802. (Cit. on pp. 111, 114).

[218] A. G. Borisov, T. Hakala, M. J. Puska, V. M. Silkin, N. Zabala, E. V. Chulkov, and P. M. Echenique: "Image potential states of supported metallic nanoislands". *Phys. Rev. B* **76** (12 2007), 121402. DOI: 10.1103/PhysRevB.76.121402. (Cit. on p. 111).

[219] K. Schouteden and C. Van Haesendonck: "Quantum Confinement of Hot Image-Potential State Electrons". *Phys. Rev. Lett.* **103** (26 2009), 266805. DOI: 10.1103/PhysRevLett.103.266805. (Cit. on pp. 111, 113, 120).

[220] K. Schouteden, A. Volodin, D. A. Muzychenko, M. P. Chowdhury, A. Fonseca, J. B. Nagy, and C. Van Haesendonck: "Probing quantized image-potential states at supported carbon nanotubes". *Nanotechnology* **21**.**48** (2010), 485401. (Cit. on p. 111).

[221] K. Schouteden and C. Van Haesendonck: "Lateral Quantization of Two-Dimensional Electron States by Embedded Ag Nanocrystals". *Phys. Rev. Lett.* **108** (7 2012), 076806. DOI: 10.1103/PhysRevLett.108.076806. (Cit. on pp. 111, 118).

[222] S. Stepanow, A. Mugarza, G. Ceballos, P. Gambardella, I. Aldazabal, A. G. Borisov, and A. Arnau: "Localization, splitting, and mixing of field emission resonances induced by alkali metal clusters on Cu(100)". *Phys. Rev. B* **83** (11 2011), 115101. DOI: 10.1103/PhysRevB.83.115101. (Cit. on p. 111).

[223] R. Fischer, S. Schuppler, N. Fischer, T. Fauster, and W. Steinmann: "Image states and local work function for Ag/Pd(111)". *Phys. Rev. Lett.* **70** (5 1993), 654–657. DOI: 10.1103/PhysRevLett.70.654. (Cit. on p. 111).

[224] R. Fischer, T. Fauster, and W. Steinmann: "Three-dimensional localization of electrons on Ag islands". *Phys. Rev. B* **48** (20 1993), 15496–15499. DOI: 10.1103/PhysRevB.48.15496. (Cit. on p. 111).

[225] H.-C. Ploigt, C. Brun, M. Pivetta, F. Patthey, and W.-D. Schneider: "Local work function changes determined by field emission resonances: NaCl/ Ag (100)". *Physical Review B* **76**.**19** (2007), 195404. (Cit. on p. 111).

[226] K. Lauwaet, K. Schouteden, E. Janssens, C. Van Haesendonck, and P. Lievens: "Dependence of the NaCl/Au(111) interface state on the thickness of the NaCl layer". *J. Phys. Condens. Matter* **24**.**47** (2012), 475507. (Cit. on p. 111).

[227] M. Feng, J. Zhao, and H. Petek: "Atomlike, Hollow-Core-Bound Molecular Orbitals of C60". *Science* **320**.**5874** (2008), 359–362. DOI: 10.1126/science.1155866. (Cit. on pp. 111, 113, 134).

[228] Note that in Refs. [115] and [. 116] a shortened notation is used, e.g. 1^+ for $\Psi^{(1^+)}$. (cit. on p. 111).

[229] B. Borca, S. Barja, M. Garnica, D. Sánchez-Portal, V. M. Silkin, E. V. Chulkov, C. F. Hermanns, J. J. Hinarejos, A. L. Vázquez de Parga, A. Arnau, P. M. Echenique, and R. Miranda: "Potential Energy Landscape for Hot Electrons in Periodically Nanostructured Graphene". *Phys. Rev. Lett.* **105** (3 2010), 036804. DOI: 10.1103/PhysRevLett.105.036804. (Cit. on pp. 111, 134).

[230] N. Armbrust, J. Güdde, P. Jakob, and U. Höfer: "Time-Resolved Two-Photon Photoemission of Unoccupied Electronic States of Periodically Rippled Graphene on Ru(0001)". *Phys. Rev. Lett.* **108** (5 2012), 056801. DOI: 10.1103/PhysRevLett.108.056801. (Cit. on p. 111).

[231] G. Giovannetti, P. A. Khomyakov, G. Brocks, V. M. Karpan, J. van den Brink, and P. J. Kelly: "Doping Graphene with Metal Contacts". *Phys. Rev. Lett.* **101** (2 2008), 026803. DOI: 10.1103/PhysRevLett.101.026803. (Cit. on pp. 113, 124).

[232] Y. Suganuma and M. Tomitori: "Tunneling condition dependence of electron standing waves in vacuum gaps on Au(111) and Si(001) observed by scanning tunneling microscopy". *Surf. Sci.* **438**.**1-3** (1999), 311 –318. DOI: 10.1016/S0039-6028(99)00596-8. (Cit. on p. 113).

[233] C. L. Lin, S. M. Lu, W. B. Su, H. T. Shih, B. F. Wu, Y. D. Yao, C. S. Chang, and T. T. Tsong: "Manifestation of Work Function Difference in High Order Gundlach Oscillation". *Phys. Rev. Lett.* **99** (21 2007), 216103. DOI: 10.1103/PhysRevLett.99.216103. (Cit. on pp. 116, 124).

[234] J. Li, W.-D. Schneider, R. Berndt, and S. Crampin: "Electron Confinement to Nanoscale Ag Islands on Ag(111): A Quantitative Study". *Phys. Rev. Lett.* **80** (1998), 3332–3335. DOI: 10.1103/PhysRevLett.80.3332. (Cit. on p. 117).

[235] J. I. Pascual, C. Corriol, G. Ceballos, I. Aldazabal, H.-P. Rust, K. Horn, J. M. Pitarke, P. M. Echenique, and A. Arnau: "Role of the electric field in surface electron dynamics above the vacuum level". *Phys. Rev. B* **75** (16 2007), 165326. DOI: 10.1103/PhysRevB.75.165326. (Cit. on p. 117).

[236] V. P. Ivanov, G. K. Boreskov, V. I. Savchenko, W. F. Egelhoff Jr., and W. H. Weinberg: "The chemisorption of oxygen on the iridium (111) surface". *Surf. Sci.* **61** (1976), 207 –220. DOI: 10.1016/0039-6028(76)90415-5. (Cit. on p. 124).

[237] C. Tao, L. Jiao, O. V. Yazyev, Y.-C. Chen, J. Feng, X. Zhang, R. B. Capaz, J. M. Tour, A. Zettl, S. G. Louie, H. Dai, and M. F. Crommie: "Spatially resolving edge states of chiral graphene nanoribbons". *Nature Physics* **7**.**8** (2011), 616–620. DOI: 10.1038/nphys1991. (Cit. on p. 128).

[238] P. Lacovig, M. Pozzo, D. Alfè, P. Vilmercati, A. Baraldi, and S. Lizzit: "Growth of Dome-Shaped Carbon Nanoislands on Ir(111): The Intermediate between Carbidic Clusters and Quasi-Free-Standing Graphene". *Phys. Rev. Lett.* **103** (16 Oct. 2009), 166101. DOI: 10.1103/PhysRevLett.103.166101. (Cit. on p. 128).

[239] S. Sakong and P. Kratzer: "Hydrogen vibrational modes on graphene and relaxation of the C-H stretch excitation from first-principles calculations". *The Journal of Chemical Physics* **133.5**, 054505 (2010), 054505. DOI: 10.1063/1.3474806. (Cit. on pp. 129, 130, 145).

[240] S. K. Singh and F. M. Peeters: "Vibrational properties of nanographene". *Nanoscale Systems MMTA* **2** (2013), 10–29. (Cit. on pp. 129, 130, 145).

[241] T. Zecho, A. Horn, J. Biener, and J. Küppers: "Hydrogen atom reactions with monolayer graphite edges on Pt(100) surfaces: hydrogenation and H abstraction". *Surface Science* **397.1-3** (1998), 108–115. DOI: http://dx.doi.org/10.1016/S0039-6028(97)00723-1. (Cit. on pp. 130, 146).

[242] J. Lahiri, Y. Lin, P. Bozkurt, I. I. Oleynik, and M. Batzill: "An extended defect in graphene as a metallic wire". *Nature nanotechnology* **5.5** (2010), 326–329. (Cit. on pp. 133, 134, 137, 139–141, 146).

[243] D. Stradi, S. Barja, C. Díaz, M. Garnica, B. Borca, J. J. Hinarejos, D. Sánchez-Portal, M. Alcamí, A. Arnau, A. L. Vázquez de Parga, R. Miranda, and F. Martín: "Electron localization in epitaxial graphene on Ru(0001) determined by moiré corrugation". *Phys. Rev. B* **85** (12 Mar. 2012), 121404. DOI: 10.1103/PhysRevB.85.121404. (Cit. on p. 134).

[244] F. Gargiulo and O. V. Yazyev: "Topological Aspects of Charge-Carrier Transmission across Grain Boundaries in Graphene". *Nano Letters* **14.1** (2014), 250–254. DOI: 10.1021/nl403852a. (Cit. on p. 134).

[245] M. Ondráček, P. Pou, V. Rozsíval, C. González, P. Jelínek, and R. Pérez: "Forces and currents in carbon nanostructures: are we imaging atoms?" *Physical review letters* **106.17** (2011), 176101. (Cit. on p. 139).

[246] F. Guinea, M. I. Katsnelson, and A. K. Geim: "Energy gaps and a zero-field quantum Hall effect in graphene by strain engineering". *Nature Physics* **6.1** (2009), 30–33. DOI: 10.1038/nphys1420. (Cit. on p. 140).

[247] N. Levy, S. A. Burke, K. L. Meaker, M. Panlasigui, A. Zettl, F. Guinea, A. H. Castro Neto, and M. F. Crommie: "Strain-Induced Pseudo–Magnetic Fields Greater Than 300 Tesla in Graphene Nanobubbles". *Science* **329.5991** (2010), 544–547. DOI: 10.1126/science.1191700. (Cit. on p. 140).

[248] Z. H. Ni, T. Yu, Y. H. Lu, Y. Y. Wang, Y. P. Feng, and Z. X. Shen: "Uniaxial Strain on Graphene: Raman Spectroscopy Study and Band-Gap Opening". *ACS Nano* **2.11** (2008), 2301–2305. DOI: 10.1021/nn800459e. (Cit. on p. 140).

[249] K. K. Gomes, W. Mar, W. Ko, F. Guinea, and H. C. Manoharan: "Designer Dirac fermions and topological phases in molecular graphene". *Nature* **7389** (2012), 306–310. DOI: 10.1038/nature10941. (Cit. on p. 140).

[250] L. Tapaszto, G. Dobrik, P. Lambin, and L. P. Biro: "Tailoring the atomic structure of graphene nanoribbons by scanning tunnelling microscope lithography". *Nat. Nanotechnol.* **3.7** (June 2008), 397–401. DOI: 10.1038/nnano.2008.149. (Cit. on p. 146).

[251] M. Bieri, M. Treier, J. Cai, K. Ait-Mansour, P. Ruffieux, O. Groning, P. Groning, M. Kastler, R. Rieger, X. Feng, K. Müllen, and R. Fasel: "Porous graphenes: two-dimensional polymer synthesis with atomic precision". *Chem. Commun.* (45 2009), 6919–6921. DOI: 10.1039/B915190G. (Cit. on p. 146).

[252] M. D. Rogers: "Partial fractions expansions and identities for products of Bessel functions". *J. Math. Phys.* **46** (2005), 043509. (Cit. on p. 151).

[253] F. Relton: *Applied Bessel Functions.* Blackie & Son, Limited, 1946 (cit. on p. 152).

[254] M. Abramowitz and I. A. Stegun: *Handbook of Mathematical Functions with Formulas, Graphs, and Mathematical Tables.* ninth Dover printing, tenth GPO printing. New York: Dover, 1964 (cit. on p. 154).

[255] Ruslan Temirov, private communication. (cit. on p. 156).

PART IV

Formal Addenda

APPENDIX E

Deutsche Kurzzusammenfassung *(German Abstract)*

Diese Arbeit handelt von Untersuchungen an Graphen-Nanostrukturen mittels Rastertunnelmikroskopie (engl. scanning tunneling microscopy, STM) und Rastertunnelspektroskopie (engl. scanning tunneling spectroscopy, STS) im Ultrahochvakuum bei tiefen Temperaturen (5,5 K). Der Schwerpunkt liegt dabei auf den lokalen elektronischen Eigenschaften. Die zugrunde liegenden Experimente basieren auf epitaktischem Graphen auf Ir(111) mit der typischen hohen strukturellen Qualität sowie auf davon abgeleiteten neuen Nanomaterialien.

Zuerst beschreiben wir die Entwicklung neuer Nanomaterialien, die den Erhalt der hohen strukturellen Qualität mit einer verminderten Substratwechselwirkung verbinden, insbesondere im Hinblick auf die quasi-relativistischen Dirac-Elektronen des Graphens. In diesem Kontext präsentieren wir die ersten Untersuchungen an Graphen-Quantenpunkten auf 15 Monolagen Silber auf Ir(111). In einer STS Studie beobachten wir einen Shockley-Oberflächenzustand, der stark demjenigen der Ag(111) Oberfläche ähnelt. Wir finden eine schwache Energieverschiebung des Bandes durch Verspannung der obersten Silberlagen sowie eine deutlich stärkere Verschiebung in Anwesenheit von Graphen. Der Oberflächenzustand ist unterdrückt, wenn die Silberlage nur noch eine einzelne Monolage hoch ist.

In einem nächsten Schritt präsentieren wir eine experimentelle Weiterentwicklung in Form eines Probensystems, in dem metallische Oberflächenzustände mit störenden Einflüssen auf die lokale Zustandsdichte vollständig unterdrückt sind. Hierbei handelt es sich um sauerstoffinterkaliertes Graphen auf Ir(111). Mittels Rastertunnelmikroskopie beobachten wir neue Sauerstoff-Überstrukturen auf Iridium unter Graphen und zwei verschiedene Aufladungseffekte in der lokalen Zustandsdichte der Quantenpunkte in STS Untersuchungen. Wir zeigen die erste eindeutige Beobachtung eingesperrter Dirac-Zustände auf

Graphen-Quantenpunkten und berechnen ausgehend von unseren experimentellen Daten eine Dispersionsrelation, die mit derjenigen einer komplementären Messung des Systems in winkelaufgelöster Photoemission übereinstimmt. Außerdem finden wir weitere Hinweise auf eine Entkopplung der Kohlenstofflage vom Metallsubstrat durch Berechnungen im Rahmen der Dichtefunktionaltheorie, einer Dirac-Signatur in STS Punktspektren sowie charakteristische Streumuster. Zusätzlich zu der Beobachtung des Dirac-Confinements sind unsere Untersuchungen damit für weitere Experimente von grundlegender Bedeutung, die Sauerstoff zur Entkopplung einer Graphenlage nutzen.

Wir erweitern unsere Studie im Hinblick auf das Spektrum der hochenergetischen, unbesetzten Oberflächenzustände in Form von Bildpotenzialzuständen. Hier zeigen wir zum ersten Mal eine Größenabhängigkeit des Spektrums aufgrund eines Confinements auf Graphen-Quantenpunkten, die als Potenzialtöpfe dienen. Wir erklären das Auftreten eines bevorzugten Zustandes im Tunnelprozess, der nicht dem Grundzustand entspricht, durch ein Zusammenspiel von lokaler Zustandsdichte und Impulserhaltung im Tunnelprozess. Die Lage der Bildpotenzialzustände kann durch Erzeugen eines zusätzlichen Potenzials in Form einer Interkalationslage beeinflusst werden. Damit realisieren wir einen Quantentopf, der sowohl in seiner Breite als auch in seiner Tiefe einstellbar ist. Außerdem diskutieren wir die Bedeutung der Messbarkeit der lokalen Austrittsarbeit für die Bestimmung des lokalen Dotierungsniveaus in Graphen(interkalations)verbindungen.

In einem weiteren Schritt wenden wir uns der Situation an den Rändern der Graphen-Quantenpunkte zu und diskutieren die Möglichkeit, die lokalen Bindungsverhältnisse an den Rändern mittels inelastischer Tunnelspektroskopie näher zu beleuchten.

Schließlich berichten wir über die Beobachtung eines metallischen Zustandes in der lokalen Zustandsdichte, der durch eindimensionale Defekte in einer geschlossenen Monolage epitaktischen Graphens auf Ir(111) generiert wird.

APPENDIX F

Liste der Teilpublikationen
(List of Publications)

Teile dieser Arbeit wurden bereits veröffentlicht in den folgenden Fachzeitschriften:
Parts of the results presented in this thesis are published/in review as follows:

[2] *Mapping Image Potential States on Graphene Quantum Dots*
Fabian Craes, Sven Runte, Jürgen Klinkhammer, Marko Kralj, Thomas Michely, and Carsten Busse
Physical Review Letters 111, 056804 (2013)
http://prl.aps.org/abstract/PRL/v111/i5/e056804

[1] *Dirac Electron Confinement on Graphene Quantum Dots*
Wouter Jolie, Fabian Craes, Marin Petrović, Nicolae Atodiresei, Vasile Caciuc, Stefan Blügel, Marko Kralj, Thomas Michely, and Carsten Busse
Physical Review B, accepted (2014)

[52] *Tuning the Electronic Properties of Graphene Quantum Dots with Silver*
Wouter Jolie, Fabian Craes, Thomas Michely, and Carsten Busse
in preparation

Abgesehen von diesen Themen habe ich an folgenden Publikationen mitgearbeitet:
Apart from these topics I also contributed to the following articles:

[109] *Ion Impacts on Graphene/Ir(111): Interface Channeling, Vacancy Funnels, and a Nanomesh*
Sebastian Standop, Ossi Juhani Lehtinen, Charlotte Herbig, Georgia Lewes-Malandrakis, Fabian Craes, Jani Kotakoski, Thomas Michely, Arkady V. Krasheninnikov, and

Carsten Busse
Nano Letters, 2013 May 8; 13(5):1948-55
http://pubs.acs.org/doi/abs/10.1021/nl304659n

[128] *Spin-polarized surface state in EuO(100)*
Jürgen Klinkhammer, Martin Schlipf, Fabian Craes, Sven Runte, Thomas Michely, and Carsten Busse
Physical Review Letters 112, 016803 (2014)
http://prl.aps.org/abstract/PRL/v112/i1/e016803

Konferenz- und Seminarbeiträge als präsentierender Autor:
Conference contributions to:

- 544. WE-Heraeus-Seminar, 11.11-13.11.2013, Bad Honnef (DE)
- Universidad Autónoma de Madrid, 17.04.2013, Madrid (ES)
- The European Workshop on Epitaxial Graphene'13, 27.01.-31.01.2013, Aussois (F)
- 29th European Conference on Surface Science, 02.09.-07.09.2012, Edinburgh (GB)
- Seminar zur Oberflächenforschung, 20.01.2012, Bonn (DE)
- SFB 608 PhD Workshop, 28.09.-30.09.2011, Hamburg (DE)
- The Capri Spring School 2011: Topological Insulators, 10.04.-17.04.2011, Anacapri (IT)
- SFB 608 PhD Workshop 2010, 01.09.-03.09.2010, Amsterdam (NL)

APPENDIX G

Offizielle Erklärung

Ich versichere, dass ich die von mir vorgelegte Dissertation selbständig angefertigt, die benutzten Quellen und Hilfsmittel vollständig angegeben und die Stellen der Arbeit - einschließlich Tabellen, Karten und Abbildungen -, die anderen Werken im Wortlaut oder dem Sinn nach entnommen sind, in jedem Einzelfall als Entlehnung kenntlich gemacht habe; dass diese Dissertation noch keiner anderen Fakultät oder Universität zur Prüfung vorgelegen hat; dass sie - abgesehen von unten angegebenen Teilpublikationen - noch nicht veröffentlicht worden ist, sowie, dass ich eine solche Veröffentlichung vor Abschluss des Promotionsverfahrens nicht vornehmen werde. Die Bestimmungen der Promotionsordnung sind mir bekannt. Die von mir vorgelegte Dissertation ist von Priv.-Doz. Dr. Carsten Busse betreut worden.

Köln, 17.02.2014

Fabian Craes